Optics of Diatom Frustules
Toward Applications and Photobiology

Dissertation

zur Erlangung des Grades eines
Doktors der Naturwissenschaften
(Dr. rer. nat.)

am Fachbereich Physik
der Freien Universität Berlin

vorgelegt von

Mohamed Ghobara

Berlin
2024

Erstgutachter: Prof. Dr. Paul Fumagalli

Zweitgutachterin: Prof. Dr. Stephanie Reich

Tag der Disputation: 10/02/2025

For my father & my mother spirits……..

Mahmoud Essam Ghobara

(1942/2013)

Thanaa Ghobara

(1949/2016)

Abstract

Diatoms are an outstanding group of unicellular microalgae that can be found in almost all aquatic ecosystems, playing critical roles in the global carbon fixation and oxygen cycle. The cell wall surrounding diatom living cells, named frustule, is synthesized from amorphous hydrated silica with outstanding properties and plenty of geometries and ultrastructures varying between different species. The frustule consists of subcomponents; valves and girdle bands, held together in the living state but can be extracted and retrieved after death. The retrieved valves/girdle bands exhibit an outstanding ultrastructure, including the presence of nano-/micro-pores arrays resembling the artificial photonic crystal slabs and diffraction gratings. That is why the optical properties and light modulation capabilities of these siliceous parts have recently captured a wide interest and have been suggested for several optical applications as an eco-friendly and cost-effective alternative to artificial structures. Despite the previous efforts to understand the light modulation capabilities of these frustules and their subcomponents, more efforts are still required, and many missing gaps need to be filled. Therefore, this thesis aims to deepen the understanding of their light modulation capabilities, while focusing on their optical near field and Fresnel regime. That could help increase the applicability of their valves in optical applications and understanding the possible photobiological roles of their frustules. Additionally, the thesis also aims to investigate implementing the extracted clean valves as optical building blocks in photonic and optoelectronic applications, which adds to the previous efforts in the literature.

First, a novel analytical approach has been employed to numerically analysis the light modulation capabilities of the valve/frustule of small-size pennate diatom *Gomphonema parvulum*. The simulations were based on the 2D finite element frequency domain (FEFD) method. This approach enabled revealing the correlation of distinct optical phenomena; including thin-film interference, waveguiding, diffraction-driven focusing, photonic jet generation, Talbot effect, and guided-mode resonance, to the distinct optical elements comprising the valve/frustule. Such phenomena influence the valves'/frustules' optical near-field and Fresnel regime and overlap in a wavelength-dependent manner to yield a complex interference pattern. Moreover, in order to broaden the understanding of the diffraction-driven focusing by diatom valves, the far-field optical microscopy techniques have been employed to study this behavior mainly in the Fresnel regime of structurally distinct valves covering a wide range of geometries, ultrastructure, and sizes, showing that this phenomenon could be more widespread among diatoms. The latter study showed, for the first time, that the diatom valves could also focus the light when being illuminated from the side. The 2D FEFD numerical analysis showed an ability to predict and analytically explain such behavior. Furthermore, the optical near-field of the valves of pennate diatom *Gomphonema parvulum* and centric diatom *Aulacosira* sp. have been studied utilizing an aperture-type scanning optical near-field microscopy (a-SNOM), operated in illumination and collection mode. The latter being used for the first time to study the optical near-field of diatom valves. The SNOM results, which provided new insights especially that of collection mode, have also been compared to the 2D FEFD numerical analysis results. Additionally, a novel methodology has been developed to study the 2D periodicities and symmetries of diatoms' pore arrays based on image processing and analysis techniques, especially the 2D autocorrelation function analysis, offering an accurate and reproducible methodology that could help assess these pore arrays for relevant applications.

Toward applications, a novel method for fabricating diatom-based SERS hybrid substrates was employed by obtaining a smooth ultrathin gold film over diatom valves. This method allowed comparing the ability of structurally distinct valves in enhancing SERS signal, where the magnitude of the enhancement likely depended on the valve ultrastructure. Additionally, a preliminary study on incorporating diatom valves into organic MISM photodetectors was also carried out.

In conclusion, I believe that this thesis offers new insights and deeper analytical understanding of the abilities of diatom valves/frustules to modulate light. On the one hand, this answers some questions while opening up many new.

Abstrakt

Kieselalgen sind eine herausragende Gruppe einzelliger Mikroalgen, die in fast allen aquatischen Ökosystemen zu finden sind und eine entscheidende Rolle bei der globalen Kohlenstofffixierung und dem Sauerstoffkreislauf spielen. Die Zellwand, genannt Frustel, die die lebenden Zellen der Kieselalgen umgibt, wird aus amorphem hydratisiertem Siliziumdioxid mit herausragenden Eigenschaften in zahlreichen Geometrien und Ultrastrukturen synthetisiert, die sich zwischen den verschiedenen Arten unterscheiden. Die Frustel besteht aus Unterkomponenten, den Klappen und Gürtelbändern, die im lebenden Zustand zusammengehalten werden, aber nach dem Tod extrahiert und getrennt werden können. Die separierten Klappen/Gürtelbänder weisen eine herausragende Ultrastruktur auf, einschließlich der Anwesenheit von Nano-/Mikroporenanordnungen, die künstlichen photonischen Kristallen und Beugungsgittern ähneln. Aus diesem Grund haben die optischen Eigenschaften und Lichtmodulationsfähigkeiten dieser siliziumhaltigen Systeme in letzter Zeit großes Interesse geweckt und wurden für mehrere optische Anwendungen als umweltfreundliche und kostengünstige Alternative zu künstlichen Strukturen vorgeschlagen. Trotz der bisherigen Bemühungen, die Lichtmodulationsfähigkeiten dieser Schalen und ihrer Unterkomponenten zu verstehen, sind noch weitere Anstrengungen erforderlich, um die vielen offenen Fragen zu klären. Daher zielt diese Arbeit darauf ab, das Verständnis ihrer Lichtmodulationsfähigkeiten zu vertiefen und sich dabei auf das optisches Nahfeld und das Fresnel-Regime zu konzentrieren. Dies könnte dazu beitragen, die Anwendbarkeit der Klappen in optischen Anwendungen zu erhöhen und die mögliche photobiologische Rolle der Schalen zu verstehen. Darüber hinaus zielt die Arbeit auch darauf ab, die Implementierung der extrahierten, sauberen Klappen als optische Bausteine in photonischen und optoelektronischen Anwendungen zu untersuchen, was die bisherigen Bemühungen in der Literatur ergänzt.

Zunächst wurde ein neuartiger analytischer Ansatz verwendet, um die Lichtmodulationsfähigkeiten der Klappen/der Frusteln der kleinen pennaten Kieselalge *Gomphonema parvulum* numerisch zu analysieren. Die Simulationen basieren auf der 2D-Methode der finiten Elemente im Frequenzraum (FEFD). Dieser Ansatz ermöglicht es, die Korrelation verschiedener optischer Phänomene – darunter Dünnschichtinterferenz, Wellenleitung, beugungsbedingte Fokussierung, Erzeugung photonischer Jets, Talbot-Effekt und Resonanz im geführten Modus – mit den verschiedenen optischen Elementen aufzudecken, aus denen die Klappe/der Schalenkörper besteht. Solche Phänomene beeinflussen das optische Nahfeld und den Fresnel-Bereich der Klappen/der Frusteln und überlappen sich wellenlängenabhängig, wodurch ein komplexes Interferenzmuster entsteht. Um das Verständnis der beugungsbedingten Fokussierung durch Kieselalgenklappen zu erweitern, wurden außerdem Lichtmikroskopietechniken im Fernfeld verwendet, um dieses Verhalten hauptsächlich im Fresnel-Bereich strukturell unterschiedlicher Klappen zu untersuchen, die ein breites Spektrum an Geometrien, Ultrastrukturen und Größen abdecken, was zeigt, dass dieses Phänomen bei Kieselalgen weit verbreitet sein könnte. Die letztgenannte Studie zeigte zum ersten Mal, dass die Kieselalgenklappen das Licht auch fokussieren können, wenn sie von der Seite beleuchtet werden. Die numerische 2D-FEFD-Analyse ergab, dass ein solches Verhalten vorhergesagt und analytisch erklärt werden kann. Darüber hinaus wurde das optische Nahfeld der Klappen der pennaten Kieselalge *Gomphonema parvulum* und der zentrischen Kieselalge *Aulacosira* sp. mithilfe der optischen Nahfeldmikroskopie mit Apertur (a-SNOM) untersucht, die im Beleuchtungs- und Sammelmodus betrieben wurde. Letzterer wurde zum ersten Mal verwendet, um das optische Nahfeld von Kieselalgenklappen zu untersuchen. Die SNOM-Ergebnisse, die neue Erkenntnisse lieferten, insbesondere im Hinblick auf den Sammelmodus, wurden auch mit Ergebnissen der numerischen 2D-FEFD-Analyse verglichen. Darüber hinaus wurde eine neuartige Methodik entwickelt, um die 2D-Periodizitäten und Symmetrien der Porenanordnungen von Kieselalgen zu untersuchen, die auf Bildverarbeitungs- und Analysetechniken, insbesondere der 2D-Autokorrelationsfunktionsanalyse, basiert und eine genaue und reproduzierbare Methodik bietet, die bei der Bewertung dieser Porenanordnungen für relevante Anwendungen helfen könnte.

In Bezug auf Anwendungen wurde ein neuartiges Verfahren zur Herstellung von Kieselalgen-basierten SERS-Hybridsubstraten eingesetzt, indem ein glatter ultradünner Goldfilm über den Kieselalgenklappen aufgebracht wurde. Dieses Verfahren ermöglichte den Vergleich strukturell unterschiedlicher Klappen bezüglich der Fähigkeit zur Verstärkung des SERS-Signals, wobei das Ausmaß der Verstärkung wahrscheinlich von der Ultrastruktur des Klappen abhängt. Darüber hinaus wurde auch eine vorläufige Studie zur Einbindung von Kieselalgenklappen in organische MISM-Fotodetektoren durchgeführt.

Ich bin der Meinung, dass diese Arbeit neue Erkenntnisse liefert und zu einem tieferes analytisches Verständnis der Fähigkeiten von Kieselalgenklappen/-frusteln zur Modulation von Licht beitragen kann. Einerseits konnten dadurch einige Fragen beantwortet werden, andererseits wurden jedoch viele neue aufgeworfen, die weiter untersucht werden müssen.

Table of Contents

List of abbreviations

2D	two-dimensional
2D ACF	two-dimensional autocorrelation function
2D FFT	two-dimensional fast Fourier transform
2D PSDF	two-dimensional power spectral density function
3D	three-dimensional
A	Ampere
Å	Angstrom
a.u.	arbitrary units
AFM	atomic force microscopy
a-SNOM	aperture-type scanning near-field optical microscopy
Au	gold
C	Coulomb
CCD	charge-coupled device
CMOS	complementary metal-oxide-semiconductor
Cr	chromium
CS	cross-section
DC	direct current
DG	diffraction grating
EDLs	electric double layers
EDX	energy-dispersive X-ray
EM	electromagnetic waves
eV	electron volt
FDTD	finite difference time domain method
FEFD	finite element frequency domain method
FEM	finite element method
FIB-SEM	focused ion beam scanning electron microscopy
FWHM	full width at half maximum
GMR	guided mode resonance
HOMO	highest occupied molecular orbital
Hz	Hertz
IL	ionic liquid
LED	light-emitting diode
LM	light microscopy
LUMO	lowest unoccupied molecular orbital
mg	milligram
MISM	metal-insulator-semiconductor-metal device
ml	milliliter
mm	millimeter
mM	millimolar
MPTMS	(3-mercaptopropyl)trimethoxysilane
MSM	metal-semiconductor-metal device

Mya millions of years ago
NA numerical aperture
NIR near Infrared
nm nanometer
NPs nanoparticles
P3HT poly(3-hexylthiophene-2,5-diyl)
PAR photosynthetic active radiation
PC photonic crystal
PCBM fullerene derivative [6,6]-phenyl C_{61} butyric acid methyl ester
PDEs partial differential equations
PDMS polydimethylsiloxane
PJ photonic jet
PL photoluminescence
PMLs perfectly matched layers
PVD physical vapor deposition
R6G rhodamine 6G
RF radio frequency
rpm rounds per minute
SAM self-assembled monolayer
SBC scattering boundary conditions
SDV silica deposition vesicle
SEM scanning electron microscopy
SERS surface enhanced Raman scattering
SI international system of units
$Si(OH)_4$ silicic acid
Si-OH silanol group
SITs silicic acid transport proteins
SNOM scanning near-field optical microscopy
sp. species
SPM scanning probe microscopy
spp more than one species
SPR surface plasmonic resonance
STM scanning tunnelling microscopy
TE transverse electric field
TEM transmission electron microscopy
TIFF tag image file format
TIR total internal reflection
TM transverse magnetic field
Torr Torricelli
UV ultraviolet
V Volt
Vis visible
W Watt
Wb Weber
µl microliter
µm micrometer

1 Introduction

Throughout the last few centuries, our ability to modulate light has been developed alongside the growing understanding of its nature and its interaction with matter. Employing this knowledge led to a technological uprising with countless examples of innovative optical elements, materials, techniques, and instruments, starting with the conventional optical components operating based on the principles of geometrical optics such as lenses and mirrors—which helped develop numerous devices, including optical microscopes and telescopes—and ending with plenty of tiny optical elements (of sizes and/or ultrastructure in the μm to nm range) that could modulate light based on wave and quantum optics principles [1,2]. Such tiny optical elements enable reducing the size of photonic and optoelectronic devices while increasing their performance, a step towards the development of advanced optical communications, highly efficient sensors, and quantum computers.

The fabrication of micro-/nano-structured optical elements, such as diffraction gratings, photonic crystals [3], and metasurfaces [4], is often sophisticated, involving toxic chemicals and cleanroom techniques (such as lithography) that demand a complex infrastructure, requiring high energy and expensive operating and materials costs [5,6]. The drawbacks of current fabrication techniques, if added to the efforts to lower our ecological footprint and suppress anthropogenic climate change, will lead to the conclusion that we need alternative eco-friendly and cost-effective fabrication techniques.

Looking to nature—with an evolutionary history of more than 3 billion years [7]—living organisms have developed their own way to modulate light for survival. Today, nature is full of inspiring living organisms that can effectively modulate light based on their μm to nm structural features [8–10] and offer exceptional solutions to complex optical problems. Autotrophic organisms (*i.e.*, plants and algae) use light modulation and management to increase their photosynthetic efficiency [11] and to get natural colors for various purposes [12]. Other organisms also need light modulation, *e.g.*, for their vision systems and camouflage [13]. Such biological systems have offered inspiration for many years in various fields through the biomimicry approach [14–16]. Interestingly, the micro-/nano-structured biomaterials produced by these living organisms can be utilized as eco-friendly alternatives in applications if their materials are suitable and can be extracted.

Among the autotrophic organisms, Bacillariophyceae (**diatoms**) is considered an outstanding class of microalgae that is present in almost all aquatic ecosystems [17], including those of extreme conditions (see, for example, [18–21]). They can also be cultivated in the lab, industrial photobioreactors, or even on a larger scale for research and commercial purposes [22–25]. Diatoms build a remarkably well-designed micro-/nano-structured micro-shell (called **frustule**) made of **amorphous hydrated silica** and surrounding their living cells [17]. The size of most frustules is in the µm range, with a diameter/length varying from several µm to a few hundred µm depending on the species and environmental circumstances [17,26]; however, it can reach extreme values down to ≈ 2 µm [27] or up to a few mm [28,29]. The frustule is, in general, porous and has a petri-dish-like structure, consisting of two overlapping **valves** and surrounded by **girdle bands** (**Fig. 1.1**). According to the valve symmetry, diatoms can be generally divided into centric and pennates (see examples illustrated in **Fig. 1.1**). Recent studies suggested that some diatom frustules are built for a purpose, *e.g.*, to attain enhanced mechanical strength against predators [30–33], possess micro-/nano-fluidic properties [34,35], and exhibit potential photobiological roles [36,37]. That could partially explain the outstanding ecological success and the significant diversification of diatoms around the globe [17,38,39].

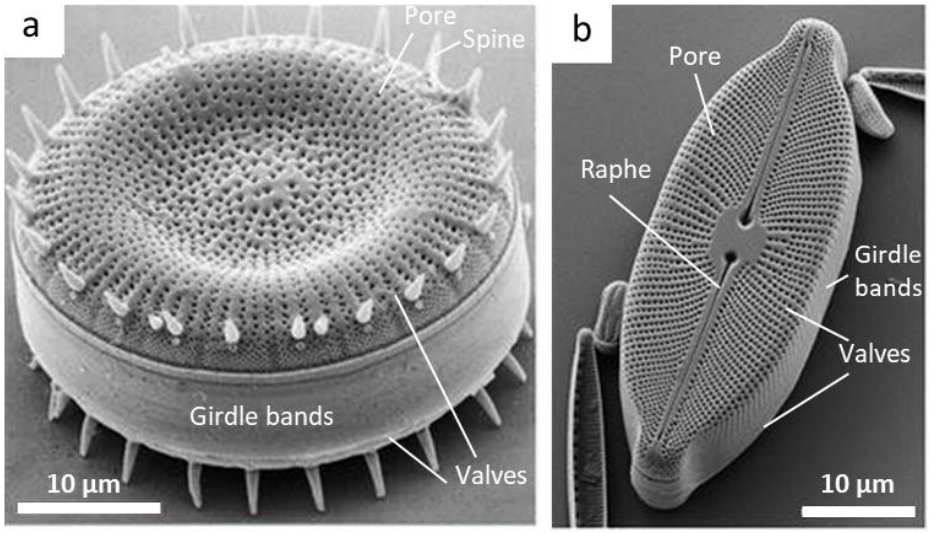

Fig. 1.1. SEMs showing intact diatom frustules of the centric *Stephanodiscus* sp. (**a**) and the pennate *Cosmioneis* sp. (**b**). The SEMs are adapted from Mann *et al.* [40].

Interestingly, it has been observed that the structure of diatom valves/girdle bands is often similar to fabricated 2D photonic crystals and diffraction gratings due to the periodicities and symmetries of their micro/nanopores, which may enable us to utilize them in applications as an eco-friendly alternative, by producing comparably complex structures simply through cultivation at ambient conditions [41–43]. These ideas motivated the study of the light modulation capabilities of diatom valves/girdle bands of a few species and have led to the successful implementation of diatom valves in a number of photonic and optoelectronic

applications on the lab scale [36,44–46], with an increasing publication record over time.

This thesis focuses on studying the light modulation capabilities of ornamented siliceous valves that could be beneficial for optical applications, but moreover, it also raises questions regarding possible photobiological roles when considering intact frustules immersed underwater. In the following sections, I will briefly introduce diatoms, followed by a summary of the state-of-the-art in the field of diatom frustule optics and photonics, while at the end of this chapter, I will illustrate the objectives and outline of the thesis.

1.1. Diatoms

Bacillariophyceae (Diatoms) is a class of eukaryotic, autotrophic, **unicellular** microalgae belonging to Kingdom Chromista [47]. Diatoms are an exceptionally ecologically successful group with huge diversity that covers almost all aquatic habitats (*i.e.*, marine, fresh, brackish, etc.) and even extend to humid terrestrial places [17], enabling maintaining their considerable contribution to the carbon and oxygen cycle on a global scale [48,49]. Depending on the species, diatom living cells could occur either separated or in colonies and can exist as planktonic (*i.e.*, floating within the photic zone), benthic/periphytic (*i.e.*, living near the floor), epiphytic (*i.e.*, adhered to submerged plants), epizoic (*i.e.*, adhered to marine animal bodies), or epilithic (*i.e.*, adhered to the submerged rocks) [17,40]. **Fig. 1.2** shows examples of diatom living cells, as appearing under light microscope (**LM**). During their diplontic life cycle, diatoms mainly reproduce via asexual reproduction by mitosis [17], while at certain stages and/or under certain environmental circumstances, they could initiate sexual reproduction, leading to auxospores formation [50,51].

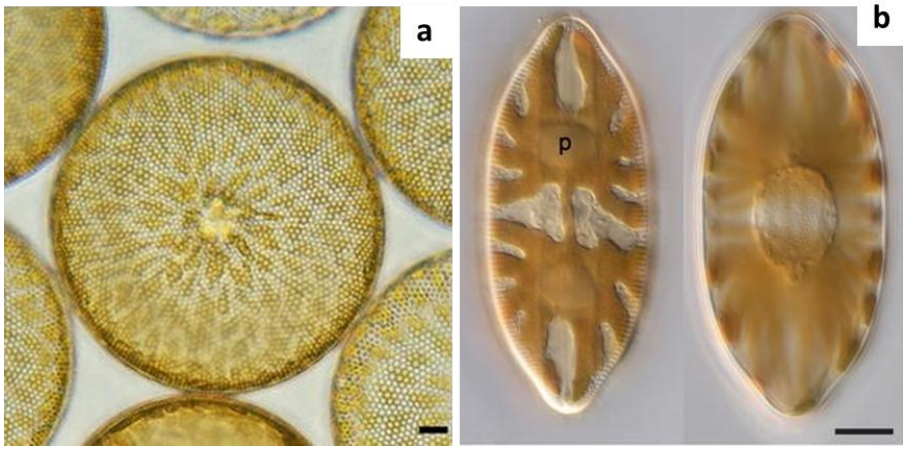

Fig. 1.2. LM micrographs showing living diatom cells of the centric *Coscinodiscus* sp. Containing many small chloroplasts (**a**) and the pennate *Lyrella* sp. Containing a large lobed chloroplast (**b**). Scale bars are 10 µm. These figures are merged from Mann *et al.* [40].

Diatoms are a very diverse group with a vast number of species, potentially up to 10^5 or even more [52,53], with a wide range of morphologies and ultrastructures (*e.g.*, **Fig 1.3**). Such diversity evolved relatively quickly if compared to the photosynthetic evolutionary history extending over 3.4 billion years [54], given that the first diatom observed in fossil records returns to the early Jurassic period (since about 200 Mya) [55] and that a higher diversification was correlated to the Cenozoic era (especially in the range 66–16 Mya) [56].

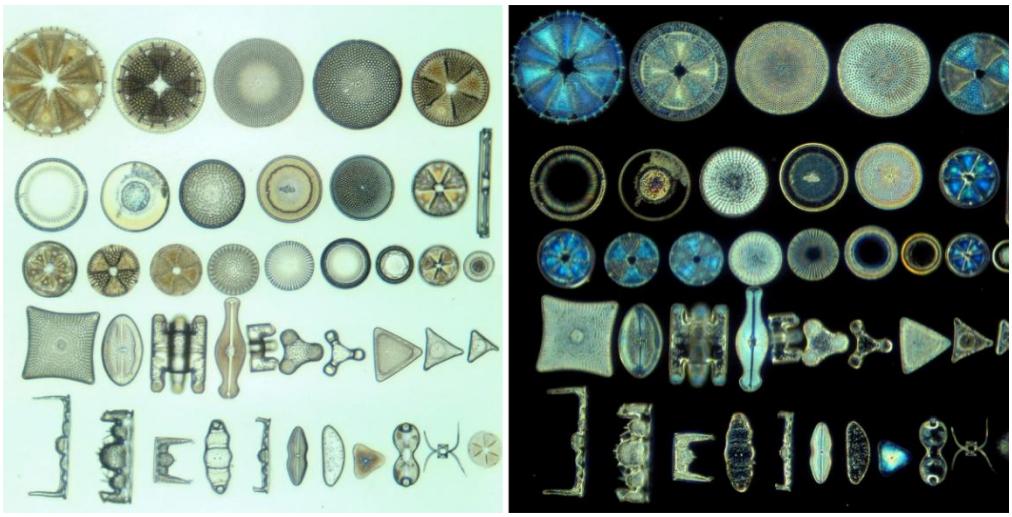

Fig. 1.3. An optical micrograph showing arranged clean valves of different diatom species on a microscope slide under bright-field (at left) and dark-field (at right) optical microscope, reflecting the diversity of diatom shapes. The different optical appearance of the valves indicates their different light modulation capabilities, which depend on their ultrastructure as well as illumination direction. This arrangement was prepared and imaged by **Mr. Emiliano Bellotti** (Italy, 2023), and is used here after his kind permission.

The frustule (*i.e.*, the siliceous cell wall of diatoms) is considered one of the most outstanding features of diatoms, which shows remarkable evolutionary progress for silica biomineralization. In the following subsections, I will briefly explain the geometry and ultrastructure of diatom frustules (**Subsection 1.1.1**), their biogenesis and morphogenesis (**Subsection 1.1.2**), and the utilization of these frustules in various applications (**Subsection 1.1.3**).

1.2.1. Frustule geometry and ultrastructure

As mentioned, the geometry and ultrastructure of diatom frustule and its parts have a huge variety (*e.g.*, **Fig. 1.3**) and can be considered a species-specific feature, which enabled early diatomists to classify diatoms into **species** (*i.e.*, a taxonomic level that contains all living organisms having common unique features) and **genera** (*i.e.*, a taxonomic level that includes all species having similar features) [17]. Despite this diversity, the frustules generally have a **petri-dish-like** configuration (see **Fig. 1.1**, which is further illustrated in **Fig. 1.4**). In this configuration, the **epivalve** is slightly

bigger than the **hypovalve**, and both are connected through a girdle (which consists of girdle bands). Each valve together with its adjacent girdle band(s) is known as a theca; therefore, in total, the whole frustule can be considered as a merge of two thecae (a hypotheca fitted into an epitheca) [17]. In living cells, different frustule parts are backed with organic matrices, holding them together [57].

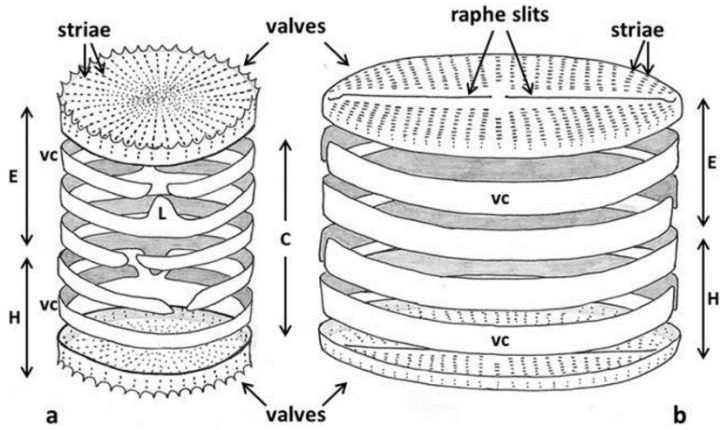

Fig. 1.4. A schematic diagram illustrates the petri-dish like structure of a centric (**a**) and a raphid pennate (**b**) frustule. E stands for epitheca; H for hypotheca; C for girdle (consisting of girdle bands); L for tongue-like extension; and VC for valvocopula (*i.e.*, girdle band adjacent to the valve). This figure is reproduced from Cox [58].

The progress in understanding the complex ultrastructure of diatom frustules was associated with the advancement of microscopy techniques. The major tools used to study the frustule morphology and ultrastructure are summarized in **Table A.1** (**Appendix A**). During the last century, the frustules of many species and genera have been extensively studied using electron microscopy, which enables the revealing of their outstanding diverse micro- and nano-features (see, for example, **Figs. 1.1** and **1.5**, and see further Round *et al.* [17]). The frustules of most diatom species are porous with **pore diameters** mostly ranging from **3 nm** to **2 µm** and pore spacing ranging from **a few tens** or **hundreds of nm** to **a few µm**, depending on the species [17,26]. The valves of some diatom species exhibit a complex multilayer structure (*e.g.*, **Fig. 1.5b**), where each layer has its distinct porosity scale and periodicity, while other species show simpler structures (*e.g.*, **Fig. 1.5a**). The same also for the girdle, as some species have simple girdle bands, while other species show complex structures [17,59].

The major perforation of the valves is called **areolae** (*singular* areola) and is often arranged in rows, the so-called **striae** (*singular* stria) [17]. There are different 3D designs of areolae, including lineolate (having elongated pores, such as *Navicula* spp. [17]), punctate (having round or oval pores with a simple channel structure, *e.g.* **Fig. 1.5a**), and loculate (having complex pores with a chamber-like structure, *e.g.* **Fig. 1.5b**) areolae [60]. In many species, the areolae are covered from the inner or outer face with a mesoporous thin layer of silica, the so-called **pore occlusion** [60], as can

be seen in **Fig. 1.5**. It should be noted that the multilayer nature of the valve can be linked to the presence of loculate areolae (see, for example, Figures 2 and 3 in [61]).

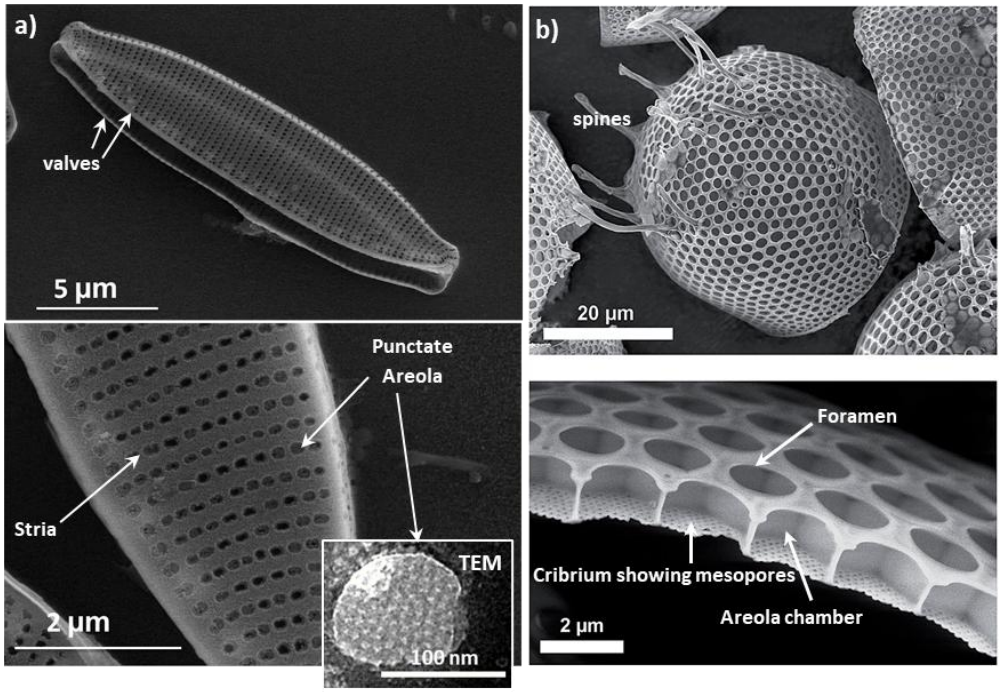

Fig. 1.5. (**a**) SEMs showing the outer valve face of the pennate diatom *Nitzschia palea*, which have punctate areolae arranged in transverse striae. The inset in (**a**) is a TEM showing the hymenate pore occlusion covering the areolae entrance that cannot be revealed under SEM. (**b**) SEM of the outer valve face of the centric diatom *Stephanopyxis turris* with a cross section in a single valve showing their loculate areolae with outer foramen layer (consisting of large pores) and inner cribrium layer (consisting of mesopores). **Fig.** (**b**) is adapted from Jantschke *et al.* [62]. The whole figure is modified from Ghobara *et al.* [60].

According to the valve symmetry, diatoms are divided into two major classes: centrics and pennates of radial or bilateral symmetry, respectively (*e.g.* **Fig. 1.1**). While the pennates can be subdivided according to the presence or absence of a special structure called **raphe** (*i.e.*, a fissure in the valve face, see for example **Figs. 1.1b** and **1.4b**) into three categories: araphid, monoraphid, biraphid. The raphid pennate diatom can be further divided according to the position of the raphe in the valve [17,40].

Finally, it should be noted that there are many terms associated with the valve/frustule geometry and ultrastructure, as can be seen in [17,26,40], which are not all included in the thesis. Newly introduced terms will be explained throughout the thesis, where necessary.

1.2.2. The frustule biogenesis and morphogenesis

The intricate ultrastructure of diatom siliceous frustules leads to questions: how can living cells synthesize such structures naturally from silica? how is the

morphogenesis of this glassy structure (of nanoscale ultrastructural features) reproducible between individuals of the same species? and how have these microorganisms evolved? Although the complete understanding is not there yet, I will briefly illustrate the answers to some of these questions up to what has been understood so far.

In a dividing diatom cell, after the completion of mitosis, cytokinesis, and the formation of the so-called **silica deposition vesicle** (**SDV**), the biogenesis and morphogenesis of new valves start inside the SDV [63], which appears at the equator (*i.e.*, the middle) of the cell in the example illustrated in **Fig. 1.6**. Within the SDV, the valve formation often starts from a central nucleation site. During the progress of valve formation, the micro-/nano-pores and other 3D complex ultrastructural features are constructed (see, for example, Figures 10-15 in [63]). After the completion of this step, the new valves are exocytosis, and the new daughter cells are released, each with a parental epivalve and a new hypovalve (**Fig. 1.6**). Thereafter, a lateral SDV specific for the first girdle band is formed, helping the cell grow and increase its height. Additional girdle bands—if needed—are formed subsequently after the exocytosis of the formed band [63].

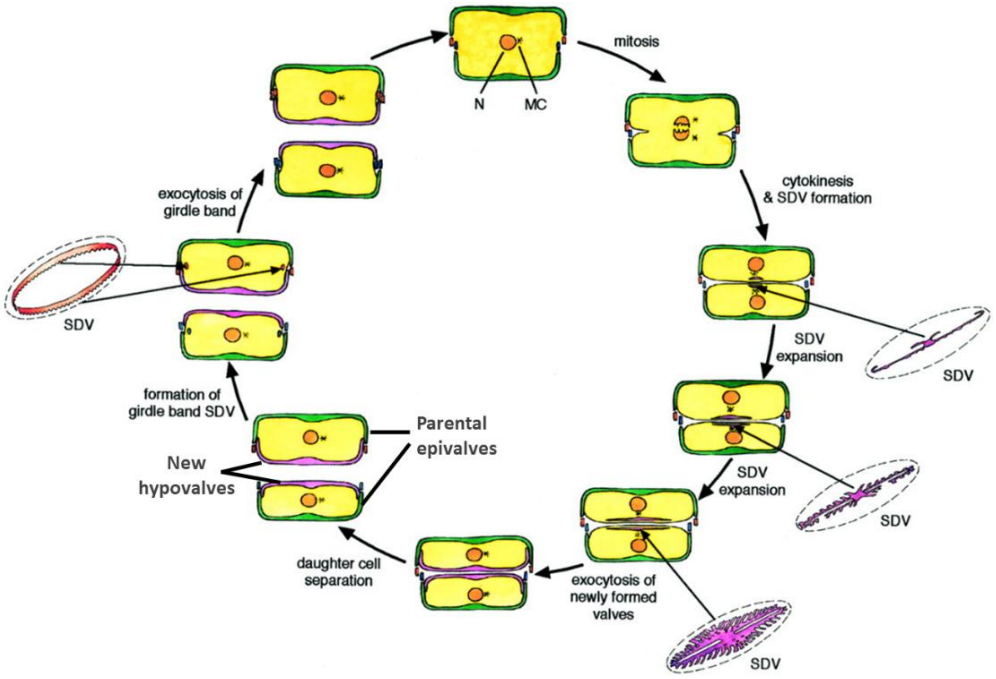

Fig. 1.6. A schematic diagram showing the valve/girdle band biogenesis. N stands for Nucleus and MC for microtubule center. The parental valves (epivalves) have a green color, while new valves (hypovalves) have a violet color. The figure is modified from Zurzolo *et al.* [64].

Despite the explained knowledge of different steps for valve/girdle band biogenesis, understanding the molecular mechanisms occurring inside the SDV to help shape their complex ultrastructure is still incomplete [65]. Generally, to have a

successful morphogenesis process on the molecular level, we need sufficient amounts of the precursor(s), an efficient transportation mechanism for the precursor from outside the cell to inside the SDV, establishing a nucleation site, precise morphogenesis mechanisms (somehow genetically encoded, as it is preserved over generations for each species), and appropriate physico-chemical factors contributing to morphogenesis [63,65].

As the biogenesis and morphogenesis of diatom valves/girdle bands is a **bottom-up building approach**, thus the living cells need a flux of silica precursor inside SDVs to be condensed and form the frustule's complex silica structures. Generally, silicic acid **$Si(OH)_4$**—available in all aquatic habitats—is considered the essential precursor for silica biomineralization [66]. It is mainly present in its monomer form in aqueous solutions at concentrations below 2 mM (the saturation concentration at neutral pH) and can spontaneously condense at higher concentrations to yield oligomers, polymers, and even nanoparticles [67]. Diatoms uptake silicic acid from the surrounding environment by two modes: active or passive transport, depending on its concentration gradient [67]. This helps living cells accumulate it, even if it is present in low concentrations, by active transport utilizing silicic acid transport proteins (**SITs**) found on the cell membrane [67]. Surprisingly the uptaken silicic acid is present in a soluble state (not condensate) in the cytosol, even for concentrations exceeding the natural saturation limit. This is probably due to the formation of stable complexes with organic molecules that help inhibit the uncontrolled condensation inside diatoms [67]. The presence of special vehicles termed **silicon transport vesicles** (of nanometric sizes) has been hypothesized, helping transport the precursor to the SDV, where the controlled condensation occurs.

Different models have been proposed to explain the molecular mechanisms of valve morphogenesis inside the SDV. Some of these models do not depend on the presence of organic molecules or pre-templates such as **diffusion-limited aggregation** [66], while other models suggest the presence of a **pre-template** and propose different roles of organic molecules in the morphogenesis process. The pre-template models have been supported by revealing many **organic molecules** associated with the morphogenesis process, including **silaffins**, **silacidins**, **cingulins**, **silicanins**, and **long-chain polyamines** [68–70]. Interestingly, **cytoskeleton** elements; including **microtubules** and **actin filaments**, were also found to play crucial roles in morphogenesis [63,71–74]. Finally, despite all the models and debates, more efforts are still needed to unveil the actual morphogenesis mechanisms.

1.2.3. Utilization of diatom frustules in applications

For a long time, fossil diatom frustules have been utilized in various applications as a source of porous silica because of their unique physical and chemical properties,

including high porosity, relatively high surface area, biocompatibility, high absorptivity, and also being commercially available in considerable amounts and for competitive cheap prices (from a few tens to a few hundred dollars per metric ton depending on the grade and the industry involved) [75–78]. These fossil frustules are obtained from **diatomite** (also known as diatomaceous earth), which is a soft, lightweight **sedimentary rock** composed mainly of siliceous diatom remnants deposited and preserved since very long time ranging from thousands to millions of years [75,77,79]. The true nature of diatomite was discovered in the 19th century in the Lüneburg Heath, north Germany, and simultaneously in, North America near West Point, NY [80]. In the last century, diatomite commercial production has been started, producing various commercial grades that are widely used in filtration and purification, thermal insulation, agriculture (as soil amendments and mechanical insecticides for dry conditions), as a carrier (for instance, as a carrier for nitroglycerin in Alfred Nobel's dynamite), food additives, building materials, fillers, and abrasives [75–77,79,81]. The estimated amount of diatomite available in the known mines can cover the current market size for about 350 years; thus—despite being unsustainable—it can cover the needs for a relatively long time [81]. Fossil frustules have also been employed as a valuable tool in gas and oil exploration, in archaeology, and as ecological and paleoenvironment indicators [82].

In recent years, the utilization of diatom siliceous parts (mainly valves) in many nanotechnological applications has been studied, including the fabrication of sensing platforms (relaying on different working mechanisms [83–88]), catalysis platforms [89–93], microfluidic systems [87,94,95], superhydrophobic surfaces [96], supercapacitors [97], batteries [98], and drug delivery systems [99,100], as well as photonic and optoelectronic applications [36,44] (see, further, reviews in [44,60,77,101,102]). Many nanotechnological applications require intact diatom valves with high homogeneity and purity, which diatomite usually cannot offer. That is why in many nanotechnological relevant studies the diatom valves were extracted from cultivated living cells, which is considered a sustainable approach. As the frustule in living diatom cells is associated with the protoplast as well as other organic components and matrices, including the diatotepum (*i.e.*, a thin layer separates the protoplast and the frustule) and the envelope (*i.e.*, an organic encasing surrounds the frustule) [57,103]. Therefore, sample processing (via oxidization and digestion, *e.g.*, by employing acids or hydrogen peroxide) is required to eliminate such components and retrieve the siliceous parts of the frustule (valves and girdle bands) separated for further studies and applications [104]. Furthermore, in many cases, chemical (and/or physical) modifications are required to amend the physical and chemical properties of the valves to the desired nanotechnological application. Different modification approaches have been reviewed in [105–107].

1.2. **Frustule optics and photonics** (State-of-the-art)

In recent decades, the optics and photonics of diatom frustules have received increasing attention. So far, the frustules (mainly valves) of only a few diatom species (representing fewer genera) have been studied. The conclusions from these studies do not lead to general assumptions for all diatom species and genera, and the huge ultrastructural diversity of diatom frustules drives the conclusion that many more features are still hidden and awaiting exploration. A comprehensive review of previous studies—before the thesis—has already been published in **Ghobara *et al.*** [44]. Here, I briefly summarize the major features reported in previous work, considering the recent advances in this field at the time of preparing the thesis.

1.2.1. Photoluminescence

Photoluminescence (**PL**) occurs when molecules/atoms absorb photons to be excited to a higher energy level, then re-emitting these photons and relax back to ground level. Clean diatom valves have been reported to exhibit PL when illuminated by shorter wavelengths (*e.g.*, UV radiation, which leads to PL mainly in the blue spectral range) [108–111], similar to silica nanoparticles [112], mesoporous silica [113], and fused silica glass. This behavior is correlated to the excitations of the surface silanol groups (Si-OH) and surface defects (*e.g.*, the non-bridged oxygen hole centers). Therefore, increasing the surface defects and silanol groups would increase the PL signal magnitude. Interestingly, the PL signal has been found to be dependent on the species, the frustule ultrastructure, the surrounding environment, the culture age, and the cleaning method [109,111]. Furthermore, the PL signal can be adjusted by modifying the chemical composition of the valves, *e.g.*, by doping the silica with germanium oxide [114] or organic dyes [115], and it can also be quenched, *e.g.*, by doping the silica with nickel [116].

1.2.2. Photonic crystal features

Photonic crystals (**PCs**) are structures having a periodic feature with a periodicity scale comparable to light wavelength λ, which could occur in one-, two-, or three-dimensions. In the case of dielectric PCs, the electric permittivity (ε) periodically changes within the structure, which influences the light propagation inside it. That leads to PC characteristics, including the possible presence of **photonic bandgap** at which specific frequencies ($f = c/\lambda$, where c is the speed of light) cannot propagate within the periodic structure, analogous to the electronic bandgap in semiconductors [117,118]. The bandgap can be either **complete** (such as the example shown in **Fig. 1.7**) or **incomplete** (where a range of frequencies is not propagated only at certain direction(s) in the lattice at a given light polarization) depending on the PC structural parameters and refractive index contrast within it. The PCs can control light

propagation through such photonic bandgaps (that can be tuned) or by introducing defects and cavities, which increase their applicability. In recent decades, PCs have been implemented in several applications, for example, optical communications and the fabrication of photonic integrated circuits, lasers, solar cells, imaging systems, and various sensors [119].

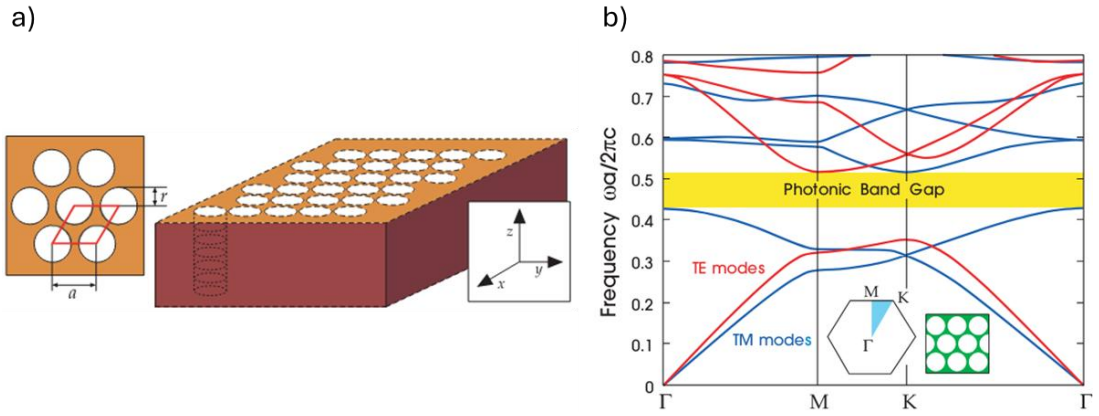

Fig. 1.7. (**a**) An example of a 2D PC consisting of pores (of a radius *r* and spacing *a*) drilled within a dielectric slab and filled with air. The pore array exhibits a hexagonal lattice structure. (**b**) The photonic band structure of the hexagonal lattice in (**a**), considering the material of the slab has high ε (= 13), which—together with lattice parameters—leads to a complete photonic band gap (the yellow-shaded area). The blue and red lines represent TE and TM bands, respectively. The inset in (**b**) shows the first Brillouin zone. This figure consists of merged figures obtained from Joannopoulos *et al.* [120].

Many examples of PCs have been found in living organisms, giving them a spectacular structural coloration for several purposes [13,121]. When looking at diatom valves/girdle bands of different species, one can find several examples that look like 2D PC slabs of periodicities occurring in the **UV-Vis-NIR spectral ranges** and thicknesses in the range of a few hundred nm to a few µm (see SEMs of different species in [17,26]). But still, the valves/girdle bands are of finite size and often have more complicated ultrastructure (such as the presence of multilayers and other optical components) and/or additional periodicities and symmetries [122,123] (see further **Appendix B**), which need to be considered when analysis their PC features.

In 2004, the photonic band structure and waveguiding properties of the valves and girdle bands of the centric *Coscinodiscus granii* (both have PC slab-like structures and periodicities comparable to the visible spectral range, but each has distinct symmetry and lattice parameters) have been numerically analyzed for the first time [42]. The authors explained that the waveguided modes coupled into the valve/girdle can be further split into distinct PC modes that lead to photonic resonances, some of which occur in the visible spectral range [42]. Since then, the resemblance of diatom valves/girdle bands to PC slabs has captured a wide interest. Yamanaka *et al.* [124] have hypothesized that the experimentally observed attenuation in the blue light wavelengths propagated through a *Melosira variance*

valve can be attributed to the parabolic dispersion relations observed for the blue spectral range in the calculated photonic band structure (see Figure 4 in [124]), which means that the group velocities become slower at this spectral range. Later, Goessling and his coworkers [43,125] experimentally observed that the girdle bands of the centric *Coscinodiscus granii* could display a photonic pseudo bandgap (*i.e.,* incomplete bandgap) at the near infrared (**NIR**) spectral range, which has been confirmed through the FDTD simulations [43,125]. They also observed that the pseudogap can be shifted to the visible spectral ranges by changing the incident angle Θ_{inc} (see Figure 3 in [125]). Very recently, the light modulation capabilities, including PC features, of valves/frustules of the pennate *Nitzschia filiformis* have been experimentally and numerically studied [126].

Still, more efforts are needed to unveil the possible PC features of different valves/girdle bands, which could be beneficial for applications but also may determine possible photobiological relevance (if any).

1.2.3. Far-field diffraction grating behavior

A few studies have examined the far-field diffraction grating behavior of a few diatom valves (belonging to the genus *Coscinodiscus*) when normally illuminating their surface (see, e.g., **Fig. 1.8**).

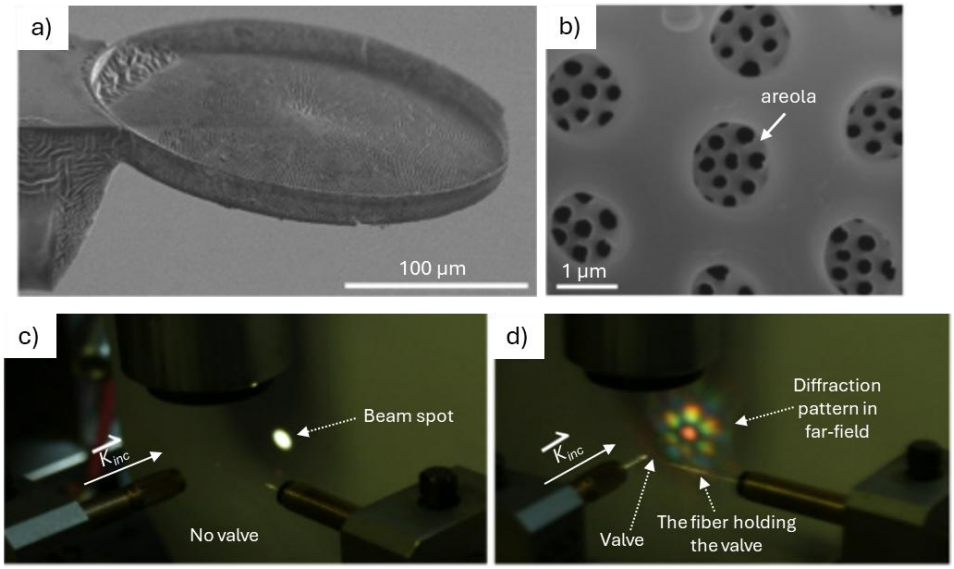

Fig. 1.8. (**a**) SEM showing a *Coscinodiscus walesii* valve glued to an optical fiber. (b) SEM showing the valve's areolae, which have a hexagonal arrangement pattern. (**c**) The supercontinuum white light source gave a white spot on a flat white paper placed in the optical far-field when there was no diatom valve encountering the beam path. (**d**) A hexagonal diffraction pattern was generated in transmittance in the far-field by inserting a *C. walesii* valve in the beam path (the beam size was about 20 µm). This figure consists of merged and modified figures obtained from Kieu *et al.* [127].

In Losic *et al.* [41], the illumination of a *Coscinodiscus* sp. valve (or its Polydimethylsiloxane (PDMS) replica) with a He-Ne laser generates a hexagonal

diffraction pattern in transmittance with peaks up to the second order of diffraction in air. Noyes *et al.* [128] demonstrated that illuminating the valves of *Coscinodiscus wailesii*—mounted on a needle tip—generated a hexagonal diffraction pattern in air (also in water) of high intensity in transmittance and of lesser intensity in the reflectance. Their experimental results agreed with the theoretical expectation for a 2D diffraction grid of a pore spacing of about 2 µm (the same as the studied valve). Similar results were observed in Kieu *et al.* [127], where a hexagonal diffraction pattern was obtained in far-field upon illuminating a *Coscinodiscus wailesii* valve—mounted on a supporting optical fiber—with a supercontinuum laser source in air, as demonstrated in **Fig. 1.8d**. In all cases, the symmetry of the diffraction pattern was correlated to the symmetry of pore arrays in the studied valve.

1.2.4. Diffraction-driven focusing in diatom valves

The ability of some diatom valves to act as microlenses and focus the incident light in the transmittance is considered one of the most interesting light modulation capabilities yet discovered. In Stefano *et al.* [129], when a clean valve of the centric diatom *Coscinodiscus wailesii* (of diameter ≈ 150 µm) was illuminated with a 100 µm laser beam (diode laser, 785 nm), the beam was confined into a tiny spot (of full-width at half maximum FWHM = 8.1 µm at its narrowest point) that occurred in transmittance, about 104 µm behind the valve center, correlated to the position of the hyaline area (*i.e.*, an areolae-free zone of diameter ≈ 15 µm) (**Fig. 1.9**). This behavior was mainly linked to the diffraction contribution from all areolae.

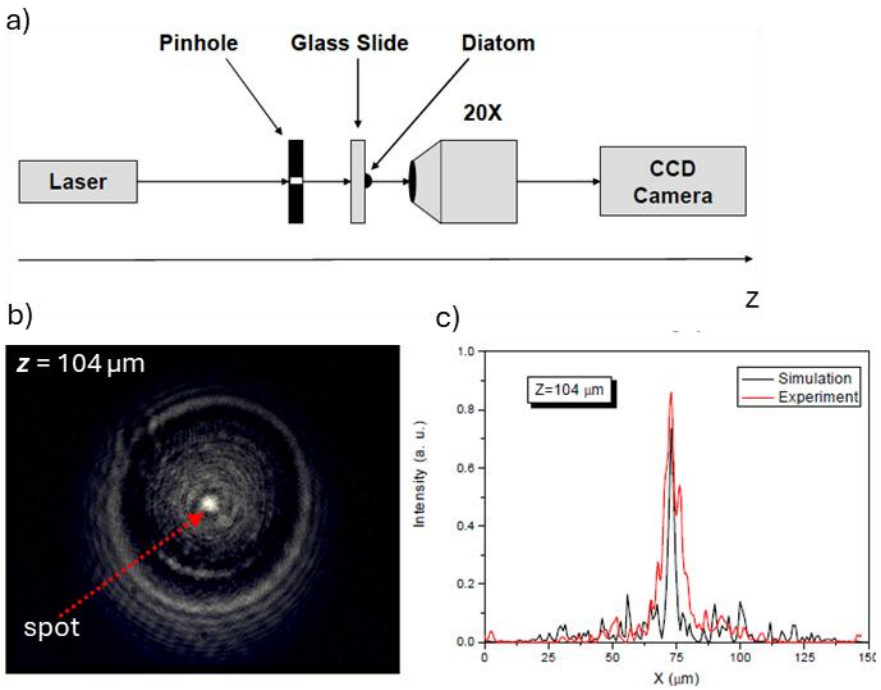

Fig. 1.9. (**a**) The experimental setup employed to study the focusing ability of *Coscinodiscus wailesii* valves. (**b**) The experimental results at the focusing maximum behind a *C. wailesii* valve (in the transmittance). (**c**) Fitting the experimental results to the simulation results

(obtained by the Wide-Angle Beam Propagation Method) at focusing maximum. This figure consists of merged figures obtained from Stefano *et al.* [129].

Later, the visible light focusing ability has been reported for a few centric (mainly belonging to *Coscinodiscus* and *Arachnoidiscus* genera) [130–137] and pennate (very recent studies [138,139]) diatoms. All studies confirmed that this behavior is linked to the diffraction contributed by the valves' ultrastructure, which leads to a complex interference pattern with alternating constructive and destructive interference maxima [130,133,134,140]. In some cases, the consecutive interference maxima observed in the simulations cannot be observed in the experimental results due to the resolution limitation of the optical system used for imaging [140]. Some studies have shown that the focusing of Photosynthetic active radiation (**PAR**) can occur inside the frustule in water and cytoplasm, which has been assumed to be correlated to photosynthesis, while the harmful UV radiation is found to be attenuated or rather focused at larger distances outside the frustule [137,139–141]. All these studies have raised the question of whether this type of focusing is widespread among different genera and species and how we could expect a given valve to induce diffraction-driven focusing.

1.2.5. Employing diatom valves in optical applications

The focusing abilities observed in some diatom valves suggested utilizing them as diffractive **microlenses** in applications, and an array of these valves could potentially act as an **array of microlenses**. For example, De Tommasi *et al.* [132] have utilized the valves of *Arachnoidiscus* sp. combined with optical eigenmode decomposition to achieve a sub-diffraction focusing spot in the far-field that can be employed in **super-resolution microscopy**. The valves of *Coscinodiscus* spp. (or their template replica) can also be utilized as **micro-diffraction gratings** based on their far-field diffraction grating behavior [41]. Interestingly, Maibohm *et al.* [133] suggested employing the valves of *Coscinodiscus granii*—which displayed consecutive constructive and destructive interference spots along their optical axis—in **optical switching**.

Moreover, some valves (with or without modifications) have been investigated as optical components in a number of photonic and optoelectronic devices (sometimes as an analogous or alternative to PC slabs). For instance, some valves have been proposed as **PL-based sensors** [111,142], and some have been proposed to improve the performance of **Fluorescence-based sensors** [143,144]. The valves of a few species, mostly belonging to the genus *Pinnularia*, have been extensively investigated in fabricating surface-enhanced Raman scattering (**SERS**)-**based sensors** after being modified or coated with a plasmonic material (often metallic nanoparticles) [145,146]. Additionally, it has been proposed that utilizing diatom valves in optoelectronic devices (such as solar cells) could enhance the absorption within the photoactive layer [147–149], which could explain the

successful attempts for employing valves in **solar cells** reported in the literature [98,150,151].

Furthermore, depositing dense layers of the valves on substrates could be interesting for some applications. For example, Su *et al.* [152] showed that the drop-casted layers of clean frustules (and also dried intact cells) over glass substrate exhibit UV filtering capabilities, and the magnitude of filtering depends on the species utilized. This could potentially be employed in fabricating bio-based **UV filters**.

Currently, many challenges are still confronting the incorporation of diatom valves/girdle bands in commercial optical devices, which require more research efforts in various directions—among other things—to (i) investigate the light modulation capabilities of more valves/girdle bands (with various designs), (ii) understand the physical phenomena behind these abilities, (iii) enabling better control of the arrangement, bonding, and monolayer formation of the valves/girdle bands over various substrates, and (iv) building different strategies to modify their optical properties.

1.2.6. Potential roles of the frustule in diatom photobiology

Photobiology is the study of the influence of light on living organisms and their biological functions. Light—especially PAR, where λ ranges from 400 nm to 700 nm—is essential for diatom living cells, like any autotrophic organism that relies on photosynthesis for survival [153]. A number of mechanisms have been developed in diatoms to maximize photosynthesis efficiency (by optimizing PAR inside chloroplasts, where the photosynthetic pigments and photosystems exist) and simultaneously protect the cell from high light intensities and/or harmful UV spectral ranges. These mechanisms include regulations on the molecular, intracellular, and behavioral levels [44,45]. Interesting examples of these mechanisms are the phototactic observed in pennates [154]—where the pennate living cells move toward or away from a light source depending on its spectral composition and its intensity—and chloroplast migration observed in polyplastidic centrics [155]—where the chloroplasts migrate inside the cell toward or away from the frustule depending on the light.

In recent years, it has been hypothesized that diatom frustules may also play photobiological roles. It has been proposed that the diffraction-driven focusing spots observed for PAR spectral range could improve photosynthesis by enhancing the PAR inside chloroplasts [137–141]. That is often suggested, combined with having different mechanisms to shield the cells from harmful UV radiation [37,156]. Moreover, the evanescence coupling between guided modes and chloroplasts has also been suggested [42]. Furthermore, a wavelength-dependent transmittance has

been reported for a *Coscinodiscus wailesii* valve, suggesting that the shorter wavelengths (blue spectral range) could be much attenuated inside the cell compared to the longer wavelengths (red spectral range) [128]. That may help avoid high blue light intensities, which is dominant underwater [157]. Additionally, Romann *et al.* [136] observed an orientational dependent focusing behavior in *Coscinodiscus centralis* valves in a way that could help trap the light inside the cell and minimize backscattering.

Still, there is no clear experimental evidence of the photobiological roles of diatom frustules reached, given that many studies built the assumptions on the observed light modulation behavior of clean valves in air. Therefore, more efforts are needed to investigate these assumptions.

1.3. Objectives of the thesis

The objectives of the thesis can be summarized as follows.

- To make progress in understanding the light modulation capabilities of structurally distinct diatom valves employing numerical and experimental techniques (considered **fundamental study**). On the one hand, this could help select suitable species for the target applications; on the other hand, it could help to understand the possible photobiological roles when considering their intact frustules in their natural habitat.
- To preliminary investigate the utilization of diatom valves as optical building blocks into photonic and optoelectronic devices (considered **application study**). This could enhance light management inside the optoelectronic devices and, thus, increase the efficiency of these devices (if optimized).

1.4. Outline of the thesis

The thesis is organized as follows. **Chapter 2** covers all physics background needed to understand the thesis, including the background of the major experimental and numerical methods used. **Chapter 3** describes materials, methods, numerical analysis conditions, and experimental setups used throughout the following chapters. While the main results are presented and discussed in **Chapters 4** – **7**. In **Chapter 4**, a novel analytical approach is proposed to analyze light modulation capabilities of the structurally complex valve/frustule of pennate diatom *Gomphonema parvulum* (used as a model) in the Fresnel regime and optical near-field employing the Finite element frequency domain (FEFD) method. The proposed approach helps to emphasize the role of integrated optical components and understanding overlapping optical phenomena. **Chapter 5** reveals the diffraction-

driven light-focusing capabilities of a number of structurally distinct diatom valves by employing far-field optical microscopy while applying trans-illumination or side-illumination, emphasizing the role of valves' ultrastructure. In **Chapter 6**, the near-field light modulation capabilities of the valves of the pennate *Gomphonema parvulum* and the centric *Aulacoseira* sp. are experimentally investigated using an aperture-type scanning optical near-field microscopy (a-SNOM). **Chapter 7** explores the influence of utilizing structurally distinct diatom valves in fabricating SERS hybrid substrates on the SERS signal enhancement magnitude. Following that, **Chapter 8** gives a summary of the main outcomes and conclusions. Additionally, **Appendix B** demonstrates a proposed methodology for evaluating periodicities and symmetries of 2D pore arrays that appear in diatom frustules and their degree of perfection. **Appendix C** offers a preliminary study on incorporating diatom valves as optical building blocks into MISM organic photodetectors.

2 Theoretical Background

2.1. Electromagnetic waves propagation in dielectric media

At a macroscopic scale, light-matter interaction can be explained based on the well-established principles of geometrical optics, which help explain some optical phenomena, such as light focusing by lenses and mirrors, employing ray tracing models [1]. By revealing the wave nature of light during the 19th century, **wave optics** emerged as a branch of optics that helps explain optical phenomena such as diffraction, interference, and polarization. Understanding light as an electromagnetic (**EM**) wave with a given wavelength (λ) and frequency (f) has revolutionized science and technology [2,158]. Later, quantum optics arose to explain the quantum-level light-matter interaction, which further boosts technology [159]. Most of this thesis is related to wave optics while dealing with EM wave propagation in **dielectric media**.

Generally, the propagation of EM waves can be explained with the help of Maxwell's equations and their derivatives. The macroscopic Maxwell's equations, which are relevant to this thesis, can be written in their differential form (SI units) as follows [160,161].

$$\nabla \cdot \mathbf{D} = \rho \quad (\mathbf{2.1})$$

$$\nabla \cdot \mathbf{B} = 0 \quad (\mathbf{2.2})$$

$$\nabla \times \mathbf{E} = -\frac{\partial \mathbf{B}}{\partial t} \quad (\mathbf{2.3})$$

$$\nabla \times \mathbf{H} = \mathbf{J} + \frac{\partial \mathbf{D}}{\partial t} \quad (\mathbf{2.4})$$

Where **D** stands for electric displacement (C/m^2), **B** for magnetic flux density (Wb/m^2), **E** for electric field strength (V/m), **H** for magnetic field strength (A/m), ρ for volume electric charge density (C/m^3), **J** for electric current density (A/m^2).

In **lossless dielectric** media, where the electrical conductivity is neglectable, the absorption of propagated EM waves is negligible. The EM waves propagate within such media affected by their **electric permittivity** ($\varepsilon = \varepsilon_o\varepsilon_r$, where ε_o and ε_r refer to permittivity of free space and a medium, respectively) and **magnetic permeability** ($\mu = \mu_o\mu_r$, where μ_o and μ_r refer to permeability of free space and a medium, respectively). Considering **linear**, **isotropic**, and lossless dielectric media

free of charges ($\rho = 0$) or **current** ($\mathbf{J} = 0$), the four Maxwell's equations can be written in their **frequency domain form** as follows [161].

$$\nabla \cdot \mathbf{D} = 0 \quad (\mathbf{2.5})$$
$$\nabla \cdot \mathbf{B} = 0 \quad (\mathbf{2.6})$$
$$\nabla \times \mathbf{E} = -i\omega\mathbf{B} \quad (\mathbf{2.7})$$
$$\nabla \times \mathbf{H} = \ i\omega\mathbf{D} \quad (\mathbf{2.8})$$

In the frequency domain form, the **time-harmonic conditions** are applied, where the electric field (as well as magnetic field) is assumed to vary sinusoidally with time, $\mathbf{E}(t) = \mathbf{E_0}e^{i\omega t}$, where ω is the angular frequency (ω = 2π*f*). The time derivative $\partial/\partial t$ in **eqs. 2.3** and **2.4** is then replaced by $i\omega$, as seen in **eqs. 2.7** and **2.8**.

The following constitutive relations are often used to replace **D** and **B** in the previous equations.

$$\mathbf{D} = \varepsilon_0\varepsilon_r\mathbf{E} = \varepsilon\mathbf{E} \quad (\mathbf{2.9})$$
$$\mathbf{B} = \mu_0\mu_r\mathbf{H} = \mu\mathbf{H} \quad (\mathbf{2.10})$$

From the previous equations and conditions, the **wave equation** can be derived and can be written for the electric field as follows [161].

$$\nabla^2\mathbf{E} + \omega^2\mu\varepsilon\mathbf{E} = 0 \quad (\mathbf{2.11})$$

or

$$\nabla^2\mathbf{E} + K^2\mathbf{E} = 0 \quad (\mathbf{2.12})$$

Also known as **Helmholtz equation**, where wave number $K = \omega\sqrt{\mu\varepsilon}$.

If we consider a **heterogeneous non-magnetic** medium (comparable to the porous diatom frustules, where the electric permittivity spatially changes between the frustule and surrounding medium that also fills the pores), the wave equation can also be written as follows.

$$\nabla^2\mathbf{E} + {K_0}^2n^2\mathbf{E} = 0 \quad (\mathbf{2.13})$$

Where wave number $K_0 = \ \omega\sqrt{\mu_0\varepsilon_0} = \frac{\omega}{c} = \frac{2\pi}{\lambda_{vacc}}$, $\varepsilon_r = n^2$, and $\mu_r = 1$. *n* stands for refractive index, λ_{vacc} for light wavelength in free space/air, *c* for velocity of light in vacuum.

In this thesis, a numerical analysis for the wave propagation will be carried out employing the wave equation in its frequency domain form implemented in the **Finite element method** (see, further, **sections 2.4** and **3.2**).

2.2. Optical field regions

Generally, when an antenna emits EM waves, the space surrounding it can be divided into three major regions, including reactive near-field, radiative near-field, and far-field, depending on the wavelength, antenna dimensions, and the distance from it [162]. The radiative near-field and far-field are also known as the Fresnel and Fraunhofer regimes, respectively. These concepts can also be used to describe the optical field regions surrounding an object (of a size comparable to or larger than λ) interacting with light. The optical reactive near-field describes the EM field at the surface of (or at observation distances R << λ from) an object scattering light, where phenomena such as evanescence can be observed. While the radiative near-field (*i.e.*, Fresnel regime) describes the EM field in an intermediate transition region between the reactive near-field and far-field, where Fresnel diffraction dominates. The optical far-field (*i.e.*, Fraunhofer regime) describes the EM field at observation distances R >> λ from the object [163]. In the context of diffraction, the transitions between different optical regions are often defined through the so-called **Fresnel number** ($N_F = r^2/\lambda R$, where r is the radius of the object) [164], as illustrated in the example shown in **Fig. 2.1**. In this thesis, the optical phenomena that occur within the reactive near-field (will be named **near-field**) and radiative near-field (will be named **Fresnel regime**) are investigated, as they are more relevant to photonic and optoelectronic applications as well as photobiology.

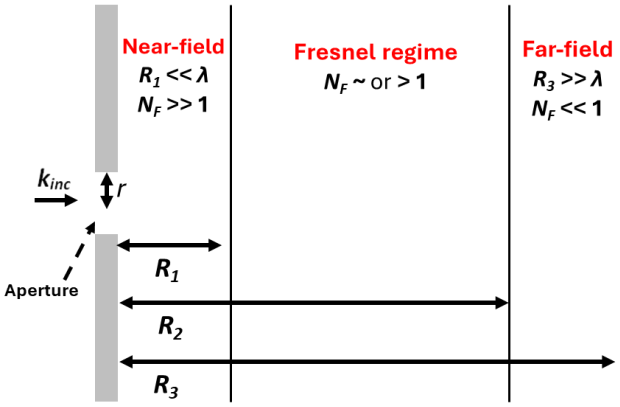

Fig. 2.1. A sketch showing an aperture illuminated from the *left-hand side*. The regions beyond the aperture can be separated into three regions depending on the Fresnel number. R_1, R_2, and R_3 represent different observation plane distances from the aperture.

2.3. Micro-optics and relevant optical phenomena

The size of most diatom frustules/valves is in the micrometer range; therefore, the relevant optical phenomena are discussed in the frame of **micro-optics** [165]. Micro-optics is a field of optics that has been developed in recent years to understand and engineer light interactions with microscopic objects, which helped technology in the miniaturization of optical devices by shrinking their optical elements' size, leading to

a dramatic boost in the efficiency and performance of those devices while decreasing their size and price [165]. In contrast to the macroscopic objects, light **diffraction** and **interference** become significant and dominate the light modulation behavior of microscopic objects (with a size comparable to λ).

2.3.1. Diffraction

Light Diffraction is a fundamental phenomenon where light bends when it passes near the edges of an obstacle or through an aperture [1,166]. The diffraction effects can be neglected if the aperture (or the obstacle) is much larger than the incident wavelength λ (**Fig. 2.2a**) but becomes more significant when decreasing the size, approaching λ (**Fig. 2.2b**) [163].

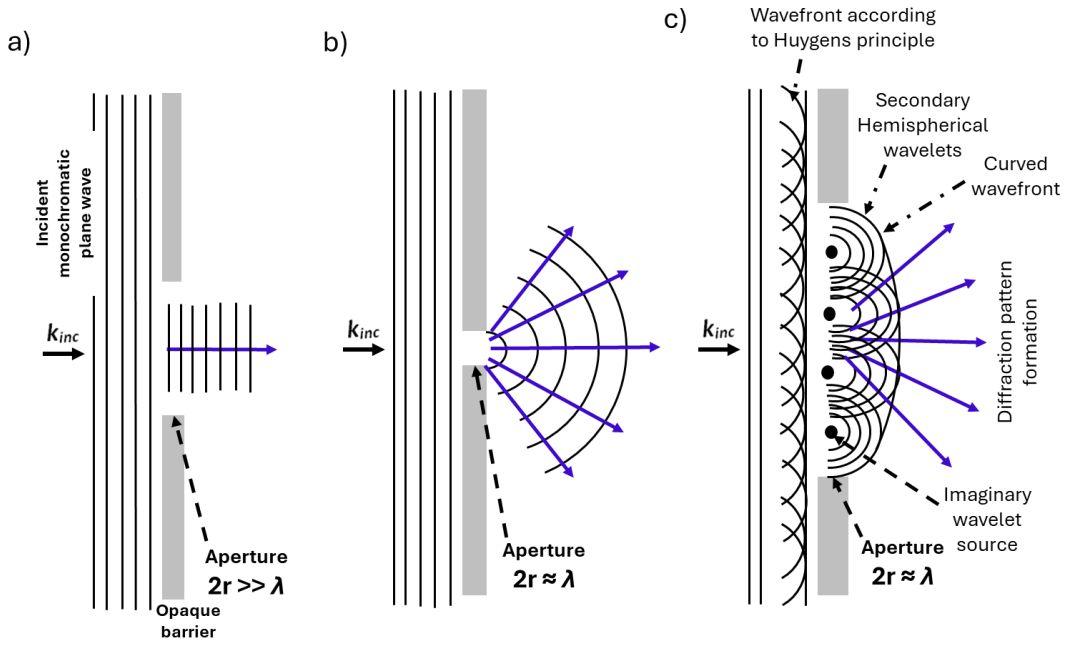

Fig. 2.2. A schematic diagram showing a plane wave illuminating an aperture of a large-size (**a**) or a small-size (**b**). The diffraction is only observed in (**b**), where the wavefront diverges and spreads out after passing the aperture, as the blue arrows indicate. By considering the Huygens' principle in (**c**), when illuminating the small-size aperture, each point of the aperture (*e.g.*, the black dots) can be a source of a secondary wavelet that will spread out and interfere, generating a diffraction pattern in the near- and far-field.

When diffraction occurs, a diffraction pattern (consisting of alternative bright/dark fringes) is generated. That can be explained with the help of **Huygens' principle** (also known as Huygens–Fresnel principle), which defines the wavefront of a given propagated plane wave as an envelope consisting of a sum of infinitesimal secondary wavelets. According to this principle, when a planar wavefront reaches an aperture, the interference changes, and each point of the aperture can be considered as a point source producing a **secondary wavelet** that will **interfere** with each other's producing the diffraction pattern (**Fig.2.2c**). Generally, the diffraction pattern generated in the optical far-field can be approximated by Fraunhofer

diffraction, while the diffraction pattern generated in the Fresnel regime can be approximated by Fresnel diffraction.

In Fresnel diffraction, the **Fresnel-Kirchhoff integral** can be employed to determine the diffraction pattern generated by any given arbitrary structure (*e.g.*, an aperture) [163]. If we consider an aperture of area *A* and the diffraction pattern is observed at a distance *R* from the aperture, the total electric field at each point of the observation plane can be calculated as an integral of all point sources over the aperture area. The integral can be written as follows (see [163] for more details).

$$\mathbf{E}_i(x_i, y_i) = \frac{1}{i\lambda} \iint_A \mathbf{E}_0(x_a, y_a) e^{i\emptyset(x_a, y_a)} \frac{e^{iKR}}{R} \, dx_a dy_a \qquad (\mathbf{2.14})$$

Where (x_a,y_a) and (x_i,y_i) represent the coordinates of any point on the aperture and at the observation plane, respectively, which occur at a distance R from each other. This formula includes the arbitrary amplitude $\mathbf{E_0}$ and phase Φ of the electric field at any position [163].

Among various examples of diffraction, **edge diffraction** is considered a daily-life phenomenon [1] that could be important for the light modulation behavior of microscopic objects, including diatom frustules/valves (especially that of small size). Generally, when light encounters an obstacle/aperture, a characteristic edge diffraction pattern will be generated, including bright fringes alternating with dark fringes occurring around the edges, where the brightest and widest fringe is the closest to the edges. The amplitude and the width of these fringes decreases with increasing the distance from the edges (see Figure 18R in [1]). Other relevant diffraction phenomena, including diffraction grating, will be illustrated separately below.

2.3.2. Interference

Light interference is considered a fundamental phenomenon, which can describe how the EM waves could interact when meeting at a given point in space [1]. Although the diffraction phenomenon is often accompanied by interference, not all interference is associated with (or caused by) a diffraction, such as thin-film interference. To explain the interference of EM waves, the principle of **wave superposition** can be applied. When two parallel EM waves—of electric field amplitudes $\mathbf{E_1}$ and $\mathbf{E_2}$, having the same wavelength λ, polarization, and direction—meet at a point in space, they will superpose, as the examples illustrated in **Fig. 2.3**. The resulting wave amplitude depends on the superposed waves' amplitudes as well as the phase difference between them ($\Delta\Phi$) [1,167]. When the superposed waves are entirely *in-phase* ($\Delta\Phi = 0, \lambda, 2\lambda, 4\lambda$, etc.), the maximum **constructive** interference is reached, where the resulting wave amplitude $\mathbf{E_{total}} = \mathbf{E_1} + \mathbf{E_2}$ (*e.g.*, **Fig. 2.3a**). On the other hand, when the waves are entirely *out-of-phase* ($\Delta\Phi \approx \lambda/2, 3\lambda/2, 5\lambda/2$, *etc.*),

the maximum **destructive** interference is reached, where $\mathbf{E_{total}} = \mathbf{E_1} - \mathbf{E_2}$ (*e.g.*, **Fig. 2.3b**).

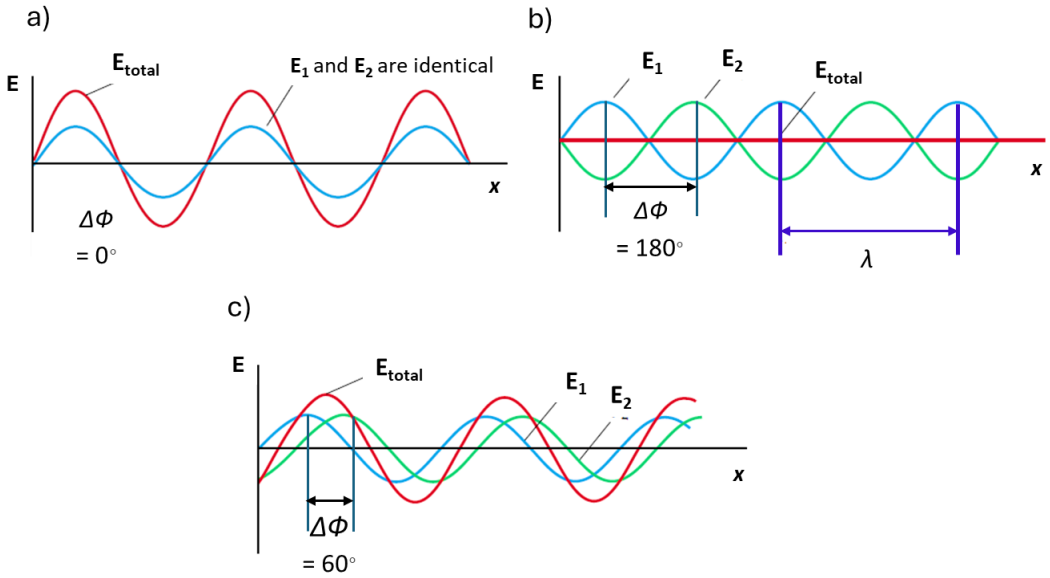

Fig. 2.3. A sketch showing the superposition of two identical sinusoidal waves propagating in the same direction when they are entirely *in-phase* (**a**), entirely *out-of-phase* (**b**), or have $\Delta\Phi$ of 60° (**c**). The wavelength can be defined as the distance between two consecutive crests or troughs. **Figs.** (**a**), (**b**), and (**c**) are modified and adapted from Serway and Jewett [167].

Thin-film interference is a daily-life example of the interference that causes (or contributes to) structural coloration in many living organisms [168] and could be relevant to diatom valves/girdle bands that consist of a simple silica layer often with a few hundred nm thickness. As illustrated in **Fig. 2.4**, when light incident on an optically thin slab of a lossless dielectric material (of thickness D_{sl} and *refractive index* n_{sl}) embedded in a homogenous medium (n_m), it will partially reflect and refract at the 1st interface (between medium and slab). The refracted light will travel inside the thin slab reaching the 2nd interface (between slab and medium), where it will partially reflect (to travel again inside the slab toward the 1st interface) and refract (to leave out the slab to the transmittance). This cycle of reflection and refraction will be repeated each time the light wave reaches an interface. The light waves leaving the slab in the reflectance interferes either constructively or destructively depending on $\Delta\Phi$ that is caused by the optical **path-length difference** of the waves (which corresponds to the distance that light travelled within the slab multiplied by n_{sl}) and the possible change in the phase at reflection at the 1st interface ($\Delta\Phi = 180°$, if $n_{sl} > n_m$). On the other hand, the light waves leaving the slab in the transmittance will also interfere, but in a converse way to give the maximal transmittance at the wavelengths that give the minimal reflectance and *vice versa* [1]. The wavelengths at which the maximal constructive or destructive interference occurs for a given thin slab can be determined through simple thin-film interference equations (see, *e.g.*, **eqs. 2.15** and **2.16**) [167]. While, for calculating the theoretical dependency of the

transmission and reflection coefficients on λ_{vacc}, the complex Fresnel equations should be used, which can also show the positions of maximal constructive or destructive interference [168].

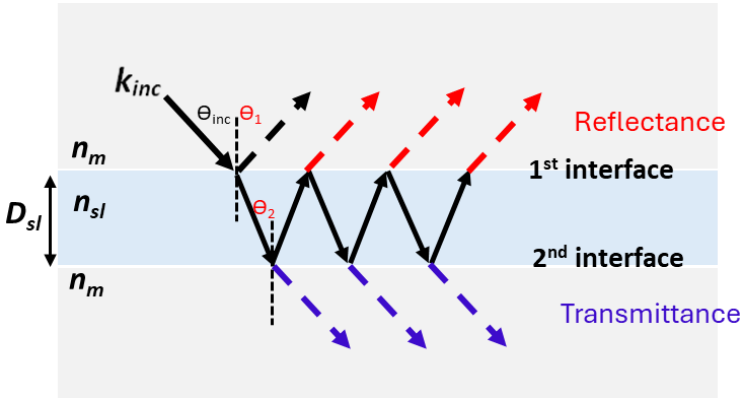

Fig. 2.4. A diagram showing the light interaction with a thin slab, leading to thin-film interference. Θ_1 indicates the angle of reflection, and Θ_2 the incident angle at the 2nd interface. Note that $\Theta_1 = \Theta_{inc}$. It should also be noted that, under normal illumination, all angles are equal to zero and their Cosine equals to 1.

$$2\, n_{sl}\, D_{sl} = \left(m + \frac{1}{2}\right) \lambda_{vacc} \qquad \textbf{Constructive interference} \qquad (\textbf{2.15})$$

$$2\, n_{sl}\, D_{sl} = m\, \lambda_{vacc} \qquad \textbf{Destructive interference} \qquad (\textbf{2.16})$$

These equations assuming light illuminates the slab normal to its surface, and $n_{sl} > n_m$, so 180° phase change occurs for the reflection at the 1st interface. Where m is an integer (0, 1, 2, 3, …) and λ_{vacc} is the light wavelength in vacuum/air.

2.3.3. Diffraction-driven focusing

At the macroscale, light focused by lenses (or mirrors) can be explained via ray tracing of refraction (or reflection), where the diffraction and interference are neglectable [1,167]. At this scale, when parallel light rays incident on a lens (or a mirror), the refracted (or reflected) rays will converge and concentrate (focused) at a point (named a focal spot), which occurs at a specific distance from the lens (or the mirror), known as focal length Z_f [167]. The focusing can then be considered refraction- (or reflection-) driven focusing.

In the last few decades, many micro-optical elements have been fabricated via micro- and nano-fabrication techniques to focus light on the microscale, including microlenses and their arrays [169], metalenses [170,171], and mesosize dielectric structures of different geometries (see below). For dielectric microlens, light focusing is a hybrid between refraction and diffraction, and the extent of diffraction contribution depends on the lens size (with respect to λ), reaching an almost pure **diffraction-driven focusing** by approaching λ [163].

In the case of refraction-driven focusing, the chromatic aberration is caused by the refraction angle (influenced by the natural dispersion of dielectric materials), where the focal spot of shorter λ (*e.g.*, blue light) occurs at a closer Z_f than that of longer λ (*e.g.*, red light), as illustrated in **Fig.2.5a**. In contrast, in case of diffraction-driven focusing, the chromatic aberration is caused by the divergent angle of diffraction, where the focal spot of longer λ occurs at a closer Z_f than that of shorter λ [163], as illustrated in **Fig.2.5b**.

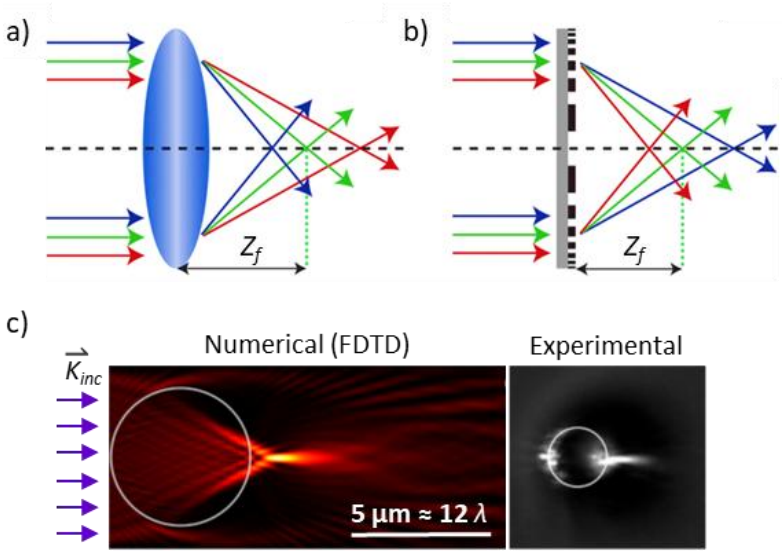

Fig. 2.5. (**a**) a Sketch showing the chromatic aberration of a refractive lens, while (**b**) a sketch showing the chromatic aberration of a zone-plate. The blue, green, and red arrows in (**a**) and (**b**) represent the blue-, green-, and red-light rays, respectively. (**c**) Numerical and experimental results showing PJ generation by a PDMS microcylinder (*diameter* = 5 µm), where n_m = 1, n_{PDMS} = 1.41, and λ = 405 nm. **Figs.** (**a**) and (**b**) are modified from Wang *et al.* [172], while **Fig.** (**c**) is adapted and modified from Liu and Lin [173].

In the 80th of the last century, a distinct type of diffraction-driven focusing behavior was observed while exploring the light intensity distribution in the near-field of dielectric spheres and cylinders, with a size comparable to but exceeding λ. A high-intensity localized beam was noted either inside (*i.e.*, **internally**) or close to the surface at the rear side (in the **near-field**) of these structures at non-resonant conditions, after illumination with a plane wave [174]. The location of these spots, as well as their intensity, were correlated to refractive index contrast (Δn) and the size parameter ($X = 2\pi r/\lambda$, where r is the radius). Later, this focusing behavior was confirmed and well-defined through several numerical and experimental studies (see, for example, **Fig. 2.5c**) and known in many publications as "**photonic jet** (**PJ**)" or "photonic nanojet (PNJ)" [175–179]. PNJ terminology was coined by Chen *et al.* [175] and was used extensively afterwards, probably associated with the similarity of the generated focusing beam to the generated jets in fluid dynamics, besides their frequently reported subwavelength-FWHM (full width at half maximum) [180].

A major difference between this type of focusing and typical microlensing is that PJ generation is not limited to the spherical, cylindrical, or lens geometries but has also been reported for a wide range of symmetric and asymmetric **non-spherical mesosize** (*e.g.*, of size 2 - 40 λ_{vacc}) dielectric objects [181–183]. Depending on Δn and X, the PJ parameters, such as position, intensity, and FWHM, can be determined. PJ can be observed inside the mesosize object or at its boundary (see, *e.g.*, [184]), and it can propagate without divergence over a specific length in the near-field and Fresnel regime zone that could reach up to a few-tens of λ [181,185]. Moreover, the generated PJ can be influenced dramatically by resonance phenomena (*e.g.*, [186,187]) and can be tuned and/or curved (*e.g.*, generation of the so-called **photonic hook** [188]).

Recently, PJ focusing has received increasing attention and has been utilized in numerous applications [181,182,189,190] to achieve super-resolution in optical microscopy [190–192], subwavelength photolithography [193], optical trapping [194], and enhancing Raman scattering [195,196], Fluorescence [197], and absorption in optoelectronic devices [181].

2.3.4. Diffraction grating

Human-made diffraction gratings (**DGs**) have revolutionized science, especially the field of spectroscopy, achieving vast progress in various fields. Today, different types of 1D and 2D DGs can be designed and customized for the desired application [198]. In nature, different types of DGs have been found to be the reason why many living organisms have iridescent colors [13,168].

Fig. 2.6 shows a simple example of DGs, which can be seen as a slab (of refractive index $n_g > 1$) penetrated by slits (of diameter $2r$) filled with air (of $n_m = n_a = 1$), while the whole DG is embedded in air. These slits are periodically arranged in 1D with a spacing d. The normal incident light will be diffracted at each grid slit. The diffracted light from all grid slits will interfere and yield separated orders of diffraction in the far-field, which can be determined by solving the grating equation (**eq. 2.17**, at normal incidence). From this equation, it can be seen that the DG will exhibit wavelength-dependent angular dispersion when illuminated by white light.

$$Sin\ \theta_m = m\left(\frac{\lambda}{d}\right) = m\left(\frac{\lambda_{vacc}}{n_{m^*}\, d}\right) \qquad (\mathbf{2.17})$$

Where Θ_m is the diffraction angle for a given diffraction order, m is an integer that refers to the diffraction order (0, 1, 2, *etc.*), and λ is the wavelength of light in medium ($\lambda = \lambda_{vacc}/n_m$).

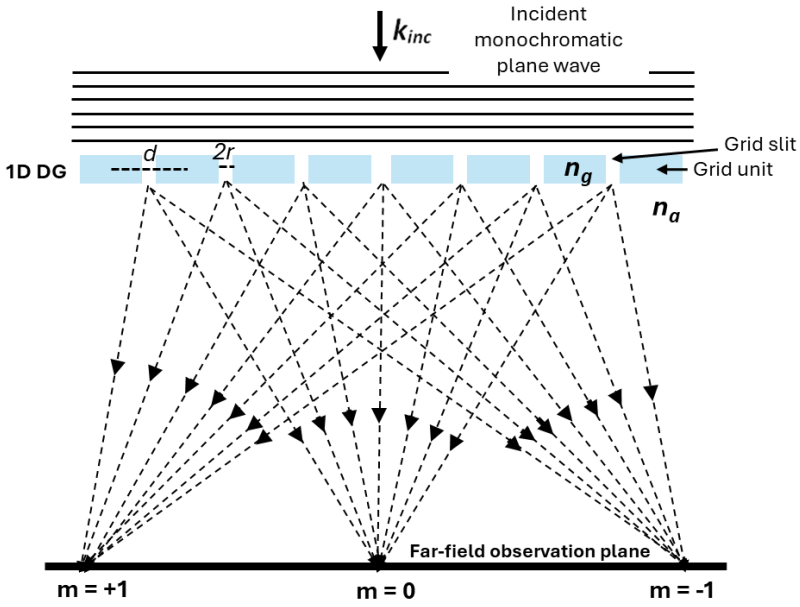

Fig. 2.6. A schematic diagram showing an example of DGs. It should be noted that the black-dashed light rays aim only to simplify and approximate the diffraction wavefronts directions, while in reality the interference pattern is much more complicated, especially if Huygens's principle is considered. m stands for the diffraction order.

In the Fresnel regime zone of DGs, the interference between different orders of diffraction yields a phenomenon known as "**Talbot effect**" that has been first observed by Henry F. Talbot [199] and well-described by Lord Rayleigh [200]. The Talbot effect is also known as self-images of the DG, where a specific interference pattern is formed in the grating's near-field and Fresnel regime zone when illuminated (see, for example, **Fig. 2.7**). This pattern consists of periodic bright fringes alternating with dark fringes representing an image copy of the DG repeated at fixed distances equal to **Talbot length** "Z_T" [200,201]. Depending on the number of diffraction orders that interfere, additional sub-images at fractions of Z_T could appear [202]. The Talbot length can be calculated according to **eq. 2.18**, specified for DGs with small *d* (which is applicable for the diatom valves/girdle bands) [200].

$$Z_T = \frac{\lambda}{1-\sqrt{1-\frac{\lambda^2}{d^2}}} = \frac{\lambda_{vacc}}{n_m\left(1-\sqrt{1-\left(\frac{\lambda_{vacc}}{n_{m^*}\,d}\right)^2}\right)} \qquad \textbf{(2.18)}$$

In recent years, the Talbot effect has been studied in both 1D and 2D diffraction gratings using theoretical and experimental approaches [202–206], and has been utilized in applications, for instance, displacement Talbot lithography [207,208], fluorescence Talbot microscopy [209], and image sensors [210].

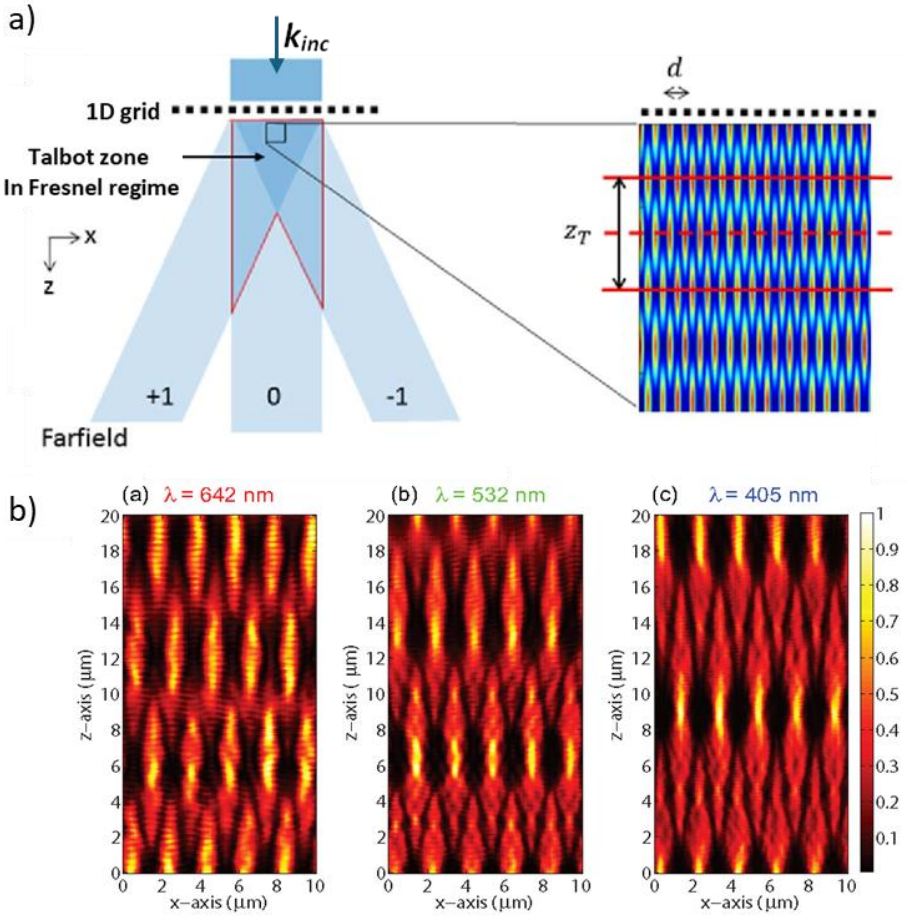

Fig. 2.7. (**a**) A sketch showing 1D DG (at the left). By zooming the Fresnel regime zone of the diffraction grating, a periodic pattern can be observed (at the right), which can then be called Talbot zone. (**b**) *z-x* slices in the 3D intensity distribution (measured and recorded by a high-resolution interference microscope) at the Fresnel regime zone of a 2 μm-period grid at different laser lines showing the interference pattern of the optical Talbot effect in transmittance. The grid surface occurs at z = 0 μm and is trans-illuminated from the bottom. **Fig.** (**a**) is adapted from Ye *et al.* [211], while **Fig.** (**b**) is adapted from Kim *et al.* [202].

2.3.5. Waveguiding

As illustrated in **Fig. 2.8a**, when light travels from an optically denser medium (of higher n) to an optically rarer medium (of lower n), and incident on the interface between the two media at $\Theta_{inc} > \Theta_c$ the so-called **critical angle** (which can be determined from **eq. 2.19**), it will totally reflect to the denser medium [167]. This phenomenon is known as **total internal reflection** (**TIR**) and is considered the core mechanism for light guiding via optical fibers. For an optical fiber with a core of higher refractive index (n_{wg}), surrounded by a cladding of lower refractive index ($n_{cladding}$), the incident light can be coupled (if $\Theta_{inc} < \Theta_{acc}$ the acceptance angle of the optical fiber, which can be calculated by **eq. 2.20** [212]) and propagated within its core, when TIR conditions at the core/cladding boundaries can be satisfied (**Fig. 2.8b**). As illustrated in **Fig. 2.8c,** each time the TIR occurs at the interface, an

evanescent field (non-propagating) is generated, which penetrates the transmittance medium for a short distance (typically >> λ) characteristic with an exponential decay.

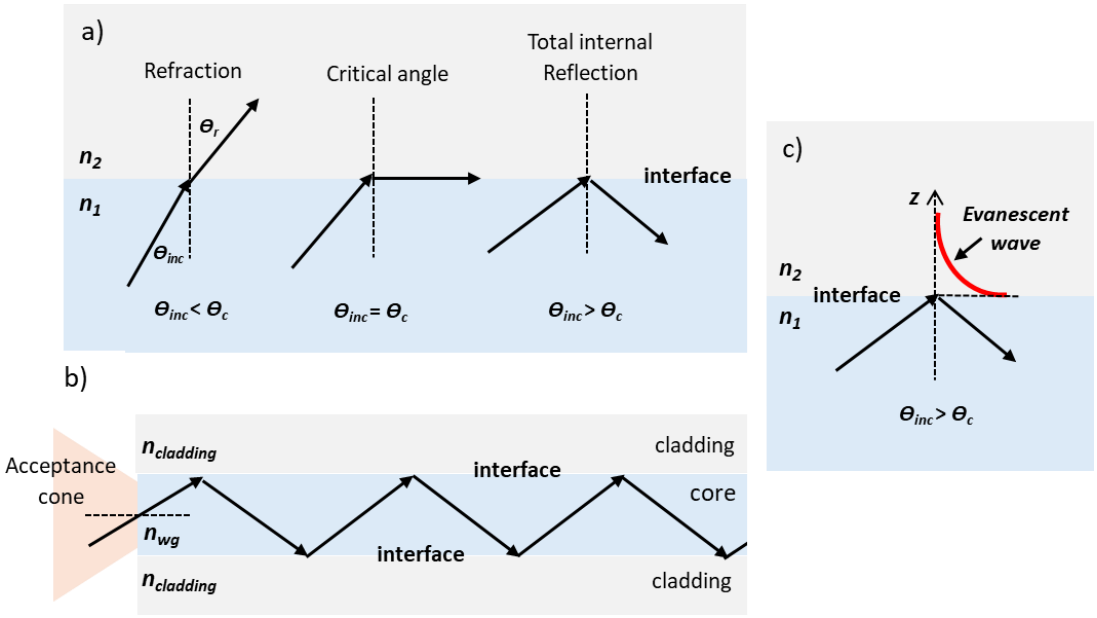

Fig. 2.8. (**a**) A schematic representation showing different states for light travelling from a higher refractive index medium (n_1) to a lower one (n_2), which enables TIR only if $\Theta_{inc} > \Theta_c$. Θ_r is the angel of refraction. (**b**) A sketch showing the principle of coupling and waveguiding of light into the optical fibers. (**c**) The Evanescent wave generated at the position of TIR.

$$\sin\theta_c = \frac{n_2}{n_1} \sin\theta_r = \frac{n_2}{n_1} \quad \textbf{(2.19)}$$

Derived from **Snell's law**, where $\sin\Theta_r = \sin 90° = 1$ and $n_1 > n_2$.

$$\sin\theta_{acc} = \left(\frac{\sqrt{n_{wg}^2 - n_{cladding}^2}}{n_m} \right) \quad \textbf{(2.20)}$$

Where n_m is the refractive index of the medium from which light coupling occurs.

By reducing the width of an optical fiber, approaching λ (as in the case of micro-/nano-optical fibers [213]), it became a waveguide. The number of supported modes within a waveguide is affected by its width W_{wg} (with respect to the wavelength of propagated light inside λ_{wg}), while the zero mode can always be supported [212]. Each mode has a specific field distribution inside the core and has a distinct propagation constant [212]. The mode confinement (inside the core) and the penetration depth of its evanescent field (into the cladding) depend on W_{wg} and Δn [212,214].

The optical fibers are widely used to guide light over long distances with minimum losses enabling optical communications [215]. While more recently, micro-/nano-optical fibers have been fabricated and shown superior properties compared

to the larger size optical fibers (see Figure 1 in [213]), making them suitable for various applications (see Figure 9 in [213]).

2.3.6. Guided-mode resonance

Guided-mode resonance (**GMR**) is considered a type of Wood's anomalies reported by Robert W. Wood [216]. This phenomenon has been observed in resonant diffraction gratings (of different geometries and configurations [217]) and PC slabs [218,219] of a period d comparable to λ. **Fig. 2.9** sketches the GMR mechanism, assuming a free-standing resonant dielectric 1D DG illuminated with a plane wave. At specific combination of various parameters related to the grating (including its refractive index n_g, its period d, fill factor ff (*i.e.*, the grid unit width/d), and its thickness D), the surrounding medium (including n_m) and the incident light (including its λ_{vacc}, incident angle Θ_{inc}, and polarization) [216,220,221], the resonant conditions are reached, where the diffracted waves can be coupled, waveguided, and interfere inside the DG (considered as inhomogeneous waveguide), as illustrated in **Fig. 2.9**. During resonance, an intense EM field can be observed inside the grating associated with an evanescence field (see, for example, Figure 3 in [217]). Moreover, due to the periodic nature of the grid, the guided modes cannot be sustained and leak out from the waveguide region [216] to interfere constructively at reflectance and destructively at transmission. That gives a characteristic spectrum with anomalous reflectance/transmittance values at GMR conditions, enabling highly selective light filtering capabilities [216,222].

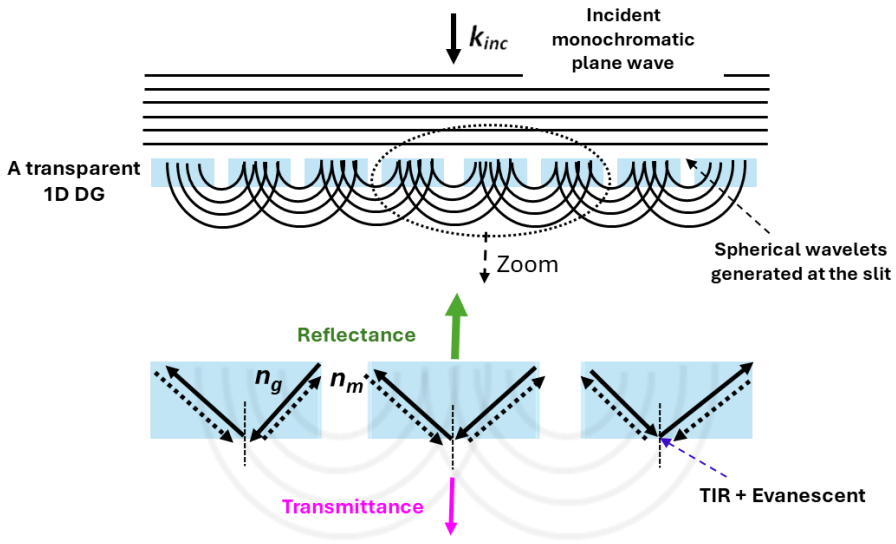

Fig. 2.9. A schematic representation showing a transparent 1D DG under resonant conditions. When the incident plane wave reaches DG, its interference changes, and each slit can be considered a source of hemispherical wavelets (according to Huygens' principle). These wavelets can be partially coupled inside the grid units. Only if the resonant conditions are reached, the waves are strongly coupled and guided through the DG structure. During GMR, the reflectance increases significantly, while the transmittance reduces. It should be

noted that the thin-film interference can occur in the background depending on the DG thickness.

Possible GMR modes can occur each time the resonant conditions are reached. For each mode (which can be obtained at a narrow range of λ_{vacc}, called a bandwidth), the resonance reaches the maximum at a specific wavelength $\boldsymbol{\lambda_{vacc,GMR}}$, which can be tailored (*i.e.*, shifting toward higher or lower wavelengths) by tuning the parameters mentioned above. The GMR modes can be determined by solving the Eigenvalue equation or employing different numerical analysis techniques [217]. In recent years, GMR has been involved in several applications, including the fabrication of highly efficient sensors and highly selective optical filters [220,223,224].

2.4. Finite element method

The finite element method (**FEM**) is often used as a powerful numerical analysis technique for solving scientific problems in various fields, including optical problems, via solving the relevant partial differential equations (**PDEs**) [225,226]. This method relies on **mathematical discretization** of the simulation domain into elements of finite size connected to each other through nodes, which gives the domain a mesh appearance (see, *e.g.*, **Fig. 2.10b**). There are several types of finite element geometry that can be employed for discretizing the domain, which gives flexibility in meshing the irregular and complex structures. In general, the size of finite elements (*i.e.*, the mesh size) is crucial when considering the accuracy of the calculations and the results. The more accurate results require smaller mesh sizes [226]. The main constraint for using a very dense mesh is the higher computational power required in the system used for analysis. In the two-dimensional (**2D**) simulation domain (used in this thesis), finite elements often have a **polygonal** geometry, including triangular and quadrilateral shapes.

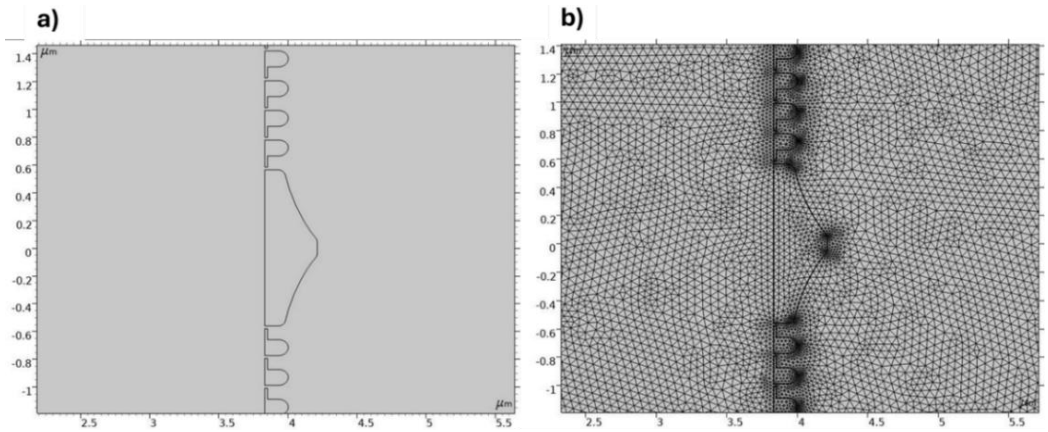

Fig. 2.10. An example of the discretization of the 2D simulation domain. The smaller structures within the simulation domain (**a**) lead to smaller finite elements, as seen in the discretized domain (**b**).

Currently, there are several commercially available software packages to perform FEM, including **COMSOL Multiphysics**. In COMSOL Multiphysics, there are a few modules that can solve optical problems, including Ray optics, wave optics, and RF modules. The **wave optics module**—suitable for studying the EM wave propagation and investigating phenomena such as diffraction, interference, scattering, and waveguiding—was selected and employed in all simulations shown in this thesis. Within the wave optics module, there is an ability to perform **frequency domain** analysis [227], which provides the solution for the wave equation in its frequency domain form (**eq. 2.13**). The simulation method can be called then finite element frequency domain (**FEFD**) method. Under these conditions, the mathematical representation of the electric field component of a plane wave propagating in the 2D simulation domain can be written as follows [161].

$$\mathbf{E} = \mathbf{E_0}\, e^{-i\mathbf{k}\cdot\mathbf{r}} \qquad (\mathbf{2.21})$$

Where **K** is the real wave vector (*i.e.*, without an imaginary component), **r** is the position vector. It should be noted that this equation is derived from the wave equation [161].

After defining the physics and the governing equation that need to be solved, the boundary conditions of the simulation domain should also be defined. In EM simulations, using suitable boundary conditions is crucial to prevent the reflections at these boundaries, so we are sure that the boundaries are transparent for the incident/scattered waves. Among different boundary conditions available in the wave optics module, the scattering boundary condition (**SBC**) is often used as a perfect transparent boundary for the scattered (outgoing) waves, which could be either a planar, spherical, or cylindrical wave [227]. Additionally, it is also perfectly transparent for the normal incident (incoming) waves. The mathematical equation of the plane scattered wave is illustrated in **eq. 2.22** [227]. The SBC also enables selecting the wave polarization to become *out-of-plane* (oscillating in *z*-direction) or *in-plane* (oscillating in *x*- or *y*-directions), for a 2D simulation domain extends in the *x*-*y* plane. The **perfectly matched layers** (**PMLs**), which are more efficient in absorbing the incident waves with an incline incident angle, can also be used where no scattered waves are required.

$$\mathbf{E} = \mathbf{E_{sc}}\, e^{-ik(\mathbf{n}\cdot\mathbf{r})} + \mathbf{E_0}\, e^{-ik(\mathbf{K}\cdot\mathbf{r})} \qquad (\mathbf{2.22})$$

After determining the simulation conditions, numerical calculations are carried out at each node. Thereafter, the solution is assembled and interpolated across the whole simulation domain using a set of matrixes and equations. After obtaining the solution, further **post-processing** steps are required to visualize the solution and extract the information from it in the form of plots, graphs, contour maps, *etc*.

2.5. Scanning near-field optical microscopy

The conventional optical microscopes are used to magnify and disclose microscopic objects—using visible light and a set of lenses—which has been widely employed in various fields with different configurations [228]. As the distance between the object under observation and the objective lens (*i.e.*, the **working distance**) is much larger than the wavelength of light, we call these optical microscopes **far-field systems**. In such systems, the lateral resolution of microscopic features is constrained by the Abbe diffraction limit [228], see **eq. 2.23**.

$$\Delta = \frac{\lambda_{vacc}}{2n_m \, sin\alpha} = \frac{\lambda_{vacc}}{2NA} \qquad (\mathbf{2.\ 23})$$

Where Δ is the minimum lateral resolving distance, and α is the half angle of the light cone enters the objective.

To overcome the diffraction-limited resolution of conventional optical microscopy, various techniques—based on different physical principles—have been developed, including super-resolution microscopy [229], confocal microscopy, electron microscopy, and scanning probe microscopy (**SPM**). In general, the SPM relies on scanning the sample in proximity to its surface using a sharp tip (of nanometric dimensions, often fixed on a cantilever) and includes techniques such as scanning tunnelling microscopy (**STM**) and atomic force microscopy (**AFM**) [230]. The STM relies on electrons tunnelling from the tip to the sample (or *vice versa*) under an applied voltage, thus being limited to conductive materials under high vacuum conditions. While AFM relies on tip-sample interactions, exhibiting either attraction or repulsion forces depending on the distance between them (**Fig. 2.11**). In both cases, the probe scans the sample surface while measuring the changes in tunnelling current (in the case of STM) or in the cantilever deflections (in the case of AFM), which enables collecting information about that surface, including its topography with atomic resolution.

Scanning near-field optical microscopy (**SNOM**) can be considered an expansion of SPM, which relies on merging near-field optics and AFM principles. When the SNOM probe is scanning the near-field of a sample (and possibly could also scan its Fresnel regime zone), it could reveal its optical features with subwavelength resolution, while simultaneously showing its topographical features with nanoscale resolution [231,232]. There are two major types of SNOM: **apertureless** (**s-SNOM**) and **aperture** (**a-SNOM**), depending on whether a **nanoaperture** (of subwavelength dimensions) is present or absent at the tip of the scanning probe. The a-SNOM can be operated either in **transmission** or **reflectance** configuration. Each configuration can be operated either in the **illumination** or **collection** mode [233]. In this thesis, an a-SNOM operated in transmission

configuration was employed in both illumination and collection modes (**Fig. 2.12**), see further **subsection 3.4** (**Chapter 3**).

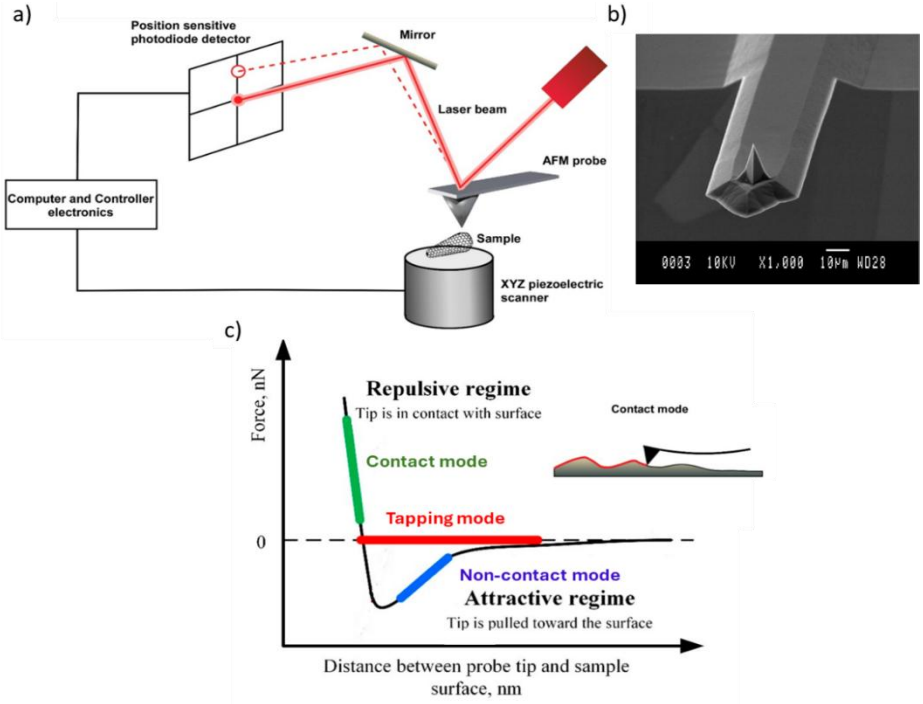

Fig. 2.11. (**a**) A sketch showing an AFM, where its probe (consists of a cantilever with a sharp tip) scans the surface of the sample. The cantilever deflections that occur during scanning can be detected with the help of a laser and position-sensitive photodetector. (**b**) An example of AFM probes, as observed under SEM. (**c**) A plot showing the dependency of the forces governing the tip-sample interaction on the distance between them. In the case of the contact mode, the probe deflections are caused by the repulsion between the tip and sample, while in the non-contact mode, they attract each other. **Fig.** (**a**) is adapted from Rousso and Deshpande [234], (**b**) is adapted from Florea *et al.* [235], while (**c**) is modified from Dzedzickis *et al.* [236].

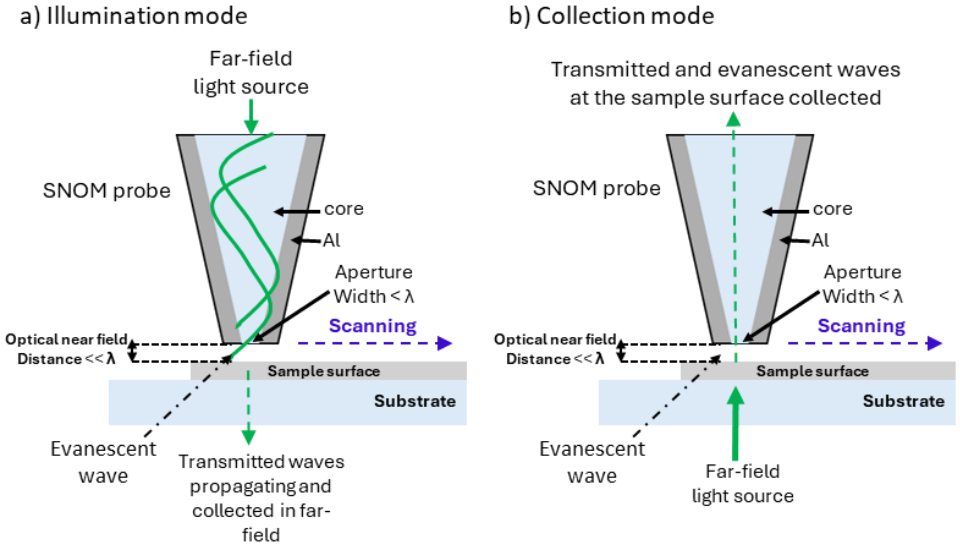

Fig. 2.12. Schematic representations showing the SNOM principle in the transmission configuration, while operated in the illumination (**a**) or collection (**b**) modes. Al stands for the Aluminum coating of the SNOM probe.

In the illumination mode, the nanoaperture of the SNOM probe acts as a nano-size light source, potentially can be approximated as a point-like source, illuminating small areas (of dimensions approximately equal to the aperture size) of the sample. During scanning, the evanescence field emanating from the nanoaperture can be locally coupled to the sample (**Fig. 2.12a**). The scattered or decoupled waves at the sample surface are transferred into propagating waves that are transmitted and can be collected and detected in the far-field. At the end of the scan, an optical image is retrieved, where each pixel represents the overall intensity collected over the whole field of view when illuminating a small area with this single pixel at its center. In the collection mode, samples are illuminated with a light source in the far-field, while the nanoaperture locally collects propagating and non-propagating fields in the optical near-field (**Fig. 2.12b**). At the end of the scan, an optical image is retrieved, where each pixel represents the intensity of local (propagating and non-propagating) fields at this pixel. Unlike the illumination mode, the collection mode thus enables detecting the evanescent waves directly at the surface. Interestingly, in both cases, the measurements can be coupled with spectroscopy to obtain spectral information at each pixel.

This technique became well-established and has been applied in various fields, for example, to study nanoparticles [233], photonic crystal structures [237,238], optical nanofibers [239], photovoltaics [240], and diffractive microelements [241,242].

2.6. Surface-enhanced Raman spectroscopy

Raman spectroscopy is a non-destructive label-free analysis technique that enables investigating the **Raman-active molecular vibrational modes** (*i.e.*, the vibrational modes that are associated with changes in the molecule **polarizability**), leading to qualitative and quantitative information about the chemical composition of a given sample [243,244]. This technique relies on the photon **inelastic scattering** by molecules (known as **Raman scattering**, after its discoverer Sir Chandrasekhara V. Raman) and has been widely applied in various fields, including chemical analysis, biomedical diagnosis, environmental monitoring, and forensics.

When a sample (consisting of Raman-active molecules) is illuminated with light (preferably a laser source), a fraction of non-absorbed photons will be scattered either elastically (*i.e.*, without changing their energy, the majority of scattered photons producing strong **Rayleigh scattering**) or inelastically (*i.e.*, with changing their energy result from the associated changes in molecule vibrational energy level, the minority of scattered photons producing **Raman scattering**), as demonstrated in **Fig. 2.13a**. The Raman scattered photons could have a lower or higher energy (**Stokes** or **anti-Stokes modes**, respectively) compared to the incident photons (**Fig.**

2.13a). This energy difference is known as **Raman shift**, which is used to study and analyze the obtained **Raman spectrum** [244]. The Raman shift is often measured by **wavenumber** units (cm^{-1}), which equal the reciprocal of the wavelength (in cm).

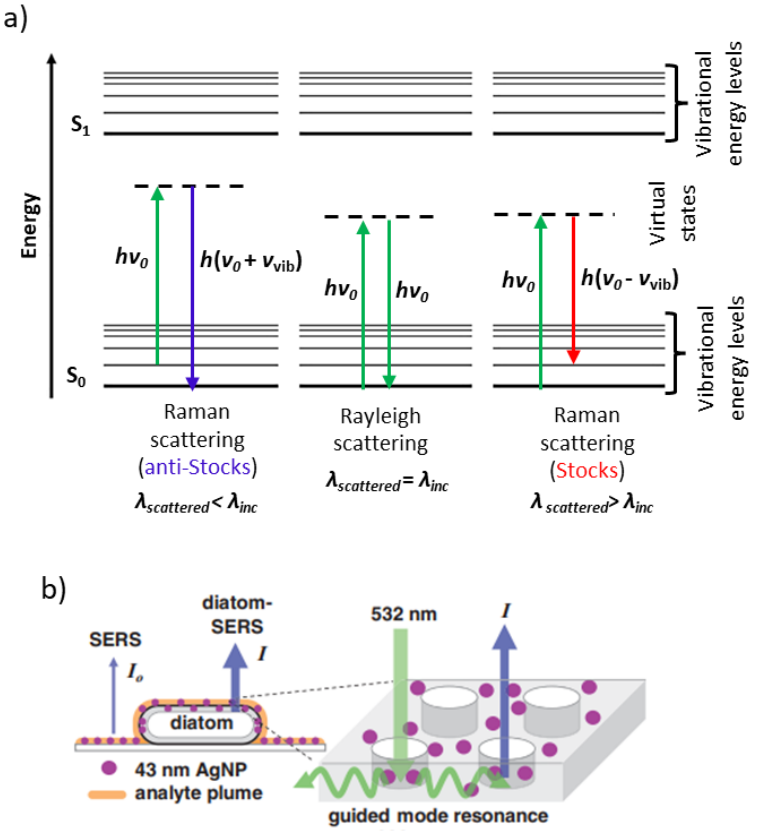

Fig. 2.13. (**a**) Jablonski energy level diagram of spontaneous scattering. In the frame of quantum mechanics, the scattering involves transitions to the so-called **virtual states**. In Rayleigh scattering such transition does not change the associated photon frequency (and, thus, the scattered light wavelength $\lambda_{scattered}$), while in Stocks or anti-Stocks Raman scattering the photon frequency is changed (and, consequently, $\lambda_{scattered}$). S_0 and S_1 stand for the molecular energy levels, where each energy level consists of a number of vibrational levels, ν_0 stands for the frequency of incident light, ν_{vib} for the frequency corresponding to the vibrational level change, and h for the Planck constant. (**b**) A sketch showing an example of diatom-based SERS hybrid substrate, where the SPR of silver nanoparticles could couple to GMR induced by the PC structure of a diatom valve to enhance the SERS signal of adsorbed analyte molecules. **Fig.** (**a**) is modified from Dey [245], while (**b**) is adapted from Kraai *et al.* [246].

Due to the low photon yield from Raman scattering (compared to that of Rayleigh scattering), the Raman signal is very weak. Therefore, some approaches have been employed to enhance the signal and, thus, the detection sensitivity [243,247]. Among these approaches, surface-enhanced Raman spectroscopy (**SERS**) is considered a powerful technique widely used for chemical analysis with a detection sensitivity that could reach down to a single-molecule level [248,249]. SERS is often achieved by having the analyte molecules adsorbed on the surface of metallic nanoparticles (NPs), ultrathin, or rough (*i.e.* nanostructured) metallic films

[250–252]. In this case, the obtained signal enhancement is attributed mainly to two mechanisms: the **chemical** and **EM**, the latter has the greater contribution. In the EM-based mechanism, the excitation of **surface Plasmon resonances** (**SPR**)—both localized (in the case of NPs or nanostructured metal surfaces) or delocalized (in continuous metallic films)—leads to enhancing the local EM field in proximity to the adsorbed molecules. That is expected to greatly enhance the signal, as the SERS enhancement $g \propto |\mathbf{E_{loc}}/\mathbf{E_0}|^4$, where $\mathbf{E_{loc}}$ is the local electric field and $\mathbf{E_0}$ is the incident electric field [253].

An additional enhancement for the SERS signal can be achieved by employing the so-called **SERS hybrid substrates** [254]. For instance, utilizing a resonant DG or PC coated with plasmonic active material leads to the coupling of, *e.g.*, GMR at certain frequencies to the **SPR**, which increases $\mathbf{E_{loc}}$ significantly, and, thus, yields a higher g [254–257]. This has been the major reason for employing diatom valves in fabricating SERS hybrid substrates in the literature (see the example shown in **Fig. 2.13b**).

3 Materials and Methods

3.1. Materials and sample preparation

3.1.1. Diatom samples

Table 3.1 summarizes different diatom samples used in this thesis. Some of the obtained samples required further processing (including extraction, separation, and/or purification steps) to obtain clean valves suitable for further studies and applications. In general, sample processing aims to (i) remove the associated organic matter (especially in the case of cultivated/living samples) and retrieve the siliceous valves, (ii) reduce the impurities and non-siliceous content (such as calcite and other oxides in the case of fossil samples), and if necessary (iii) increase the size uniformity of the valves within the final purified sample. It should be noted that different diatom sample processing procedures are already established in the literature [104,258–260]; however, selecting a suitable method depends on the nature of the sample, its impurities, and the purpose of using it.

Table 3.1. Different diatom samples used in the experimental work. It should be noted that the sample processing methods mentioned in the table are explained in **section A.2** (**Appendix A**).

The sample	Provider (source)	Sample processing	Chapter/Appendix	Abbr.
Living culture of the pennate diatom ***Gomphonema parvulum***	Kindly provided by Dr. Cathleen Oschatz (Max Planck Institute of Colloids and Interfaces, Potsdam, Germany)	H_2O_2 treatment	Chapter 5 Chapter 6 Chapter 7	***GP***
Living culture of the centric diatom ***Coscinodiscus radiatus***			Chapter 5 Chapter 7	***CR***
Celatom®LCS-3 (Natural grade diatomite sample mainly containing ***Aulacoseira* spp.**)	Purchased from EP minerals company (USA)	HCl treatment + Settling	Chapter 5 Chapter 6 Chapter 7	***Aula***
Fossil valves of the pennate diatom ***Pinnularia* cf. *gigas***, from diatomite deposits occurs at Ugchelen (Netherlands)	Purchased from Mr. Michel Haak (Netherlands)	Not required (obtained as clean valves suspended in water)	Chapter 5	***Pin***

A fossil valve of the centric diatom ***Actinoptychus heliopelta***, from diatomite deposits occurs at Dunkirk, Maryland (USA)	A gift from Mr. Emiliano Bellotti (Italy)	Not required (obtained as arranged clean valves on a substrate)	Chapter 5 (5.2)	***Acto***
A fossil valve of the centric diatom ***Craspedodiscus coscinodiscus***, from diatomite deposits occurs at Dunkirk, Maryland (USA)				***Cosc***
A fossil valve of the pennate diatom ***Stauroneis phoenicenteron*** from diatomite deposits occurs at Loch Cuithir, Isle of Sky (Scotland)				***Staur***
A fossil valve of pennate diatom ***Pinnularia viridis*** obtained from diatomite deposits occurs at Loch Cuithir, Isle of Sky (Scotland)				***Pinn***
A recent valve of pennate diatom ***Didymosphenia geminate*** collected from Gunpowder falls, Maryland (USA)				***Did***
Moronita© (processed diatomite sample mainly containing ***Ethmodiscus rex***)	A gift from Mr. Juan Muñoz (Sevilla, Spain)	Not required (obtained as a powder of processed clean sample)	Appendix C	***Ethmo***

3.1.2. Dispersing clean diatom valves over glass substrate

Dispersing clean diatom valves—of a microscopic size—over a macroscopic substrate, such as the clean glass substrates used here (see the preparation method of the clean glass substrates in **section A.3**, **Appendix A**), is often required to obtain a monolayer that facilitates their study and implementation in applications.

The clean valves—suspended in deionized water, unless otherwise stated—were dispersed over the clean glass substrates to form a monolayer via **drop casting**, employing an automatic micropipette. In all cases, the suspended valves were ultrasonicated for a few minutes in an ultrasonic bath each time before drop casting to disperse the valves well in the suspension. The valves' concentration and drop size were optimized for each sample to avoid valves' accumulation within the obtained monolayer. The obtained monolayers were left to dry on a flat surface at ambient

conditions. These monolayers were used in the studies shown in **Chapters 5-7** and **Appendix C**, as well as in examining the valves' ultrastructure using optical and electron microscopy. However, it should be noted that some specifications and customization for preparing the valves' monolayer for some studies were implemented, as demonstrated below.

For the **side-illumination** study (**section 5.3**, **Chapter 5**), the concentration of each sample was adjusted to avoid agglomeration of the valves in the monolayer to preclude the interference of scattered light from overlapping or adjacent valves and to minimize the shadowing effect as much as possible.

For the **SNOM** measurements, the valves were spread over a glass substrate coated with a gelatine layer. The gelatine layer was crucial for fixing the valves while scanning their surface with the SNOM probe. It was obtained by dipping the clean glass substrates into 1% gelatine aqueous solution (65° C) and left to dry overnight in a tilted position at ambient conditions. Thereafter, a drop (≈ 5 µl) of the suspended valves (in deionized water) was deposited over the gelatine and left to dry on a flat surface at ambient conditions. This method has been developed and optimized together with **Dr. Martina Gilic**. It should be noted that the deposited valves were placed over the gelatine layer but still immersed in air (*i.e.*, did not sink into or fill with the gelatine), as confirmed by the SNOM shear force images obtained by **Professor Paul Fumagalli**.

For one of the photoactive electrodes prepared for the **MISM** photodetector preliminary study (see $\mathbf{S_{PP}M_{Au+Ethmo}}$ electrode fabrication, **subsection C.1.1**, **Appendix C**), the following method was employed to obtain a relatively uniform and dense layer of *Ethmo* valves over glass substrates. Briefly, the processed *Ethmo* valves were suspended in ethanol (70%) with a concentration of 0.4 g/l. About 50 µl of the valve suspension was spread over a clean glass substrate and left to dry on a flat surface at ambient conditions, away from any vibrational sources as possible. This step was repeated seven more times to have, in total, eight dried drops over the substrate. An example of the films obtained by this method is shown in **Fig. A.3** (**Appendix A**). It should be noted that this method was optimized after studying the influence of different parameters, including solvent type, valves' concentration, drop size, and number of drops, on the film uniformity.

3.2. Numerical analysis

In this thesis, a **COMSOL Multiphysics 5.5** version was utilized for numerical analysis. The 2D **FEFD** simulations were employed mainly to analyze (i) the light modulation by the valve/frustule of ***GP*** (demonstrated in **Chapter 4**), (ii) the diffraction-driven focusing induced by ***Aula*** valves under side-illumination (demonstrated in **Chapter 5**, **section 5.3**), (iii) the diffraction-driven focusing induced by ***GP*** and ***Aula*** valves under

trans-illumination (demonstrated in **Appendix A**, **subsections A.10** and **A.12**, respectively), and (iv) the SNOM results of ***GP*** and ***Aula*** valves (demonstrated in **Chapter 6**). For this, the detailed valve ultrastructure of ***GP*** and ***Aula*** was investigated to obtain statistically representative models for numerical analysis, as demonstrated below.

3.2.1. Building statistically representative models

The *GP* Valve

To analyze the role of the structural features in *GP* valves in a methodical fashion, a statistical 3D model of a *GP* valve was created (**Fig. 3.1**). This 3D model was constructed using the geometry building tools in **COMSOL Multiphysics®**, based on the weighted mean (X_w) values of the *GP* valve's structural parameters (illustrated in **Table 4.1**, **Chapter 4**).

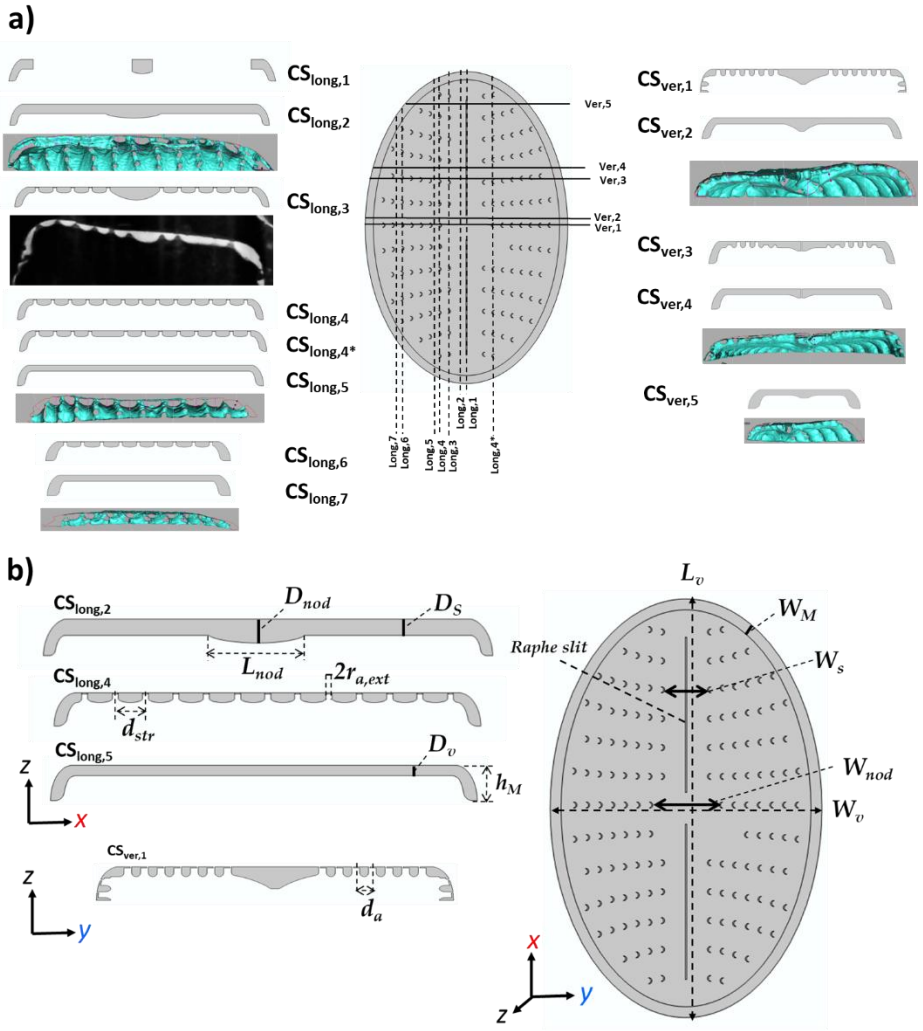

Fig. 3.1. (**a**) The selected vertical and longitudinal CSs across the statistically representative 3D valve model that is shown at the center (at its external top view). The selected **five vertical CSs** and the **eight longitudinal CSs** are schemed at the right and left, respectively, along with some 2D cross-sections from the 3D reconstructed data (obtained from Dr.

Cathleen Oschatz) to show comparable places in the valve, reflecting the similarity between the final 2D CSs and the actual structure. (**b**) Some major structural parameters in the 3D model and 2D CSs (see **Table 4.1**). This figure is reproduced from Ghobara *et al.* [261].

The required structural parameters needed for the construction of the 3D model were extracted from 2D SEM micrographs and 3D reconstructed valves (both were acquired by **Dr. Cathleen Oschatz** based on the methodology described in Ghobara *et al.* [261]) using **ImageJ** software by averaging a number of measurements in each image $X_{av,i}$ and calculating the corresponding standard deviation $dX_{av,i}$. To obtain not only the variation of the parameter within one valve but also across different valves, the weighted mean X_w of the parameter (**eq. 3.1**) was calculated, including its internal and external errors, dX_{int} (**eq. 3.2**) and dX_{ext} (**eq. 3.3**), respectively. If dX_{int} was larger than dX_{ext}, the variation within the valves (within $dX_{av,i}$) was larger than the variation between valves and *vice versa*. This analysis helped the estimation of the significance of the structural precision with the variation seen in the simulation results upon changes in the corresponding structural parameter.

$$X_w = \frac{\sum \frac{1}{dX_{av,i}{}^2} X_{av,i}}{\sum \frac{1}{dX_{av,i}{}^2}} \quad (\mathbf{3.1})$$

$$(dX_{int})^2 = \frac{1}{\sum \frac{1}{dX_{av,i}{}^2}} \quad (\mathbf{3.2})$$

$$(dX_{ext})^2 = \frac{1}{(n-1)\sum \frac{1}{dX_{av,i}{}^2}} \sum \left(\frac{X_{av,i}-X_w}{dX_{av,i}}\right)^2 \quad (\mathbf{3.3})$$

The numerical calculations were performed on 2D cross-sections, which allowed greater structural variability with moderate simulation times and reduced the complexity in the obtained results. For this, representative 2D longitudinal ($CS_{long,i}$) and vertical ($CS_{ver,i}$) cross-sections were extracted from the 3D model to cover all distinct structural features (**Fig. 3.1a**). At this point, the cross-sectioning across the 3D model produced sharp edges, which were smoothed to resemble the reconstructed data from FIB-SEM, as shown in **Fig. 3.1a**.

The *Aula* Valve

The *Aula* valve structural parameters were extracted from SEMs of 20 different valves (the raw SEMs were acquired by **Dr. Martina Gilic**) using **ImageJ** software. The thicknesses of different parts were measured from broken valves, while the average lattice parameters of the areolae arrays—which occur at the valve face and the mantle—were measured, and the lattice type was assigned using the newly developed methodology outlined in **Appendix B**. After that, the X_w of each parameter, its internal (dX_{int}), and external (dX_{ext}) errors were calculated based on

eqs. 3.1, **3.2**, and **3.3**, respectively. Based on the weighted mean (X_w) values of the structural parameters (illustrated in **Table 5.2**, **Chapter 5**), a total of **four horizontal** and **two longitudinal** 2D CSs were built to cover different structural features of the *Aula* valve (**Fig. 3.2**). It should be noted that *Aula* $CS_{long,i}$ and $CS_{hor,i}$ represent the *z*-*y* and *x*-*y* planes in the 3D valve, respectively. It should also be noted that the numerical analysis of $CS_{hor,i}$ were only relevant for the side-illumination study (see **subsection 3.2.4**).

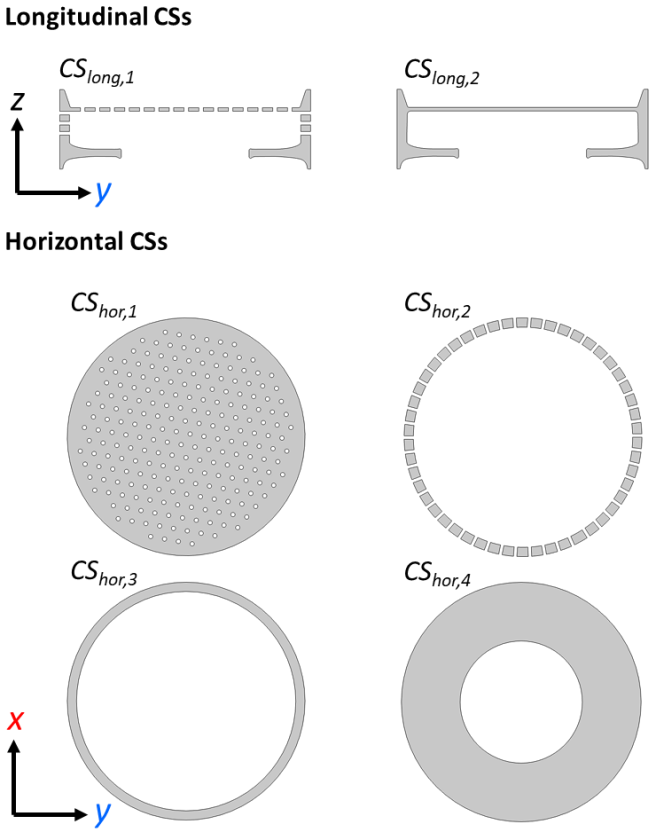

Fig. 3.2. The representative 2D CSs of the *Aula* valve. The $CS_{long,1}$ and $CS_{long,2}$ show the valve with and without areolae, respectively. The $CS_{hor,1}$ shows the porous plate of the valve face, which has a disc-like structure of an approximated height of 200 nm. Moreover, $CS_{hor,2}$ and $CS_{hor,3}$ show the mantle with and without areolae, respectively. Furthermore, $CS_{hor,4}$ shows the Ringleist, which has a hollow disc-like structure.

3.2.2. Analysis of the light modulation by GP valve/frustule

The numerical analysis of the wave propagation across *GP* CSs was performed inspired by the procedures demonstrated in a COMSOL application note [262]. Unless otherwise stated, each 2D CS was placed into a rectangular simulation box (100 µm height (*y*-axis) and 40 µm width (*x*-axis)) at a distance of 4 µm from the input boundary (**Fig. 3.3**), which was illuminated (normal to its surface) with a plane wave of 80 µm size (centered at *y* = 0), defined by a transverse (*i.e.*, *out-of-plane*) electric field of strength $\mathbf{E_{input}}$ = 1.00 V/m. The scattering boundary condition (**SBC**) was applied to the input boundary at the left, while the remaining boundaries were

set as perfectly matched layers (**PMLs**) to avoid nonphysical reflections. This configuration was chosen after optimization to ensure the receiving of a plane wave as perfect as possible at the position of the CS.

Unless otherwise stated, the calculations were performed as parametric sweeps, changing the vacuum wavelength of the input wave λ_{vacc} from 300 nm to 800 nm in 50 nm steps to cover the main radiation of the solar spectrum. Across all wavelengths, the refractive index of the amorphous silica constituting the *GP* valve n_v was set to 1.46 [263], while the refractive index of the surrounding medium n_m was set to n_a = 1.00 or n_w = 1.33, representing air or water, respectively. The mesh size was controlled by the physics and, in all cases, was much smaller than λ_{vacc} (reaching a few nm, but having a maximum size of $\lambda_{vacc}/n/5$ [227]) and automatically adapted to the complexity of the geometry of the CSs. To study the influence of the refractive index contrast, parametric sweeps of $1.00 < n_m < 1.46$ and $1.00 < n_v < 1.9$ were performed.

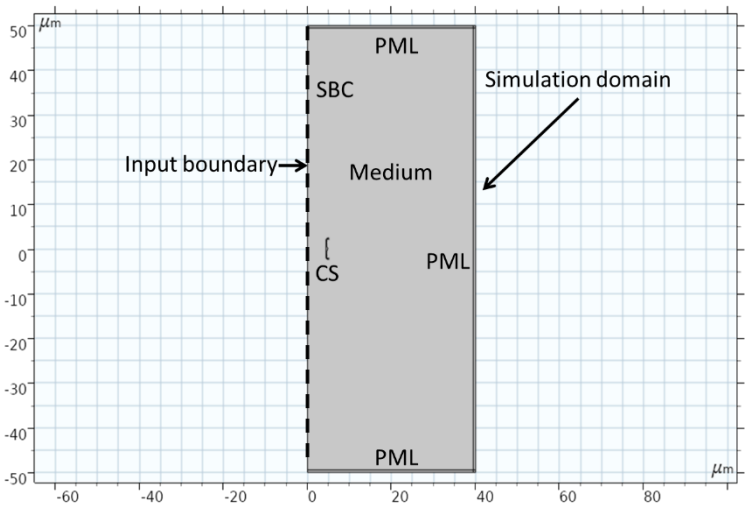

Fig. 3.3. The optimized simulation domain.

Moreover, the results were compared to simulation results of 2D analytical models of distinct optical components, such as thin slabs, as well as lens-like, grid-like, and fiber-like structures of silica, under identical conditions. This allowed more detailed study of the effect of distinct structural parameters (*e.g.*, length, thickness, striae spacing, and areolae diameter) on the light interference patterns. Furthermore, to understand the relevance of the observed optical phenomena of the valve's CSs to the photobiology of living cells, the effect of adding 4 girdle bands and a hypovalve to selected CSs was studied in water.

After computation, unless otherwise stated, two-dimensional images displaying the distribution of the normalized electric field strength $\mathbf{E_{Norm}}$ within the simulation domain were obtained, with a strength scale (0 to 2 V/m) depicted with a color code ranging from blue ($\mathbf{E_{Norm}} < \mathbf{E_{input}}$) to white ($\mathbf{E_{Norm}} = \mathbf{E_{input}}$) to red ($\mathbf{E_{Norm}} >$

$\mathbf{E_{input}}$). Where necessary, the $\mathbf{E_{Norm}}$ values were extracted at precise (*x*, *y*) positions in the simulation domain by creating 2D cutlines.

3.2.3. Simulation conditions for the Aula valve side-illumination study

The numerical analysis of the wave propagation across *Aula* CSs was carried out by implementing the same conditions used in the previous subsection but with minor modifications. Here, the simulation domain has a 90 µm height (*y*-axis) and 50 µm width (*x*-axis), to obtain a deeper field behind *Aula* CSs (of larger size compared to *GP* CSs), while keeping the simulation time almost the same. The simulations were carried out at only three λ_{vacc} (470 nm, 590 nm, and 660 nm), equivalent to the λ_{max} of the used LEDs in the experimental setup (see **subsection 3.3.2**). Both polarizations of **E** field (*out-of-plane* and *in-plane*) were considered in the simulations.

After computations, 2D images illustrating $\mathbf{E_{Norm}}$ distribution within the simulation domain were obtained, with a strength scale starting from 1 V/m that only emphasizes the constructive interference (where $\mathbf{E_{Norm}} > \mathbf{E_{input}}$), while keeping the destructive interference and $\mathbf{E_{input}}$ (where $\mathbf{E_{Norm}} \leq \mathbf{E_{input}}$) not emphasized.

3.2.4. Simulation conditions for the trans-illumination study

To mimic the relevant experimental conditions as possible (see **subsection 3.3.1**), the simulation domain and conditions used in **subsection 3.2.2** were considerably modified. The modified simulation domain (80 µm height (*y*-axis) and 100 µm width (*x*-axis)) included a part of the glass substrate (assuming its refractive index $n_{sub} = n_v = 1.46$) underneath the CSs, as shown in **Fig. 3.4**. Here, the SBC was applied to the input boundary at the bottom, where a plane wave, of 90 µm size (centered at $x = 0$), was launched. The relevant *GP* and *Aula* CSs were separately imported and placed above the substrate, having either their outer or inner face upward. It should be noted that the transmitted wave across the glass substrate has an average strength value $\mathbf{E_{Norm,back}} \approx 1.185$ V/m (larger than $\mathbf{E_{input}}$), as it is launched from a higher refractive index medium (of n_{sub}) to be transmitted in air (of n_a), where the transmission coefficient $t = 2*n_{sub}/(n_a + n_{sub})$, under normal incidence.

Although the illumination used in the experiment has a very large spectral width (*i.e.*, covers a wide range of wavelengths including visible light), the CMOS camera used for imaging has its maximum quantum efficiency in the range of 470-520 nm (see section 8.7 in [264]). Therefore, the experimental results could primarily be compared to the simulations approximately at λ_{vacc} **= 500 nm**. Both polarizations of **E** field (*out-of-plane* and *in-plane*) were considered in the simulations.

After computation, 2D images displaying the distribution of $\mathbf{E_{Norm}}$ within the simulation domain were obtained, with a strength scale (0.185 to 2.185 V/m) depicted with a color code ranging from blue ($\mathbf{E_{Norm}} < \mathbf{E_{Norm,back}}$) to white ($\mathbf{E_{Norm}}$ **=**

$\mathbf{E_{Norm,back}}$) to red ($\mathbf{E_{Norm}}$ > $\mathbf{E_{Norm,back}}$). Such color code was chosen to elucidate the constructive and destructive interference induced by the CSs above the substrate. Where relevant, 2D $\mathbf{E_{Norm}}$ profiles were extracted by creating 2D cutlines at precise positions in the simulation domain above the CS. The obtained $\mathbf{E_{Norm}}$ profiles (named $\mathbf{E_{Norm,CS}}$) were normalized to $\mathbf{E_{Norm,back}}$ (*i.e.*, $\mathbf{E_{Norm,CS}}$/$\mathbf{E_{Norm,back}}$) to obtain a comparable result to the experiment, where also the extracted line profiles were normalized to the background during analysis (see **subsection 3.3.1**).

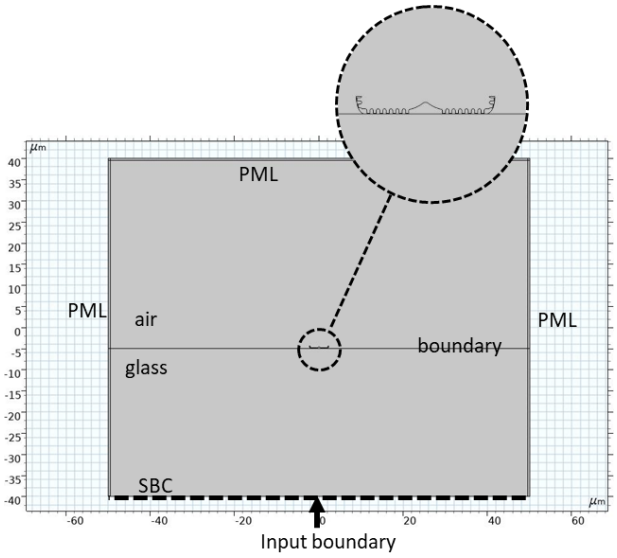

Fig. 3.4. The simulation domain for the trans-illumination study.

3.2.5. Simulation conditions for the SNOM study

Here, the simulation domain and conditions were adapted to mimic the situation of SNOM measurements (see **section 3.4**). The 2D CSs were placed over a glass substrate (of n_{sub} = 1.46) covered by a gelatine layer (of n_{gel} = 1.54 [265], assumed to be 5 µm thick), as illustrated in **Fig. 3.5**. Note that, changing the thickness of gelatine layer (between 1 – 10 µm) found to lead to negligible changes in the average transmittance $\mathbf{E_{Norm}}$ (in the range of ± 0.005 V/m). The simulations were carried out at two λ_{vacc} (532 nm and 808 nm), the same as the lasers' wavelengths used in the measurements.

In the illumination mode (**Fig. 3.5a**), the simulation domain has 25 µm height (*y*-axis) and 40 µm width (*x*-axis). The input wave (of $\mathbf{E_{input}}$ = 1 V/m) was initiated only from a small area (100 nm width) to mimic the aperture of the SNOM tip (obtaining a finite local illumination source). The influence of illuminating different parts of the CS, representing different areas of the valve, was investigated while having either the inner or the outer face upward. After computations, 2D images illustrating $\mathbf{E_{Norm}}$ distribution within the simulation domain were produced, with a strength scale in the range of 0.0 to 0.5 V/m to show the tip-valve interaction.

In the collection mode (**Fig. 3.5b**), the simulation domain and conditions are similar to that of the trans-illumination study (the previous subsection). Here, the simulation domain has a reduced size (of 40 µm height (*y*-axis) and 100 µm width (*x*-axis)), as only the optical near-field is relevant, which helped reduce the simulation time. In this case, the transmitted wave across the glass substrate and gelatine layer has an average strength value $\mathbf{E_{Norm,back}}$ (≈ 1.187 V/m). No significant changes in $\mathbf{E_{Norm,back}}$ were observed by changing the simulation domain size. Both polarizations (*out-of-plane* and *in-plane*) of **E** field were considered in the simulations. When relevant, the extracted 2D $\mathbf{E_{Norm}}$ profiles at the optical nearfield of the CSs (named $\mathbf{E_{Norm,CS}}$) were normalized to $\mathbf{E_{Norm,back}}$ to obtain a comparable result to the experimental results (see the analysis of the SNOM optical images in **subsection 3.4.1**).

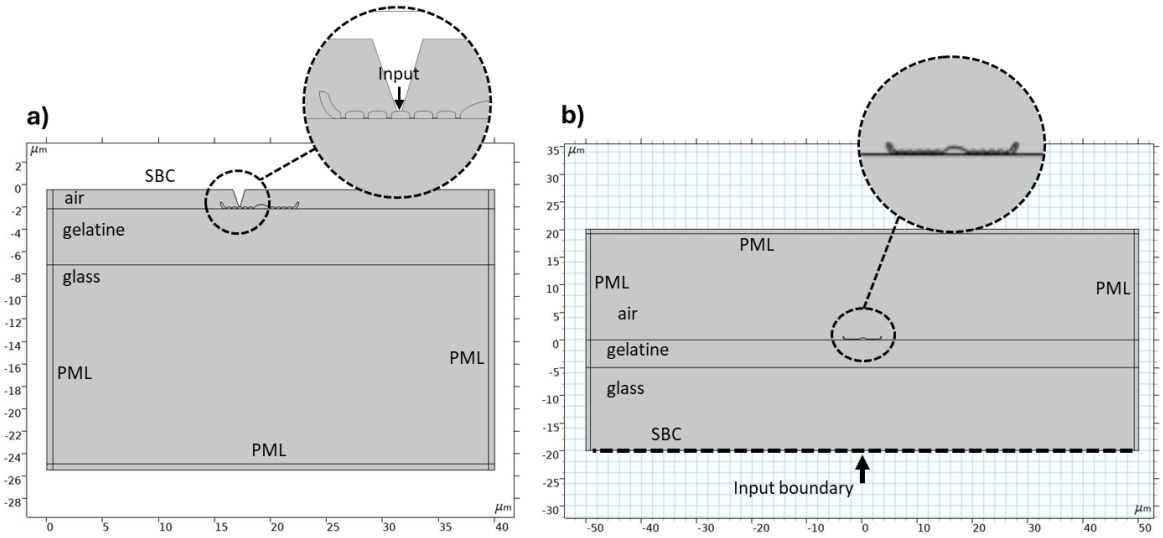

Fig. 3.5. Simulation domain for two distinct SNOM modes; illumination (**a**) and collection (**b**). The position of the SNOM tip in the illumination mode was changing to illuminate different parts of the CS.

3.3. Far-field optical microscopy

Far-field optical microscopy is not only used to investigate the morphology of microscopic objects but can also show how light interacts with these objects. This approach has been used in the literature to study the light modulation capabilities of diatom valves (*e.g.* [137,139,140]). Here, far-field optical microscopy is used to investigate the diffraction-driven light-focusing abilities of diatom valves, employing two illumination techniques: trans- and side-illumination, as demonstrated below.

3.3.1. Trans-illumination

The trans-illumination is a standard used technique for optical microscopy, where the light propagates along the optical axis to reach the objective directly after being

transmitted through the sample. The trans-illumination measurements were carried out utilizing a trinocular optical microscope (Kyowa KN-50TC, Kyowa optics, Japan), a semi-plan 40x objective (NA 0.65, WD 0.38 mm) or 10x objective (NA 0.25, WD 8.57 mm), and a grayscale CMOS camera (ARTCAM-500MI-BW-WOM, Artray, Japan) connected to a personal computer (PC) that records images via a home-written LabVIEW program. A tungsten-halogen lamp (20 W, 6V)—of a continuous spectrum that covers visible light and NIR wavelengths—was utilized as the illumination source, operating at its maximum intensity. In the microscope, the light was going through an Abbe condenser to be focused on the examined valves. The condenser's vertical position, as well as the iris aperture, was adjusted to optimize the light cone reaching the valves on top of the glass slide, obtaining a beam of about 10 mm diameter. The transmitted light through the valve was collected by the objective, which directed the light to the grayscale CMOS camera through a standard tube (**Fig. 3.6a**). The imaging parameters, including exposure and gain, were controlled via the home-written LabVIEW program.

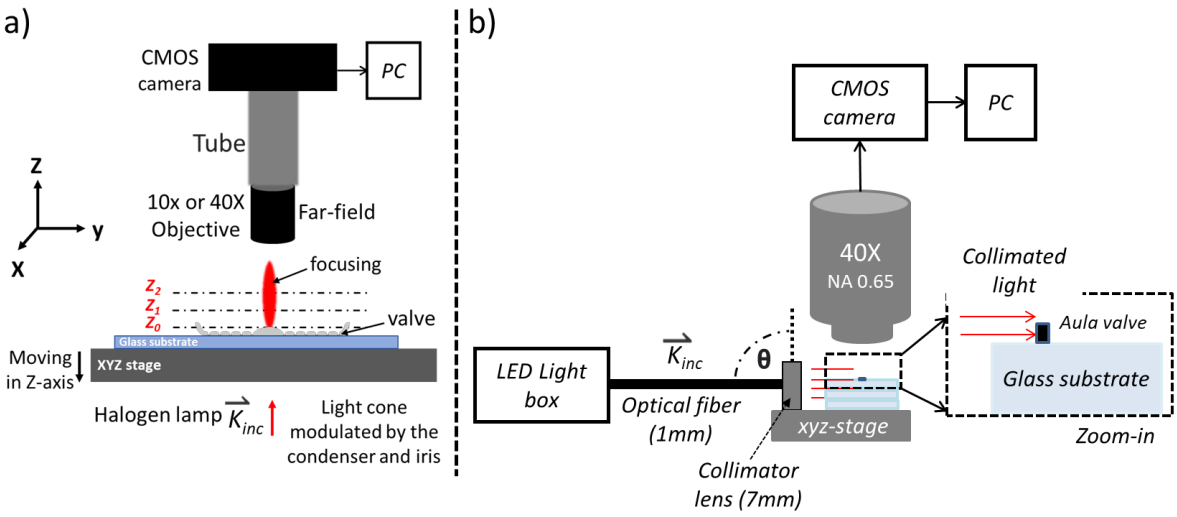

Fig.3.6. Sketches showing the experimental setup of the (**a**) trans- and (**b**) side-illumination technique. In all cases, the light cone and the objective are much larger than the size of the studied valves.

All experiments were conducted in air and a dark room (*i.e.*, without an external light source). For each measurement, the microscope focal plane was adjusted to the best focus of the valve z_0, at which the striae and other structural features of the valve were resolved (if possible). It should be noted that there was a slight uncertainty in the actual z_0 position due to the 3D structural complexity of some valves, such as the ***Acto*** valve. Thereafter, a ***z*-scan** was carried out by manually moving the microscope stage away from the objective (*i.e.*, defocusing) using the microscope fine knob at fixed steps (***z*-steps**) in order to collect information at different 2D focal planes in the vicinity of transmittance above the valve (**Fig. 3.6a**). The 2D images collected by this method could provide valuable information on the

light modulation capabilities of diatom valves (including diffraction-driven focusing), considering only the propagating fields that can be observed in the far-field and with the Abbe diffraction limit. The height of the minimal ***z***-step that can be achieved by the fine knob was calibrated against a mechanical stage of high-resolution ***z***-steps (1 µm/step) and was found to be approx. 1.4 µm ± 0.1 µm. The minimal steps (approx. 1.4 ± 0.1 µm) were used to study the small valves, while larger steps (approx. 7.0 ± 0.5 µm) were used for the larger valves. In some cases, the camera saturation was reached for a given valve. In this case, the exposure value was reduced (via the LabVIEW program) to reveal the required information (see, for example, **Fig. A.4** in **Appendix A**), while keeping the light intensity fixed. Finally, the obtained raw images were used for analysis without processing.

Analysis of the obtained images

For each studied valve, a set of grayscale images (representing different z_i planes) was obtained per measurement while tracking the diffraction-driven focusing behavior. These images were imported to **ImageJ** software, and their actual dimensions were specified in micrometers. A selected line profile across the focal spot/area was extracted at each focal plane z_i, showing the grayscale intensity ***I*** across that line (*e.g.*, **Fig. A.4b**). The average background grayscale value was extracted from areas in the image outside the valve. The focal plane showing the maximum focusing was determined by comparing the grayscale intensity of the focusing spot/area at different z_i. The extracted line profiles were imported to **Igor Pro** software, where they were normalized to the corresponding background to obtain the normalized grayscale intensity I_{Norm} (of relative grayscale values, **Relative G.S.**), which was now independent of illumination and camera settings.

3.3.2. Side-illumination

The term 'side-illumination' refers to the illumination technique employed in optical microscopy, where the illumination reaches the sample from the side (*i.e.*, perpendicular to the optical axis of the objective). It can be considered a type of dark-field optical microscopy that is mainly used to image the scattered light by the specimen while excluding the non-scattered light, which gives the micrograph a dark background and enhances the contrast [266]. In regular dark-field optical microscopy, a dark-field condenser blocks the direct light (from the illumination source) from reaching the objective [266]. While, in the side-illumination technique employed here, there is no need for a dark-field condenser, as the light enters the image field perpendicular to the objective axis.

This technique has been used in literature to investigate the diffraction-driven focusing behavior (specifically PJ generation) of, for example, artificial dielectric microdisks [267,268] and microcylinders [269] as well as living cells [270]

and other biomaterials [271]. It should also be noted that this technique has also been applied to diatoms while briefly investigating the light interaction with the girdle bands of *Coscinodiscus granii* [42].

The experimental setup of the side-illumination technique is sketched in **Fig. 3.6b**. The side-illumination experiments were carried out utilizing the same optical microscope and camera used in the trans-illumination study. The illumination was provided by a light-emitting diode (LED), fixed in a home-built LED box. The unpolarized light was guided from the LED box via an optical fiber (1 mm core, M71L01, Thorlabs, USA) connected to a collimator (F280SMA-850, Thorlabs, USA) to obtain a collimated beam of about 7 mm diameter falling onto the sample from the side. The optical fiber and the collimator were fixed on the *x-y-z* controllable stage of the microscope about 13 mm away from the objective's optical axis. Unless otherwise stated, the beam was centered on the substrate plane with a 5° tilt from the top (*i.e.*, Θ is 85°). The 5° tilt helped to provide the maximum light intensity on the top of the substrate where the valves occur by reducing the shadowing effect. As this experimental setup is a home-built, its ability to reveal the diffraction-driven focusing was confirmed using a typical PJ generator (see **section A.6** in **Appendix A**).

All experiments were conducted in air and a dark room. A red LED ($\lambda_{max} \approx 660$ nm) was utilized for most experimental work, including the comparisons between the distinct valves, as it has been found to give a more apparent diffraction-driven focusing beam/spot. For the wavelength-dependence study (in the case of *Aula* valves), two additional LEDs have been utilized, representing blue ($\lambda_{max} \approx 470$ nm) and orange ($\lambda_{max} \approx 590$ nm) colors. It should be noted that the trans-illumination was applied to visualize the valves before turning it off to capture the scattered field induced only by side-illumination.

As already mentioned, the valves were imaged almost perpendicular to the propagation direction of incident light to capture mainly the scattered light fraction. Best images were obtained with a 5° tilt of the illumination source, although this leads to a probability that light will partially be reflected by the glass substrate and collected by the objective together with the scattered light. Nevertheless, the images of glass substrate without diatom valves are homogenously dark, which means the reflected fraction is negligible. By repeating the experiment on distinct substrates of different degrees of reflectivity (*e.g.*, metal and plastic), it has been confirmed that the observed focusing behavior of the valves was independent of the substrate type underneath. Nevertheless, focusing spots/beams seem clearer on a glass substrate. Finally, unless otherwise stated, the obtained raw images were used without processing.

3.4. Scanning near-field optical microscopy

All SNOM measurements were conducted by **Professor Paul Fumagalli**. The measurements were carried out in a dark room in the air using a home-built setup, located in AG Fumagalli, physics department, FU Berlin. The experimental setup is described in [272] in detail. Two illumination sources were employed in this study, including a frequency-doubled Nd:YAG laser and a diode laser, generating green (λ_{exc}= 532 nm) and NIR (λ_{exc}= 808 nm) laser lines, respectively. The SNOM probe is based on a multimode fiber (LovaLite, type E50, HPSC10 multimode fiber, France) that is coated with Aluminium while leaving a 100 nm aperture at its tip without coating. The substrates were fixed on an automatic high-resolution *x-y-z* stage, controlled by a home-written LabView program. In all measurements, the uncoated aperture was in contact with the valve surface (equivalent to AFM contact mode). The measurements were carried out by scanning the valve surface with the SNOM probe at a controllable speed to collect **topographical** and **optical** information at each pixel simultaneously. During the scan, the probe was adjusting its height on the ***z***-axis, responding to the valve topography and geometry employing a feedback loop to keep the aperture and the valve surface in contact. The setup was operated in transmission configuration with the flexibility to change between illumination and collection modes (**Fig. 3.7**).

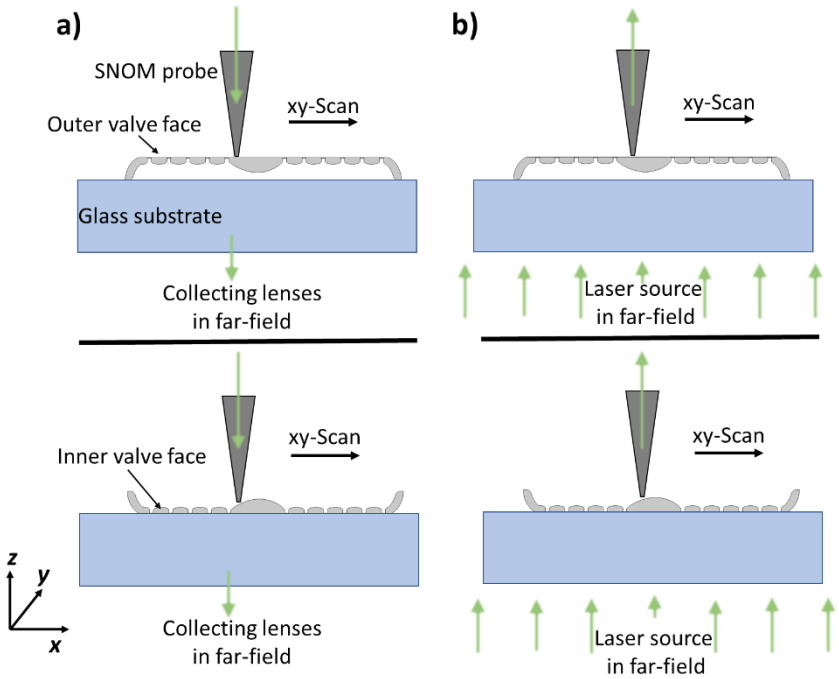

Fig. 3.7. Sketches show the SNOM illumination (**a**) and collection (**b**) modes, while scanning the outer (at the top) or inner (at the bottom) valve faces. Note that the collecting lenses in (**a**) is much larger than the size of the studied valves.

In the illumination mode (**Fig. 3.7a**), the valve surface (outer or inner) was illuminated via the SNOM nanoaperture. In this configuration, the wave evanescent

from the nanoaperture can be coupled into the nanostructures of the valves. The transmitted light was collected by focusing lenses placed in the far-field. In the collection mode (**Fig. 3.7b**), the laser source (of a diameter larger than the valves' size) was used to illuminate the sample, while the SNOM nanoaperture was collecting the light intensity distribution over the valve surface (*i.e.*, near-field) pixel-by-pixel via scanning.

In all cases, the scanning speed, scanning area, and resolution (*i.e.*, number of pixels per scan) were adjusting to explore different features. It should be noted that the scanning time sometimes reached a few days per scan to obtain high-resolution results. The collected light at each pixel was guided through the optical fiber and dispersed on a **fiber optic spectrometer** (AvaSpec-ULS2048, Avantes) to obtain the photon counts for each wavelength across the full spectrum. The final optical images were extracted from a home-written LabView program by integrating the photon count of the wavelengths in a window covering about 90% of the laser line width. Simultaneously, shear-force images were also extracted for each scan showing the topography of the scanning area.

3.4.1. Analysis of the SNOM optical images

The extracted optical images were obtained in Tag Image File Format (**TIFF**) format. The processing and analysis of the extracted images were carried out, respectively, via **Gwyddion** (version 2.63) and **ImageJ** software. In the analysis, the average background intensity $I_{background}$, accompanied by a standard deviation value associated with the noise in the background, was estimated from areas outside the diatom valve in the raw image (*e.g.*, the dashed circles in **Fig. 3.8**).

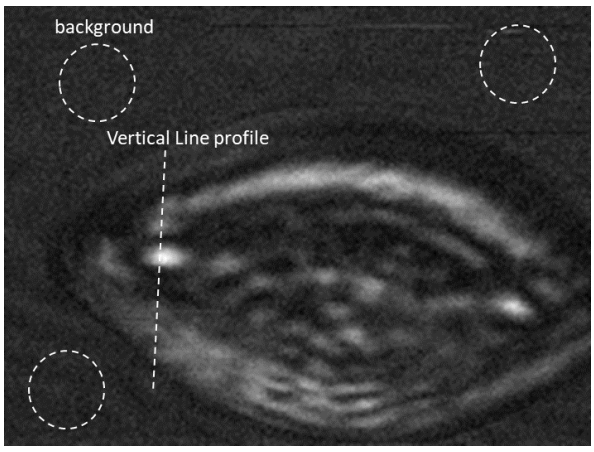

Fig. 3.8. An example of the extracted SNOM optical images showing *GP* outer valve face in the collection mode at green laser. The $I_{background}$ was estimated from the dashed circles, while the dashed line represents an example of the extracted line profiles.

Different features were analyzed in the optical images by extracting a line profile showing the light intensity distribution $I_{line\_profile}$ across this line. The extracted

line profiles were imported into **Igor Pro** software, where they were normalized to the average background intensity to obtain the normalized line profile ($I_{Norm} = I_{line\_profile}/I_{background}$).

3.5. Diatom-based SERS hybrid substrates

3.5.1. Hybrid substrates preparation

The hybrid substrate consists of clean diatom valves (dispersed on a clean glass substrate) and is coated with an ultrathin gold layer (plasmonic material). In order to obtain a homogenous ultrathin gold film over the silica surface of diatom valves as well as on the glass substrate, a molecular adhesive self-assembled monolayer (**SAM**) was applied (**Fig. 3.9**) before gold deposition, following a similar method to that described in Stec *et al.* [273].

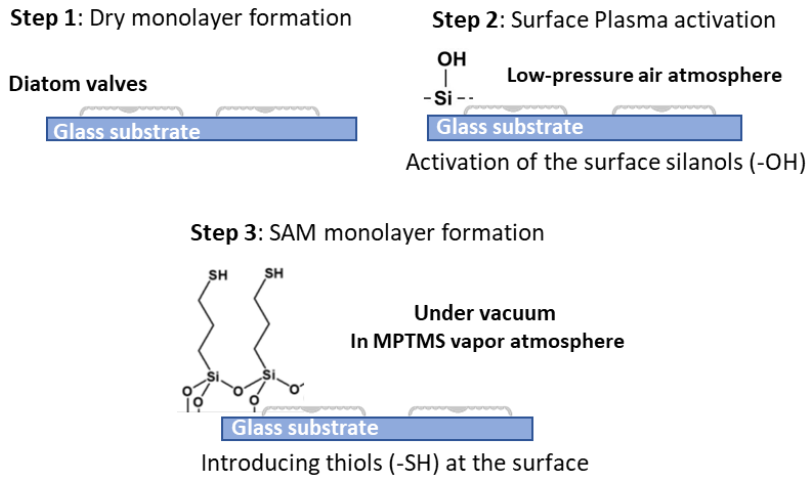

Fig. 3.9. A Sketch briefly showing the steps for the self-assembled monolayer (SAM) formation.

Briefly, the silica surface of the obtained valves' monolayers (as well as the glass substrate in the areas uncovered with valves) was activated via a plasma cleaner (Harrick PDC-32G, USA) employing a Radio Frequency (RF) generator (≈ of 10 MHz) to generate and excite the plasma in a low-pressure air atmosphere. The device was operated at its mid-power for 10 min. This step was critical to activate and increase the density of free silanol groups (Si-OH) on the silica surfaces. Thereafter, the substrates were transferred into a vacuum desiccator, where an Eppendorf filled with about 80 µl of (3-mercaptopropyl)trimethoxysilane (**MPTMS**) was opened to produce its vapor after pulling the air from the desiccator using a rough vacuum pump for about 40 min. The samples were left in these conditions for three days to ensure that the MPTMS vapor formed a monolayer over the siliceous substrates.

The substrates, activated with SAM monolayer, were transferred into a Physical vapor deposition (**PVD**) chamber (KJLC Nano 36, located in a clean room at AG Bolotin, physics department, FU Berlin) immediately after releasing the vacuum inside the desiccator using dry nitrogen. The substrates were fixed tightly inside the deposition chamber (**Fig. 3.10**), and then a high vacuum of 10^{-6} Torr was obtained using a turbomolecular pump.

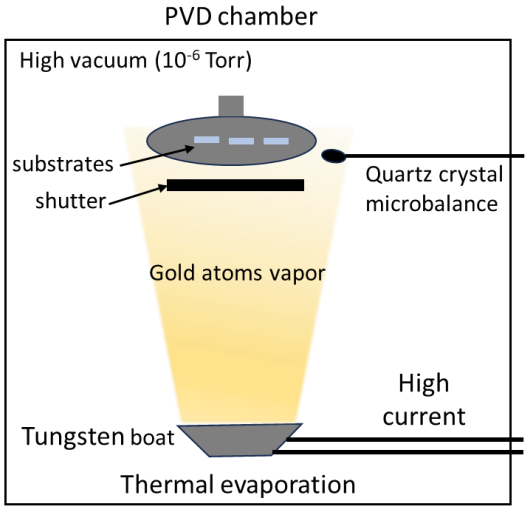

Fig. 3.10. A sketch briefly shows the Physical vapor deposition (PVD) chamber.

The gold deposition was conducted using a thermal evaporation technique with an evaporation rate of 0.1 Å/s, reaching a final thickness of 100 Å (= 10 nm). The evaporation parameters (including the rate and power) were controlled via an electronic monitor integrated into the device. The shutter helps protect the substrates while heating gold before having a stable evaporation rate. The gold film thickness was estimated using an integrated quartz crystal microbalance. After deposition, the vacuum was released, and the hybrid substrates were stored in a clean, dry place till further use.

Finally, it should be noted that a **reference substrate** was fabricated with the same methodology but without the diatom valves' monolayer.

3.5.2. Characterization of the obtained gold film

The scanning electron microscopy (Hitachi SU8030, Japan) was carried out by **Dr. Martina Gilic** to investigate the ultrastructure of the deposited gold film over glass substrate as well as diatom valves using a secondary electron detector and an acceleration voltage of 15 KV. **Professor Louisa Reissig** and **Dr. Martina Gilic** carried out a further characterization for the reference substrate (*i.e.*, without diatom valves) using atomic force microscopy (AFM, located at the Institute of Physics, Belgrade, Serbia) and UV-Vis spectroscopy. The mechanical stability and adhesion of the ultrathin film to glass substrates were tested using a scotch tape test.

3.5.3. SERS measurements and analysis

All Raman measurements were carried out **together with Dr. Martina Gilic**. A confocal Raman microscope (Horiba XploRA, located at AG Reich, physics department, FU Berlin), operating in a backscattering configuration and equipped with a charge-coupled device (CCD) camera, was used for SERS measurements. Rhodamine 6G (**R6G**) was utilized as a probe molecule. For the measurements, about 7 µl of R6G dissolved in ethanol (of concentration 1 mM) was dropped on top of the gold film and left to dry under ambient conditions. Using ethanol as a solvent helps to distribute R6G relatively well over the substrates, thus, obtaining more comparable and reproducible results. Before measurements, calibration of the spectrometer was carried out using a silicon substrate, which has a characteristic Raman band at 520 cm^{-1}.

In the measurements, the spectra were acquired using the following parameters: a red excitation laser of λ_{exc} = 638nm, 1% power filter, pin-hole size of 300 µm, slit size of 50 µm, 1200 $lines.mm^{-1}$ grating, a spectral range of 500 – 2100 Cm^{-1}, and 100x objective lens (NA 0.9). The excitation laser polarization was set to be horizontal. These parameters were selected after optimization to maximize the signal-to-noise ratio (SNR) and minimize the background obscuring the signal as possible. The green excitation laser (λ_{exc} = 532 nm) was unsuitable for the measurements as it showed a strong photoluminescence background, which obscured the signal. The spectra were monitored and recorded by **LabSpec** software. All measurements were carried out in air with an integration time of 15 seconds and averaged over 5 accumulations, while applying an **automatic flat correction**. Moreover, SERS mapping was carried out by scanning selected areas with a resolution of 1 µm/step in the case of *Aula* (or 0.5 µm/step in the case of *CR* and *GP*) and an integration time of 1 s per step.

Finally, further data analysis was carried out by importing the obtained spectra into **Igor Pro** software to determine different R6G vibrational bands and compare the distinct substrates.

4 Numerical analysis of the light modulation by the valve/frustule of *Gomphonema parvulum*

The results and discussions shown in this chapter have already been published in:

Ghobara, M.; Oschatz, C.; Fratzl, P.; Reissig, L. Numerical Analysis of the Light Modulation by the Frustule of *Gomphonema parvulum*: The Role of Integrated Optical Components. Nanomaterials 2023, 13, 113, https://doi.org/10.3390/nano13010113. Used here under terms and conditions of the Creative Commons Attribution (CC BY 4.0) license (https://creativecommons.org/licenses/by/4.0/).

This chapter aims to expand the knowledge on the light modulation capabilities of diatom frustules by concentrating on small pennates, which form a large and diverse group often underrated in such studies. The frustule of biraphid pennate ***GP*** is used here as a model. Moreover, a novel analytical approach was employed to enhance the understanding and minimize computational costs by (i) reducing the complex 3D structure (the complete valve or frustule) into 2D cross-sections and, further, by (ii) disassembling the distinct optical components. This approach helps to understand the overlapping optical phenomena and reveals the role of integrated optical components within the solar spectrum range. Furthermore, by investigating the influence of different structural parameters (using analytical models) as well as refractive index contrast on the observed phenomena, this study opens the door for predicting the light modulation by other pennate frustules of similar structure but different dimensions.

4.1. Structural analysis of the *GP* frustule

GP is a benthic asymmetric biraphid pennate species. It is widely distributed in various aquatic ecosystems, mainly freshwater ecosystems, and has several varieties that differ, to some extent, in shape and size [274,275]. The frustules of the studied *GP* strain (**Fig. 4.1** and **Table 4.1**) are of elliptic to ovate shape (length L_v, width W_v) consistent with the previous structural description of some *GP* strains reported in [274].

The two valves, epivalve and hypovalve, have a face of thickness D_v, a curved mantle (*i.e.*, an elevated edge of the valve) of height h_M and width W_M, and are connected by girdle bands (approximately four). The face of each valve is divided by a raphe slit (length L_{ra}, width W_{ra}), which lies in a thickened area along the apical axis of the valve called the sternum with a maximum thickness D_S and a half-width $½W_S$.

The raphe slit is interrupted at the zone of the central nodule, dividing it into two slits with a spacing d_{ra}. The nodule (L_{nod}, W_{nod}), which is not placed precisely in the center along the apical axis but shifted by about 0.18 µm towards one side, is a dome-shaped area that appears in the inner valve face and reaches a maximum thickness D_{nod}. At the valve apexes, where the raphe slits end, the sternum slightly increases its thickness at the inner face, sometimes merging with the mantle, which could also be associated with the presence of apical nodules [17]. On both sides of the sternum (or nodule), rows of punctate areolae (*i.e.*, pores) with a spacing of d_a, so-called striae, extend towards the mantle. The striae occur after the sternum or the nodule except for a single stria at the nodule zone shortened by 1 µm that gives the valve, along with the shifted position of the nodule, the asymmetry. The striae are slightly bent or tilted (**Fig. 4.1**) with an average striae spacing expanding from $d_{str,min}$ to $d_{str,max}$, resulting in about 13 visible striae per valve. The areolae are visibly smaller on the outer face of the valve compared to the inner face, with diameters of $2r_{a,ext}$ and $2r_{a,int}$, respectively. The areolae are further covered with so-called flab-like pore occlusions (of a predicted thickness of $D_{occ} \approx 0.02$ µm), leaving a crescent-like slit, reaching a width of W_{occ}.

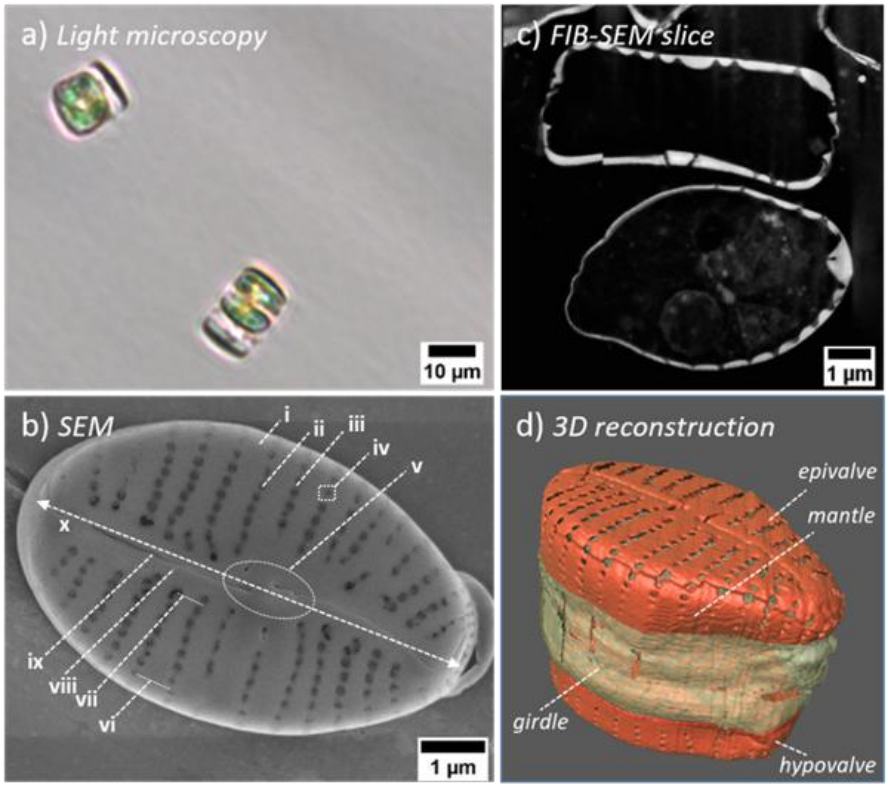

Fig. 4.1. Light microscopy of *GP* living cells (**a**), SEM of the outer valve view (**b**), FIB-SEM slice showing cross-sections of two individual cells (**c**), and 3D reconstruction of the frustule showing valves in red and girdle bands in white (**d**). Some structural features are illustrated in (**b**), including: costae (i), striae (ii), a shortened stria (iii), punctate areola covered with a flab-like occlusion (iv), nodule zone (v), striae spacing max (vi)/min (vii), sternum (viii), raphe slit (ix), and the apical axis (x). This Figure is reproduced from Ghobara *et al.* [261], and is adapted from a figure provided by Dr. Cathleen Oschatz.

Statistical analysis shows that all studied valves are of comparable dimension, with structural parameters varying by less than 10% (**Table 4.1**). The only exceptions (with deviations up to 17%) are the thickness of the sternum D_s, as well as the width W_{ra} and spacing d_{ra} of the raphe slit, the mantle height h_M, and the width of pore occlusion slit W_{occ}. With the exception of D_s and W_{occ}, these parameters display dominant dX_{ext}, indicating a relatively large variation between valves. This is also the case for the thickness of the nodule zone D_{nod}, the valve length L_v and width W_v, and raphe slit length L_{ra} but with a dX_{ext} up to 5%. Interestingly many of these parameters are found not to influence the obtained interference patterns significantly. In contrast, structural parameters describing the dimensions and spacing of the areolae ($2r_{a,ext}$, $2r_{a,int}$, and d_a), striae spacing (d_{str}), and the thickness of the valve D_v display a comparably small variation between valves, evident by their dominant dX_{int} of up to 7%. These are the parameters that can dramatically change the interference patterns in the simulations (see below).

Table 4.1. Statistical analysis of the structural parameters of *GP* valves (weighted mean, internal and external errors—the bold print indicates the significant error—and its precision in %). This table is reproduced from Ghobara *et al.* [261].

Parameter	Description	X_w (µm)	dX_{int} (µm)	dX_{ext} (µm)	Precision (%)
L_v	Valve length	**7.1**	0.006	**0.2**	3
W_v	Valve width	**4.59**	0.006	**0.07**	2
D_v	Thickness of the valve	**0.17**	**0.01**	0.004	6
D_{nod}	Thickness of the nodule zone	**0.38**	0.009	**0.02**	5
W_{nod}	Width of the nodule zone	**0.86**	**0.03**	0.02	4
L_{nod}	Length of the nodule zone	**1.568**	0.002	0.002	0.1
D_S	Maximum thickness of the sternum except the nodule zone	**0.26**	**0.03**	0.01	**12**
$½W_s$	Half-width of the sternum	**0.32**	**0.02**	0.01	5
L_{ra}	Raphe slit length	**5.8**	0.006	**0.2**	3
W_{ra}	Raphe slit width	**0.023**	0.0004	**0.004**	**17**
d_{ra}	Raphe slit spacing at nodule zone	**0.54**	0.004	**0.06**	**11**
$d_{str,min}$/ $d_{str,max}$	Striae spacing (center to center)	**0.49 / 0.57**	**0.03 / 0.02**	0.02 / 0.01	6 / 4
d_a	Areolae spacing (center to center)	**0.214**	**0.008**	0.006	4
$2r_{a,ext}$	Areolae diameter (2x radius) outer face	**0.100**	**0.007**	0.002	7
$2r_{a,int}$	Areolae diameter (2x	**0.15**	**0.01**	0.008	7

	radius) inner face				
h_M	Mantle height	**0.58**	0.004	**0.08**	**14**
W_M	Mantle width	**0.184**	**0.009**	0.004	5
W_{occ}	Width of the pore occlusion slit	**0.017**	0.002	0.002	**12**

The fine structure of the girdle bands is not studied in detail, as they are comparably simple and do not contain structural features relevant to the light propagation apart from their width, height, and spacing, which are estimated as $W_{girdle} = W_M$, H_{girdle} = 2.84 µm, and d_{girdle} = 10–50 nm, respectively. This is in contrast to the girdle bands of some larger species, such as *Coscinodiscus* spp., in which their porous structure dramatically influences the light propagation [125] and, thus, has to be considered during simulations of the whole frustule.

It should also be noted that finer structural features, such as the undulations on the silica or apical pore field, are also not considered in this study, as these do not fall into the length scales close to the studied λ_{vacc} range and are assumed not to be a determinant to the obtained near-field interference patterns.

Furthermore, the content of elements in the silica (available through energy-dispersive X-ray (EDX) mapping analysis) should be considered in the future, as additives can lead to spatial changes in $n_v(x,y,z)$ similar to what has been reported for some pennate valves in Soto *et al.* [263]. Changes in n_v could significantly influence light propagation, especially in a low-contrast medium. However, the general trends and features seen here should also then be relevant.

4.2. Numerical analysis of the 2D cross-sections—the role of optical components

All studied CSs show structural features in the length scales of visible light and induce an interference pattern in the **near-field** and **Fresnel regime zone**, as is evidenced by the red and blue areas (*e.g.*, **Fig. 4.2**).

It is evident that distinct structural features in the CSs induce a specific contribution to the interference pattern. Patterns of structurally complex CSs can be explained by the addition of interference patterns of "their distinct structural components" (*e.g.*, **Fig. 4.3**), such as slab-like, lens-like, grid-like, and fiber-like structures. The near-field interference patterns of such components can often be predicted by theory, *e.g.*, the thin-film interference of thin slabs or guided-mode resonance of grid-like structures (see below). Therefore, a range of optical phenomena occurring in the CSs featuring these specific structural components were studied separately. It should be noted that the presence or absence of pore occlusions in CSs with a grid-like structure did not show a significant effect on the

near-field interference pattern either in the longitudinal or vertical CSs (see, *e.g.*, **Fig. 4.2**). Therefore, pore occlusions are not considered in further discussions.

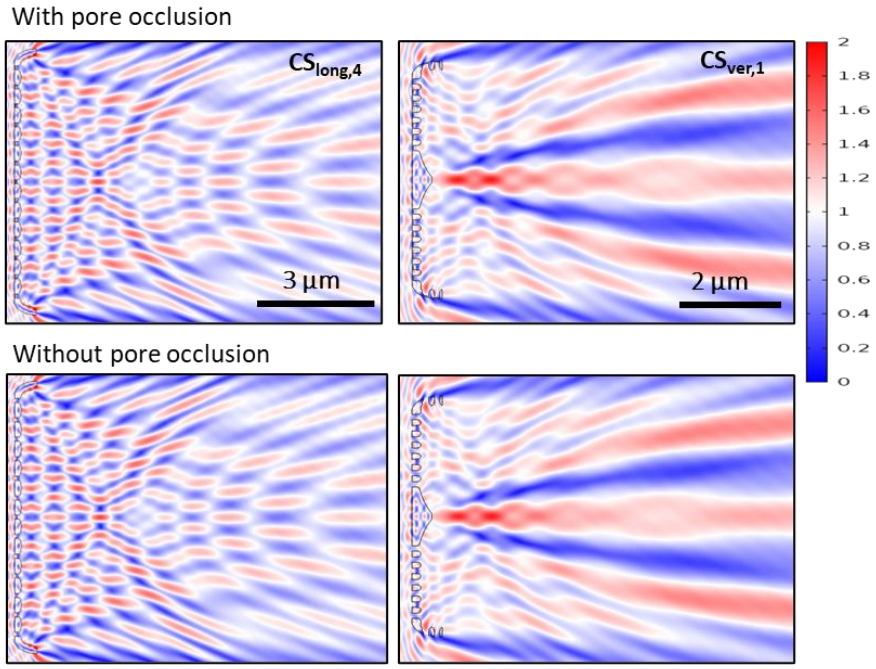

Fig. 4.2. The effect of pore occlusions on the interference pattern of $CS_{long,4}$ and $CS_{ver,1}$ at λ_{vacc}= 350 nm. The blue, red, and white colors of the color code indicate $\mathbf{E_{Norm}}$ < 1 V/m (a reduction in strength), $\mathbf{E_{Norm}}$ > 1 V/m (an increase in strength), and $\mathbf{E_{Norm}}$ = 1 V/m ($\mathbf{E_{Norm,input}}$), respectively. This Figure is reproduced from Ghobara *et al.* [261].

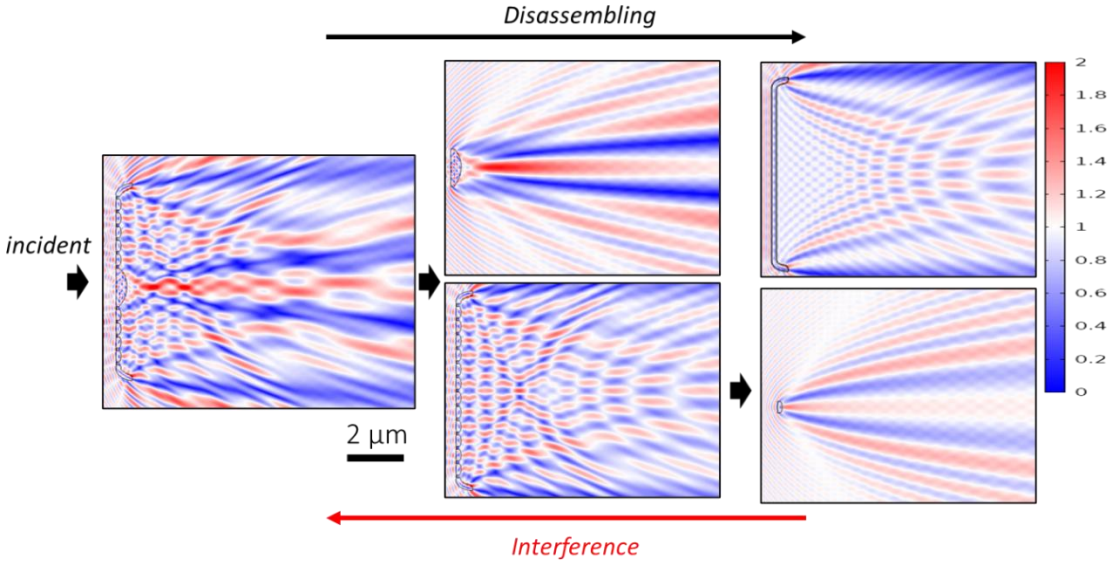

Fig. 4.3. The complex interference pattern observed in $CS_{long,3}$ at λ_{vacc}= 350 nm, at the left. The disassembling of its distinct structural components shows the contribution of each element to the interference pattern. The color code is given in V/m units. This Figure is modified from Ghobara *et al.* [261].

The idea of "building" the CSs through the addition of optical components is sketched in **Fig. 4.4** (see also all CSs in **Fig. 3.1**, **Chapter 3**). The simplest form of a

longitudinal cross-section ($CS_{long,5}$ or $CS_{long,7}$, which differ in length) is similar to a thin slab of corresponding thickness (A in **Fig. 4.4**) with curved and extended edges (B in **Fig. 4.4**). Slicing the valve across the areolae of consecutive striae leads to the addition of a grid-like structure with spacing d_{str} ($CS_{long,4}$ or $CS_{long,6}$, which differ in d_{str} and length (*i.e.*, grid units)). The presence of 1 µm shortened stria on one side of the valve leads to a defect in the grid-like structure that appears in $CS_{long,4*}$. It should be noted that the areas between the areolae have a plano-convex lens-like structure (C in **Fig. 4.4**) corresponding to the shape of the costae (*i.e.*, the ribs). When approaching the center of the valve, the grid is interrupted by the presence of the nodule zone, adding a larger plano-convex lens-like structure (D in **Fig. 4.4**) slightly off-center to the grid ($CS_{long,3}$). As soon as the sternum zone is approached, the grid-like structure disappears, but the overall thickness of the CS increases ($CS_{long,2}$). Slicing directly along the apical axis, the slab-like structure is further cut by the raphe slits, leaving a CS featuring only a lens-like structure in the center and two curved edges ($CS_{long,1}$).

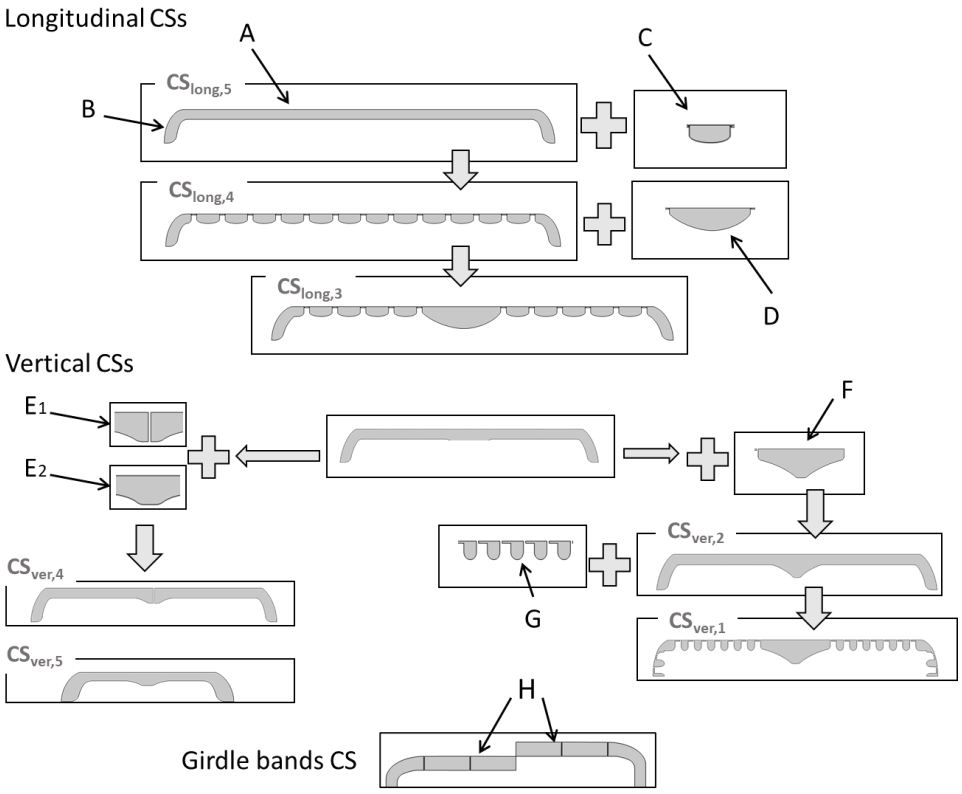

Fig. 4.4. A schematic diagram illustrates the idea of "building" CSs by adding different optical components. (**A**) A thin-slab element, (**B**) a curved, fiber-like structure, (**C**) a grid unit of lens-like structure, (**D**) lens-like structure, (**E_1** and **E_2**) increased thickness with and without the raphe slit, respectively, (**F**) triangular-like structure, (**G**) the grid-like structure in vertical CSs, (**H**) four rectangular, fiber-like structures. This Figure is adapted from Ghobara *et al.* [261].

In the case of vertical CSs, the thin-slab elements with curved elongated edges (similar to, *e.g.*, $CS_{long,5}$) are divided at the center either by adding the sternum

(with or without its slit, E_1 or E_2 in **Fig. 4.4**, respectively) or the slightly thicker nodule zone (F in **Fig. 4.4**) of a triangular-like structure ($CS_{ver,4}$/$CS_{ver,5}$ or $CS_{ver,2}$, respectively). It should be noted that the raphe slit in these structures, which only leads to an interruption of around 23 nm between the two parts, does not lead to significant changes in the near-field interference pattern. In all cases, the thin-slab area in the vertical CSs on both sides of the raphe or nodule can be further divided by a grid-like structure (G in **Fig. 4.4**) with spacing d_a of varying length ($CS_{ver,3}$ or $CS_{ver,1}$, respectively) corresponding to the slicing of the areolae within one stria.

It should be noted that the width of the curved and elongated edge varies slightly between the CSs depending on the position of slicing within the mantle (0.184 µm ≤ $W_{M,CS}$ ≤ 0.334 µm). Adding girdle bands to both sides of the CSs (while building 2D CSs across the complete frustule) further elongates the edge by adding these fiber-like structures (H in **Fig. 4.4**).

In general, the existence of the thin-slab elements leads to the occurrence of two distinct interferences: (i) thin-film interference and (ii) edge diffraction, overlaying in the transmittance region. The existence of fiber-like structures—the mantle and, additionally, the girdle bands in the complete frustule—leads to (iii) waveguiding behavior, which affects the corresponding edge diffraction pattern. Moreover, the finite size of the CSs, or the presence of thickened protruding structures associated with the cutting of the nodule zone or the sternum, results in increased interference between the transmitted and the diffracted waves from two (or more) edges. This leads to additional phenomena: (iv) diffraction-driven focusing and, further, (v) photonic jet generation in the transmittance. Furthermore, the grid-like structures lead to (vi) a characteristic diffraction grating behavior as well as (vii) guided-mode resonance, which leads to dramatic changes in the interference pattern at a specific range of wavelengths.

4.3. The Observed Optical Phenomena: Description and Analysis

All cross-sections can modulate light effectively, and generally, the modulation strength is strongly dependent on λ_{vacc} and Δn. As mentioned, a number of distinct optical phenomena were observed and correlated to the optical components in the CSs. Here, these phenomena are separately demonstrated, accompanied by the theoretical expectation, elucidating the role of the corresponding structural parameters where necessary.

4.3.1. Thin-Film Interference

The theoretical calculations—performed using [276], which calculate the reflectance (R) and transmittance (T) based on the complex Fresnel equations—show that for a

slab of thickness D_{sl} = D_v = 170 nm and refractive index n_{sl} = n_v = 1.46 embedded in air, the intensity of the reflected light is maximal at λ_{vacc} ≈ 330 nm (and approaching the second maximum in the NIR), while destructive interference occurs at λ_{vacc} ≈ 495 nm (dashed lines in **Fig. 4.5a**) under normal illumination. This means that the amount of light, which transmits through the thin-slab element of the valve, is attenuated for UV wavelengths, while the green wavelengths are largely unaffected by thin-film interference effects. In contrast, the interference pattern of thin-slab element of the sternum (D_s = 260 nm) shows an attenuated transmission at λ_{vacc} ≈ 305 nm and 505 nm, while the element at the nodule zone (D_{nod} = 380 nm) mostly affects transmission around λ_{vacc} ≈ 320 nm, 445 nm, and 740 nm (dashed lines in **Fig. 4.5a**).

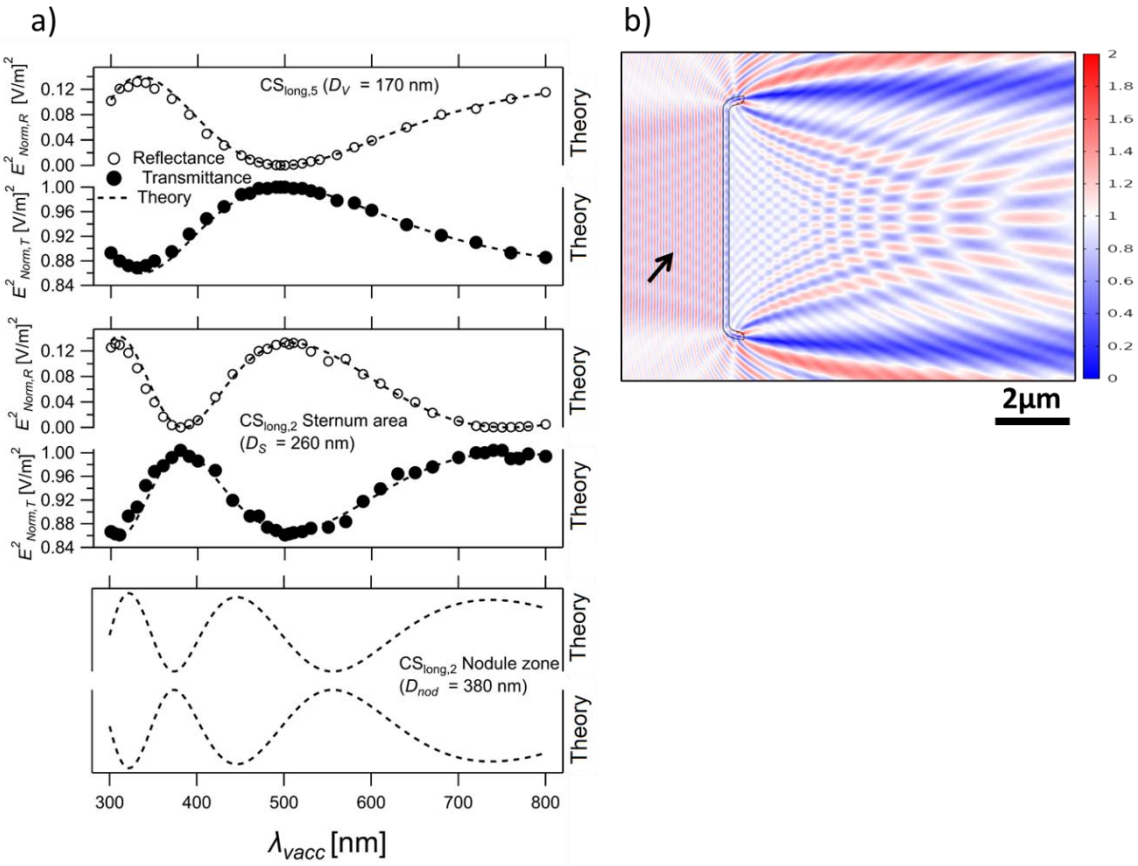

Fig. 4.5. (**a**) The plots show the extracted $\mathbf{E^2_{Norm,R}}$ and $\mathbf{E^2_{Norm,T}}$ of CS$_{long,5}$ and CS$_{long,2}$ compared to the theoretical calculation for the studied λ_{vacc} range. The estimated error in the extracted $\mathbf{E_{Norm}}$ is up to ± 0.006 or ± 0.01 V/m in CS$_{long,5}$ or CS$_{long,2}$, respectively. The extraction method of $\mathbf{E_{Norm,R}}$ and $\mathbf{E_{Norm,T}}$ from the simulation domain, as well as the error estimation, is illustrated in **Fig. 4.6**. (**b**) CS$_{long,5}$ shows the maximum constructive interference at reflectance (λ_{vacc} = 330 nm); the black arrow indicates the formation of non-physical standing waves between the reflected and the incident wavefronts. This Figure is modified from Ghobara *et al.* [261].

As illustrated in **Fig. 4.5a**, the dependency of the reflectance and transmittance intensity of the CSs with thin-slab elements on λ_{vacc} is in good agreement with theoretical calculations, which agreed with the expectation from

thin-film interference theory. However, it should be noted that extracting the data points from the complex interference pattern in the near-field of CSs is not trivial. In the case of reflectance, the formation of a seemingly standing wave in the $\mathbf{E_{Norm}}$ presentation is caused by the interference of the reflected and the incoming waves (see **Fig. 4.5b**). This makes the $\mathbf{E_{Norm}}$ value strongly position-dependent. The strategy illustrated in **Fig. 4.6** was followed to overcome this problem and to minimize the edge diffraction effects.

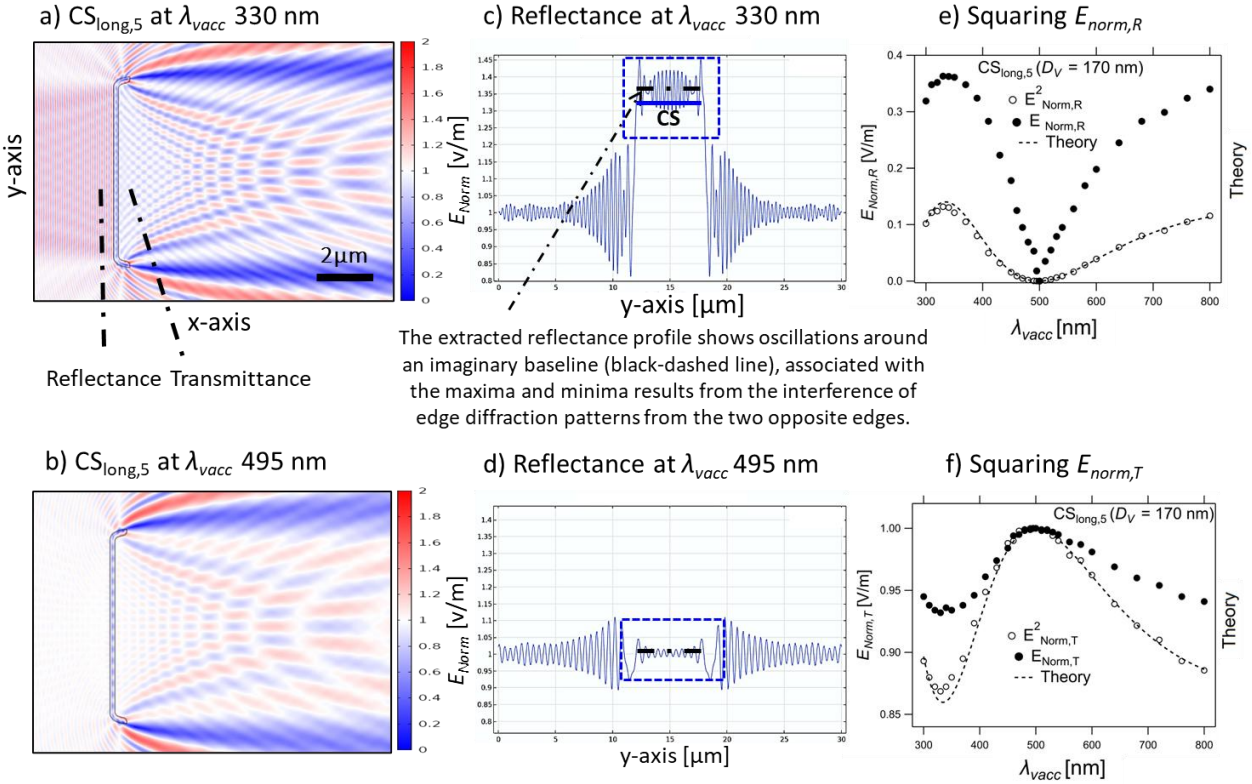

Fig. 4.6. An example shows the interference pattern of CS$_{long,5}$ at λ_{vacc} 330 nm (**a**) and 495 nm (**b**), alongside the extraction method of $\mathbf{E_{Norm,R}}$ that shows the maximum (**c**) and minimum (**d**) reflectance. The reflectance and transmittance should produce a flat wavefront, confirmed through the simulation of an extended thin slab (of L_{sl} 80 μm in a larger simulation domain). Therefore, the oscillations that appear in the extracted reflectance in (**c** and **d**) were associated with edge diffraction. Thus, to read out the CSs' reflectance and transmittance with the presence of overlayed edge diffraction, the position of the baseline was estimated (associated with the expected flat wavefront) as an average between the maxima and minima in the observed oscillations (dashed black line in **c** and **d**). The error in the measurements was estimated by averaging the extracted $\mathbf{E_{Norm}}$ from three consecutive x-lines close to the CS. Squaring the $\mathbf{E_{Norm}}$—after the subtraction of $\mathbf{E_{input}}$ from the extracted $\mathbf{E_{Norm}}$ only in the case of reflectance—gave the best match to theoretical calculations (**e** and **f**). This Figure is reproduced from Ghobara *et al.* [261].

Moreover, as the theoretical calculations expect the intensity of the reflectance and transmission, squaring the extracted $\mathbf{E_{Norm}}$ values was required to obtain a match between both the shape and magnitude of the reflectance and transmission spectra (**Figs. 4.6e and f**, respectively). It should be noted that—using

the method described in **Fig. 4.6**—$\mathbf{E_{Norm,R}}$ and $\mathbf{E_{Norm,T}}$ values associated with the sternum of $CS_{long,2}$ were extractable, while this was not the case for the nodule zone due to its finite length (L_{nod}). Despite that, the expected constructive and destructive maxima of the nodule zone were observed in the simulation results.

Furthermore, the influence of changing the slab thickness D_{sl}, the refractive index of CS n_v, or surrounding medium n_m on the reflectance and transmittance was studied and found to be in good agreement with the theoretical calculations and the expectations from thin-film interference theory (see **section A.7**, **Appendix A**).

4.3.2. Edge diffraction

For an optically transparent thin slab, the characteristic pattern of edge diffraction results from the interference of the secondary wavelets generated at each edge and the incident wavefront above the edge or the transmitted wave through the slab [277]. The generated edge diffraction pattern includes bright fringes alternating with dark fringes, which appear in our simulation domain—on the *y*-axis—above and below the edge, as in the case of a rectangular thin slab of length L_{sl} = 20 µm, $D_{sl} = D_v$, and $n_{sl} = n_v$ (**Fig. 4.7a**).

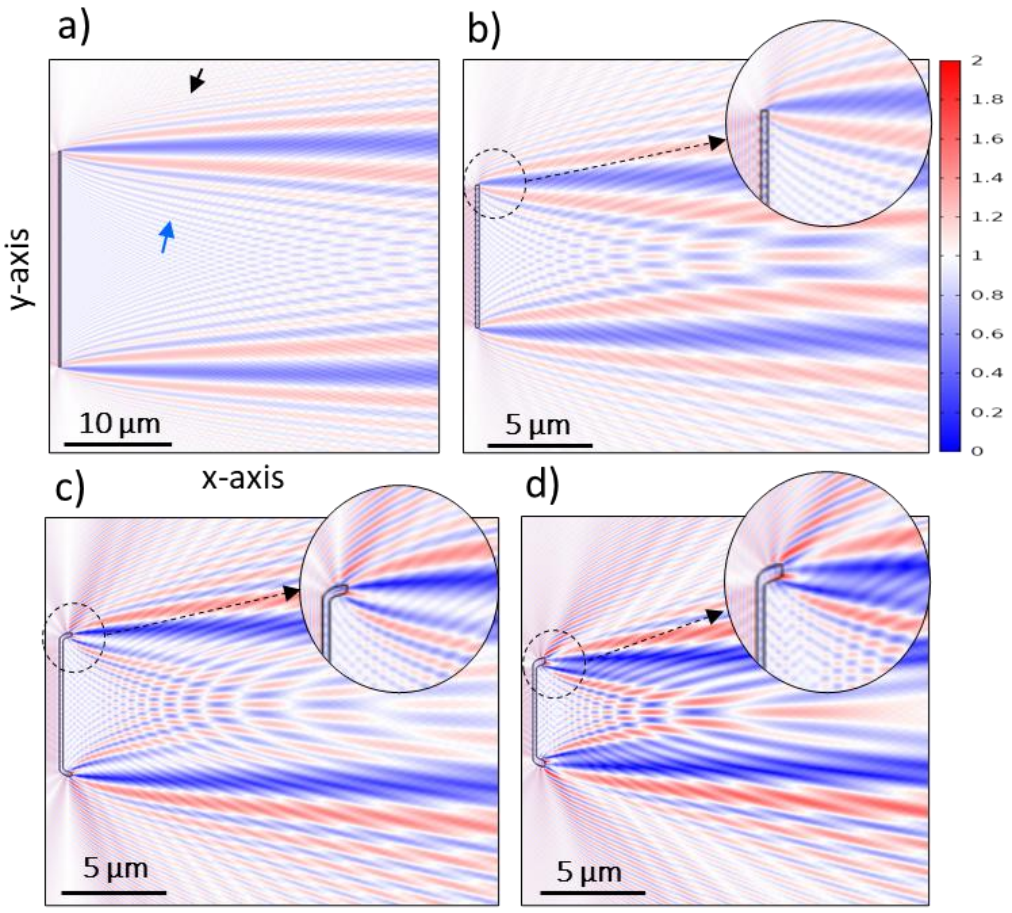

Fig. 4.7. A thin slab of 20 µm length (**a**), $S_{ana,long5}$ (**b**), $CS_{long,5}$ (**c**), and $CS_{long,7}$ (**d**) at λ_{vacc} = 300 nm in the air. The black and blue arrows in (**a**) indicate the edge diffraction fringes outside

and inside the transmittance region, respectively. The insets in (**a**) to (**c**) are a zoom of the edge region. The color code is given in V/m units. This Figure is modified from Ghobara *et al.* [261].

By reducing L_{sl} of the thin slab (approaching the length of CSs), the secondary wavelets produced at the two opposite edges increasingly interfere with each other inside the transmittance region. This can be seen in the case of $S_{ana,long5}$ (*i.e.*, a rectangular thin slab equivalent to $CS_{long,5}$ but with straight edges (**Fig. 4.7b**)), $CS_{long,5}$ (**Fig. 4.7c**), and $CS_{long,7}$ (**Fig. 4.7d**). This disturbs the characteristic fringes of the edge diffraction, leading to a diffraction-driven focusing and, further, a photonic jet generation that is discussed separately (see below).

Moreover, unlike $S_{ana,long5}$, where the diffraction occurs at straight edges, the edge diffraction in CSs involves curved edges (*i.e.*, the mantle). In this case, additional secondary wavelets produced from the infinitesimal points at the curved part fronting the incident wave will also contribute to the edge diffraction pattern [278]. Additionally, the tilt of the curved edges with respect to the thin-slab element ($\Theta_M \approx 70°$) leads to further changes to the edge diffraction pattern compared to a non-tilted edge. The effect of tilt is evident when comparing the edge diffraction pattern of a thin slab equivalent to the mantle dimensions ($S_{ana,M}$) in a tilted position (**Fig. 4.8a**) *vs.* a non-tilted position (**Fig. 4.8b**).

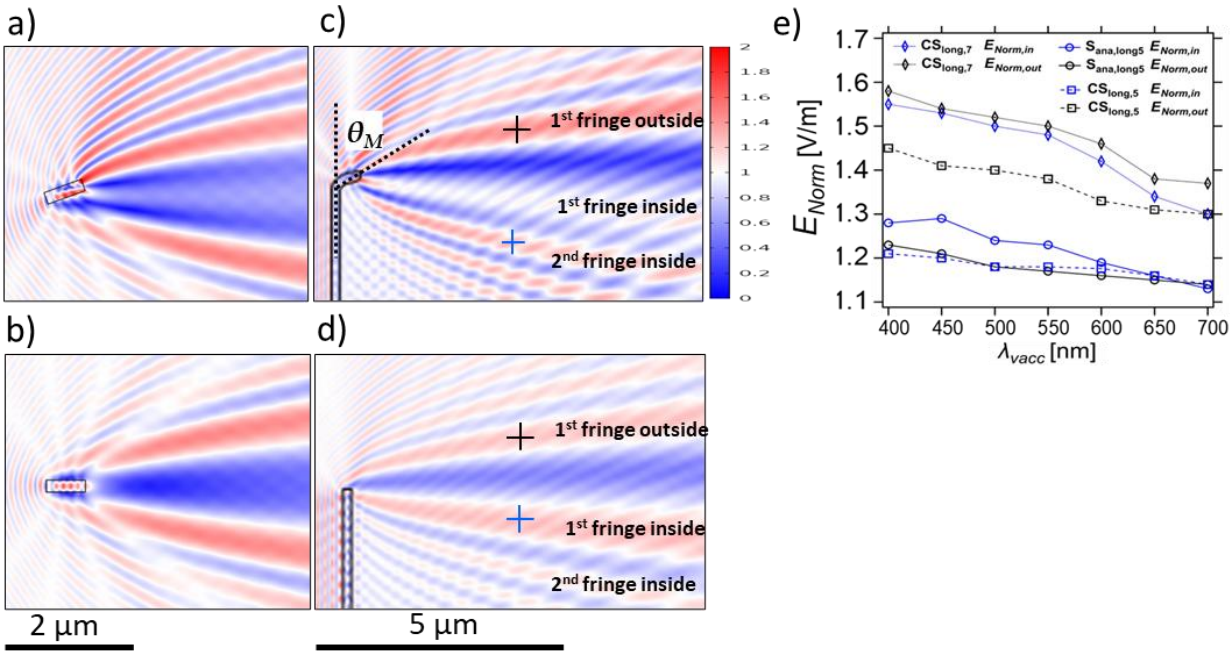

Fig. 4.8. Tilted $S_{ana,M}$ in (**a**) compared to non-tilted position in (**b**) at λ_{vacc} 300 nm in air. The edge diffraction fringes in $CS_{long,5}$ (**c**) and $S_{ana,long5}$ (**d**) at λ_{vacc} 300 nm in the air. The plot in (**e**) shows the dependency of the edge diffraction fringes strength on λ_{vacc} alongside the changes in the $\mathbf{E_{Norm,in}}$ and $\mathbf{E_{Norm,out}}$ for $CS_{long,5}$, $CS_{long,7}$, and $S_{ana,long5}$. While the plot in (**f**) shows the difference in $\mathbf{E_{Norm,in}}/\mathbf{E_{Norm,out}}$ ratios. The Crosses in (**c**) and (**d**) represent examples of the *x*-*y* positions considered for $\mathbf{E_{Norm}}$ extraction that are plotted in (**e**). The error was up to ± 0.07, ± 0.05, or ± 0.03 V/m in the case of $CS_{long,5}$, $CS_{long,7}$, or $S_{ana,long5}$, respectively. The error in the

measurements was estimated by averaging the extracted $\mathbf{E_{Norm}}$ from three consecutive points at the same fringe. This Figure is modified from Ghobara *et al.* [261].

The influence of tilted curved edges on the CSs' edge diffraction fringes—which involve waveguiding behavior (see below)—becomes evident when comparing the bright fringes outside and inside the transmittance region of the CSs if compared to those of $S_{ana,long5}$. This modulation includes: (i) increasing $\mathbf{E_{Norm}}$ of some fringes while decreasing others (**Fig. 4.8c** *vs.* **4.8d**, see also **Fig. 4.8e**), and (ii) a spatial delay of the inside diffraction fringes (clear for the first and second fringes in **Fig. A.8a** *vs.* **b**, **Appendix A**). In all cases, the $\mathbf{E_{Norm}}$ of diffraction fringes decreases with increasing λ_{vacc} (**Fig. 4.8e**, and further visualized in **Fig. A.8**), as expected from the Fresnel–Kirchhoff integral.

4.3.3. Waveguiding behavior

The contribution of the fiber-like components (*i.e.*, the mantle and girdle bands) to the interference pattern of CSs is complicated due to their waveguiding behavior. These components are of dimensions comparable to λ_{vacc} (considered as the core), and if embedded within a homogenous medium of lower refractive index (considered as the cladding), a symmetric waveguide behavior would be expected [212]. As can be understood from **subsection 2.3.5** (**Chapter 2**), when a plane wave illuminates the waveguide with $\Theta_{inc} < \Theta_{acc}$ of the fiber-like components, it can be coupled inside. The coupled light within the waveguide propagates in discrete modes, and the number of supported modes depends on the waveguide width W_{wg} and λ_{wg} [212]. In all cases, the zero mode can be supported within the waveguide regardless of its W_{wg} and λ_{wg} [212].

Fig. 4.9a shows a stationary-wave-like interference pattern inside a rectangular slab similar to $S_{ana,M}$ but of 2 µm height, which may indicate waveguiding behavior as appears in our simulation domain. This is also observed in $S_{ana,M}$ (**Figs. 4.8a** and **b**), although its limited height (h_M = 0.58 µm).

Moreover, as shown in **Fig. 4.9b**, by approaching the structure of a cross-section across the complete frustule via adding four girdle bands (H_{girdle}, W_{girdle})—two adjacent to the epivalve and the other two adjacent to the hypovalve with a step difference equaling W_{girdle} on the *y*-axis and a spacing d_{girdle} = 10 nm on the *x*-axis—the waveguiding behavior was further modulating the edge diffraction fringes. This includes an additional spatial delay, especially of the inside fringes (indicated by the black arrows in **Figs. 4.9b** and **c**). It should be noted that a weak coupling of the guided wave between the closer and further girdle bands is noted in the air (**Fig. 4.9b**). In contrast, this coupling becomes strong in water at higher λ_{vacc} (**Fig. 4.9c**).

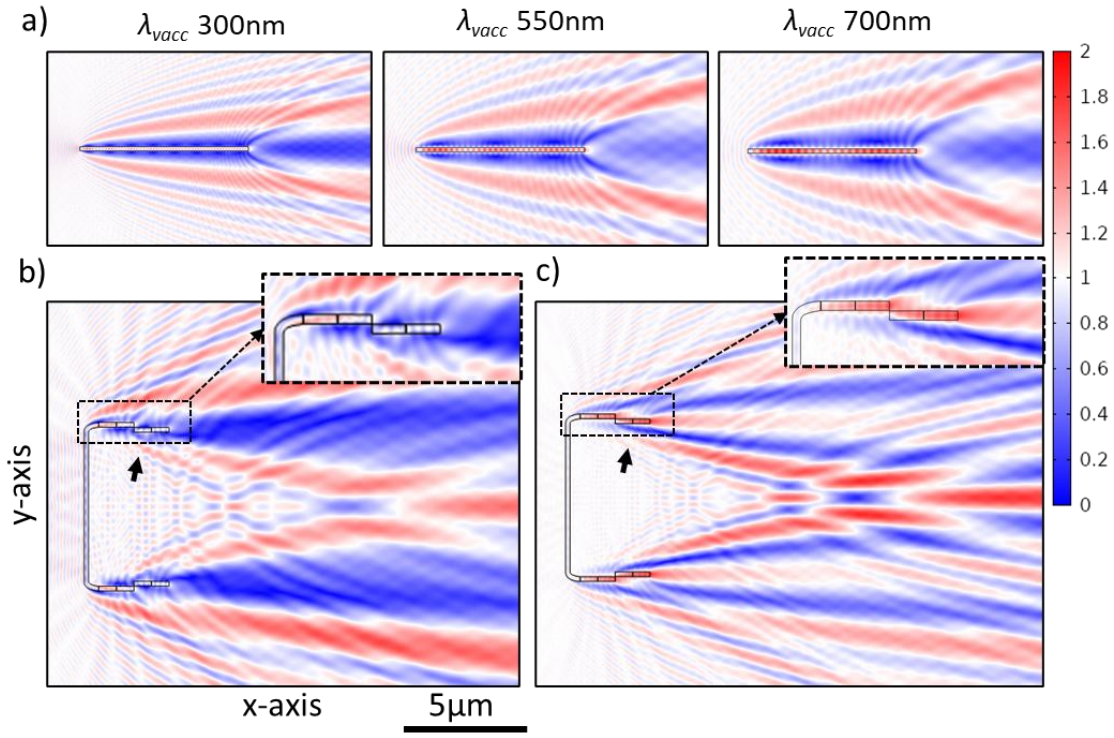

Fig. 4.9. A rectangular thin slab of 2 µm height and W_M width in air (**a**), $CS_{long,5}$ with four girdle bands in air (**b**) and in water (**c**) at λ_{vacc} 550 nm. The zoom inset in (**c**) seemingly shows a coupling behavior of the guided wave in water that is not observed in air (**b**). The color code is given in V/m units. This Figure is modified from Ghobara *et al.* [261].

Furthermore, in most simulations carried out here, the incident wave falls onto the CSs' outer faces. Alternatively, by rotating the CSs 180°, the incoming wave falls onto the CSs' inner faces, reaching the mantle first and partially coupled inside (**Fig. 4.10**). As there are two opposite curved edges for each CS, the coupled waves at each edge extend to the rest of the CS and interfere together, leading to the characteristic interference pattern observed inside the CSs in **Fig. 4.10**. Such **mantle-coupled guided waves** are observed across the whole studied λ_{vacc} range in air and appearing in all CSs. It is also accompanied by relatively stronger evanescence and simultaneous changes to the transmittance and reflectance interference patterns (**Fig. 4.10**).

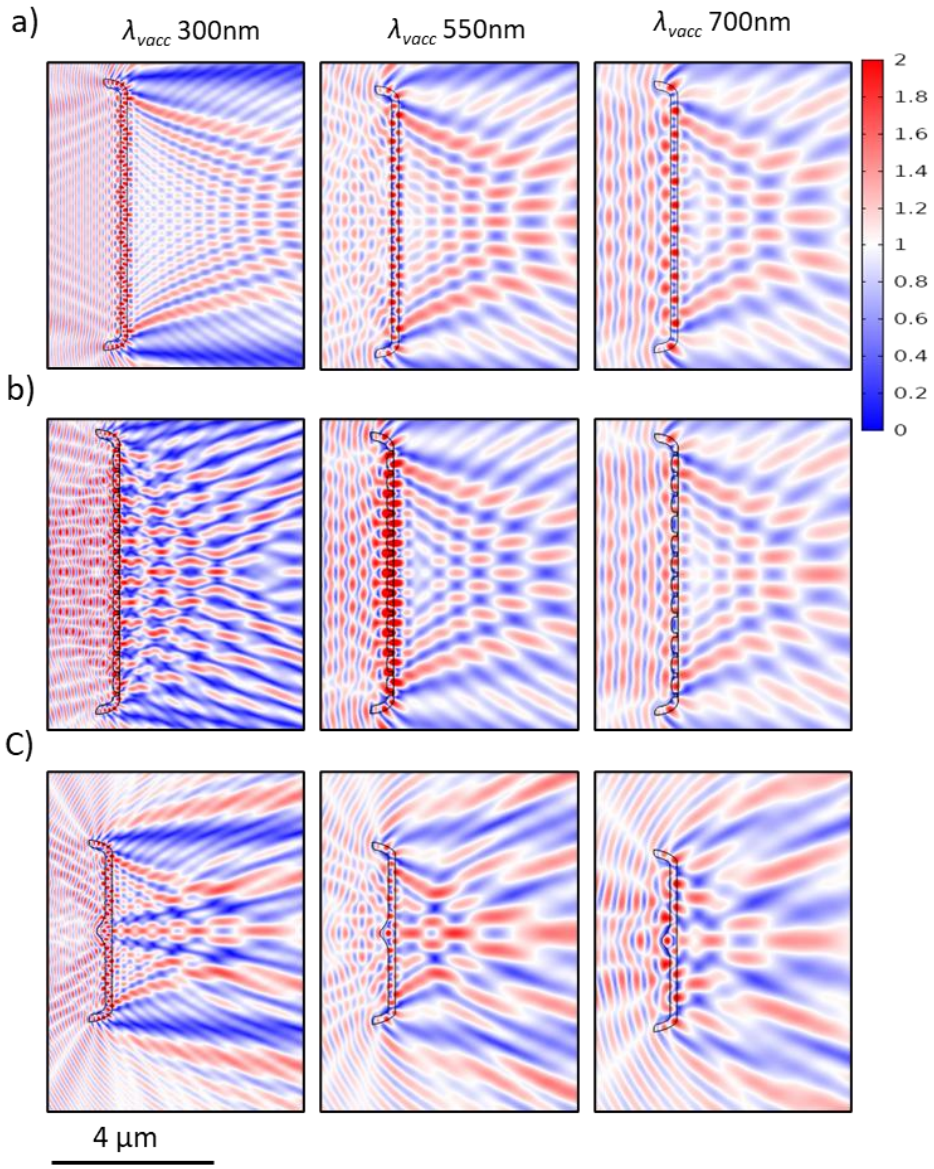

Fig. 4.10. The mantle-coupled guided waves appear in $CS_{long,5}$ (a), $CS_{long,4}$ (b), and $CS_{ver,2}$ (c) in the air. The color code is given in V/m units. This Figure is reproduced from Ghobara *et al.* [261].

4.3.4. Diffraction-driven focusing behavior in the Fresnel zone

As explained, a consequence of reducing L_{Sl} of the thin slab element is the arising of a distinct interference pattern with bright spots (considered as diffraction-driven focusing spots) alternating with dark spots in the transmittance, which are further influenced by the edge geometry and their waveguiding behavior in the case of CSs. This pattern (*e.g.*, of $CS_{long,5}$ in **Fig. 4.11a**) is quite similar to the pattern of the transmitted light through an aperture (see Figure 1 in [279]). The intensity of these spots, as well as their size, depend on the diffraction fringes they involve. This is why the highest intense spots appear at the right-hand side of the interference pattern associated with the more intense diffraction fringes inside the transmittance region (*e.g.*, **Fig. 4.11a**).

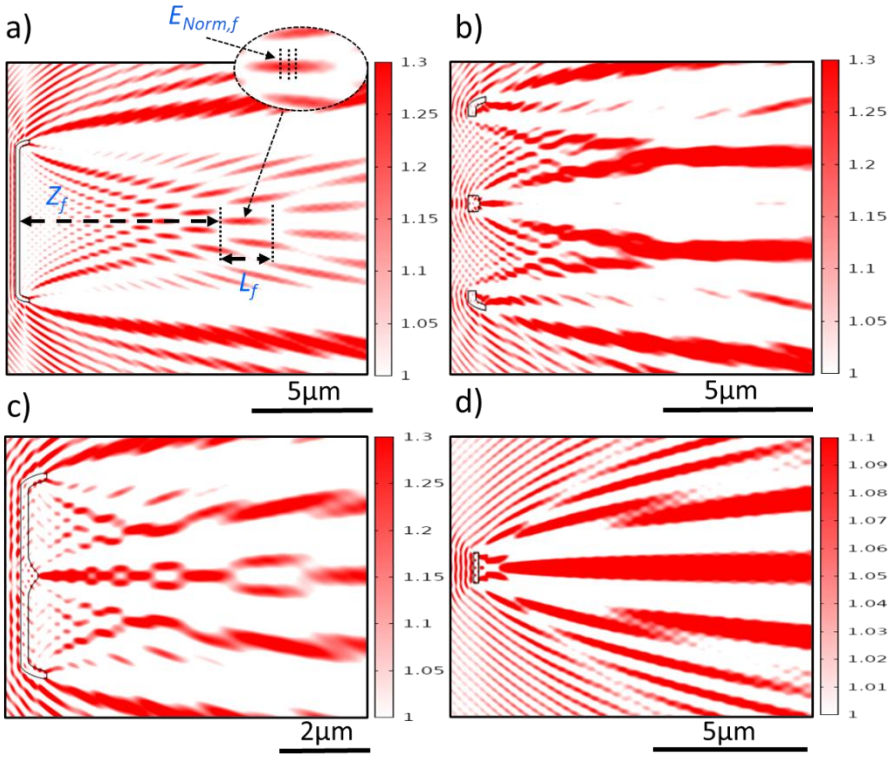

Fig. 4.11. The interference patterns of $CS_{long,5}$ (**a**), $CS_{long,1}$ (**b**), and $CS_{ver,2}$ (**c**) at λ_{vacc} 300 nm in air. The interference pattern of $S_{ana,long5}$ of L_{sl} = 1 µm at 330 nm in air (**d**). The considered focusing parameters are illustrated in (**a**). The color code aims to emphasize constructive interference, including the focusing spots and is given in V/m units. This Figure consists of modified and merged figures from Ghobara *et al.* [261].

Adding more edges to the CSs, for instance, in $CS_{long,1}$ (where two raphe slits representing four additional edges are introduced) or in $CS_{ver,1}$ and $CS_{ver,2}$ (where an increased thickness associated with the nodule is introduced at the center of CSs), leads to the presence of additional point sources—secondary wavelets—interfering with the transmitted wave. This leads to splitting the associated CS's interference pattern into two separate but smaller patches of these spots, as can be seen in $CS_{long,1}$ (**Fig. 4.11b**) and $CS_{ver,2}$ (**Fig. 4.11c**).

Moreover, three parameters can be considered to study each of these focusing spots, as illustrated in **Fig. 4.11a**: the focal length Z_f (*i.e.*, the distance between the CS and a selected focusing spot), its length L_f, and strength $\mathbf{E_{Norm,f}}$. It should be noted that, due to the presence of local variation in the strength of the diffraction-driven focusing spots, the $\mathbf{E_{Norm,f}}$ of a selected spot was estimated by averaging the $\mathbf{E_{Norm}}$ extracted from three consecutive positions at this spot, as illustrated in **Fig. 4.11a** (the dashed black lines in the zoom-in), and the associated standard deviation considered the corresponding error.

With increasing λ_{vacc}, all these spots move toward the CS, decreasing Z_f (*e.g.*, **Fig. 4.12b**) and L_f (*e.g.*, **Fig. 4.12c**) and fading in intensity (*e.g.*, **Fig. 4.12a**), see further **Fig. A.9** in **Appendix A**. It should be noted that in this case, $\mathbf{E_{Norm,f}}$ of the spots is affected in this case by two factors: the reduction of the strength of the secondary

wavelets produced from the edges (as expected from the Fresnel–Kirchhoff integral) and the change caused by thin-film interference affecting the transmittance. In **Fig. 4.12a**, the correlation between the transmittance intensity—calculated using [276], see **subsection 4.3.1**—and $E^2_{Norm,f}$ of the focusing spots is to some extent evident.

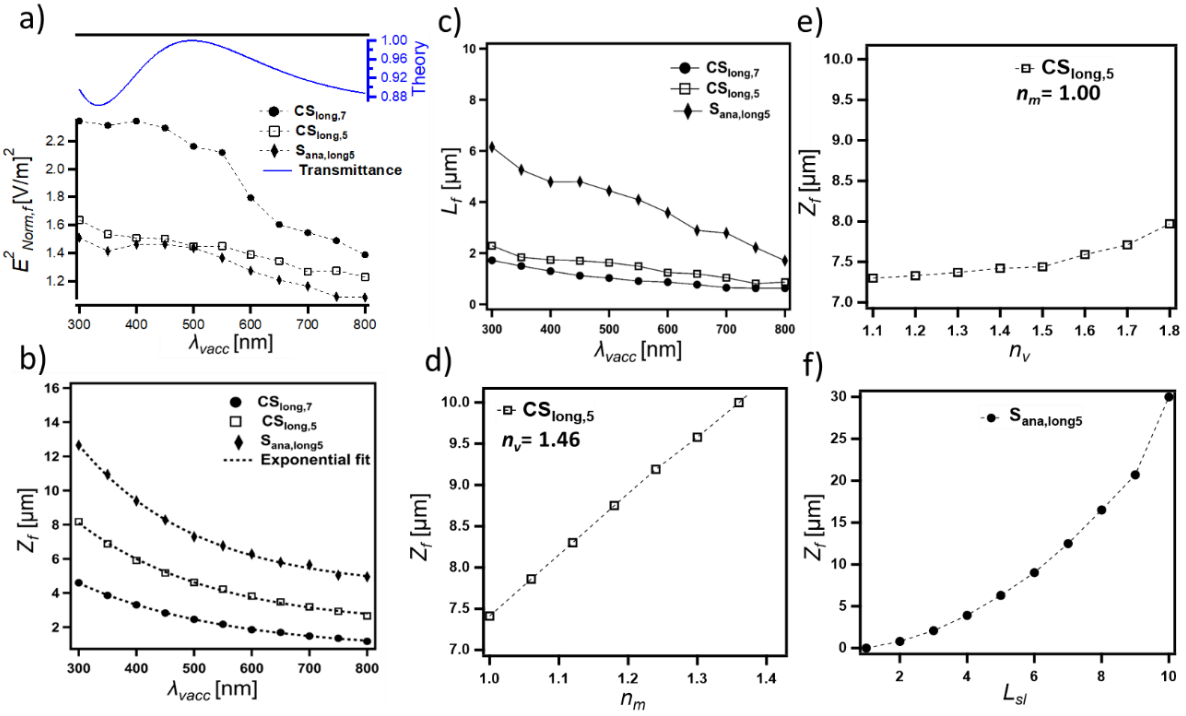

Fig. 4.12. (**a**) The dependency of the intensity $\mathbf{E^2_{Norm,f}}$ of selected spots (the last larger and clearer focusing spot appeared at the optical axis of the CS within the simulation domain was selected for the measurement, *e.g.*, the spot illustrated in **Fig. 4.11a** for $CS_{long,5}$) on λ_{vacc} compared to the theoretical transmittance spectrum (blue). The oscillation in the transmittance intensity due to thin-film interference seems to affect the intensity of these spots accordingly. The extracted $\mathbf{E_{Norm,f}}$ has an error up to ± 0.02 V/m associated with the local variation in the strength of the selected spot. (**b** and **c**) The dependency of Z_f and L_f of the same selected spots on λ_{vacc} in air, respectively. (**d**) The dependency of Z_f of $CS_{long,5}$ on n_m at n_v = 1.46 and λ_{vacc} 330 nm. (**e**) The dependency of Z_f of $CS_{long,5}$ on n_v at n_m = 1.00 and λ_{vacc} 330 nm. (**f**) The dependency of Z_f of $S_{ana,long5}$ on L_{sl} in air at λ_{vacc} 330 nm. This Figure consists of modified and merged figures from Ghobara *et al.* [261].

Furthermore, increasing n_m (for n_v = 1.46), and, thus, decreasing Δn, leads to a significant increase in Z_f (*e.g.*, **Fig. 4.12d**) and L_f concurrently with a reduction in $\mathbf{E_{Norm,f}}$. This is not the case for changing n_v (for n_m = 1.00), where the changes in Z_f (*e.g.*, **Fig. 4.12e**) and L_f are relatively negligible.

As this phenomenon is directly relevant to the distance between the edges; therefore, increasing L_{sl} of $S_{anal,long5}$, and, thus, the distance between the generated secondary wavelets, dramatically increases Z_f (**Fig. 4.12f**) and L_f while slightly decreasing $\mathbf{E_{Norm,f}}$. For a much larger thin slab, as the edge diffraction becomes insignificant again, this phenomenon becomes neglectable. Changing D_{sl} (from 50 to

400 nm) of $S_{anal,long5}$ at λ_{vacc} 330 nm leads to negligible changes in Z_f and L_f, while $\mathbf{E_{Norm,f}}$ increases from 1.04 V/m (D_{SI} = 50 nm) to 1.38 V/m (D_{SI} = 400 nm).

From the observed edge diffraction and waveguiding behavior, it can be concluded that changing the edge geometry can dramatically affect these focusing spots; for instance, the increased $W_{M,CS}$ in $CS_{long,7}$ likely contributed to its increased $E^2_{Norm,f}$ if compared to that of $CS_{long,5}$ (**Fig. 4.12a**).

4.3.5. Photonic Jet generation

As demonstrated in **subsection 2.3.3** (**Chapter 2**), the photonic jet (PJ) can be considered a type of diffraction-driven focusing. It is observed as a distinct focusing phenomenon in some CSs (all vertical CSs, $CS_{long,1}$, $CS_{long,2}$, and $CS_{long,3}$), linked to the presence of an increased thickness in the CS either by introducing the nodule zone (*e.g.*, **Fig. 4.13**) or the sternum (*e.g.*, **Fig. 4.14a**), which significantly affects the associated interference pattern. By separating the related optical components (*e.g.*, $CS_{ver,2/nodule}$ and $CS_{long,3/nodule}$ in **Figs. 4.13c** and **d**, respectively), their correlation to this phenomenon becomes evident.

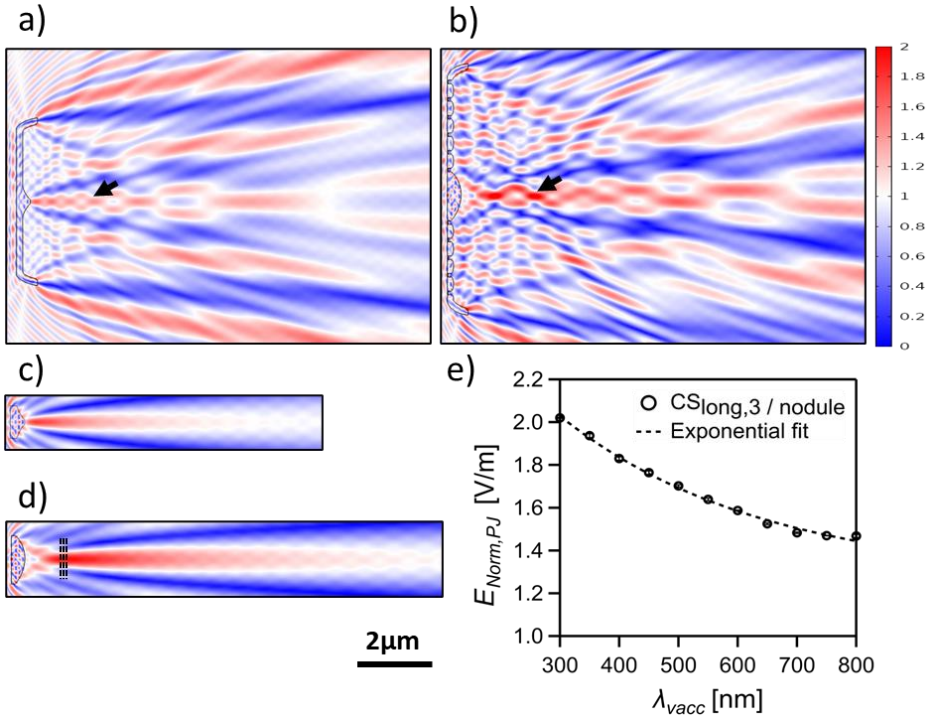

Fig. 4.13. PJ generation in $CS_{ver,2}$ (**a**) and $CS_{long,3}$ (**b**) compared to the disassembled nodule zone $CS_{ver,2/nodule}$ (**c**) and $CS_{long,3\ /nodule}$ (**d**) at λ_{vacc} 350 nm in the air. (**e**) The plot shows the λ_{vacc} dependency of $\mathbf{E_{Norm,PJ}}$ of the PJ generated by $CS_{long,3\ /nodule}$. The $\mathbf{E_{Norm,PJ}}$ was estimated by averaging the $\mathbf{E_{Norm}}$ extracted from three consecutive positions at around the PJ maximum, as indicated in (**d**, the dashed black lines), and the associated standard deviation considered the corresponding error. The estimated $\mathbf{E_{Norm,PJ}}$ has an error up to ± 0.009 V/m associated with the local strength variation. The color code is given in V/m units. This Figure is reproduced from Ghobara *et al.* [261].

Moreover, it is expected from the previous work on PJ generation by artificial structures that the characteristic features of the PJ beam (*i.a.*, the position, length, waist size, and maximum intensity) can be changed with changing parameters such as n_v, n_m, and incident λ_{vacc}, as well as the structure size [181,279]. As illustrated in **Figs. 4.13e** and **4.14b**, the maximum strength of the PJ ($\mathbf{E_{Norm,PJ}}$) generated by $CS_{long,3/nodule}$ decreases exponentially with increasing λ_{vacc} combined with a slight decrease in its distance from $CS_{long,3/nodule}$ and an increase in its waist size. Furthermore, changing the refractive index contrast Δn by either varying n_v (n_m = 1) or n_m (n_v =1.46), but keeping $n_v > n_m$, leads to similar changes in the PJ parameters (**Fig. 4.14c** *vs.* **d**). Where the $\mathbf{E_{Norm,PJ}}$ increases, its waist size decreases, and the distance to $CS_{long,3/nodule}$ slightly decreases with increasing Δn. Similar trends were observed by Salhi *et al.* [279] that the PJ intensity decreases while its waist size increases with increasing λ_{vacc} (see Figure 6 in [279]) or reducing Δn (see Figure 5 in [279]).

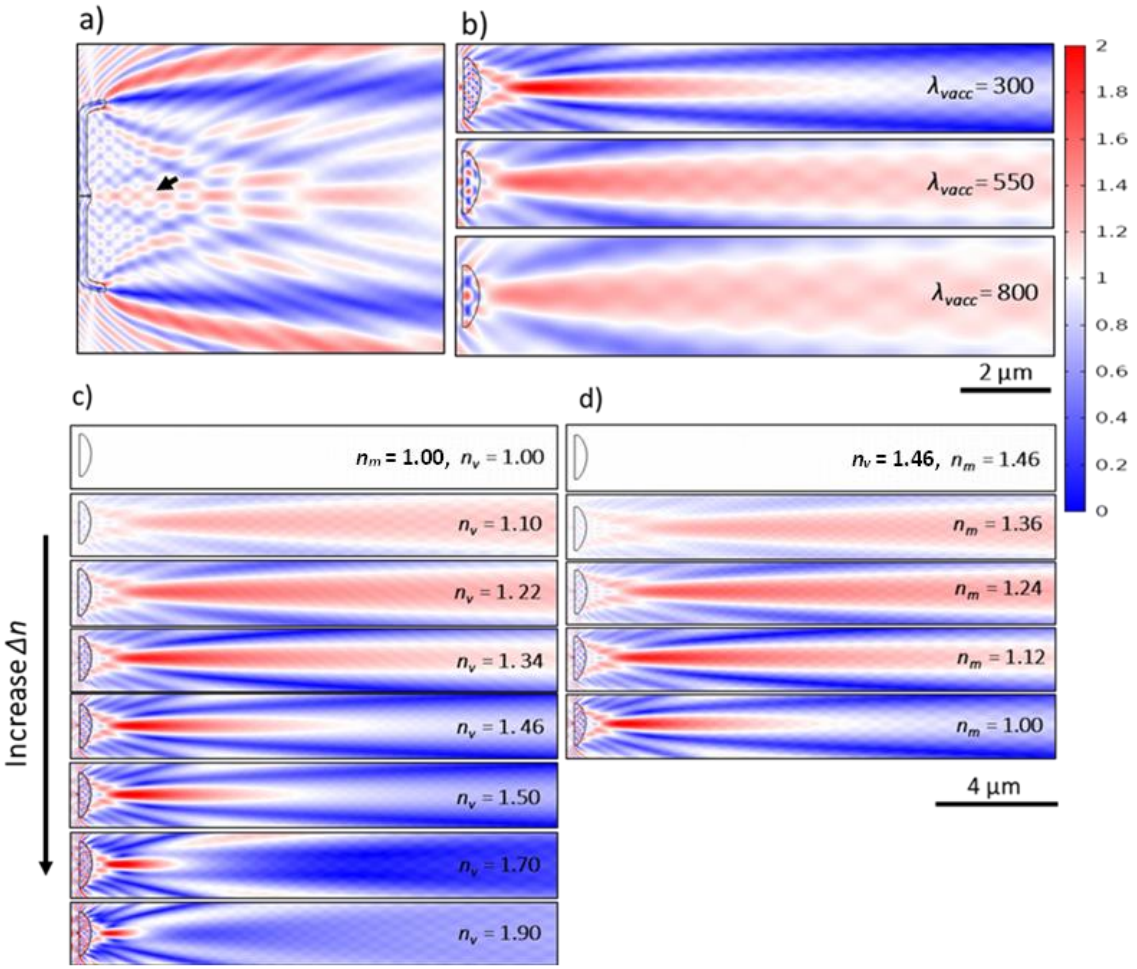

Fig. 4.14. Photonic jet generation in $CS_{ver,4}$ at λ_{vacc} 350 nm (**a**), the λ_{vacc} dependency of the generated PJ by the disassembled lens-like structure ($CS_{long,3\ /nodule}$) in the air (**b**), the Δn dependency of the generated PJ by $CS_{long,3\ /nodule}$ at λ_{vacc} 300 nm while changing n_v for n_m = 1 (**c**) or changing n_m for n_v = 1.46 (**d**). In both (**c**) and (**d**), the images were arranged to show Δn increasing toward below. The color code is given in V/m units. This Figure is modified from Ghobara *et al.* [261].

Furthermore, an intense beam observed inside the simulation domain for a $S_{anal,long5}$ of L_{sl} = 5 µm, appears as a PJ emerging after the diffraction-driven focusing spots within the transmittance region. By further reducing L_{sl}, the generation of PJs occurs very close to the surface of the rectangular slab (**Fig. 4.11d**), leaving no space for the formation of the diffraction-driven focusing spots, which could also be the case for PJ generation by the nodule or the sternum of small dimensions. This means that even the CSs without the increased thickness at the middle can generate a pronounced PJ if their length, thickness, and edge geometry enable it.

4.3.6. Diffraction grating behavior in the Frensel zone: the Talbot effect

The grid-like element in some CSs—as it is composed of optically transparent material—considers a transmission grating [163,280], where the diffraction orders mainly appear in the transmittance. As our simulations provide high-resolution information of the Fresnel zone, we expect to obtain a periodic interference pattern matching the so-called Talbot effect (see **subsection 2.3.4**, **Chapter 2**) in the transmittance associated with the grid-like element. For a one-dimensional grid (with a period that allows ± 1st diffraction order), this effect would lead to a distinct interference pattern in our 2D simulation domain consisting of linear arrays of periodically arranged bright fringes (*i.e.*, high-intensity spots)—on the *y*-axis—alternating with dark fringes, where the two consecutive bright fringes have a spacing equal to the grid period *d*. Each linear array of bright fringes represents an image copy of the grating repeated at fixed distances—on the *x*-axis—equal to "Talbot length Z_T" [200] alternating with other secondary copies occurring at $Z_T/2$ with a lateral shift—on the *y*-axis—equaling *d*/2. The Talbot length Z_T can be calculated according to **eq. 2.18** (see **Chapter 2**).

This explains the intense interference pattern which dominates the transmittance region of $CS_{long,3}$, $CS_{long,4}$, and $CS_{long,6}$ at a range of wavelengths (*e.g.*, $CS_{long,4}$ in **Fig. 4.15a**), which interrupts the edge diffraction pattern and the associated diffraction-driven focusing. As expected, this pattern occurs only where at least ± 1st orders of diffraction are present in the transmittance beside the 0th order. The possible number of diffraction orders can be calculated under normal incidence using the grating equation (**eq. 2.17**, **Chapter 2**). By solving this equation for the CSs, the presence of ± 1st orders of diffraction is possible only at $\lambda_{vacc} < d*n_m$ ($d = d_{str}$ or d_a in the case of longitudinal or vertical CSs, respectively), while the ± 2nd orders of diffraction can occur only at $\lambda_{vacc} < (d*n_m)/2$, which falls mostly outside the studied λ_{vacc} range. This explains the observation of Talbot pattern in $CS_{long,3}$ (d_{str} = 490 nm), $CS_{long,4}$ (d_{str} = 500 nm), and $CS_{long,6}$ (d_{str} = 565 nm) at λ_{vacc} < 490 nm, 500 nm, and 565 nm, respectively, in the air (n_m = 1.00) and λ_{vacc} < 652 nm, 665 nm, and 752 nm, respectively, in water (n_m = 1.33). However, it cannot be obtained in $CS_{ver,1}$ (d_a = 214

nm) (**Fig. 4.16b**) at the studied λ_{vacc} range either in air or water, which is confirmed for an equivalent analytical grid without nodule $G_{ana,ver1}$ (**Fig. 4.16c**).

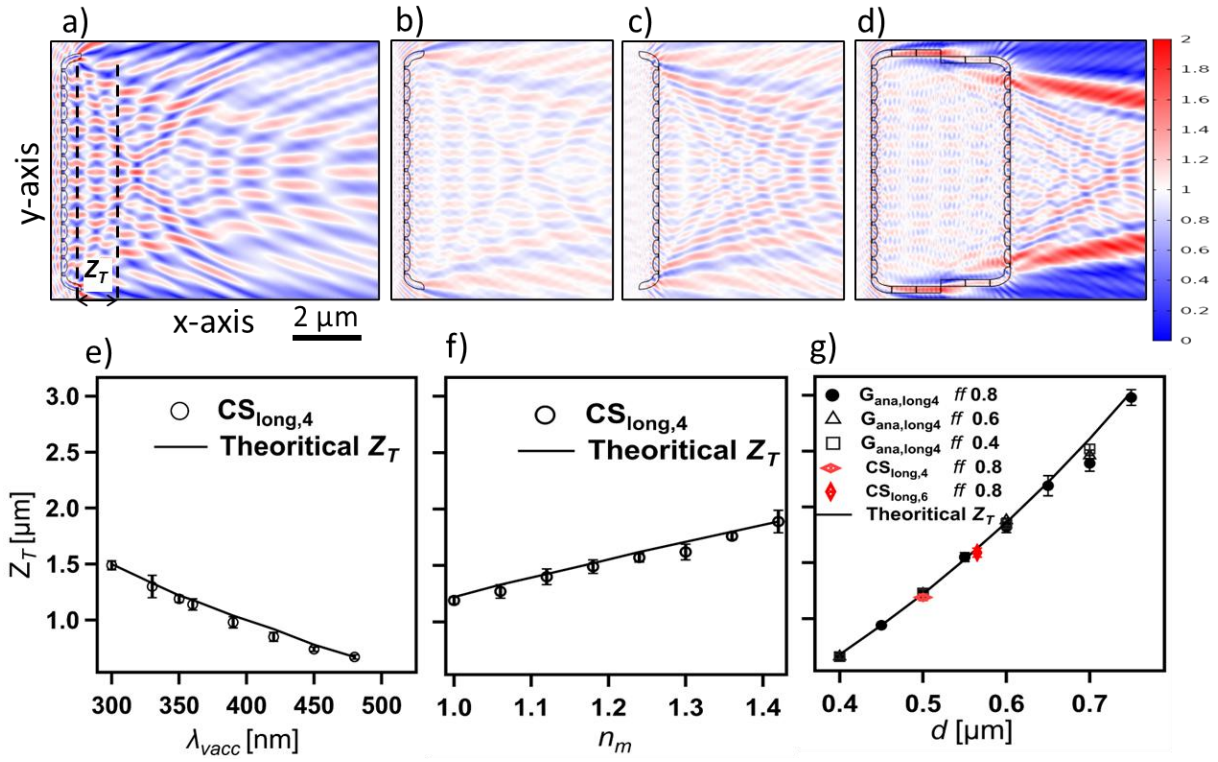

Fig. 4.15. The interference pattern of $CS_{long,4}$ displays the Talbot pattern dominating the transmittance region at λ_{vacc} = 350 nm in air (**a**) and in water for the light incident on the outer face (**b**) or the inner face (**c**). The distance between the two black, dashed lines (considered as the Talbot planes) in (**a**) is the so-called Talbot length (Z_T). The Talbot pattern in $CS_{long,4,\ frustule}$ at λ_{vacc} = 350 nm immersed in water (**d**). The graphs illustrate the dependency of Z_T on λ_{vacc} in $CS_{long,4}$ in air (**e**) and on n_m (n_v = 1.46) at λ_{vacc} = 350 nm (**f**). A graph shows the dependency of Z_T on d of $G_{ana,long4}$ with different fill factors (ff) at λ_{vacc} = 350 nm in air (**g**). The error bars in the graphs represent the uncertainty in the measured Z_T. The color code is given in V/m units. This Figure is reproduced from Ghobara *et al.* [261].

The dependency of Z_T on λ_{vacc} and Δn is investigated utilizing $CS_{long,4}$ (d_{str} = 500 nm), while its dependency on structural parameters is further studied on an equivalent analytical grid $G_{ana,long4}$ of rectangular grooves. The distinct difference between $CS_{long,4}$ (**Fig. 4.15a**) and $G_{ana,long4}$ (**Fig. 4.16a**) is the presence of the mantle as well as the lens-like grid units in $CS_{long,4}$, where the curved surface of the lens occurs at the inner valve face (**Fig. 4.4**) and has a depth of 70 nm out of the total valve thickness D_v = 170 nm. Despite this, no significant change is observed on Z_T between the actual and analytical grid of the same d (**Fig. 4.15a** *vs.* **4.16a**), except for the increased deformation of the fringes in the case of $CS_{long,4}$. In all cases, the extracted Z_T has a slight deviation compared to theoretical predictions (**Figs. 4.15** and **4.16**) due to the deformation of Talbot fringes caused by edge diffraction, a consequence of the limited number of grid units [281]. This deformation leads to uncertainty while defining the Talbot planes (indicated by black dashed lines in **Figs. 4.15a** and **4.16a**).

Thus, the extraction of Z_T is based on an average accompanied by a deviation representing the uncertainty in the position of the Talbot planes on the *x*-axis. The extraction of Z_T from $CS_{long,3}$ or $CS_{long,6}$ faces more difficulties related to the presence of the nodule zone or the stronger edge effect, respectively.

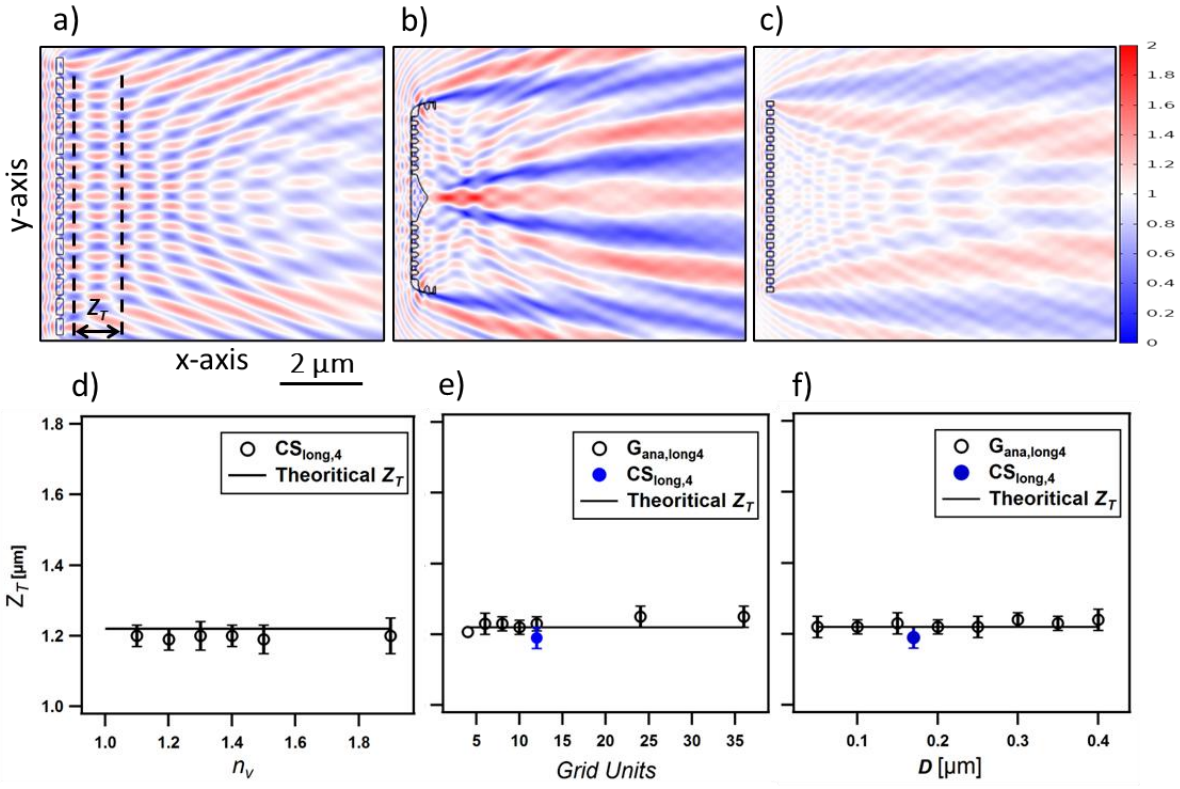

Fig. 4.16. The analytical grid $G_{ana,long4}$ equivalent to $CS_{long,4}$ (**a**), $CS_{ver,1}$ (**b**), and the analytical grid $G_{ana,ver1}$ equivalent to $CS_{ver,1}$ (**c**) at λ_{vacc}= 350 nm in the air. The three graphs show the independency of Z_T on the changes in n_v (n_m =1.00) of $CS_{long,4}$ (**d**), the grid units number of $G_{ana,long4}$ (**e**), or its thickness (**f**) at λ_{vacc}= 350 nm in the air compared to the theoretical expectation. The error bars in graphs represent the uncertainty in the measured Z_T due to deformation of the fringes. This Figure is reproduced from Ghobara *et al.* [261].

As illustrated in **Fig. 4.15**, the Talbot length Z_T associated with $CS_{long,4}$ increases with decreasing λ_{vacc} or increasing n_m (for n_v = 1.46), which perfectly matches the theoretical expectation from **eq. 2.18** and is correlated with the changes in Θ_m, which correspond to the ± 1 diffraction orders that can be calculated from **eq. 2.17**. While a dramatic change in Z_T can be induced by changing the grid period *d* of $G_{ana,long4}$ (**Fig. 4.15g**). In contrast, neither changing the fill factor *ff* (*i.e.*, the grid unit width/*d*) (**Fig. 4.15g**), the number of grid units (**Fig. 4.16e**), nor the thickness *D* of $G_{ana,long4}$ (**Fig. 4.16f**) changes Z_T. The same conclusion is obtained for changing n_v (at n_m = 1) of $CS_{long,4}$ (**Fig. 4.16d**).

Another important feature to study in Talbot effect is $\mathbf{E_{Norm}}$ strength of the generated bright spots. Interestingly, no significant λ_{vacc} dependency is noticed for the maximum strength of the Talbot bright fringes $\mathbf{E_{Norm,Talbot}}$ of $CS_{long,4}$, which vary

within the range of 1.36–1.56 V/m (with errors up to ± 0.07 V/m). Generally, the $\mathbf{E_{Norm,Talbot}}$ shows dependencies on Δn, D, and ff but is independent on the grid unit number. Decreasing Δn (from 0.46 to 0.06) either by changing n_v or n_m decreases the $\mathbf{E_{Norm,Talbot}}$ of $CS_{long,4}$ with the same magnitude, *e.g.*, $\mathbf{E_{Norm,Talbot}}$ reaches 1.14 ± 0.02 V/m in water (n_v = 1.46, n_m = 1.33) at λ_{vacc} 350 nm. Additionally, increasing the D of $G_{ana,long4}$ (from 50 nm to 400 nm) increases $\mathbf{E_{Norm,Talbot}}$ (from 1.11 ± 0.01 V/m to 1.71 ± 0.05 V/m), while decreasing ff increases the transmitted light through the areolae and, thus, enhances $\mathbf{E_{Norm,Talbot}}$ significantly.

4.3.7. Guided-mode resonance

For a specific range of wavelengths, the grid-like element exhibits another phenomenon, guided-mode resonance (GMR). As already explained in **subsection 2.3.6** (**Chapter 2**), GMR occurs when the resonance conditions are reached, where a dramatic drop in transmittance and increase in reflectance can be observed, leading to the characteristic spectrum of GMR. In our simulation domain, during GMR, a characteristic interference pattern (resulting from the interference of guided waves) is expected inside the grid-like element (*e.g.*, **Fig. 4.17**), with intense nodes reaching the maximum at the middle of the grid and decaying towards the edges with a simultaneous evanescence in the proximity of the grid surface.

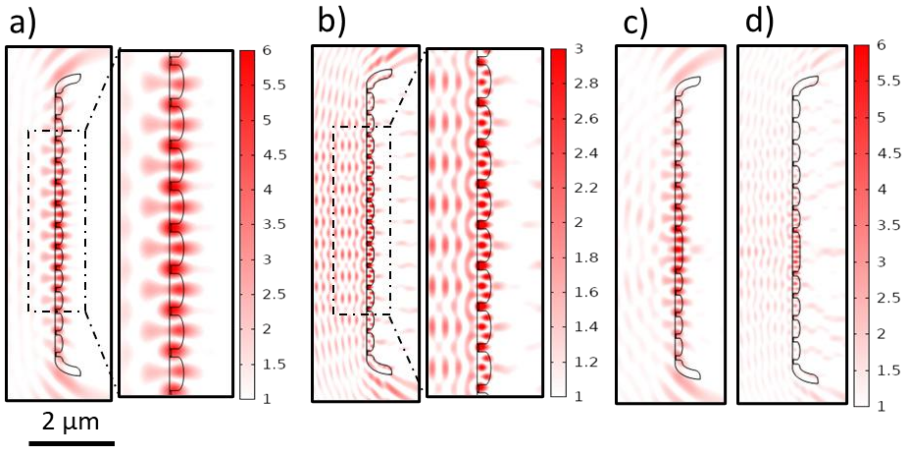

Fig. 4.17. Grid-coupled GMR of $CS_{long,4}$ at the maxima of zero (**a**) and first modes (**b**) and of $CS_{long,4*}$ at the maxima of zero (**c**) and first modes (**d**) in air. The $\mathbf{E_{Norm,\ GMR}}$ is 6.31 (**a**), 4.01 (**b**), 6.67 (**c**), and 5.17 (**d**) V/m at $\lambda_{vacc,GMR}$ 553 nm, 303 nm, 559 nm, and 307 nm, respectively. The color code emphasizes the $\mathbf{E_{Norm}}$ enhancement in red ($\mathbf{E_{Norm}}$ > 1 V/m) while both the $\mathbf{E_{input}}$ and the $\mathbf{E_{Norm}}$ reduction are in white ($\mathbf{E_{Norm}}$ ≤ 1 V/m), not emphasized. This Figure is reproduced from Ghobara *et al.* [261].

In the CSs with a grid-like element ($CS_{long,3}$, $CS_{long,4}$, and $CS_{long,6}$), the $\mathbf{E_{Norm,T}}$ dramatically drops at specific ranges of λ_{vacc}, reaching a minimum value at $\lambda_{vacc,GMR}$ before returning to its normal limits with a simultaneous increase in $\mathbf{E_{Norm,R}}$, which matches the expected behavior of GMR. Nevertheless, the extraction of $\mathbf{E_{Norm,T}}$ or $\mathbf{E_{Norm,R}}$ employing the same method described in **Fig. 4.6** is complicated due to the

presence of other overlayed phenomena, such as the Talbot effect in the case of the first mode. Alternatively, to study the GMR behavior and to define $\lambda_{vacc,GMR}$, finer sweeps—down to 1 nm steps—are applied concurrently with observing the $\mathbf{E_{Norm}}$ strength inside the waveguide, which reaches its maximum $\mathbf{E_{Norm,GMR}}$ at $\lambda_{vacc,GMR}$.

The first mode of GMR is observed at $\lambda_{vacc,GMR}$ 295 nm, 303 nm, and 339 nm for $CS_{long,3}$, $CS_{long,4}$, and $CS_{long,6}$, respectively. While the zero modes are obtained at $\lambda_{vacc,GMR}$ 523 nm, 553 nm, and 613nm, respectively, in the air. The presence of a defect in $CS_{long,4*}$ causes a slight shift in $\lambda_{vacc,GMR}$ to occur at 559 nm and 307 nm for the zero (**Fig. 4.17c**) and first modes (**Fig. 4.17d**), respectively, where the maximum $\mathbf{E_{Norm,GMR}}$ is associated with the defect rather than the geometrical center of the grid-like element. Further, by increasing Θ_{inc}, a splitting in the modes is observed (*e.g.*, zero mode of $CS_{long,4}$ in **Fig. 4.18a**) combined with a decrease in $\mathbf{E_{Norm,GMR}}$ at $\lambda_{vacc,GMR}$. Such behavior is expected (see, *e.g.*, Figure 3 in [216]).

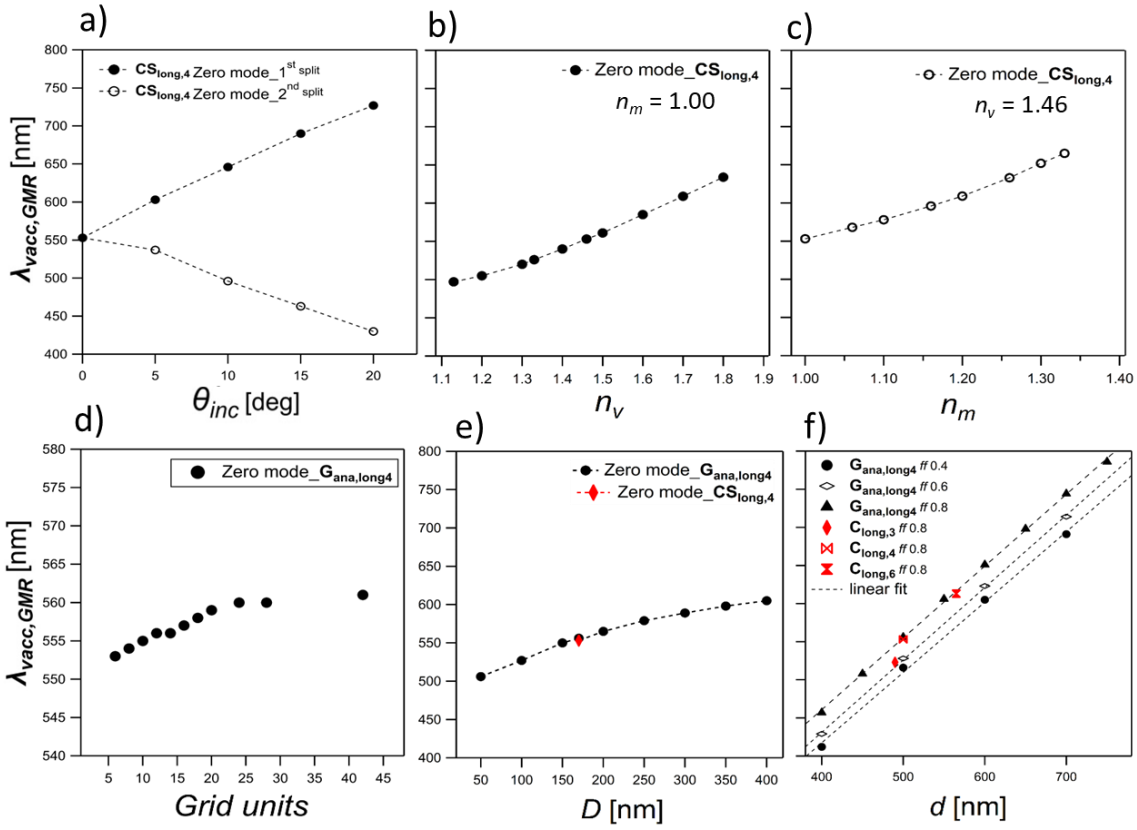

Fig. 4.18. The graphs show $CS_{long,4}$ $\lambda_{vacc,GMR}$-dependency of zero mode on Θ_{inc} (**a**), changing n_v (at n_m =1.00) (**b**), and changing n_m (at n_v =1.46) (**c**). While graphs in (**d**), (**e**), and (**f**) show $\lambda_{vacc,GMR}$-dependency of zero mode on changing grid units, *D*, or *d* (at different *ff*), respectively, of $G_{ana,long4}$ in air. The color code is given in V/m units. This Figure is modified from Ghobara *et al.* [261].

Moreover, increasing Δn by increasing n_v (n_m = 1.00) leads to a red shift in $\lambda_{vacc,GMR}$ of the zero mode of $CS_{long,4}$ (**Fig. 4.18b**) and a simultaneous increase in $\mathbf{E_{Norm,GMR}}$ from 1.50 V/m (n_v = 1.13) to 8.04 V/m (n_v = 1.80). In contrast, increasing Δn

with decreasing n_m (n_v = 1.46) leads to a blue shift in $\lambda_{vacc,GMR}$ (**Fig. 4.18c**) associated with an increase in $\mathbf{E_{Norm,GMR}}$ from 1.38 V/m (n_m = 1.33) to 6.31 V/m (n_m = 1.00).

Furthermore, the influence of the structural parameters on GMR is studied on $G_{ana,long4}$, where only slight shifts occur for $\lambda_{vacc,GMR}$ (zero and first modes at 556 nm and 303 nm, respectively) compared to $\lambda_{vacc,GMR}$ of $CS_{long,4}$. Although further analysis is focused on the zero mode, similar trends are expected for the first mode. Increasing the grid unit number of $G_{ana,long4}$ leads to slight red shifts in $\lambda_{vacc,GMR}$, which is more significant for grid units < 20 (**Fig. 4.18d**), combined with a dramatic increase in $\mathbf{E_{Norm,GMR}}$, reaching 11.70 V/m for 42 grid units. By increasing D of $G_{ana,long4}$, a red shift in $\lambda_{vacc,GMR}$ occurs (**Fig. 4.18e**), accompanied by less dramatic changes in $\mathbf{E_{Norm,GMR}}$, with a maximum (6.14 V/m) at D = 250 nm. Finally, increasing the d of $G_{ana,long4}$ (at the same ff) causes a dramatic red shift in $\lambda_{vacc,GMR}$ (**Fig. 4.18f**) and a simultaneous decrease in $\mathbf{E_{Norm,GMR}}$. This explains the $\lambda_{vacc,GMR}$ shift observed for $CS_{long,3}$ and $CS_{long,6}$ associated mainly with the change in d_{str}. Decreasing the fill factor ff (from 0.8 to 0.4) causes a blue shift in $\lambda_{vacc,GMR}$ (**Fig. 4.18f**) combined with a decrease in $\mathbf{E_{Norm,GMR}}$.

4.4. The complete frustule immersed in water

As previously demonstrated, adding the girdle bands spatially delays the inner edge diffraction fringes, probably due to the delay of the interference between the secondary wavelets generated at the edges—due to waveguiding behavior—and the transmitted wavefront through the CS (**Figs. 4.9b** and **c**). By further adding a similar, but smaller, CS representing a hypovalve—to build a CS in the complete frustule—almost all inner edge diffraction fringes, and, as a consequence, the diffraction-driven focusing spots, are removed from inside the frustule to appear beyond the hypovalve, as can be seen in the $CS_{long5,frustule}$ (**Fig. 4.19a**), and, therefore, become irrelevant to photosynthesis. At the same time, thin-film interference still affects the area inside the frustule.

Moreover, the generated PJ by the nodule, or the sternum, is still observed inside the frustule (*e.g.*, $CS_{long3,frustule}$ in **Fig. 4.19b**). Interestingly, the direction of this PJ follows Θ_{inc} of the incident wave (**Fig. 4.20a**). This behavior is confirmed for $CS_{long,3/nodule}$ (**Fig. 4.20b**) but with more stability inside the complete frustule, given that it occurs at a larger Θ_{inc} range (**Fig. 4.20a**). The nodule integrated into the hypovalve of $CS_{long3,frustule}$ also generates a PJ but beyond the frustule (**Fig. 4.19b**). Another stronger PJ appears beyond the hypovalve observed in all CSs of the complete frustule associated with the frustule's edge diffraction (black arrows in **Fig. 4.19**).

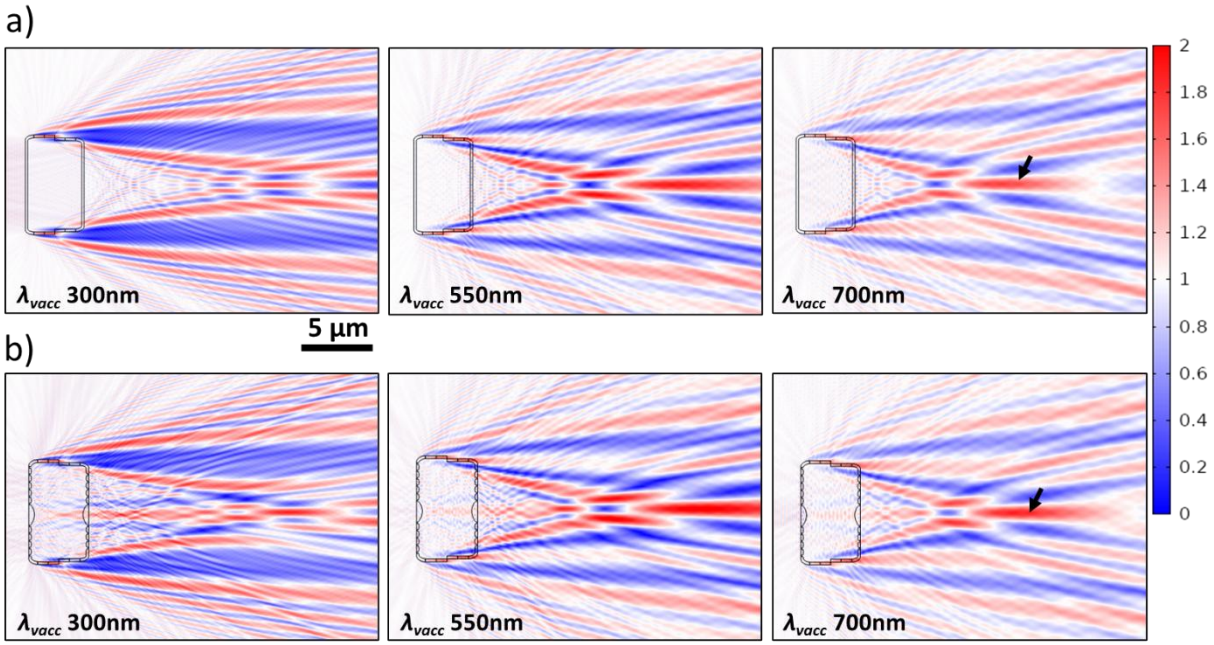

Fig. 4.19. The interference pattern of $CS_{long5,frustule}$ (**a**) and $CS_{long3,frustule}$ (**b**), which represent a complete frustule consisting of $CS_{long,5}$ or $CS_{long,3}$, respectively, immersed in water at different λ_{vacc}. With increasing λ_{vacc}, the diffraction-driven focusing fringes that appear outside the CSs move toward them. The black arrows indicate what seems to be a PJ. The color code is given in V/m units. This Figure is reproduced from Ghobara *et al.* [261].

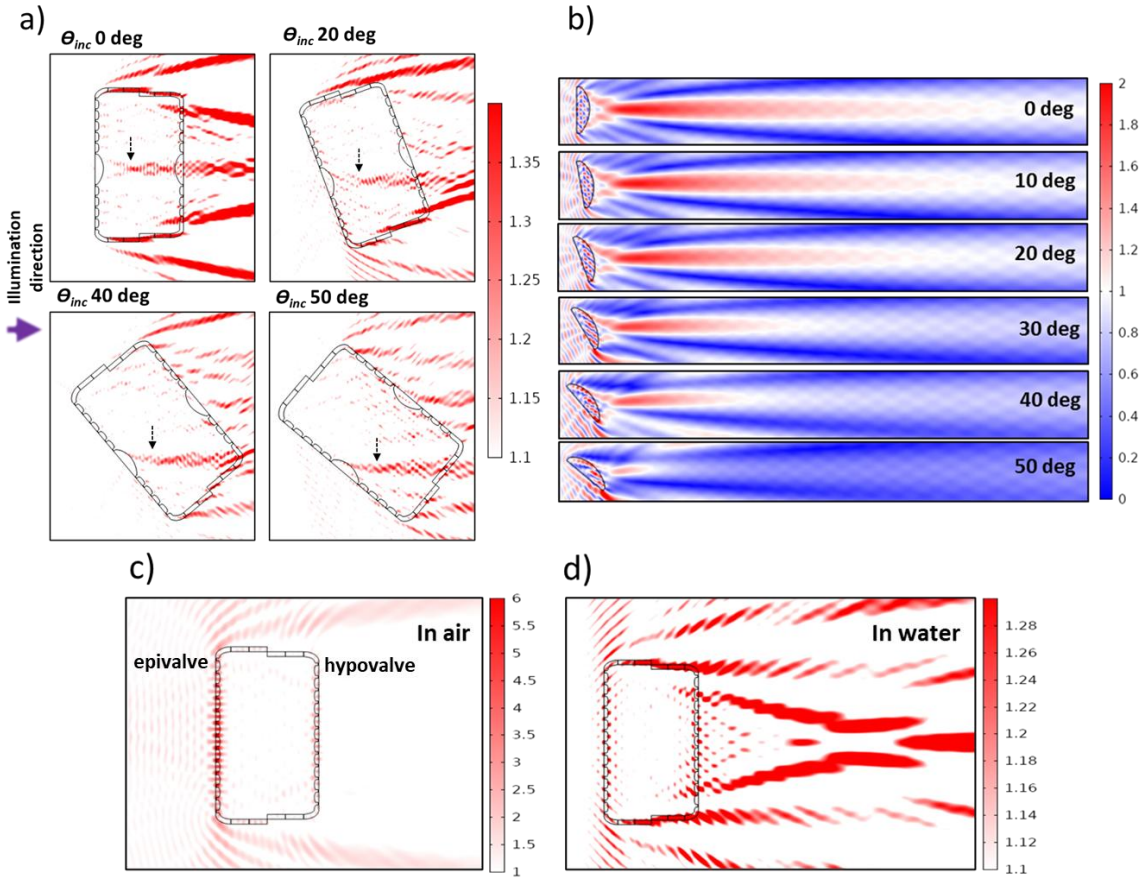

Fig. 4.20. (**a**) the Θ_{inc}-dependency of the PJ generated by the nodule inside $CS_{long3,frustule}$ at λ_{vacc} 400 nm in water. The color code starts from 1.1 V/m to emphasize the PJ from the

Talbot fringes. (**b**) the Θ_{inc}-dependency of the PJ generated by the dissembled nodule at λ_{vacc} 350 nm in air. (**c**) zero mode of the grid-coupled GMR in $CS_{long4,frustule}$ at $\lambda_{vacc,GMR}$ 553 nm in air and (**d**) at $\lambda_{vacc,GMR}$ 665 nm in water. The color codes are given in V/m units. This Figure is modified from Ghobara *et al.* [261].

Furthermore, the Talbot fringes—associated with the grid-like element—remain inside the frustule but also appear beyond the hypovalve, as can be seen in **Fig. 4.15d**. As the edge effect is minimized inside the frustule, the lateral deformation of the inside Talbot fringes becomes weaker. This is clear when comparing $CS_{long4,frustule}$ (**Fig. 4.15d**) and $CS_{long,4}$ (**Fig. 4.15b**), given that both are in the water at λ_{vacc} 350 nm.

Finally, there are no shifts in $\lambda_{vacc,GMR}$ of the zero mode observed for the epivalve in $CS_{long4,frustule}$ either in air (**Fig. 4.20c**) or in water (**Fig. 4.20d**), while the guided waves are extended from the epivalve to the hypovalve through the mantle and the girdle bands.

4.5. Further discussions

The comprehensive structural analysis of *GP* frustules utilizing FIB-SEM analysis, in addition to the regular SEM, offers high-resolution structural details crucial for predicting their light modulation abilities. While statistical analysis suggests that some critical structural parameters, such as the valve thickness D_v and striae spacing d_{str}, are reproducible between different valves within the studied culture, this likely means they might be built and optimized by the living cells on purpose to contribute to potential photobiological roles. This assumption can be tested in future through the structural analysis of the frustules of consecutive subcultures over a long period of time.

Through extensive numerical analysis, the ability of *GP* valves, as well as complete frustules, to modulate light in the near field and Fresnel zone was demonstrated and explained. Using 2D CSs and disassembling distinct optical components enables understanding complex interference patterns (*e.g.*, **Fig. 4.3**) and finding their correlation to the well-known optical phenomena in micro and near-field optics. Further, using analytical models allows the determination of the significance of structural parameters to the observed phenomena and also enables future prediction of the light modulation capabilities of other unstudied pennate species.

At this point, it should be noted that although the numerical analysis of 2D CSs gives a deeper analytical understanding of the involved optical phenomena and the general trends, there are some limitations. The actual shape and intensities of, *e.g.*, the PJ and Talbot fringes, occurring in 3D cannot be accurately predicted via 2D

simulations. Moreover, in the case of grid-coupled GMR, $\lambda_{vacc,GMR}$ and $\mathbf{E_{Norm,GMR}}$ are expected to be shifted when transferring from the 2D to 3D situation.

In the following subsections, the light modulation by an intact three-dimensional *GP* valve is predicted and discussed—in light of the obtained results—alongside its potential for applications (**4.5.1**) and, further, the hypothetic photobiological relevance of the complete frustule (**4.5.2**).

4.5.1. The light modulation by GP valve: The competing phenomena and potential for applications

The light modulation in 3D, with the presence of all integrated optical components in such small-size valves, is expected to give a more complicated interference pattern but will also show how distinct optical phenomena are competing.

The thin-film interference associated with the valve's thin-slab element is disturbed by (i) edge diffraction and (ii) the presence of integrated optical components (including the 1D grid-like and lens-like components), which cover the majority of the valve area, as can be concluded from **Figs. 3.1** and **4.1**. Nevertheless, the intensity of the reflectance and transmittance could be affected by this phenomenon. This, in turn, affects the strength of the final interference pattern, which is evident in the case of the diffraction-driven focusing spots' intensity $E^2_{Norm,f}$ (**Fig. 4.12a**). This means that, under normal incidence, the thickness D_v, as well as n_v, could be crucial for determining the λ_{vacc}-dependent reflectance/transmittance ratio of the valves. It is worth noting that many other pennate valves consist of a single optically thin, porous silica layer of a thickness $D_v \leq$ the visible light wavelengths, similar to GP valve; thus, being relevant to thin-film interference. This is distinct from the multilayer structure of some centric and pennate valves associated with the presence of loculated areolae [17], which could lead to multilayer interference. This phenomenon has not been investigated before for pennate valves. In contrast, the interference fringes have been witnessed in the reflectance spectrum of a centric valve of *Coscinodiscus wailesii* with a multilayer structure (see Figure 2 in [282]).

In large valves, the edge diffraction contribution to their light modulation behavior is expected to be less significant [141]. In contrast, in small-size valves (such as the *GP* valve), edge diffraction dominates their light modulation behavior and significantly contributes to the interference pattern in their near-field and Fresnel zone. The contribution of thickened areas within the valve (such as the nodule in *GP*) to the obtained interference pattern suggests that, even in the case of large valves with complex ultrastructure, such as the valves of *Arachnoidiscus* spp. (see Figure 3 in [131]), the diffraction from those additional edges is expected to play a significant role in their light modulation behavior.

Across the studied λ_{vacc} range, the PJ is expected to be dominant at the apical axis associated with the presence of the nodule and the sternum, which might be the case for all biraphid pennates. The PJ associated with the nodule (the maximum thickness D_{nod}) is expected to be higher in intensity and interrupt the interference pattern, as shown in **Fig. 4.13**. This PJ is similar to the focusing beam observed by De Tommasi *et al.* [139]. The PJ—especially that associated with the nodule— could have the potential in several applications to, for instance, enhance the resolution of optical microscopy, reach super-resolution imaging, improve fluorescence spectroscopy, enable subwavelength photolithography, and enhance the optical absorption in optoelectronic devices [181,283]. Additionally, by changing Δn, either via changing n_v or n_m, the features of the PJs can be tailored, as shown in (**Figs. 4.14c** and **d**), which could be interesting for future applications.

Furthermore, inside the transmittance region of *GP* valve, the Talbot interference pattern is expected to dominate at a range of wavelengths, where additional diffraction orders (± 1st orders) besides the 0th order can be present. For a clean *GP* valve immersed in air, the normal incident light of wavelengths < 500 nm is expected to generate Talbot fringes, representing an image copy of the 1D grid-like structure, which consists of the valve's costae alternating with striae of increasing spacing (d_{str}) toward the edges (**Fig. 4.1**). In general, the Talbot fringes are expected to be distorted near the valve edges, influenced by the edge diffraction and, near its apical axis, influenced by the PJ (**Fig. 4.13b**). Although the Talbot effect is well known in the near-field optics of diffraction gratings [200,284], it is often not mentioned—apart from by De Stefano et al. [129]—or analyzed in diatom-related studies. On the contrary, the analysis of far-field diffraction grating behavior is more frequent, as in [127], which is not directly relevant to photobiology or most applications. Recently, the Talbot phenomenon has been utilized in several applications, for instance, in fluorescence Talbot microscopy [285,286], displacement Talbot lithography [287,288], and image sensors [289]. However, it should be noted that the Talbot pattern produced by *GP* valves is likely inappropriate for such applications if compared to the valves of larger-size pennate species such as *Nitzschia* and *Hantzschia* spp. (see Round *et al.* [17]), where the grid-like component has an almost fixed d_{str} and is not interrupted by a sternum or nodule at the valve apical axis.

Additionally, at a narrower range of wavelengths, the 1D grid-like element is expected to initiate grid-coupled GMR, where the transmittance drops dramatically and, thus, affects the intensity of the Talbot fringes at the first GMR mode or diffraction-driven focusing spots at the zero mode. It should be, however, noted that the exact $\lambda_{vacc,GMR}$ in the 3D valve cannot be expected accurately without 3D simulations, as previously mentioned. In general, GMR is of great interest for sensing applications and optoelectronic devices [220,223,224] associated with enhancing EM fields near the valve surface through the simultaneous evanescence field. Due to the

finite size of *GP* valves and, thus, a small number of grid units, the quality of GMR is expected to be low. Hence, larger pennate valves, especially of small areolae size (large *ff*), could be more appropriate for GMR-based applications.

For the wavelengths away from the ability of the grid-like element to diffract the light (produce Talbot pattern) or initiate GMR, the diffraction-driven focusing spots are expected to dominate the interference pattern in the Fresnel zone. The PJ generated by the nodule zone (as well as the sternum) is expected to interfere with these spots (see, *e.g.*, **Fig. A.9**, **Appendix A**) to generate a **colligative diffraction-driven focusing behavior**. The observed behavior of these focusing spots is in good agreement with the focusing behavior reported in the previous work for the valves of *Coscinodiscus* spp. and *Arachinodiscus* sp. [129,131,132,137,140]. However, it should be noted that the foramen pore diameters—and the period in between—in *Coscinodiscus* spp. valves (≈1–3 µm) are comparable to the size of the whole *GP* valve.

Finally, *GP* valves could be utilized in optoelectronic and photonic applications based on and within the limits of the discussed competing phenomena. In such applications, the valves are often spread over a substrate to form a monolayer [290,291], where they occur in two configurations, either showing the outer or inner face upward (**Figs. 4.21a** or **b**, respectively). Adding the valve to a substrate would lead to changes in their light modulation abilities, which can also be predicted from the relevant theories and analyzed through numerical analysis. Recent reports showed a degree of control over the valve orientation on the substrates that could be helpful for specific applications [290].

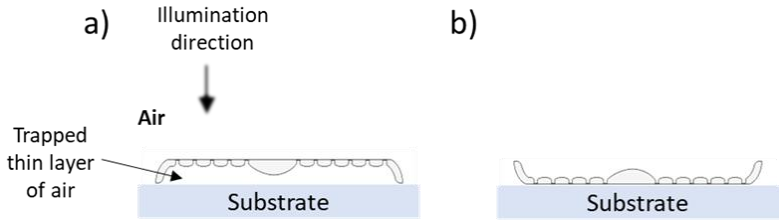

Fig. 4.21. Sketches showing a *GP* valve (represented by $CS_{long,3}$) laying on a substrate with the outer (**a**) or inner face (**b**) upward. This Figure is reproduced from Ghobara *et al.* [261].

4.5.2. Photobiological relevance of GP frustules

As *GP* living cells live underwater, understanding the case of a complete frustule in water, illustrated in **section 4.4**, is crucial for correlating the observed phenomena and the designated optical elements to hypothetical photobiological roles. Although there is significant reduction in the light modulation strength, all phenomena still occur and might have photobiological functions. The expected photobiological relevance might not only be limited to photosynthesis enhancement—by attenuating harmful radiation while maximizing absorption of PAR—but also might extend to

perform functions in putative light sensing and signalling mechanisms [44,157]. It should also be noted that *GP* is a benthic species living near the bottom of the basins, where the blue–green spectral ranges dominate due to the strong absorption of the red and infra-red wavelengths. The phenomenon increases in significance with increasing of water column depth that the light penetrates before reaching the living cells [157].

In *GP* living cells, the chloroplast occurs adjacent to the valve face—where the grid-like element (*i.e.*, the striae and costae) covers most of its area—and to the mantle and girdle bands (*i.e.*, the fiber-like elements) [292]. This gives significant importance to the Talbot effect, grid-coupled GMR, and waveguiding behavior in photosynthesis. In parallel, thin-film interference generally affects the transmittance inside the cell. PJ generation by the nodule and the sternum—although occurs inside the frustule—might not be directly relevant to photosynthesis as it occurs along the apical axis within a narrow area compared to the chloroplast area. In contrast, the diffraction-driven focusing pattern associated with the frustule edge diffraction is not relevant to photosynthesis, as it moves beyond the frustule (**Fig.4.19**).

Furthermore, the generated PJ, especially at the nodule zone, which is more intense at shorter λ_{vacc} (*e.g.*, **Fig. 4.13**) and follows the incident light direction (**Fig. 4.20a**), is expected to be related to a hypothetical PJ-based sensing mechanism for the light direction, which is proposed in **subsection 5.4.2** (**Chapter 5**). This is inspired by the mechanism that has been suggested for the spherical cells of cyanobacterium *Synechocystis* sp. [293,294].

5 Diffraction-driven focusing of visible light by diatom valves

As mentioned in **Chapter 1** (**subsection 1.2.4**), the focusing ability of a limited number of valves belonging to a few species, representing even fewer genera, has been studied so far in the literature. In **Chapter 4**, the diffraction-driven focusing ability (including PJ generation) of the *GP* valve/frustule was numerically revealed. Following that context, this chapter aims to experimentally investigate this phenomenon using Far-field optical microscopy techniques. It also seeks to expand the current knowledge by studying a number of valves—some of which have not been studied in literature before—belonging to distinct pennate and centric species representing different genera. The chapter is divided into four parts: part **5.1** describes the geometry and ultrastructure of the diatom valves studied here; part **5.2** elucidates the valves' ability to focus the normal incident light in transmittance; part **5.3** shows the ability of some valves to focus light when illuminating them from the side; and part **5.4** discusses the potential relevance of this phenomenon to applications as well as photobiology.

5.1. The geometry and ultrastructure of the studied valves

A number of structurally-distinct diatom valves belonging to **nine diatom species** (representing **eight distinct genera**) were selected for the studies to cover a wide range of geometries, sizes, and ultrastructure. That could help judge whether the diffraction-driven light focusing is spread among diatom species and genera. The main structural features of the studied valves are summarized in **Table 5.1**.

Table 5.1. Description and comparison of the studied diatom valves.

Diatom species	Geometry	Size [µm]	Ultrastructure features
CR (**Fig.5.1a**)	plate-like shape	diameter 80 – 100	The valve has hexagonal-shaped loculate areolae (*i.e.*, chamber-like voids) of an average width ≈ 1.8 µm. The areolae are open to the inner valve face with circular pores, of an average diameter ≈ 1.2 µm. These pores become smaller toward the mantle, reaching ≈ 0.7 µm. From the outer valve face, the areolae are covered by a fine silica sieve of pore diameters ranging from 0.05 – 0.1 µm. The valve has a circular hyaline area (free of pores) that occurs approximately at its geometrical center with a diameter ranging from 6 – 10 µm.

			The mantle height is about 2 µm.
Pin (**Fig.5.1b**)	Linear with rounded apexes	length 170 – 300 width 30 – 50	The valve consists of two distinct silica layers stacked together, forming elongated chambers (called alveoli) that open to the inner face with linear pores of an average width ≈ 0.9 µm, and spacing ≈ 2 µm. From the outer valve face, the alveoli are covered with a porous layer of tiny pores (called poroids) with an average diameter ≈ 0.1 µm, arranged in a hexagonal pattern with an average spacing ≈ 0.2 µm. From the inner valve face, a distinct nodule appears close to its center with an average width ≈ 7 µm and length ≈ 12 µm. Two other nodules appear at valve's apexes. The valve also has a relatively large area free of pores at the center that extends through its long axis, where a raphe slit occurs. The mantle height is about 4 µm.
GP	Elliptic to ovate	length 6.1 – 7.9 width 4.3 – 5.0	See detailed description in **Chapter 4**. See also section A.10 (**Appendix A**)
Aula (**Fig.5.1c**)	Cylindrical	diameter 6.2 – 18.2 height 2.9 – 6.2	See detailed description in **subsection 5.1.1**.
Samples consisting of an arranged valve			
Cosc (**Fig.5.2a**)	Plate-like shape	diameter 172	The valve has two dissimilar areas featuring two distinct porosity patterns. The outer part shows hexagonal-shaped loculate areolae of an average width ≈ 6 µm. The areolae open to the inner valve face with circular pores of an average diameter ≈ 2 µm and spacing ≈ 7µm. At the central part (of a diameter ≈ 53 µm), the areolae seem not hexagonal, and the pores have an average diameter of ≈ 0.7 µm and spacing of ≈ 1.8 µm. A hyaline area (of a diameter ≈3 µm) occurs approximately at the valve's geometrical center. The estimated valve thickness is about 2.3 µm (from a cracked part).
Acto (**Fig.5.2b**)	undulated plate-like shape	diameter 163	The undulated valve has ten distinct sectors of about equal size alternating with each other in up and down pattern. The inner valve face shows circular pores of an average diameter ≈ 0.28 µm and spacing ≈ 0.75 µm. A hyaline area (of a diameter ≈ 22 µm) occurs approximately at the valve's geometrical center. The estimated valve thickness is about 2 µm (from a cracked part).
Staur	Lanceolate	Length 205	From the inner valve face, a distinct thicker area of a rectangular shape appears approximately at the geometrical center (called stauros) of a width ≈ 5.7 µm. The sternum—

(**Fig.5.2c**)		Width 37	which is penetrated by the raphe—also seems distinctively thicker. The stauros and sternum—together—divide the valve into four distinct groups of pore arrays. Each group has tilted striae of an average spacing ≈ 0.7 µm, consisting of fine transversely elongated areolae of an average length ≈ 0.3 µm, width ≈ 0.15 µm, and spacing (in stria) ≈ 0.6 µm.
Pinn (**Fig.5.2d**)	Linear with rounded apexes	Length 156 Width 26	Similar to *Pin* valve, but of smaller-size structural parameters. For example, the linear pores—appear at its inner face—have an average width ≈ 0.7 µm, and a spacing ≈ 1.4 µm. The nodule close to its center has a length ≈ 5 µm and a width ≈ 3.5 µm. The apical nodules seem more distinctive here.
Did (**Fig.5.2e**)	Lanceolate with rounded Swollen apexes	Length 144 Width 42	The valve has three distinct areas: the central area (the major area), a headpole, and footpole. The headpole is larger compared to the footpole. The sternum seems thicker. Two apical nodules appear from the inner valve face at the two apexes, while the central area shows an increased thickness along with four stigmata. Striae are highly tilted at the central area and less tilted at the two apexes. The areolae are open to the inner face with elongated chambers.

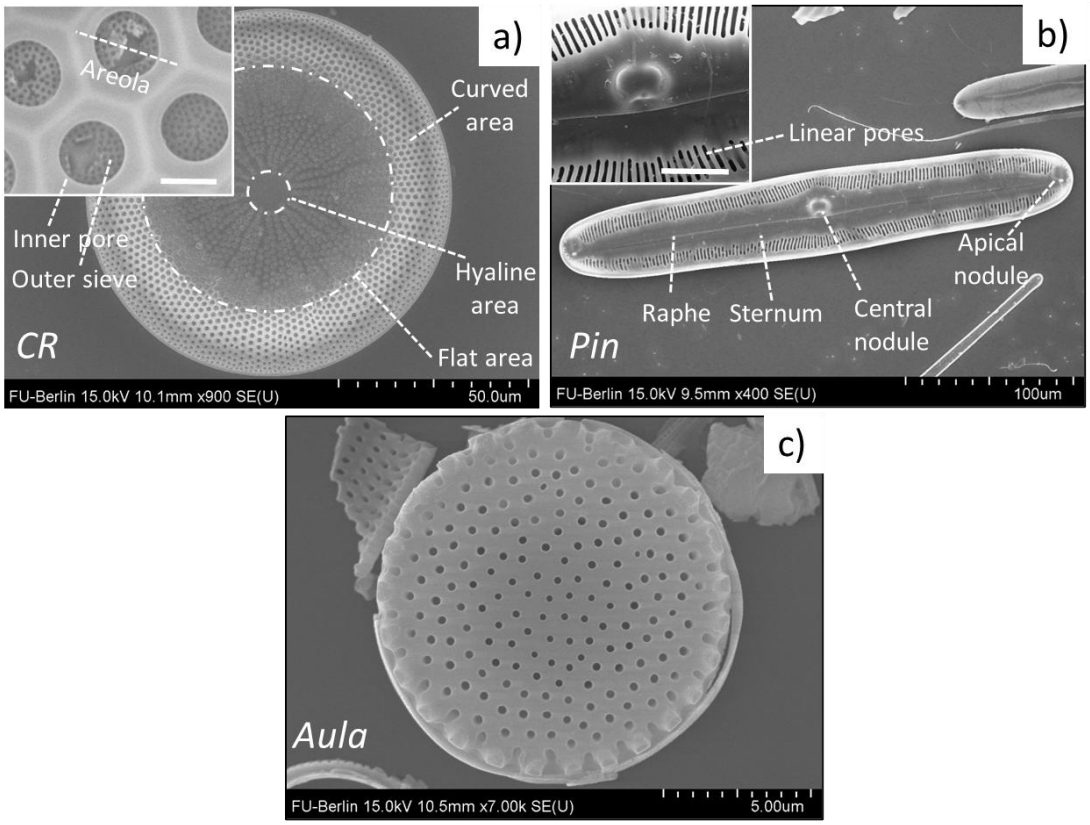

Fig. 5.1. SEMs showing the top view of the inner valve face of the centric diatom *CR* (**a**) and the pennate diatom *Pin* (**b**), as well as the outer valve face of the centric diatom *Aula* (**c**). The insets in (**a**) and (**b**) show the ultrastructural features of these valves with scale bars of 1 µm and 15 µm, respectively. The raw SEMs were captured by Dr. Martina Gilic.

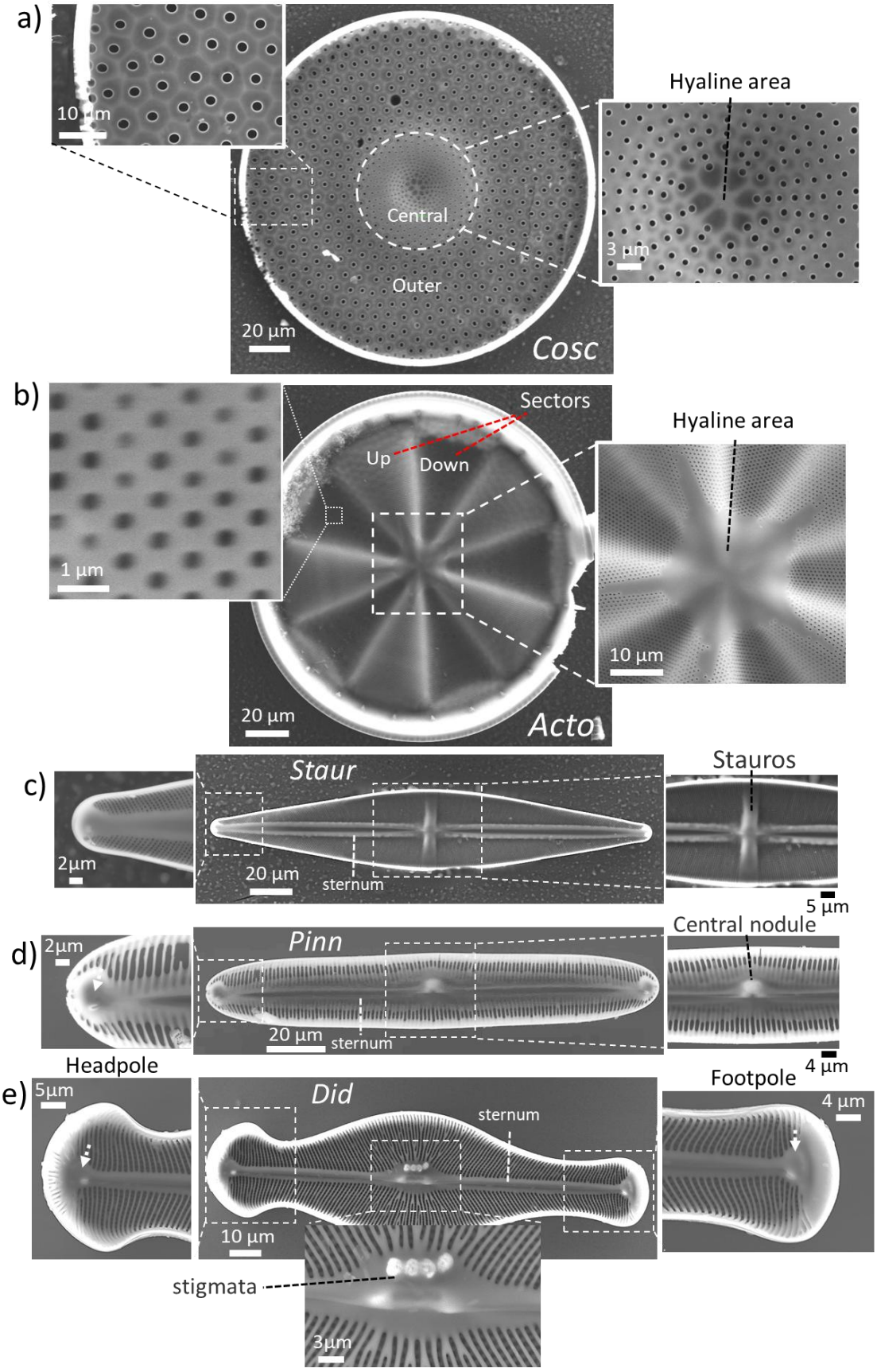

Fig. 5.2. SEMs show the ultrastructure of the inner valve face of the centric diatoms *Cosc* (**a**) and *Acto* (**b**) and the pennate diatoms *Staur* (**c**), *Pinn* (**d**), and *Did* (**e**). The white arrows indicate the increased thicknesses at the pennate apexes (*i.e.*, the apical nodules).

5.1.1. Detailed structural analysis of Aula valves

For the rigorous analysis of light focusing abilities of *Aula* valves performed in this chapter, a detailed structural analysis of *Aula* valves was carried out (**Fig. 5.3** and **Table 5.2**). In **Fig. 5.3c**, an intact *Aula* frustule—less observed in the sample—shows the two overlapping valves, epivalve and hypovalve, still conjunct and surrounded by a delicate silica layer representing traces of the so-called 'girdle'.

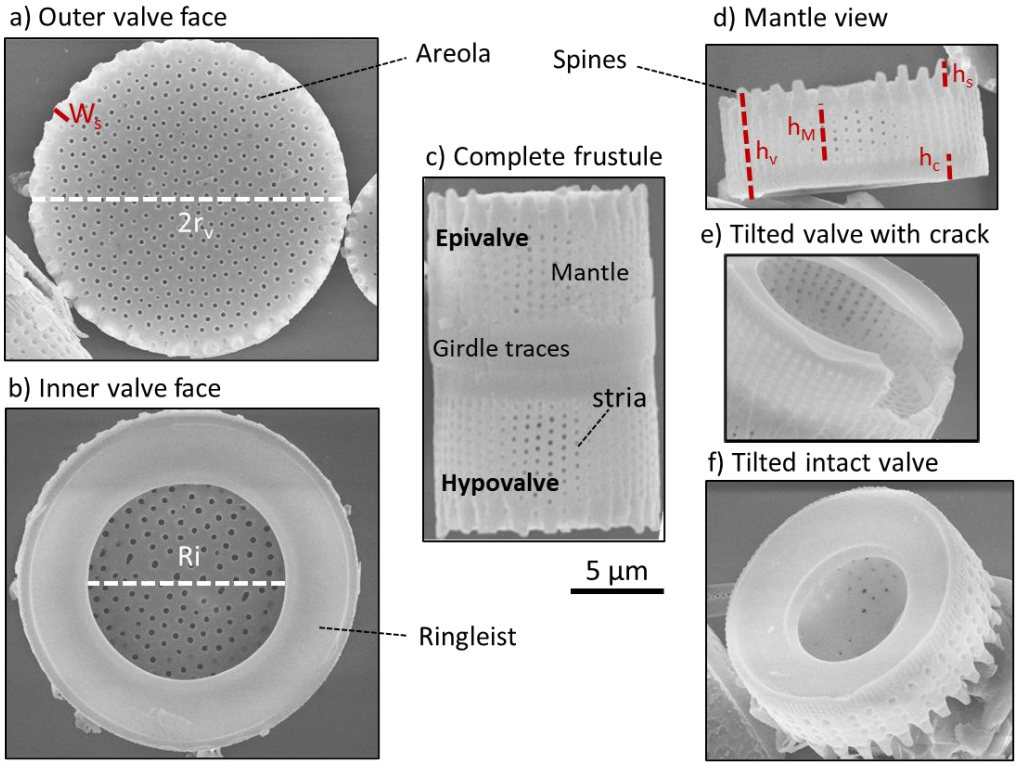

Fig. 5.3. SEMs of different *Aula* valves in the purified sample show their geometry and ultrastructural features. The raw SEMs were captured by Dr. Martina Gilic.

The valve has a 3D cylindrical shape of diameter $2r_v$ and height h_v. When a valve lies on its flat side, it has a circular appearance showing either the outer (**Fig. 5.3a**) or inner face (**Fig. 5.3b**). When a valve lies on its mantle, it has a rectangular appearance (*e.g.*, **Fig. 5.3d**). The outer valve face has a flat porous plate (**Fig. 5.3a**) of an estimated thickness $D_v \approx 0.2$ µm surrounded by an outer rim of a non-porous area of width W_s, from which the spines extrude to help the frustule to conjugate with the adjacent frustules in linear chains [17,295]. The areolae of the valve face have a round shape of diameter $2r_{a,v}$ and a spacing (center to center) $d_{a,v}$. These areolae are arranged in a quasi-periodic arrangement that can be approximated to a 2D hexagonal lattice if we tolerate imperfections up to 10 % (estimated according to the method developed in **Appendix B**). Distinct defects (*i.e.*, areolae-free zones) of a width W_d were also found in many valves (see, for example, **Fig. A.20** in **Appendix A**). Only a few valves appear with almost no defects (*e.g.*, **Fig. 5.3a**). The inner valve face has a ring-like structure called ringleist (*i.e.*, a silica ledge that protrudes from the

end of the mantle into the inner area of the valve [26]) with an opening ratio $Ri_{,\%}$ (= $Ri/2r_v$).

Table 5.2. Statistical analysis of the structural parameters of *Aula* valves (weighted mean, internal and external errors—the bold print indicates the significant error).

Parameter	Description	Weighted mean 'X_w'	dX_{int}	dX_{ext}
$2r_v$	Valve diameter (2 x radius) [µm]	**13.9**	0.006	**0.9**
h_v	Valve height [µm]	**4.4**	0.007	**0.4**
W_s	Spine area width [µm]	**0.59**	0.02	**0.04**
$2r_{a,v}$	Areolae diameter on the valve face [µm]	**0.25**	0.01	**0.02**
d_a	Areolae lattice spacing [µm]	**0.82**	0.002	**0.02**
$A_{a,v}$	The lattice angle [degree]	**60.0°**	0.008°	**1.6°**
W_d	Defect width [µm]	**3.4**	0.2	**0.8**
h_c	Collum height [µm]	**1.4**	0.008	**0.1**
h_s	Spines height [µm]	**1.00**	0.05	**0.08**
D_R	Ringleist thickness [µm]	**0.53**	0.01	**0.05**
$Ri_{,\%}$	Ringleist opining ratio [%]	**51**	0.9	**5**
D_M	Mantle thickness [µm]	**0.54**	0.008	**0.05**
$2r_{a,M}$	Areolae diameter (2 x radius) on mantle [µm]	**0.20**	0.01	**0.05**
$d_{a,M}$	Areolae spacing within stria on mantle [µm]	**0.56**	0.003	**0.04**
$d_{a,\,Mstr}$	Areolae spacing between adjacent striae on mantle [µm]	**0.8**	0.003	**0.1**
$A_{a,M}$	The lattice angle [degree]	**84.0°**	0.1°	**3.0°**

In the mantle view (**Fig. 5.3d**), the valve height h_v is separated into three distinct areas: a relatively large porous mantle of a thickness D_M, spines of a height h_s, and a non-porous (*i.e.*, hyaline) edge of a height h_c called collum [26]. The areolae of the mantle have a diameter $2r_{a,M}$ and are aligned in striae (*i.e.*, rows of pores [17]) with a spacing within a stria of $d_{a,M}$ and a spacing between two adjacent striae of $d_{a,Mstr}$. This produces a quasi-periodic arrangement that represents a 2D oblique lattice, which could be approximated to a 2D rectangular lattice if we tolerate imperfections up to 13 % (estimated according to the method developed in **Appendix B**). The imperfections in this lattice are associated with a spatial incoherence between adjacent striae.

In contrast to *GP* valves—which showed precision in building some of the structural parameters, see **Table 4.1** (**Chapter 4**)—all structural parameters of *Aula* valves showed a larger external error dX_{ext} indicating that these parameters are changing between the valves of the purified sample (**Table 5.2**). It should also be

noted that the minimum and maximum values of the structural parameters show a relatively large range compared to that of the *GP* sample (see **Table 5.1**), probably associated with the presence of valves of more than one species in the sample.

5.2. Light focusing induced by valves under trans-illumination

First, the ability of *GP* valves to induce diffraction-driven focusing under trans-illumination was experimentally investigated to validate the analytical understanding attained from the 2D numerical analysis results of *GP* CSs demonstrated in the previous chapter.

As expected, under trans-illumination, the *GP* valves showed an enhanced I_{Norm} along its apical axis (where sternum occurs) with a distinguished focusing spot occurring behind the position of the central nodule associated with generating PJ (**Fig. 5.4a**), reaching its $I_{Norm,max}$—for three analyzed valves, indicated in **Fig 5.4a**—at z_4 (≈ 5.6 ± 0.4 µm). Pronounced bright/dark contours were also observed surrounding the valves associated with the edge diffraction. At z_0, two additional maxima were observed at the valve's apexes, indicated by the green arrows in the inset (**Fig. 5.4a**), which could be related to the increased thickness at the valve apexes (see **Fig. A.25**, **Appendix A**) that is not included in the CSs but could also generate distinguished PJs. It should be noted that, under the experimental setup used, the orientation of the valves over the substrate was not possible to determine due to their small size.

Although the 2D simulation results could analytically explain the observed focusing behavior, the direct fitting of these results to the experimental observations is not straightforward. This is, on the one hand, due to the 3D complexity of the valve ultrastructure (as discussed in **subsection 4.5.1**), and on the other hand, due to the resolution limitation of the setup used, which likely cannot reveal very fine features of the interference pattern observed in the simulation results (such as, the finer diffraction-driven focusing spots). Additionally, the simulations were carried out at selected λ_{vacc}, while the trans-illumination measurements were carried out employing a tungsten-halogen lamp, covering a wide range of wavelengths (including the visible light range). Despite these challenges, **section A.10** (**Appendix A**) demonstrates the analysis of how much the 2D simulations could predict the actual position and amplitude of the experimentally observed focusing spots.

As demonstrated in the previous chapter (**subsections 4.3.4** and **4.3.5**) through the analysis of an analytical slab, the diffraction-driven focusing behavior is not limited to *GP* CSs and can be generally induced by any dielectric slab if its dimensions (length L_{sl} and thickness D_{sl}, relative to incident λ range) and Δn are appropriate. Even if the slab is lengthy and cannot induce the focusing behavior through the interference of its inner diffraction fringes, integrating a thicker

mesosize (relative to incident λ range) part into the slab could induce such behavior (see also the simulation results in **section A.11**, **Appendix A**).

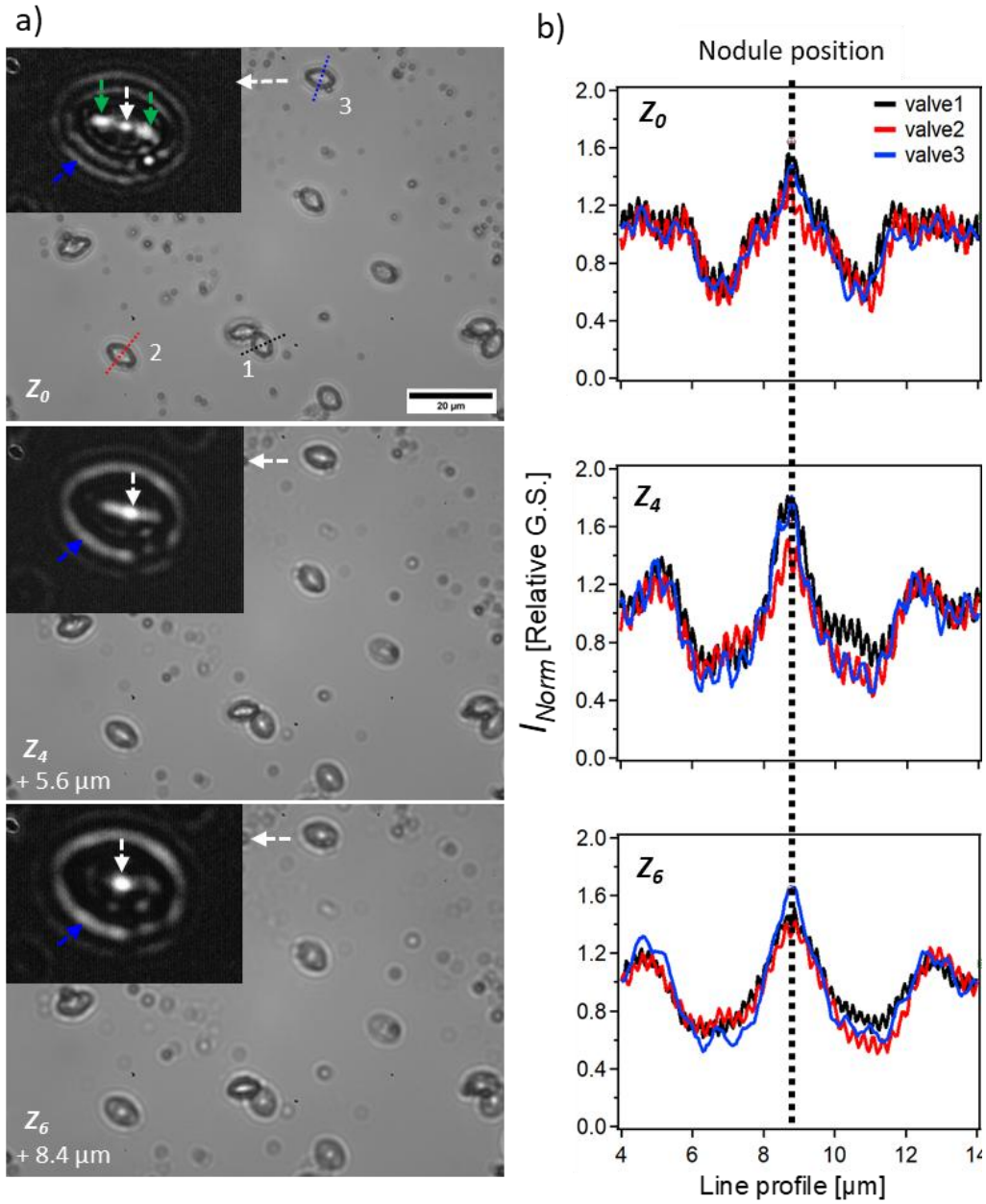

Fig. 5.4. (**a**) Trans-illumination of *GP* valves under 40x objective at three selected focal planes (z_i). Each step on the ***z***-axis is ≈ 1.4 ± 0.1 µm. The insets show a *GP* valve with a subtracted background and enhanced contrast (performed using Image J) to emphasize the focusing behavior. The white arrows in the insets indicate the focusing associated with the nodule position, while the blue arrows indicate the edge diffraction fringes outside the valves. (**b**) The normalized vertical line profiles extracted from three different valves at the three selected focal planes on the ***z***-axis. The selected valves and the position of line profiles are demonstrated in (**a**) at z_0. In the normalized line profiles, the input light intensity $I_{Norm,input} = 1$, $I_{Norm} < 1$ indicates attenuation in transmission, while $I_{Norm} > 1$ indicates the enhancement due to constructive interference. The noise in the line profiles represents the error range that is associated with the camera and the optical system.

If we expanded the developed understanding to the diatom valves of other pennate species, one could—in theory—predict whether a valve can induce a diffraction-driven focusing behavior based on (i) its dimensions and (ii) the presence/absence of integrated mesosize thicker parts. However, it should be noted that the geometry and dimensions of the mantle in these valves, as well as the presence of other diffraction sources, could influence the focusing behavior, as explained in the previous chapter.

As predicted, the other experimentally studied pennate species, which have larger size valves but with integrated mesosize thicker parts in their inner face—including the nodules and stauros (see **Figs. 5.1b** and **5.2c-d**)—also showed a focusing behavior in transmittance correlated to these parts (for example, the ***Did*** and ***Pinn*** valves, **Fig. 5.5**). In the case of the *Did* valve, the $I_{Norm,max}$ magnitude of light focusing at the apexes (head and footpoles) was larger than that at the center (**Fig. 5.5a**). In contrast, the *Pinn* valve showed a higher focusing $I_{Norm,max}$ magnitude associated with its central nodule compared to the apical nodules (**Fig. 5.5b**). In the *Did* valve, an apparent enhancement of the normalized intensity I_{Norm} was also observed along the sternum, which could be associated with its increased thickness compared to the rest of the valve (**Fig. 5.2e**).

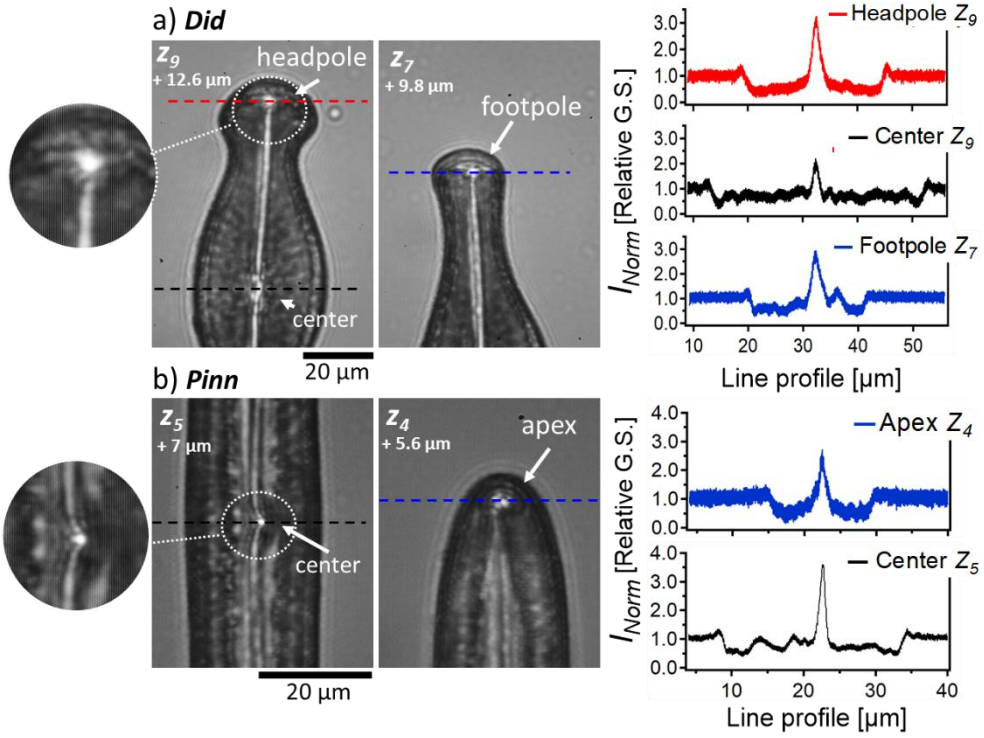

Fig. 5.5. The studied *Did* (**a**) and *Pinn* (**b**) valves—showing their inner face upward—as observed under 40x objective. The distinct parts of the valves are displayed at focusing $I_{Norm,max}$ (at the left), along with the extracted normalized line profiles (at the right). The dashed lines in the figures illustrate the positions of the extracted line profiles. In this figure, the brightness and contrast of the raw optical micrographs were enhanced to visualize the valves. Each step on the ***z***-axis is ≈ 1.4 ± 0.1 µm.

In principle, the diffraction-driven focusing that is mainly induced by these integrated parts could occur whether the valve is laid on its inner or outer face. This prediction was experimentally confirmed by observing two *Pinn* valves of similar dimensions but having a different orientation on the substrate under the same light intensity and camera settings (**Fig. 5.6**). Interestingly, the valve having its outer face upward (**Fig. 5.6b**) showed a larger focusing magnitude (**Fig. 5.6c**) and reached its $I_{Norm,max}$ at a closer distance from the valve compared to the other valve. Such observation was also noticed in the simulation results of *GP* CSs (**Fig. A.11c**, **Appendix A**) and is correlated to the mantle orientation (having the mantle either up or down) and its contribution to the observed focusing.

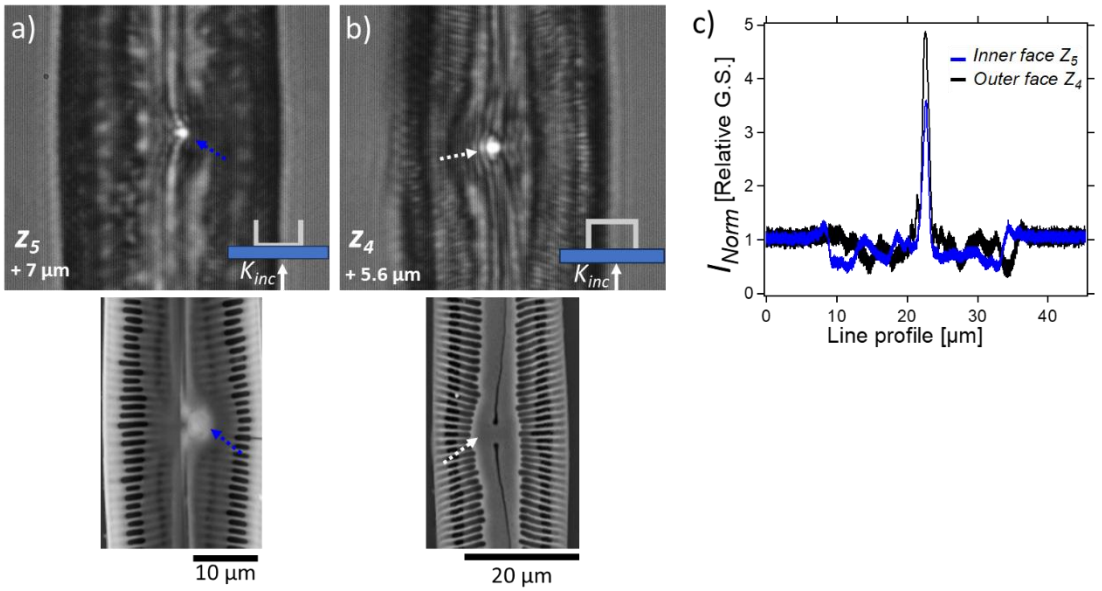

Fig. 5.6. The central nodule of two *Pinn* valves (displayed at the focusing $I_{Norm,max}$) with its inner (**a**) or outer (**b**) face upward. The orientation of the valves was confirmed by SEM (shown at the bottom) after the experiment. The dashed arrows indicate the position of the central nodule. In this figure, the brightness and contrast of the raw optical micrographs were enhanced to visualize the valves. (**c**) The extracted normalized line profiles across the two valves (through the central nodule) at $I_{Norm,max}$. Each step on the ***z***-axis is ≈ 1.4 ± 0.1 µm.

In the case of the ***Staur*** valve, a more complicated interference pattern was observed in transmittance (**Fig. 5.7**) correlated to the diffraction contributions from stauros and sternum (see the valve ultrastructure in **Fig. 5.2c**), which gave a cross-shaped enhancement. Approximately at the geometrical center of the valve, the focusing reached its maximum, yielding a spot, reaching its minimum waist (FWHM ≈ 1.4 µm) and $I_{Norm,max}$ at $\boldsymbol{z_{10}}$ (≈ 14 ± 1 µm) before it started vanishing. A splitting of the interference pattern was also observed at higher focal planes (*e.g.*, $\boldsymbol{z_{20}}$ in **Fig. 5.7**). Such splitting was previously observed and explained in *GP* CSs simulations (see **Figs. 4.11b-c**) and the simulation results shown in **sections A.10** and **A.11** (**Appendix A**).

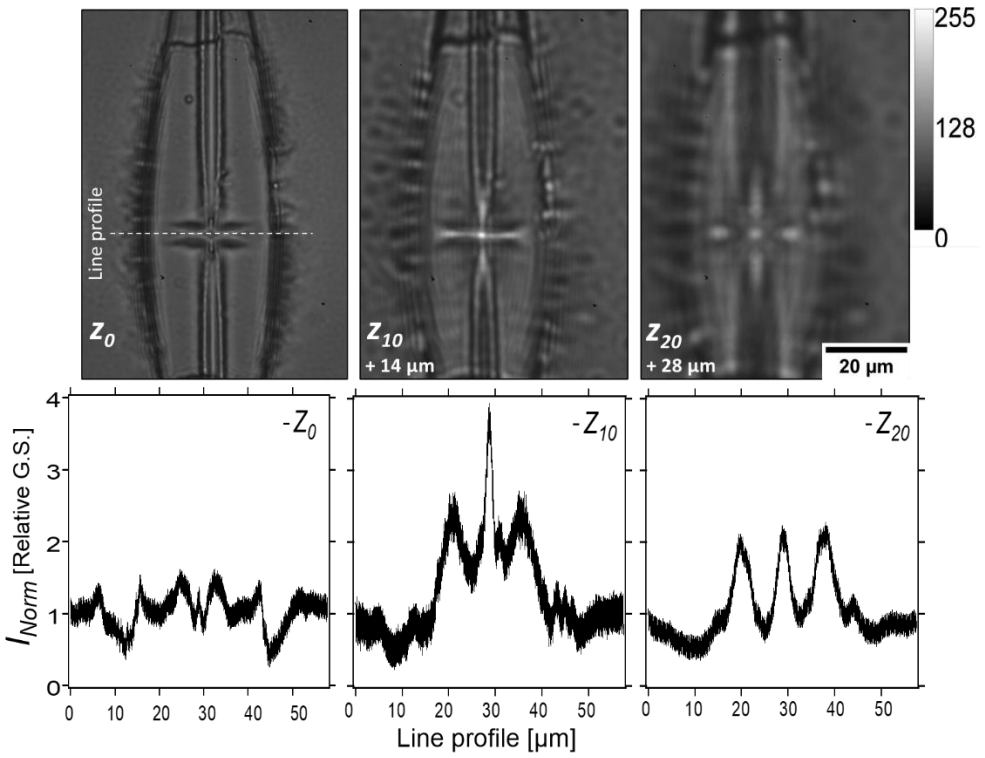

Fig. 5.7. The studied *staur* valve—showing its inner face upward—as observed under 40x objective at different focal planes z_i (at the top), along with their normalized line profiles (at the bottom). In this figure, the brightness of the raw optical micrographs was enhanced to visualize the valve. The intensity scale is a grayscale value. Each step on the ***z***-axis is ≈ 1.4 ± 0.1 µm.

Among the studied centric species, ***Aula*** valves exhibit a hollow cylindrical geometry with relatively small dimensions. The 2D numerical analysis results of *Aula* longitudinal CSs, demonstrated in **section A.12** (**Appendix A**), showed a diffraction-driven focusing behavior when illuminated normally to their surface. The experimental results confirmed the focusing behavior of *Aula* valves, such as the valve shown in **Fig. 5.8** (of a diameter ≈ 16 µm). By defocusing, a bright spot appeared above the valve in the transmittance, reaching its minimum waist (FWHM ≈ 1.7 µm) and $I_{Norm,max}$ at z_7 (≈ 10.0 ± 0.7 µm), before quickly vanishing. By increasing the distance above the valve, a spot of attenuated I_{Norm} replaced the focusing spot, as shown at z_{12} (≈ 16.8 ± 1.2 µm). By further defocusing, another focusing spot appeared, reaching its minimum waist (FWHM ≈ 4 µm) and $I_{Norm,max}$ at z_{21} (≈ 30.0 µm ± 2.1 µm). The enhancement is also accompanied by a pronounced dip in the intensity at the valve's outer rim (line profiles in **Fig. 5.8**). This behavior was reproducible among *Aula* valves (see another example shown in **Fig. A.17**), although the focusing parameters were changing among different valves, likely associated with the changes in their structural parameters (see also **section A.12**, **Appendix A**).

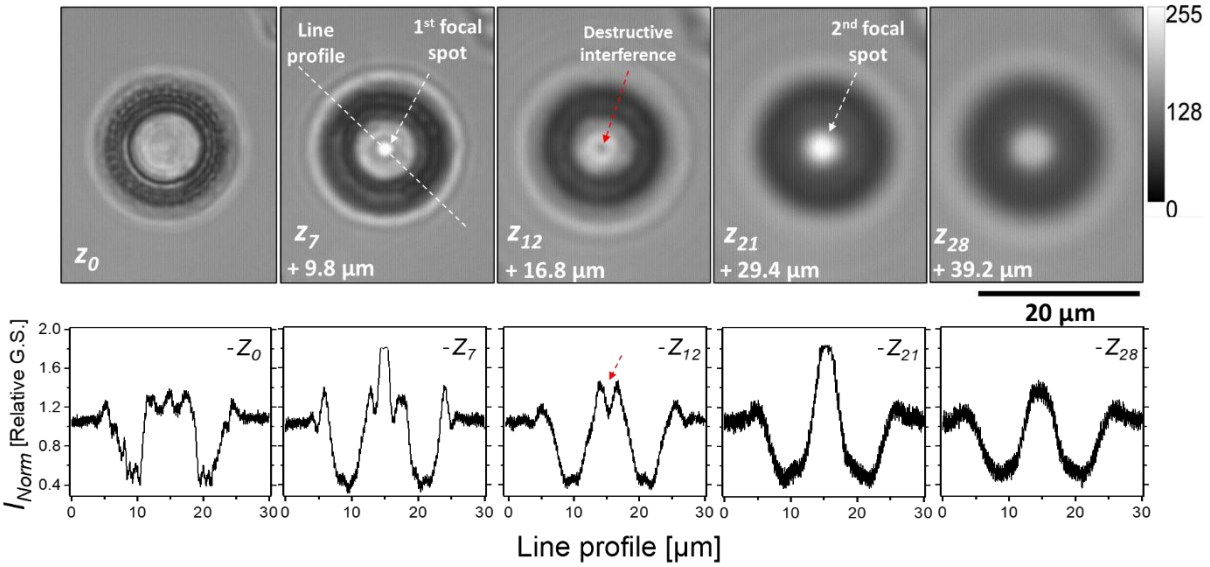

Fig. 5.8. An *Aula* valve—showing its outer face upward—observed under 40x objective at different focal planes z_i (at the top), along with the normalized line profiles at selected focal planes (at the bottom). Each step on the z-axis is ≈ 1.4 ± 0.1 µm. It should be noted that in this valve, the maxima at z_7 and z_{21} still show a partial saturation.

Moreover, the experimental results of the centric ***CR*** valves (of large diameter, **Table 5.1**) showed a focusing behavior (**section A.13**, **Appendix A**) comparable to previous work on the valves of *Coscinodiscus* spp. [135,137]. The generated focusing spot occurred directly behind the central hyaline area and had FWHM comparable to the hyaline area width. Interestingly, their girdle bands (without valves inside) also showed what seemed a focusing behavior with a focusing $I_{Norm,max}$ occurring at a higher (but still comparable) position to that of the valve (**Fig. A.18**). This emphasized that the focusing behavior of *CR* valves may not be limited to the diffraction contributions from only all areolae (which have a mesosize), as reported in the relevant literature [129,141], but there is also a significant diffraction contribution from valves' mantle.

In the case of the ***Acto*** valve (of a larger diameter), a distinct focusing spot was observed in the transmittance beyond its hyaline area (of a diameter ≈ 22 µm), as can be seen in **Fig. 5.9**. The spot reached its minimum waist (FWHM≈ 11 µm) and $I_{Norm,max}$ at z_8 (≈ 56 ± 4 µm). Additionally, a pronounced attenuation of the transmitted light intensity by the rest of the valve was observed (**Fig. 5.9**). While in the case of the ***Cosc*** valve (of comparable diameter to *Acto* valve but with different ultrastructure, see **Fig. 5.2**), a substantial attenuation of transmitted light through the whole valve was observed (**section A.14**, **Appendix A**). Nevertheless, a focusing spot of a relatively enhanced I_{Norm} compared to the rest of the valve was observed close to the valve surface (≈ z_0, where FWHM ≈ 2 µm) in the transmittance beyond its hyaline area (of a diameter ≈ 3 µm), which diverged and vanished by defocusing (**Fig. A.19**).

Interestingly, the FWHM of the focusing spots induced by *Acto*, *Cosc*, and *CR* valves seems correlated to the hyaline area width (*i.e.*, FWHM at maximum focusing < hyaline area width), suggesting a significant influence of the hyaline area that could be attributed to the interference of the light transmitted by this area and the diffracted light at its boundaries with the porous rest of the valve.

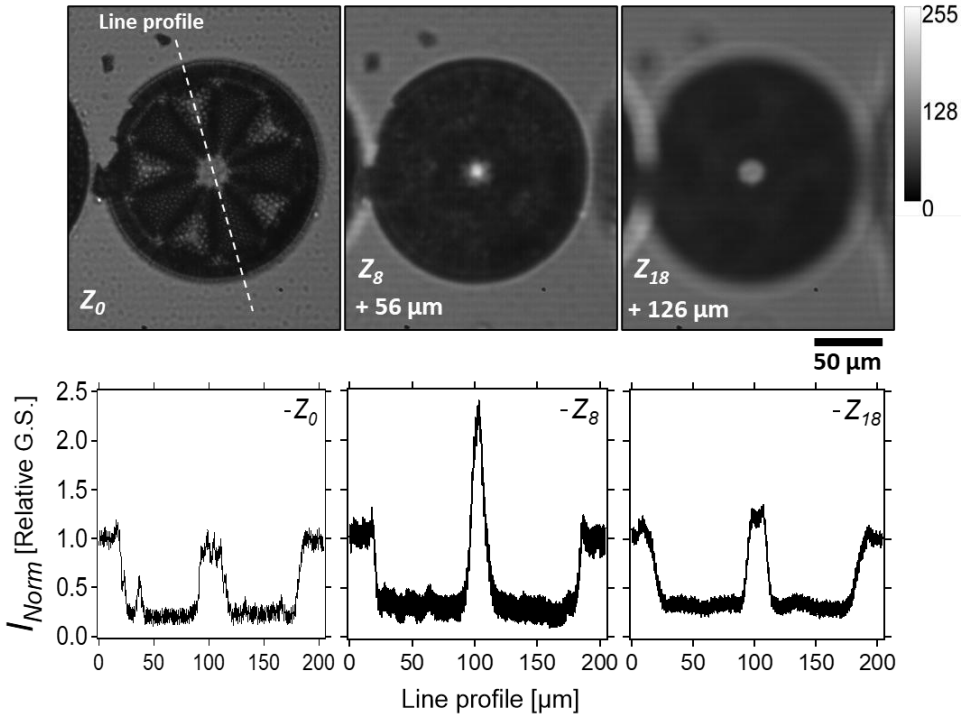

Fig. 5.9. The studied *Acto* valve—showing its inner face upward—as observed under 10x objective at different focal planes z_i (at the top), along with their normalized line profiles (at the bottom). Each step on the ***z***-axis is ≈ 7 ± 0.5 µm.

In sum, when applying the trans-illumination on the studied pennate and centric diatom valves, a pronounced modulation for the transmitted light was induced in all cases with a distinct diffraction-driven focusing behavior. Such behavior could be linked to their size and/or ultrastructure. **To the best of my knowledge**, the diffraction-driven focusing behavior of *GP*, *pinn*, *Did*, *Staur*, *Aula*, *Acto*, and *Cosc* valves has not been reported before in the literature. The focusing behavior of *GP* valves—despite their small size—was revealed and followed to a good extent the observations from the 2D numerical analysis (as demonstrated in **section A.10**, **Appendix A**). The valves of other studied pennates, which have integrated mesosize thicker parts, showed distinct focusing behavior induced mainly by the presence of these parts. The centric valves also showed an ability to induce such focusing behavior behind their hyaline area. The diffraction-driven focusing ability of *Aula* valves has been numerically analyzed, as demonstrated in **section A.12** (**Appendix A**), and the experimental results were in good agreement with the numerical analysis results.

5.3. Light focusing by illuminating valves from the side

All previous studies have investigated light focusing by illuminating diatom valves normal to their surface. To complete the picture and broaden our understanding, this part demonstrates for the **first time** the diffraction-driven light focusing induced by illuminating diatom valves from the side (employing the method described in **subsection 3.3.2**, **Chapter 3**). For this, the valves of four structurally distinct diatom species—two centrics (*CR* and *Aula*) and two pennates (*GP* and *Pin*)—were selected for the study. Additionally, in order to understand the role of the valves' ultrastructure in the observed focusing behavior, the *Aula* valves were selected for further experimental and numerical analysis. The reason for this selection is that the *Aula* valves have an appropriate size compared to the other studied valves, which facilitates their experimental and numerical analysis. Another reason why *Aula* valves are interesting is their successful implementation in several applications as an alternative to artificial sophisticated nanostructured materials, supported by the vast availability of their fossils in the market at low cost. These applications include solar cells [151,296], photocatalysts, sensors, and microfluidic systems [94,95]. Therefore, expanding our knowledge of light modulation by these valves is beneficial and could explain their success in some optical applications and inspire more.

5.3.1. Distinct valves under side-illumination

Under side-illumination, the valves of different studied species exhibited substantial light scattering induced by their ultrastructure and showed an ability to induce diffraction-driven focusing, generating distinct focusing spots/beams, as evident in the examples shown in **Fig. 5.10**. The way the valves of each species focused the light is dependent on their geometry, size, and ultrastructure.

The ***CR*** valves (of diameter 80 – 100 µm ≈ 121 – 152 $\lambda_{max,660}$, when compared to the incident light wavelength $\lambda_{max,660}$) laid on the substrate—showing either the inner or outer face upward—seem to have a large, flat central area. This flat area can be seen as a porous plate of diameter ranging from 30 µm (46 $\lambda_{max,660}$) to 60 µm (91 $\lambda_{max,660}$). The rest of the valve shows a slight curvature increasing toward the mantle, as illustrated in the SEM (**Fig. 5.1a**). By illuminating these valves from the side, the collimated beam reached the curved part and the mantle first, producing pronounced scattering (**Fig. 5.10a**). Moreover, the valves showed a distinct bright spot at the rear side of their outer rim under the 10x objective, which became elongated and more visible at a specific focal plane above the valve on the ***z***-axis (**Fig. 5.10a**). The observed spot was changing its orientation when rotating the light source in the *x-y* plane to follow the direction of the incident light.

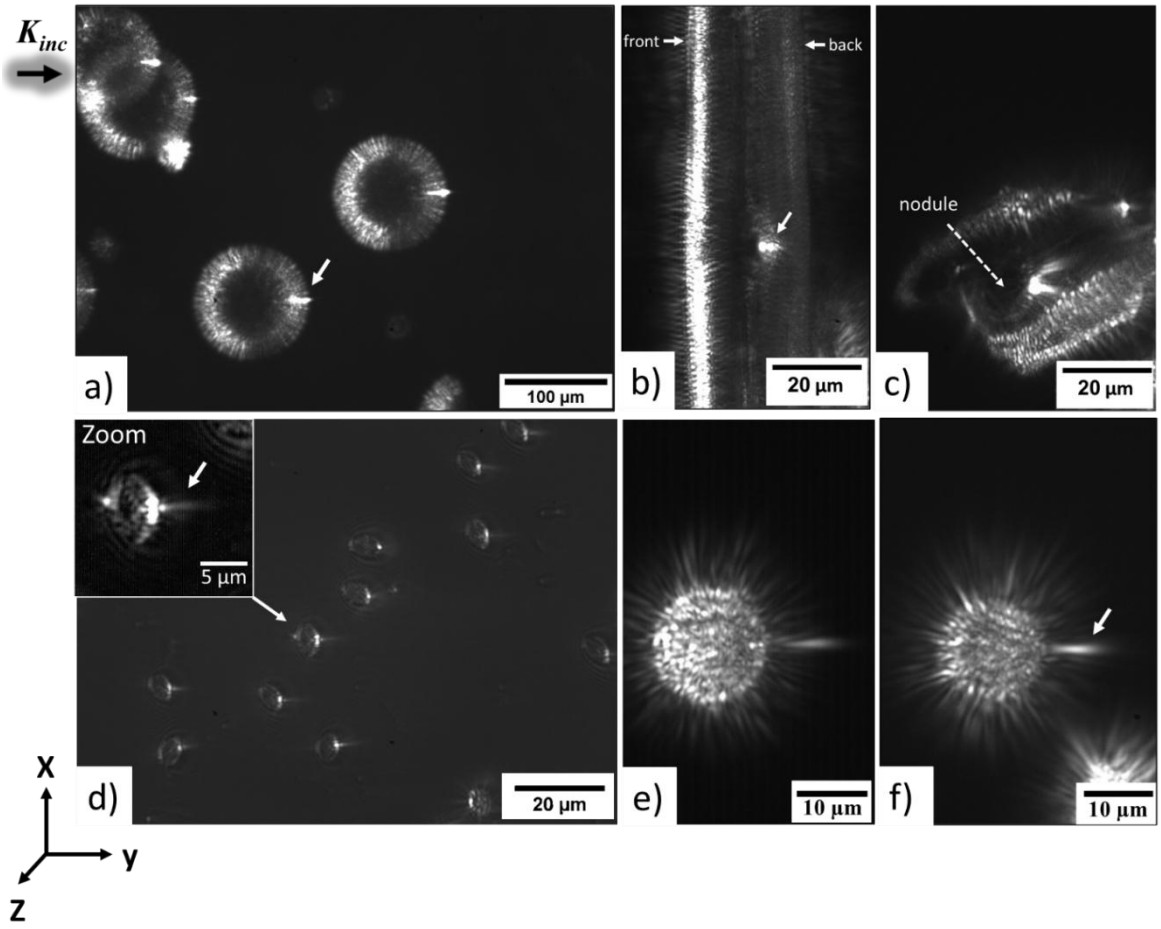

Fig. 5.10. Raw optical micrographs showing the focusing behavior of *CR* (**a**), *Pin* (**b** and **c**), *GP* (**d**), and *Aula* (**e** and **f**) valves under side-illumination, employing red LED (λ_{max} ≈ 660 nm). All micrographs were captured using a 40x objective lens, except (**a**) with a 10x objective. The camera exposure in (**b**), (**c**), (**e**), and (**f**) was the same, while it was increased in (**d**) by 40%. The inset image in (**d**) is a zoom in a single valve with a subtracted background and enhanced contrast to disclose the PJ beam.

The large ***Pin*** valves have a length of 258 – 455 $\lambda_{max,660}$ and a width of 46 – 76 $\lambda_{max,660}$, while the central nodule has dimensions of 11 – 18 $\lambda_{max,660}$. **Fig. 5.10b** shows the interaction of side-illumination with a *Pin* valve having its apical axis perpendicular to the direction of light propagation and its outer valve face upward. The part of the mantle facing the collimated beam caused a shadow effect, leading to a lower scattering at the opposite side of the mantle (**Fig. 5.10b**, front vs. back). Despite the shadow effect, a bright PJ beam appeared at the rear side of the nodule zone (**Fig. 5.10b**), having the same direction as the incident light. This beam was more evident in a cracked part of a valve showing its inner face upward and devoid of the mantle's shadow effect (**Fig. 5.10c**). Moreover, high-intensity spots were observed at the apexes of some valves that could be associated with the apical nodules. However, it should be noted that no focusing behavior associated with the whole valve is observed in the studied field of view.

Fig. 5.10d demonstrates the interaction of side-illumination with the small ***GP*** valves (of length 9 – 12 $\lambda_{max,660}$ and width 7 – 8 $\lambda_{max,660}$). A bright spot was observed at the valves' outline combined with a PJ beam on their rear side. The direction of the generated beam almost followed the incident light direction regardless of the valve's rotation on the substrate but with changes in its length. As illustrated in **Fig. 5.11**, the simulation results of wave propagation across a 2D model (representing the *GP* valve face) agree with the experimental observations. **Fig. 5.11c** shows that when the collimated light beam was parallel to the valve apical axis, the PJ beam was not observed anymore at its rear side but rather shifted to occur inside the valve face—as suggested by the simulations—combined with a faint tail on the rear side. In literature, similar results have been reported for a dielectric elliptical microcylinder [297].

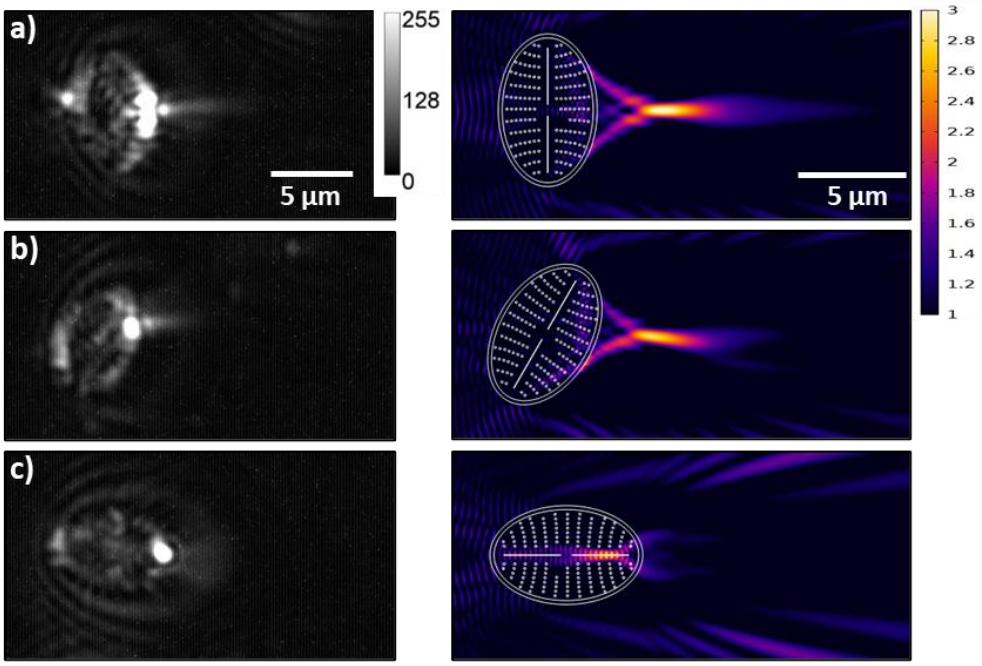

Fig. 5.11. Experimental results show the dependency of the generated PJ length and position on the valve rotation under a *left-hand* side-illumination (λ_{max} ≈ 660 nm). These valves were extracted from **Fig. 5.10d**, the background was subtracted, and the contrast was enhanced to disclose the PJ beam. The associated 2D simulation results for the wave propagation (*in-plane* **E** field) across a 2D model representing the *GP* valve face at λ_{vacc} = 660 nm show comparable results while rotating the 2D model under the same simulation conditions. The color code ranges from black (1 V/m) over purple/red (2 V/m) to yellow (3 V/m), only emphasizing the enhanced field ($\mathbf{E_{Norm}} > \mathbf{E_{input}}$), while the black areas indicate $\mathbf{E_{Norm}} \leq \mathbf{E_{input}}$, where $\mathbf{E_{input}}$ = 1 V/m.

The cylindrical ***Aula*** valves (of diameter 9 – 28 $\lambda_{max,660}$ and height 4 – 9 $\lambda_{max,660}$) showed a distinct diffraction-driven focusing behavior, as the examples shown in **Figs. 5.10e** and **f**. **Fig. 5.12** illustrates an example of observing the focusing behavior of *Aula* valve at different focal planes. For the valve in focus ($\boldsymbol{z_0}$, which in this case is approximately at the middle of valve height), the light seemed confined

within the cylindrical mantle, besides the frequent presence of two brighter spots; one on the rear side of the front wall facing the light source (to partially occur inside the valve) and the other on the back wall (to partially occur outside the valve). The two spots followed the direction of incident light. With defocusing, besides the divergence of the scattered light, the bright spot at the back wall gave a distinct PJ beam at the rear side above the valve, indicated by the white arrow at z_4 (**Fig. 5.12**). This likely means this beam has a curvature upward.

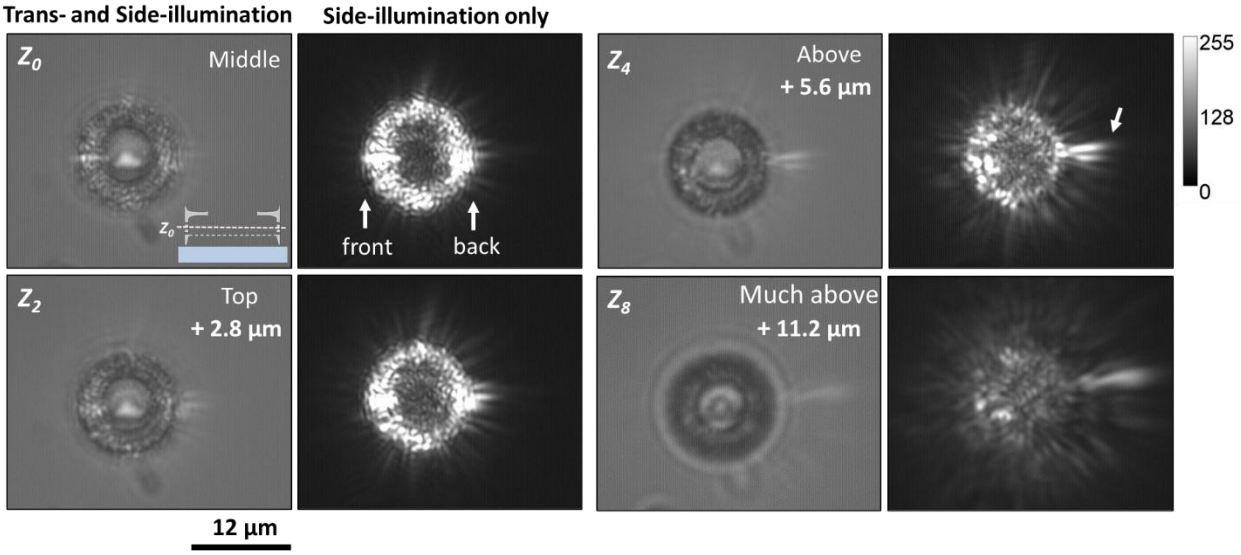

Fig. 5.12. An example of the focal-plane dependence of the observed focusing by *Aula* valves after being illuminated from the side. All micrographs are for the same valve ($2r_v \approx 12$ µm, having its inner valve face upward) illuminated from the *left-hand* side ($\lambda_{max} \approx 660$ nm) without a tilt of the light source ($\Theta_{inc} = 90°$) but at different focal planes ($\boldsymbol{z}_i$). Each step on the $\boldsymbol{z}$-axis is ≈ 1.4 ± 0.1 µm. The intensity scale is a grayscale value only associated with the side-illumination micrographs. The trans-illumination (from the Halogen lamp, 20 W) was employed to visualize the valve position before turning it off to capture the scattered light by the valve upon side-illumination.

In the following subsection, the contribution of the distinct structural features of *Aula* valves to their focusing behavior will be demonstrated while revealing the dependencies of their focusing on the incident light wavelength, valve rotation, and orientation on the substrate.

5.3.2. A deeper analysis of the side-illumination of Aula valves

Before demonstrating the simulation results for the *Aula* valve, let us first consider the case of a dielectric solid microcylinder of the same dimensions as an *Aula* valve but without ultrastructure and without being hollow (**Fig. 5.13a**). In literature, the PJ generation by solid dielectric microcylinders has already been numerically and experimentally studied (*e.g.*, [298,299]). When this microcylinder is illuminated from the side with a collimated beam, previous studies demonstrated that—besides the light scattering—a PJ beam will be generated at the rear side along its optical axis.

The 2D simulations could give a representative illustration of this behavior, as shown in **Fig. 5.13** (assuming an *x*-polarized beam illuminating a 3D microcylinder). The parameters of the PJ beam are expected to depend on parameters such as λ_{vacc} and Δn (see **subsection 4.3.5**, **Chapter 4**), as well as the microcylinder size [299]. The simulation results in **Fig. 5.13b** show the dependency of the PJ generated by $CS_{hor,c}$ on λ_{vacc}. This includes increasing the beam FWHM with increasing λ_{vacc}, concurrently with decreasing the $\mathbf{E_{Norm}}$ strength and the distance between the beam and the CS.

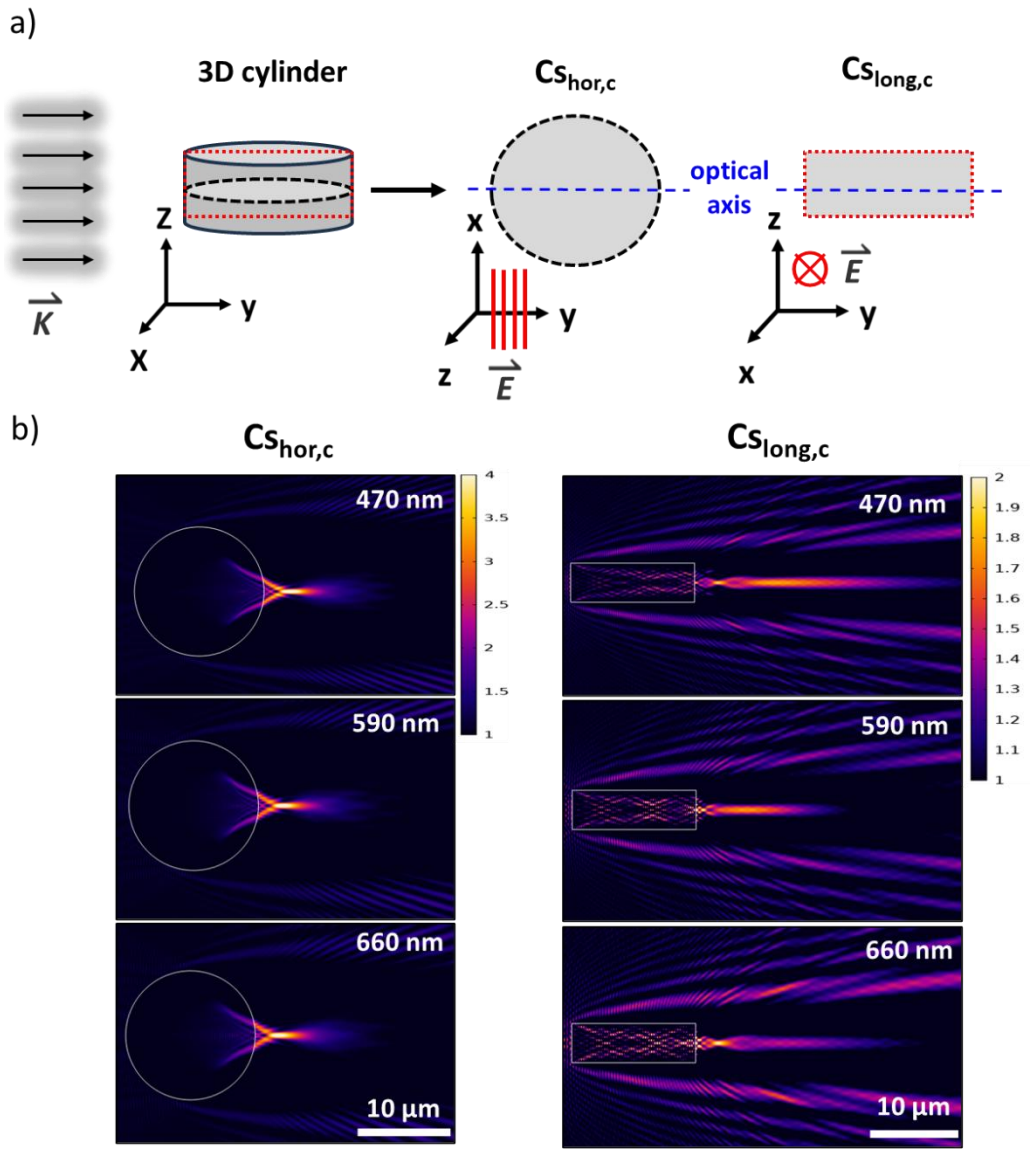

Fig. 5.13. (**a**) A sketch shows the side-illumination of a silica solid microcylinder (of the same dimensions as an *Aula* valve) alongside the extracted CSs. The longitudinal ($CS_{long,c}$) and horizontal ($CS_{hor,c}$) CSs have the same dimensions as $CS_{long,1}$ and $CS_{hor,1}$, respectively. Assuming the incident beam on the 3D microcylinder has *x*-polarization, its electric field component oscillates on the *x*-axis (perpendicular to the *y*-axis, the propagation direction), which means that it oscillates *in-plane* the 2D horizontal CS and *out-of-plane* the 2D longitudinal CS. (**b**) the numerical analysis results of the 2D CSs at different λ_{vacc}. The FWHM of the PJ beam generated by $CS_{hor,c}$ is about 570 nm, 650 nm, or 700 nm for λ_{vacc} 470 nm, 590 nm, or 660 nm, respectively. The color code is given in V/m units.

Back to the *Aula* valve, it can be seen as a hollow microcylinder distinguished by its ultrastructures, such as porosity, spines, and ringleist. Under side-illumination, these ultrastructures are expected to contribute to its diffraction-driven focusing behavior. Such contribution was already evident in the case of trans-illumination (see **section A.12**, **Appendix A**). The 2D simulation results for the side-illumination of *Aula* valve CSs are shown in **Figs. 5.14** and **5.15**, assuming an *x*-polarized beam illuminating the 3D *Aula* valve, where **E** field oscillates *out-of-plane* $CS_{long,i}$ and *in-plane* $CS_{hor,i}$ (similar to the case of solid microcylinder).

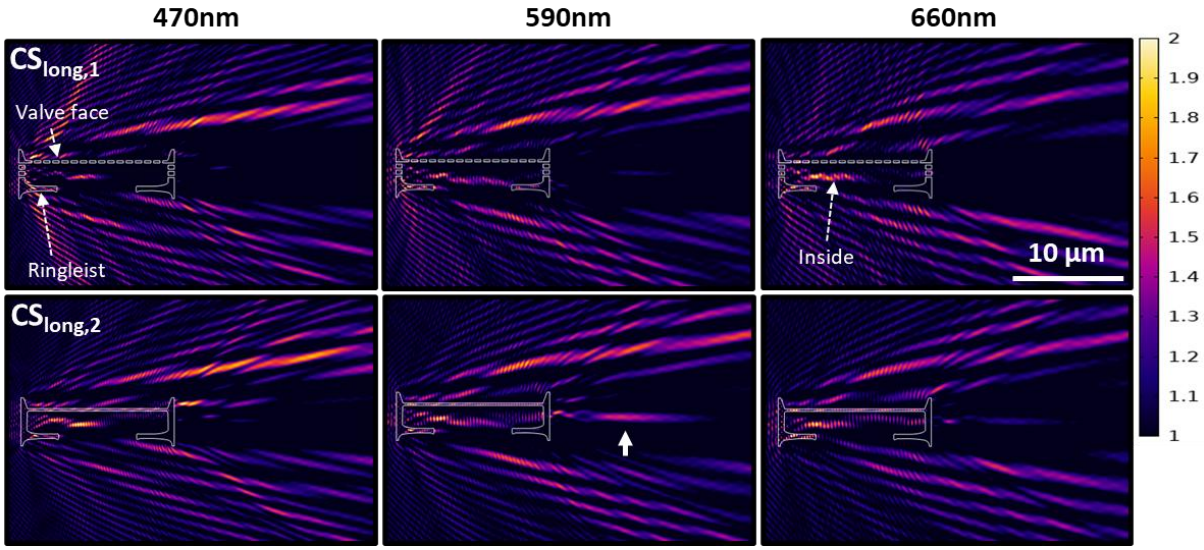

Fig. 5.14. Simulation results for a wave propagation (*out-of-plane* **E** field) across $CS_{long,1}$ and $CS_{long,2}$ of *Aula* valve at three different λ_{vacc} in the air. $CS_{long,i}$ represents *z-y* plane in the 3D valve. The color code is given in V/m units.

The side-illumination of $CS_{long,1}$ and $CS_{long,2}$ yields a complex interference pattern (**Fig. 5.14**). The PJ beam observed at the optical axis of the rear side of $CS_{long,c}$ (**Fig. 5.13b**, right side) becomes unclear at most wavelengths (*i.e.*, undistinguished from the background $\mathbf{E_{input}}$) in *Aula* longitudinal CSs. Alternatively, an intense PJ beam is observed at the rear side of the mantle wall fronting the incident wave (to occur inside the CS), resulting from the interference of inner diffraction fringes, which are formed by the interference of the transmitted wave through the mantle and the diffracted waves by the spines and collum (**Fig. 5.14**). A pronounced enhancement of a few edge diffraction fringes above and below the CSs is also observed. As previously explained in **Chapter 4**, the pattern and intensity of the edge diffraction fringes in such complex structures are influenced by the dimensions and geometry of the edges fronting the illumination source (in this case, the collum and spine edges) and by the waveguiding behavior (in this case, through the porous valve face and ringleist).

In contrast to the longitudinal CSs, the PJ is clearly visible at the rear side of $CS_{hor,1}$ (representing the porous valve face, **Fig. 5.15**), generated by the interference

of the transmitted wave across the CS, and the waves diffracted at its boundaries. The presence of areolae influences this beam by affecting the transmitted wave, which is evident when comparing the pattern and intensity of the beam in the presence (**Fig. 5.15**, $CS_{hor,1}$) and absence of areolae (**Fig. 5.13b**, $CS_{hor,c}$). In the case of $CS_{hor,1}$, the pattern and intensity of this beam show dependencies on λ_{vacc} (**Fig. 5.15**) and CS's rotational angle (see **Fig. 5.16**), which are associated with the presence and symmetry of the areolae. **Fig. 5.16** shows that at λ_{vacc} 660 nm the PJ is mainly generated in the reflectance at specific rotational angles. Such behavior is repeated each 60° when increasing the rotational angle from 0° to 360°, consistent with the expected **six-fold symmetry** of this finite 2D hexagonal photonic crystal. The influence of lattice defects—frequently occurring in the *Aula* valve face—on the rotational dependence of the generated PJ beam at λ_{vacc} 660 nm is demonstrated in **Fig. A.20** (**Appendix A**). It should also be noted that the diameter of $CS_{hor,1}$ influences the generated PJ (see **Fig. A.21**, **Appendix A**), as predicted from the literature.

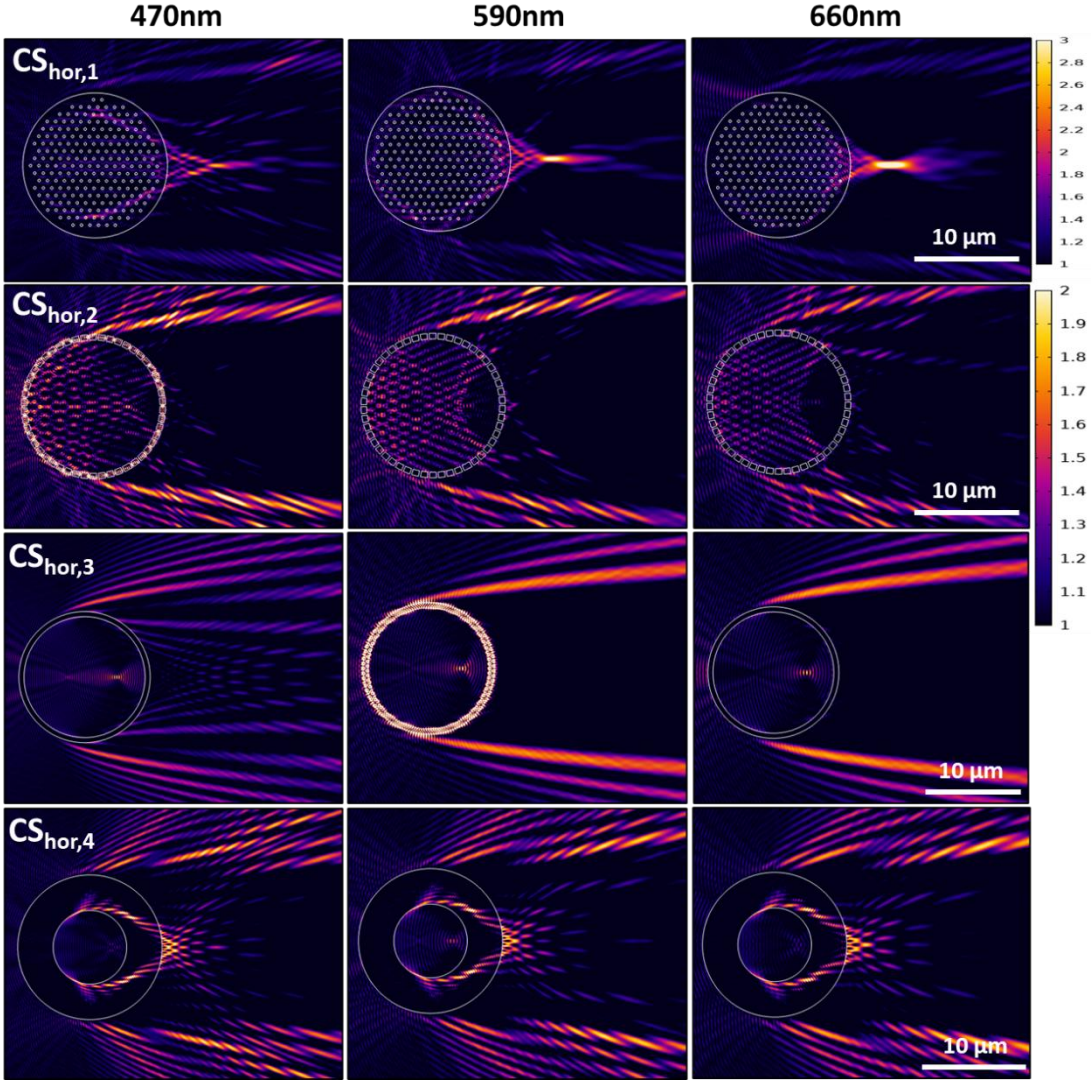

Fig. 5.15. Simulation results for wave propagation (*in-plane* **E** field) across horizontal CSs of *Aula* valve at three different λ_{vacc} in the air. $CS_{hor,i}$ represents *x-y* plane in the 3D valve. The

color code is given in V/m units. The PJ beam generated by $CS_{hor,1}$ is more pronounced at λ_{vacc} = 660 nm and is substantially reduced at λ_{vacc} = 470 nm.

Moreover, $CS_{hor,4}$ (representing the ringleist) does not show a PJ beam; however, it shows bright diffraction-driven spots at its rear side at different λ_{vacc} (**Fig. 5.15**), resulting from the interference of the transmitted wave by the CS (which influenced by the presence of a hollow area filled with air at its center) and the diffracted waves at the boundaries.

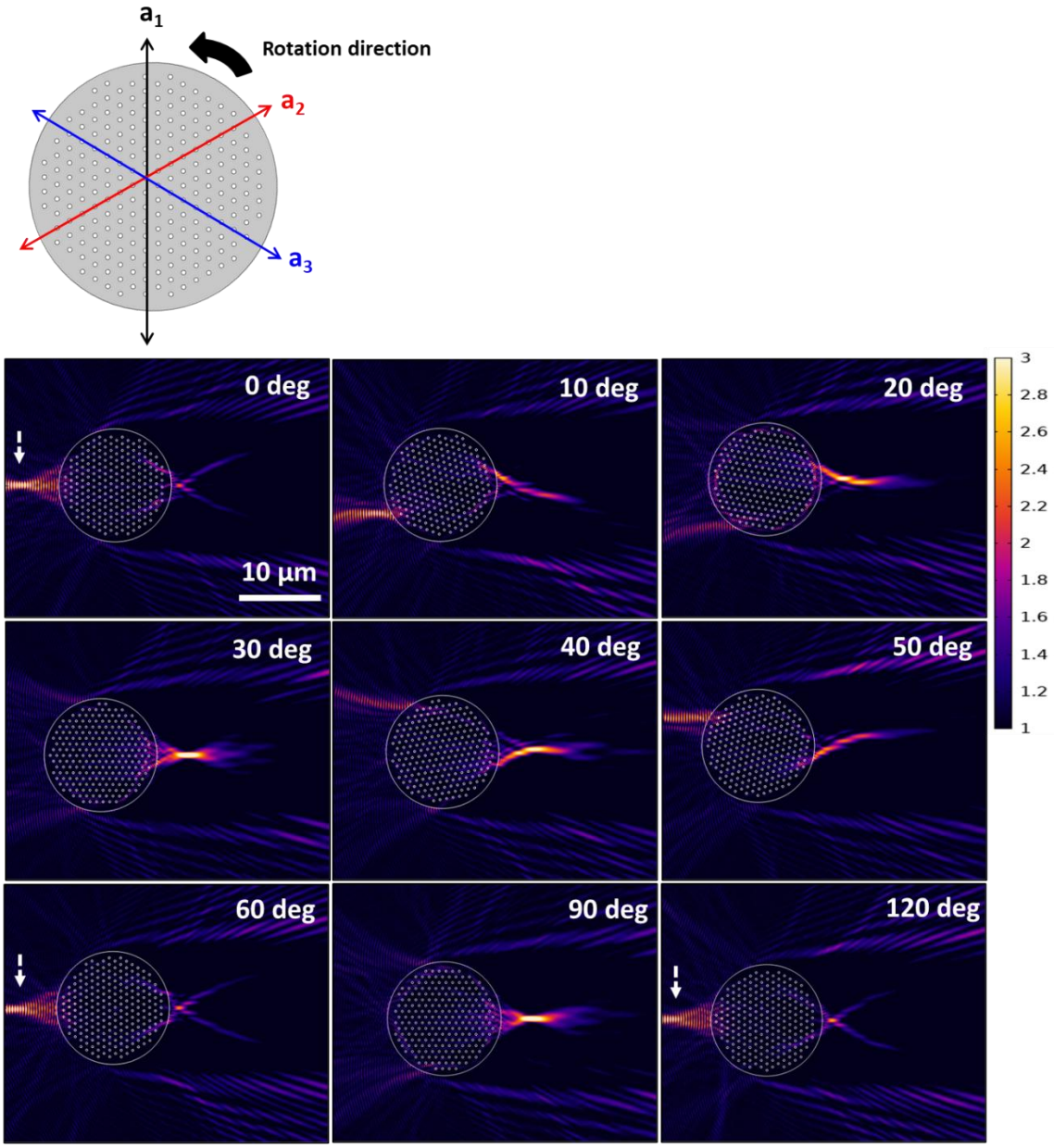

Fig. 5.16. Rotating the lattice planes ($\mathbf{a_1}$, $\mathbf{a_2}$, and $\mathbf{a_3}$) of $CS_{hor,1}$ at λ_{vacc} 660 nm (*in-plane* **E** field) in air causes changes in the position and intensity of the generated PJ beam. The white arrows indicate the formation of a PJ beam mainly in the reflectance each 60°. The color code is given in V/m units.

Furthermore, the interference patterns of $CS_{hor,2}$ and $CS_{hor,3}$ (representing the mantle) also do not show a PJ at their rear side (**Fig. 5.15**). The diffraction-driven focusing spots observed at the rear side of $CS_{hor,3}$ are not bright and become unclear (< $\mathbf{E_{input}}$) at most wavelengths. Interestingly, a small focusing spot is observed inside $CS_{hor,3}$ but opposite to the rear side. It is also worth mentioning that the presence of areolae within $CS_{hor,2}$ produces a grid-like structure that (i) increases scattering, (ii) induces a Talbot interference pattern inside the CS (**Fig. 5.15**), and (iii) is expected to enable guided-mode resonance (GMR) to couple the light at specific ranges of λ_{vacc} into the cylindrical structure, which is not investigated in this chapter.

From the simulation results, we can conclude that if an *Aula* valve is embedded in a homogenous medium (*e.g.*, suspended in air) and illuminated from the side, a diffraction-driven focusing (likely a PJ beam) will be induced inside the valve at the rear side of the mantle's front wall, similar to the observations in **Fig. 5.14**. A PJ beam is also expected at the rear side of the mantle's back wall, with significant contributions from the porous plate and ringleist, which terminate the outer and inner valve faces, respectively. Nevertheless, the influence of edge diffraction at the spines or collum facing the collimated beam, as well as the waveguiding behavior of the porous plate and ringleist, will lead to changes in the beam profile and exact position.

In the experiment, the valves were laid on a substrate, which is expected to affect their edge diffraction fringes (and likely the diffraction-driven focusing behavior) if compared to the valves suspended in a homogenous medium. Even the orientation of the valve on the substrate (having either the inner or outer valve face fronting the objective) is expected to produce a different response to the side-illumination, which was confirmed in the experimental results (see the examples shown in **Fig. 5.17**).

From the experimental results, when the outer valve face was upward (*e.g.*, **Fig. 5.17a**), the PJ beam—observed at an estimated position around z_4—showed similar results to the simulation results of $CS_{hor,1}$, where the beam was more pronounced at λ_{max} 660 nm and much reduced at λ_{max} 470 nm. When the inner valve face was upward, such changes to the PJ beam were not observed. This behavior was reproducible among different valves, as can be seen in **Fig. 5.17b** for the case of the blue LED. In both orientations, the beam seemed curved upward. It seems that the PJ generated by the outer valve face (or inner face ringleist) merged with the edge diffraction fringes above the valve (as suggested by the simulation results of $CS_{long,1}$ and $CS_{long,2}$) to yield the experimentally observed PJ beam.

At z_0, the bright spot observed at the front wall of the valve at different LEDs (*e.g.*, Fig. **5.17a**, indicated by the blue arrow) is likely associated with the inner diffraction-driven focusing shown in the simulation results of $CS_{long,1}$ and $CS_{long,2}$ (see

Fig. 5.14). Nevertheless, the experimentally observed spot might also be a result of backscattering.

Additionally, some rare experimental observations (see **Fig. A.22**, **Appendix A**) showed the PJ mainly in the reflectance, while in other few cases, the obtained PJ seemed tilted or emerging from a different place. Such observations might support the numerical analysis results shown in **Fig. 5.16**, despite the imperfections and defects that is present in the real *Aula* valve compared to the perfect hexagonal lattice of $CS_{hor,1}$. In general, the observed rotational and wavelength dependencies could be evidence of the PC features (specifically the presence of a pseudo bandgap) of the *Aula* valve face; however, further investigation is required to confirm that.

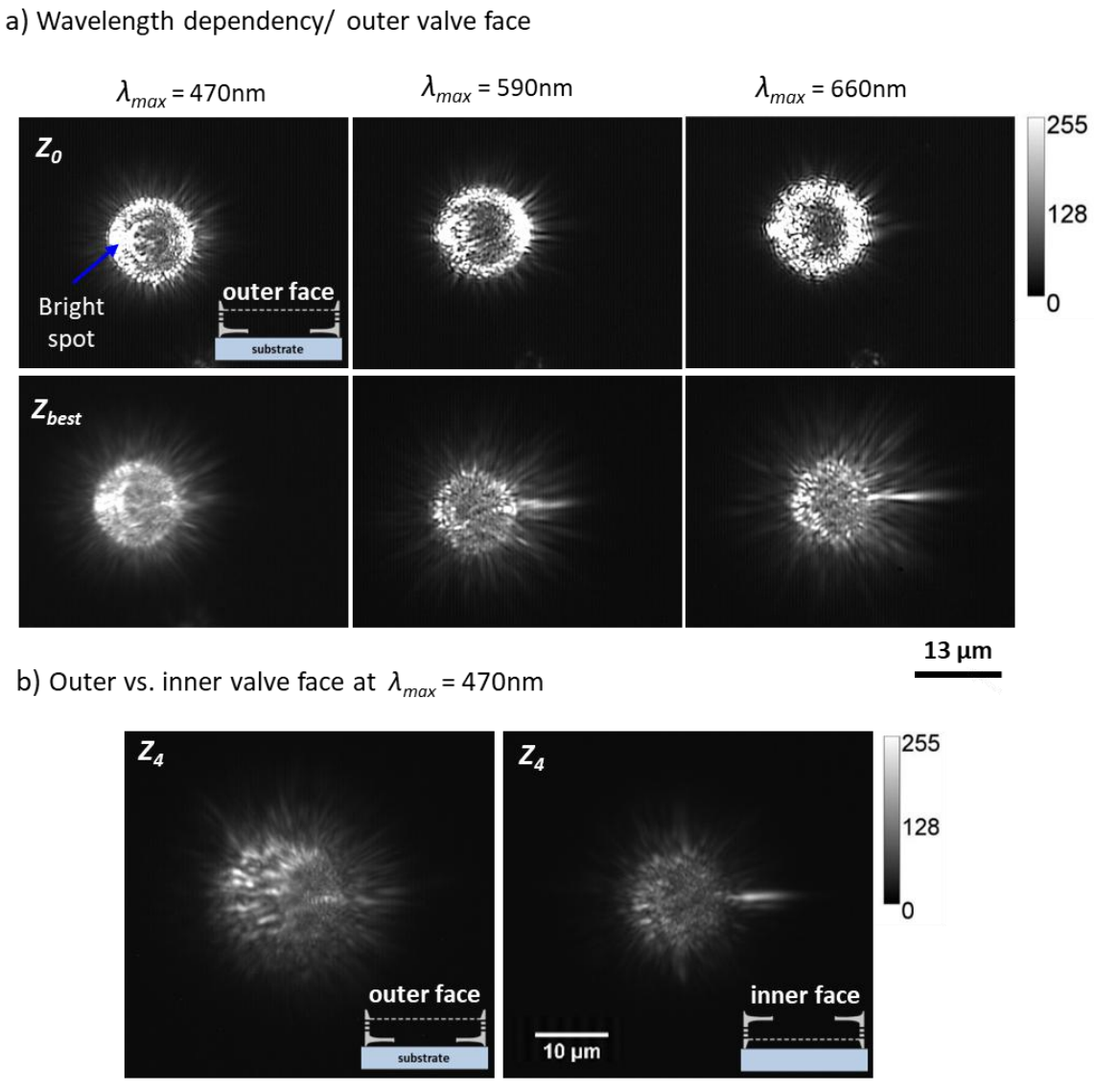

Fig. 5.17. (**a**) Experimental results show the influence of λ_{max} (by using three different LEDs) on the diffraction-driven focusing behavior of an *Aula* valve ($2r_v$ ≈ 13 µm, having the outer valve face upward, selected as an example) under *left-hand* side-illumination. $\boldsymbol{Z_{best}}$ is estimated to be around $\boldsymbol{z_4}$. (**b**) Experimental results show the focusing behavior of two different *Aula* valves having different dimeters ($2r_v$ for the left valve ≈ 17.3 µm and the right

valve ≈ 13.7 µm) and orientations, both illuminated by the blue LED. z_4 is about 5.6 ± 0.4 µm above z_0 on the z-axis.

5.4. Further discussions

Generally, the obtained results—If added to the observations demonstrated in **Chapter 4** as well as the literature (see **subsection 1.2.4**, **Chapter 1**)—support the assumption that diffraction-driven light focusing could be a more widespread phenomenon among diatom genera and species than thought before. From the results, it can be concluded that when the whole valve is in the mesosize range (relative to the incident light λ), it could induce diffraction-driven focusing behavior, regardless of light source direction (*i.e.*, if illuminated from the side or normal to its surface), as in the case of *Aula* (see **Fig. 5.8** and **subsection 5.3.2**) and *GP* (see **Fig. 5.4** and **Fig. 5.11**) valves. Such a conclusion can be extended to the frustules. If the whole frustule is in the mesosize range, it could also induce such focusing behavior (see, for example, the simulations of *GP* complete frustule in **Chapter 4**).

Moreover, regardless of the valve/frustule size, the diffraction-driven focusing could also be induced by various integrated mesosize ultrastructural features, including the presence of thickened areas within the valves of some pennates, such as the stauros or nodules, as the examples shown in **Figs 5.5** – **5.7** (under trans-illumination) and **Figs. 5.10b**–**c** (under side-illumination).

Furthermore, in the case of large centric valves (*CR*, *Acto*, *Cosc*) with a hyaline area (which is a nonporous, not necessarily thicker area, and of mesosize), the interference pattern and the diffraction-driven focusing seems more complicated with multiple diffraction contributions. For example, the focusing behavior of *CR* valves under trans-illumination (**Fig. A.18**, **Appendix A**) could be attributed to the complex interference of the light transmitted through the valve—maximized at its hyaline area—and light diffracted by the mesosize areolae, valve's mantle, and its mesosize hyaline area's boundaries. While under side-illumination (**Fig. 5.10a**), the focusing behavior may be further affected by a complex waveguiding behavior across the flat and curved parts of the valve.

The experimental techniques employed in this chapter successfully enabled the revealing of the diffraction-driven light focusing behavior induced in the Fresnel zone of diatom valves. In future, these techniques could facilitate screening valves of many diatom species for application purposes. However, some constraints should be considered. Spatially resolving fine features of the interference pattern depends on the objective (magnification and diffraction limit), the image sensor, and imaging parameters (such as exposure and gain) used.

It should be noted that the grayscale camera, while being effective, cannot provide spectral information in the trans-illumination study. Therefore, introducing

micro-spectroscopy to the experimental setup would reveal the spectral information of the transmitted light. It is also worth noting that the tungsten-halogen lamp utilized in the trans-illumination study could be replaced by a monochromatic light source (or employing optical filters, as has been carried out in [139]) to study the dependency of the focusing behavior on λ, when necessary. Additionally, the 3D reconstruction of the obtained 2D micrographs (considered as consecutive 2D slices across the interference pattern on the ***z***-axis) could also be carried out to retrieve and visualize the full interference pattern in transmittance, similar to what has been done in [135,137].

The following subsections discuss the relevance of the light-focusing capabilities of diatom valves to applications (**5.4.1**) and diatom frustules to the photobiology of living cells (**5.4.2**).

5.4.1. The relevance to applications

Focusing light on the microscale is vital for developing and miniaturizing optical devices, such as imaging systems [170]. Seeking that, different types of microlenses [169], mesosize structures [189] (especially microspheres and microcylinders), and metalenses [170,171] have been fabricated and utilized. For a range of applications (for instance, the fabrication of optical devices and integrated photonic circuits), diatom valves could offer a promising eco-friendly, cost-effective alternative to artificial structures. Such valves can be utilized in applications either separated (*e.g.*, to be fixed on an optical fiber or a specific position on a photonic circuit) or by constructing an array of valves comparable to the fabricated arrays of microlenses [169,300].

The pennate valves with integrated mesosize structures, as well as the centric valves with hyaline area, could be promising for applications to focus light under trans-illumination. Moreover, the presence of consecutive focusing spots on the ***z***-axis, as in the case of *Aula* valves (*e.g.*, **Fig. 5.8** and **section A.12**), enables utilizing such valves in optical switching, as has been suggested for the valves of *Coscinodiscus granii* by Maibohm *et al* [133]. While the mesosize valves (such as *GP* and *Aula* valves), which generate PJ beam at their rear when illuminated from the side, could be promising for some applications, such as coupling the light at a specific position in a photonic circuit. Nevertheless, the influence of waveguiding, especially in valves having pore arrays with potential PC features (such as the *Aula* valves), should be considered.

In general, the diffractive nature of this focusing would lead to chromatic aberration under white light illumination (see **Fig. 2.5b**, **Chapter 2**), which should be considered in applications. Additionally, the influence of competing optical phenomena in the Fresnel zone (such as the Talbot effect, as discussed for the *GP*

valve in **Chapter 4**) should also be considered when selecting a valve for a given application that employs a defined spectral range.

5.4.2. The relevance to photobiology

In the literature, some photobiological roles of diatom frustules have been hypothesized (see **subsection 1.2.6**, **Chapter 1**). One of the hypothesized functions is their ability to induce diffraction-driven focusing for the photosynthetic active radiation (PAR) inside the living cells (close to chloroplasts), hence improving the photosynthesis efficiency [139–141]. That is often suggested combined with having different mechanisms to shield from harmful UV radiation, high intensity, as well as excess energy dissipation [36,37,139,156], which simultaneously help minimize photoinhibition. Moreover, as already hypothesized in **Chapter 4**, the assumed photobiological roles are not only limited to the photosynthesis process but also might be involved in light sensing and signalling mechanisms. Here, a light-sensing mechanism in pennates is proposed based on the results obtained in **Chapter 4** and this chapter (see below).

It should, however, be noted that experimental studies are required for the complete frustules, with living cells inside and immersed underwater, to validate different hypotheses and assumptions. This would help to find out (i) whether the focusing behavior is still present in the case of living cells (which have additional organic layers lining the frustule from both inner and outer faces [57,103]), (ii) the localization of the focusing spots with respect to the living cell (inside and outside the cell), (iii) the possible presence of photoreceptors capable of sensing such focusing behavior, and finally (iv) the biological functions that might be regulated as a result of such light sensing.

A hypothetic light-sensing mechanism in pennates

The diatom living cells—like any living organism—can sense the surrounding environmental conditions and respond to different physical and chemical signals [44,301]. Light is a crucial factor affecting diatom growth and physiology as being photosynthetic microorganisms. Therefore, diatom living cells are expected to have photoreception mechanisms, sensing the light and its spectral composition. Different photoreceptors have already been identified through proteomic and genomic studies in diatoms, including Cryptochromes, Phytochromes, Aureochromes, and Rhodopsins [302]. Some of these photoreceptors were transferred to diatoms (from different ancestors) during evolution as they are also found in other living organisms, including plants and bacteria, while some of them are unique for diatoms [302].

Interestingly, the identified types of photoreceptors could cover the solar spectrum (see Figure 1 in [302]) and probably help regulate different physiological

processes (see, for example, Table 1 in [302]). Many of these photoreceptors are found located inside the chloroplast, the nucleus, or free in the cytosol (*i.e.*, the cytoplasm free of organelles), except for Rhodopsins that are often found integrated with cellular membranes, including plasma membranes [302]. It should be noted that, among other diatom photoreceptors, studies on Rhodopsins are scarce, and their mode of action or localization inside diatom living cells, as well as their abundance in different diatom genera/species, remain unknown [302].

As can be understood from the simulations results of *GP* complete frustule (see **section 4.4**, **Chapter 4**), the presence of the nodules or other integrated mesosize structures within pennate valves would lead to the occurrence of pronounced PJ inside the living cells associated with these structures, which would also follow the direction of incident light (**Fig. 4.20a**, **Chapter 4**). Moreover, the simulation results demonstrated in **section A.16** (**Appendix A**), suggested that the strength of the generated PJ—although being attenuated underwater—can be tuned and increased at visible light wavelengths by increasing the thickness of these mesosize structures.

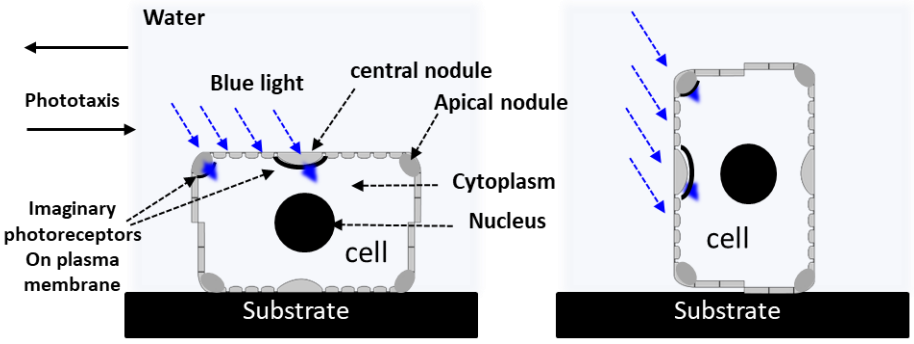

Figure 5.18. A sketch showing a pennate cell (2D CS in a *GP* frustule is used here as a model, but with adding the apical nodules) in two different orientations. The light, regardless of its direction, could generate a PJ beam at the central and apical nodules. The generated PJ beam might be perceived directly by the photoreceptors in the nucleus/chloroplast/cytosol or, instead, an imaginary network of photoreceptors (specifically Rhodopsins that could sense blue-green wavelengths [302]) present on the plasma membrane.

Fig. 5.18 sketches an example of the proposed PJ-based sensing mechanism for the light direction and probably the spectral information, which might give the cells the ability for primitive vision. The generated PJ beam could affect both the optical near-field in positions adjacent to the valve (influencing photoreceptors that may be arranged on the plasma membrane of the cell, such as Rhodopsins) and Fresnel zone inside the cell (influencing photoreceptors that may present in chloroplast, nucleus, or cytosol). The proposed mechanism is comparable to the mechanism suggested for the spherical cells of cyanobacterium *Synechocystis* sp. [293,294]. The illumination of these cells generates PJs at the shadow-side, which are perceived by a hypothesized well-distributed network of photoreceptors fixed on

the plasma membrane, triggering a cellular signal transduction cascade ending by the flagella movement toward or outward the light (see Figure 5 in [293]). However, unlike *Synechocystis* sp., the motility in raphid pennate diatoms is not involving a flagellum but rather gliding motility through the secretion of mucilage from the raphe slits [303,304]. The hypothesized sensing mechanism might help to explain the regulation of mucilage secretion through the raphe fissure and, hence, the phototaxis (*i.e.*, light-induced movements [44,304]) in pennates, which involves a signal transduction pathway that is still unknown [303].

6 Optical near-field measurements for diatom valves

In the literature, the optical near-field of the valves of pennate diatom *Nitzschia filiformis* and centric diatom *Cyclotella* sp. have been recently experimentally studied using a-SNOM setup operated in the illumination mode [126,305–307]. This mode may provide information regarding the coupling efficiency of the evanescent field emanating from the nanoaperture of the SNOM probe to the valve. Still, the collection mode could offer valuable information unparalleled in the illumination mode (as mentioned in **section 2.5**, **Chapter 2**), and it has not been used yet in the literature to study the optical near-field of diatom valves.

In this chapter, the optical near-field of *GP* and *Aula* valves was experimentally studied, employing a-SNOM in both illumination and collection modes, as demonstrated in **section 3.4** (**Chapter 3**). Moreover, the experimental results were compared to the 2D numerical analysis results where possible. Detailed geometrical descriptions of *GP* and *Aula* valves are already provided in **Chapters 4** and **5**, respectively. It should, however, be noted that *GP* valves studied here belonged to a subculture of the same strain (see **Fig. A.10**, **Appendix A**).

6.1. SNOM measurements of GP valves

The SNOM images in **Fig. 6.1** reveal the optical near-field interference patterns at the outer face of a selected *GP* valve in illumination and collection modes. The shear force image (**Fig. 6.1a**) shows that the outer valve face is almost planar with curvature at the edges, as expected from the FIB-SEM and SEM analysis carried out in the previous study (**Chapter 4** and Ghobara *et al.* [261]). It should, however, be noted that there was a remnant of organic debris over this valve.

The interference pattern appeared at green laser (λ_{exc} = 532 nm) showed more features per length scale compared to that was observed at NIR laser (λ_{exc} = 808 nm) (**Figs. 6.1b**-**c** *vs.* **Figs. 6.1d**-**e**). At first glance, both illumination and collection modes seemed to have the same interference pattern; however, the collection mode showed distinct features at green laser. In both cases, there was a dark contour (indicating an attenuation of the transmitted light intensity) surrounding the valve, associated with the mantle position, and alternating with a bright contour at the edge of the valve face. In the case of NIR, another pronounced dark contour was

observed inside the valve face (**Figs. 6.1d**-**e**). Interestingly, additional bright rings—of subwavelength features—alternating with darker ones were observed at the valve face in the collection mode at green laser (**Fig. 6.1c**). This pattern was likely associated with the evanescent component of guided waves inside the valve face. In the case of illumination mode, a similar pattern can be seen, but not clear (or hazy), which can be associated with the waves scattered at the valve face and not the evanescent component, as this mode, unlike the collection mode, cannot provide information regarding the evanescent waves at the surface (**Fig. 6.1b**).

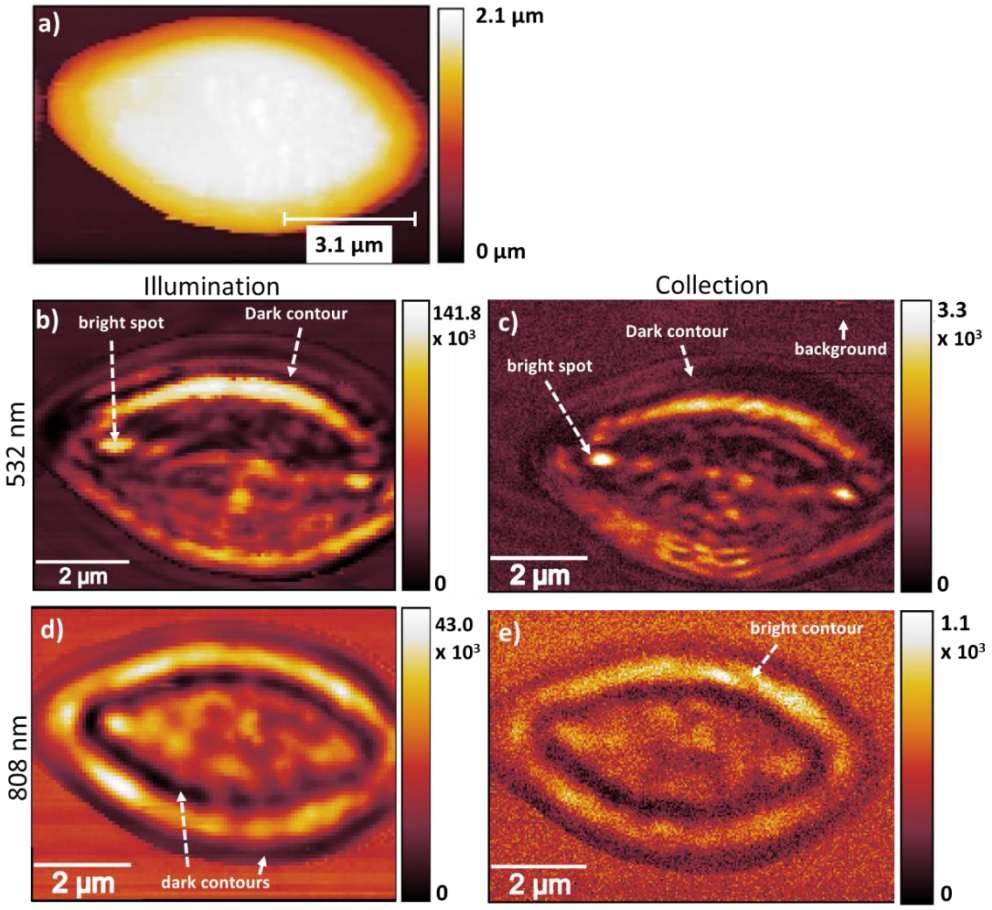

Fig. 6.1. SNOM shear-force image of a *GP* valve showing its **outer face** upward (**a**). SNOM optical images showing the optical response of this valve at green laser in illumination (**b**) and collection (**c**) modes, and at NIR laser in illumination (**d**) and collection (**e**) modes. The intensity scales are given by integrated counts. The length scale bars have an estimated error up to ± 10%. The raw SNOM images were acquired by Professor Paul Fumagalli.

Fig. 6.2a shows the analysis of what seemed like guided waves, which were not clear across the whole valve face. The intensity of the bright fringes was damping toward the valve center, and the spacing between the bright fringes $\boldsymbol{d_{fr}}$ was about 260 ± 20 nm (equals about $\lambda_{exc}/2$). The position of the bright fringes likely does not match the striae position, which has a row of areolae with a spacing $\boldsymbol{d_a}$ of 214 ± 8 nm (see **Table 4.1**), but rather the ribs (see **Fig. A.25**, and further **Fig. A.30**, **Appendix A**).

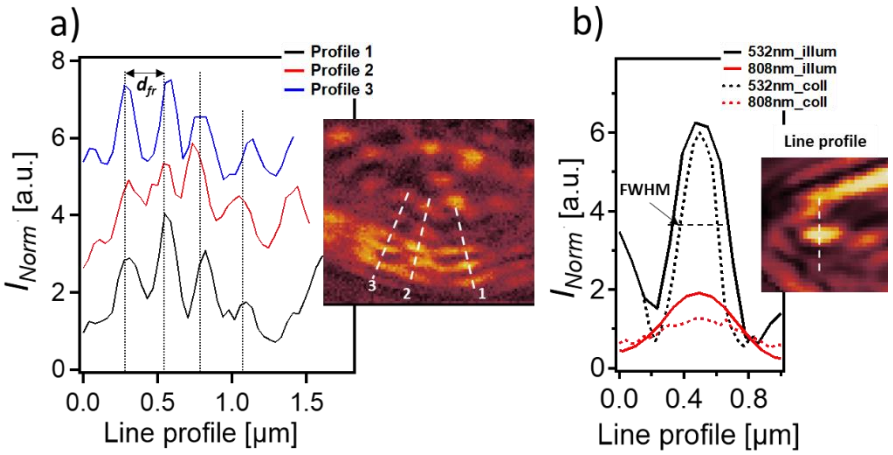

Fig. 6.2. (**a**) The normalized line profiles of the interference pattern that appeared in the collection mode at green laser. The normalized intensity for profile 2 is shifted by 2 units, and for profile 3 by 4 units to visualize them. (**b**) The normalized line profile extracted from the bright spot at different modes and laser wavelengths. The insets in (**a**) and (**b**) show the position of line profiles in the optical images.

Moreover, at green laser, two bright spots were observed close to the valve's apexes, which became unclear in the case of NIR. **Fig. 6.2b** shows line profile analysis of the observed spots. At green laser, these bright spots had a **subwavelength FWHM** of 327 ± 6 nm in illumination mode and 233 ± 18 nm in collection mode. Interestingly, these two bright spots were also observed in the far-field results (see **Fig. 5.4a**, green arrows at $\mathbf{z_0}$) and could likely be correlated with the increased thicknesses at the valve apexes (**Fig. A.25**, **Appendix A**), which may indicate the presence of apical nodules.

Fig. 6.3 demonstrates SNOM optical images in illumination and collection modes of a selected *GP* valve with its **inner face** upward, as elucidated from its shear force image (**Fig. 6.3a**). The girdle band was still attached to this valve. The shear force image shows a variation in the inner valve face thickness (**Fig. 6.3a**) as expected from FIB-SEM analysis (see, *e.g.*, the 3D reconstructed valve in **Fig. A.25**, **Appendix A**). The Nodule zone has a higher thickness, followed by the sternum area and ribs, respectively.

Also in this case, the interference pattern that appeared at green laser showed more features per length scale compared to that observed at NIR (**Figs. 6.3b-c** *vs*. **Figs. 6.3d-e**), the same observation as the outer valve face. At this orientation, the SNOM optical images of both illumination and collection modes had a similar interference pattern with no significant difference. At green laser, the dark contour, previously observed at the outer face and associated with the mantle (**Fig. 6.1**), was reduced here (**Fig. 6.3**). Alternatively, the ribbed structure of the mantle (see **Fig. A.25**) was preserved in the optical images (**Figs. 6.3b-c**). At NIR laser, dark/bright contours were still observed (**Figs. 6.3d** and **e**), while the mantle ribbed structure was suppressed.

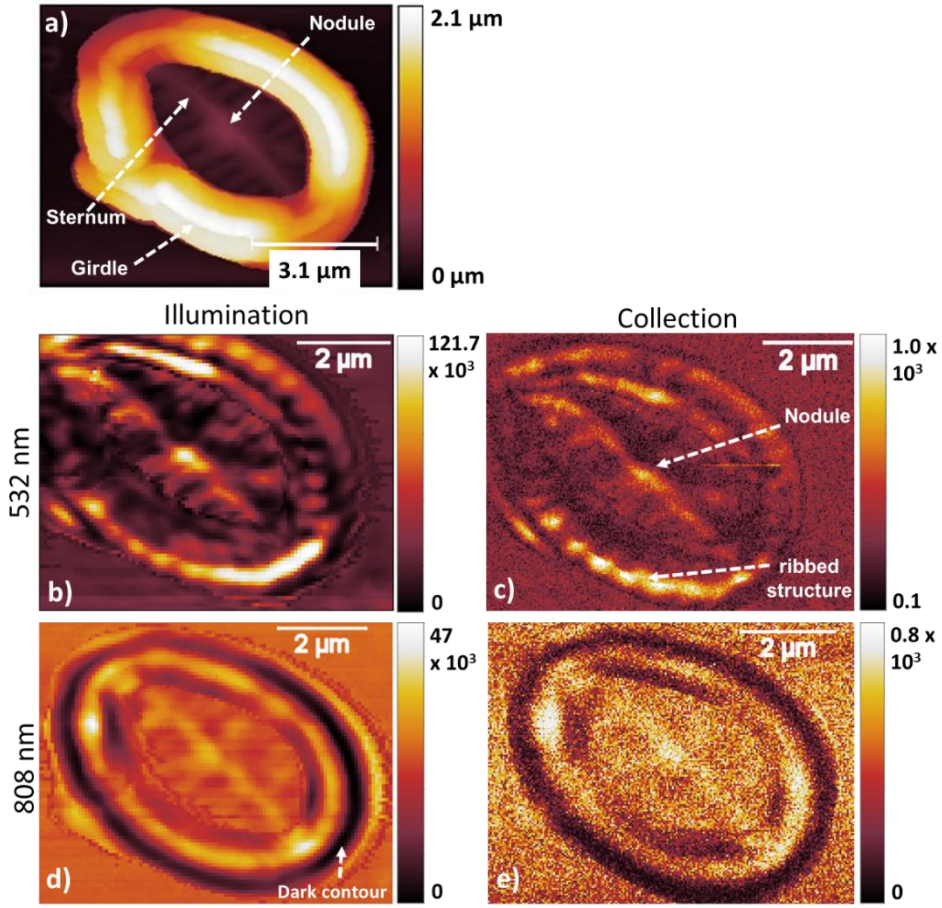

Fig. 6.3. SNOM shear-force image of a *GP* valve showing its **inner** face upward (**a**). SNOM optical images showing the optical response of this valve at green laser in illumination (**b**) and collection modes (**c**), and at NIR laser in illumination (**d**) and collection modes (**e**). The intensity scales are given by integrated counts. The length scale bars have an estimated error up to ± 10%. The raw SNOM images were acquired by Professor Paul Fumagalli.

Moreover, at both green and NIR lasers, an enhancement was observed along the sternum, with an increased intensity at the central nodule zone (**Fig. 6.3**). **Fig. 6.4a** shows the line profile analysis at nodule zone at different modes and laser wavelengths. The observed enhancement was associated with the PJ generation induced by the sternum and nodule zone. In the far-field results (**Chapter 5**), the enhancement associated with the sternum and nodule zone of *GP* valves was also observed starting from the valve face (see z_0 in **Fig. 5.4**).

Furthermore, the valve ribs were preserved in the optical images at the green laser, especially in the illumination mode **(Fig. 6.3b)**. This feature was more evident in another valve imaged under similar conditions (**Fig. 6.4b**). That means at this orientation the transmitted light through a rib was higher than that transmitted through a stria (i.e., a row of pores), as demonstrated in **Fig. 6.4c**. Similar results were reported in D'Mello *et al.* [126]. Interestingly, no guided waves were observed at the inner valve face in the collection mode (**Fig. 6.3c**). The bright spots at the valve's apexes were also observed from the inner face and were more visible at NIR laser (**Figs. 6.3d-e**).

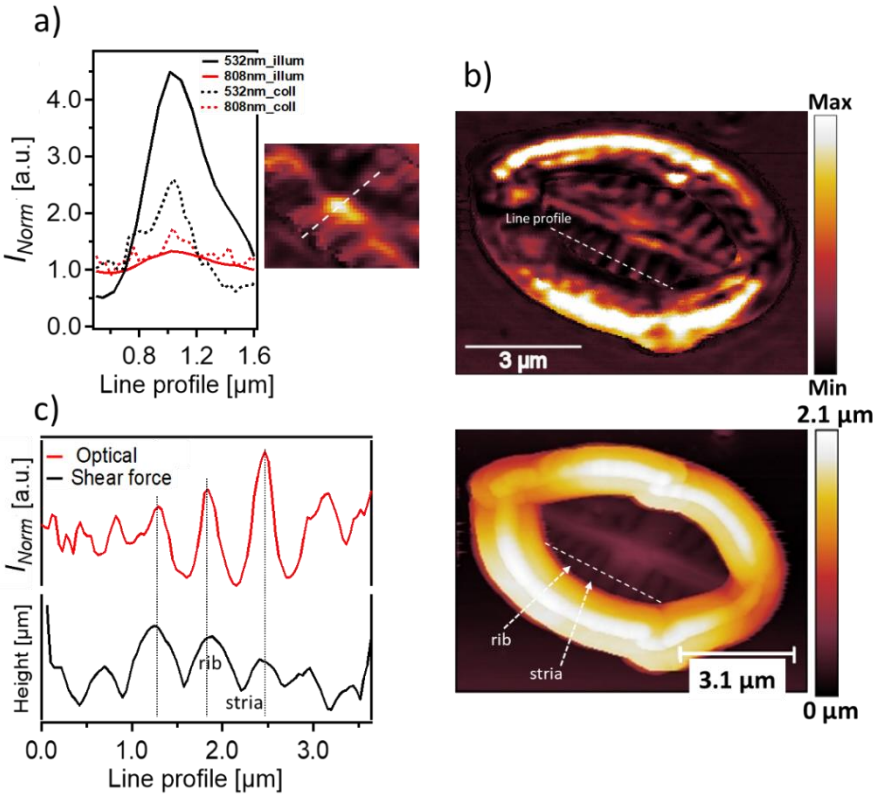

Fig. 6.4. (**a**) The normalized line profile extracted from the bright spot at the nodule zone at different modes and wavelengths. The inset in (**a**) shows the line profile. (**b**) SNOM optical image showing the optical response of another *GP* valve showing its inner face upward at green laser in the illumination mode (at the top) and its shear force image (at the bottom). The length scale bars have an estimated error up to ± 10%. (**c**) the extracted line profiles at the same position—illustrated in (**b**)—from the optical and shear-force images. The raw SNOM images were acquired by Professor Paul Fumagalli.

6.1.1. Numerical analysis of the illumination mode

Due to the mechanism of generating images in the illumination mode (briefly explained in **section 2.5**, **Chapter 2**), the numerical analysis of this mode is not straightforward and cannot be fully simulated using the approach described in **section 3.2.5** (**Chapter 3**). Nevertheless, this approach could still approximate how the SNOM probe in the illumination mode interacts with different parts of a *GP* valve.

The simulation results demonstrate that the *GP* CSs could induce distinct interference patterns when illuminated by a nano-size local source, for example, as shown in **Figs. 6.5** and **A.26** (**Appendix A**)**.** Such interference patterns are not observed when the local source illuminates the gelatine substrate underneath (**Fig. 6.5a**). When the outer face of the CS is upward, the wave emanating from the local source is coupled and guided through it (**Fig. 6.5b-c**). Additionally, more features per length scale is observed at green λ_{vacc} if compared to NIR, which may explain the experimentally obtained interference pattern at green laser (**Fig. 6.1b**) if compared to NIR (**Fig. 6.1d**).

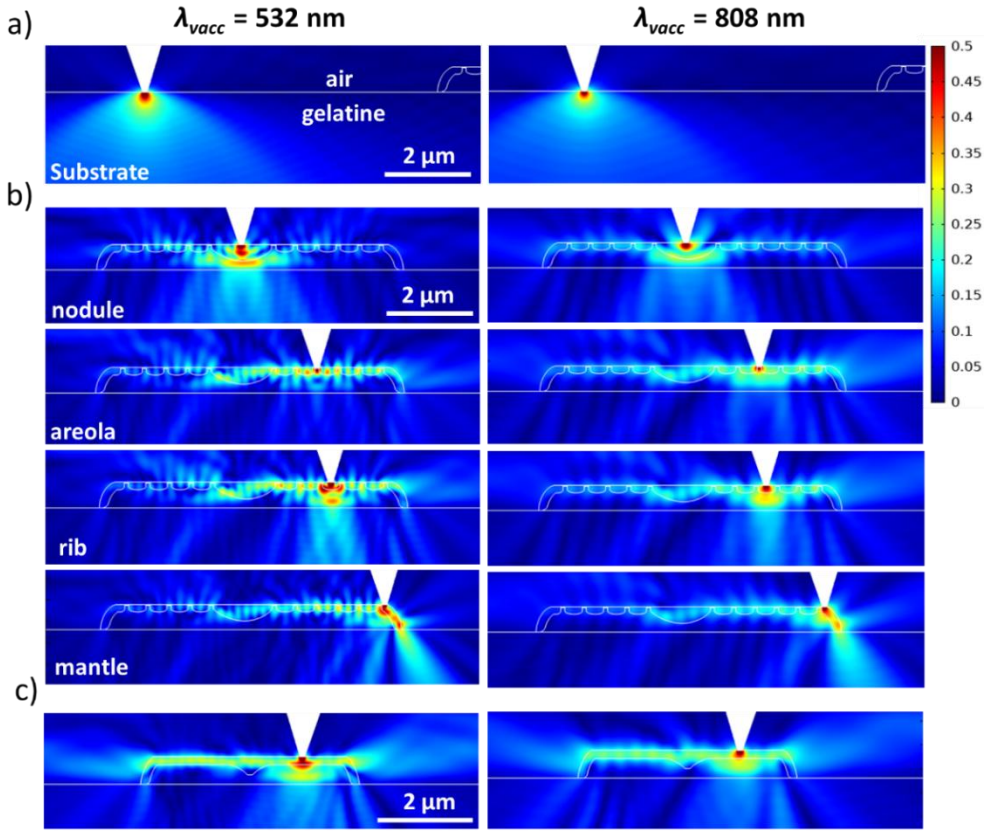

Fig. 6.5. Numerical analysis results of wave propagation (of an *out-of-plane* **E**) from a finite boundary (100 nm width) representing the SNOM tip's nanoaperture. The interaction of the local illumination source and the gelatine substrate (**a**). The interaction of the illumination source and different parts of $CS_{long,3}$ (**b**) or $CS_{ver,2}$ (**c**) that have their outer face upward. In all cases, the color code indicates $\mathbf{E_{Norm}}$, which is given in V/m units. The red and blue colors indicate maximum and minimum $\mathbf{E_{Norm}}$, respectively.

In contrast, when the inner face of the CS is upward—having its outer face in contact with the substrate underneath—the coupling and waveguiding behavior is not observed (see, *e.g.*, $CS_{long,3}$ in **Figs. A.26a-b**, **Appendix A**). That is noticed whether the substrate beneath the CS is gelatine (where $n_{sub} > n_v$, **Fig. A.26a**), or glass (where $n_{sub} = n_v$, **Fig. A.26b**). Such observation is associated with the changes in the medium (considered as the cladding) surrounding the CS (considered as the waveguide core). As already mentioned, to have guided waves inside a given core, the surrounding cladding needs to have a lower refractive index than the core. Therefore, having the gelatine layer or glass substrate (of $n_{sub} \geq n_v$) directly adjacent to the outer face (without an air layer in between) breaks up the conditions for total internal reflection (TIR), and, thus, waveguiding. By removing the substrate and keeping the CS at the same orientation suspended in air ($n_a < n_v$), the coupling and waveguiding behavior is restored (*e.g.*, **Fig. A.26c**), as the core restores the TIR conditions. The latter yields a comparable result for the situation in **Fig. 6.5b**, where both the outer and inner faces are surrounded by air with the mantle acting as a spacer between

the core and the substrate. The waveguiding can also be restored by increasing n_v to become higher than n_{sub} (*e.g.*, **Fig. A.26d**).

These results could explain the hazy interference pattern observed at the valve face in **Fig. 6.1b**, which could indicate the radiative modes (propagated and detected in the far-field) associated with the waves coupled and guided inside the valve. Such interference pattern was not observed when the inner face was upward (**Fig. 6.3b**), similar to the conclusions from the simulation results. These results also suggest that the enhancement associated with the ribs, observed in **Fig. 6.4b**, may not be related to a coupling and waveguiding behavior through the ribs—that has been previously suggested for a similar observation in D'Mello *et al.* [126]—and might be associated with the physical constraints of the SNOM tip to scan at the depressed area of the striae compared to thick elevated ribs (see the height profile in **Fig. 6.4c**). Such physical constraints might reduce the coupling efficiency of the evanescent waves emanating from the nanoaperture to the valve where the striae occur, and, thus, reduce the transmittance at these pixels. Further interpretation of the experimental results needs a more sophisticated simulation approach that is left for future work.

6.1.2. Numerical analysis of the collection mode

In this subsection, the ability of the 2D simulations to predict and explain the experimentally obtained interference pattern in the collection mode is investigated. For this, the numerical analysis approach described in **subsection 3.2.5** (**Chapter 3**) was employed. The situation of *y*-polarized and *x*-polarized waves (for the light waves propagating on the ***z***-axis) were considered in the simulations, as demonstrated in **Fig. 6.6a**. This is because it was difficult to determine the polarization of the green laser reaching the valve, while the NIR laser reaching the valve was unpolarized (the optical fiber depolarized it).

In general, the simulation results show that the interference pattern induced by the *GP* CSs in transmittance at λ_{vacc} = 532 nm was visually more intense and had more features per length scale compared to that obtained at λ_{vacc} = 808 nm, such as the examples shown in **Fig. 6.6a** *vs.* **Fig. 6.7a** (see also **Fig. A.27a** *vs.* **A.28a**). That is the same observation for the CSs suspended in a homogenous medium (**Chapter 4**), where the strength of the interference pattern was generally reduced with increasing λ_{vacc}. It should be, however, noted that sometimes the vertical line profiles extracted at the CSs' interface at λ_{vacc} = 808 nm showed peaks of comparable (or even higher) intensity to those extracted at λ_{vacc} = 532 nm, associated with the mantle-coupled guided waves (*e.g.*, **Figs. 6.7c-b** *vs.* **6.6c-b**). It is also noticed that the interference pattern induced by a plane wave of an *out-of-plane* **E** is more intense than that of an *in-plane* **E**, as can be seen in, *e.g.*, **Figs. 6.6a** and **6.7a**.

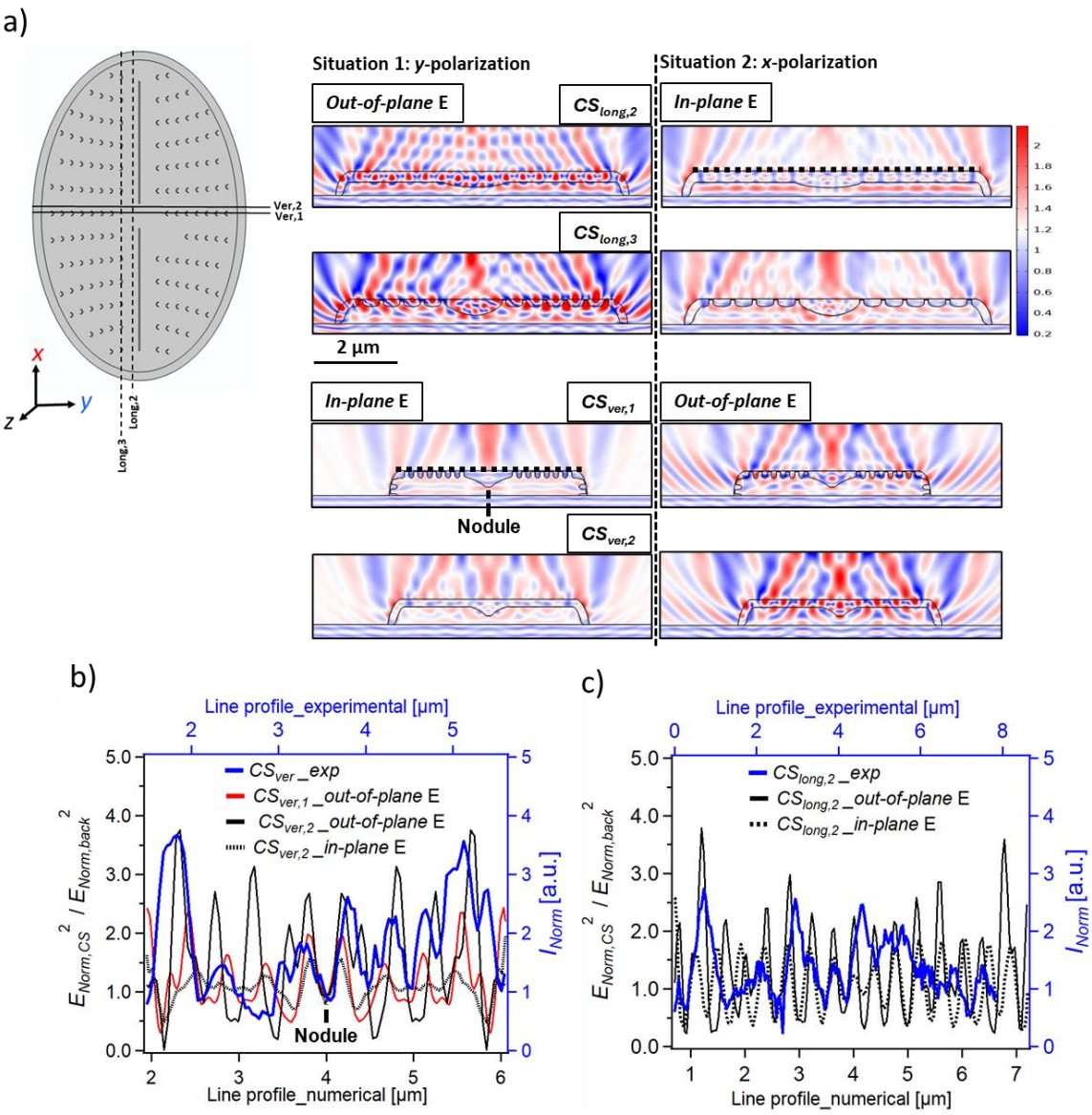

Fig. 6.6. (**a**) The 2D simulation results for selected CSs (showing their **outer face upward**) at $\boldsymbol{\lambda_{vacc}}$ **= 532 nm** in air considering *y*-and *x*-polarizations. It should be noted that for the *y*-polarized plane wave, the electric field oscillates *out-of-plane* the longitudinal CSs and *in-plane* the vertical CSs. While for the *x*-polarized plane wave, the electric field oscillates *in-plane* the longitudinal CSs and *out-of-plane* the vertical CSs. The color code is given in V/m, and the white color indicates $\mathbf{E_{background}}$ over gelatine substrate (= 1.187 V/m). The simulated wave was initiated from the bottom. Comparing the normalized vertical (**b**) and longitudinal (**c**) line profiles extracted from the experimental (blue trace on blue axes) and numerical data at comparable places in the valve at the optical near-field at λ_{vacc} = 532 nm. The black dashed lines in (**a**) indicate the position of the extracted line profiles from simulation domain.

The mantle-coupled guided waves (reported in **subsection 4.3.3**, **Chapter 4**) are observed in the CSs showing their outer face upward, where the incident wave can be coupled into the CS through the mantle's edges. That is evident for a plane wave of an *out-of-plane* **E** and clearer in the CSs without areolae, such as $CS_{long,2}$ and $CS_{ver,2}$ (**Figs. 6.6a** and **6.7a**). When flipping the CSs over the substrate to have their

inner face upward, such behavior is not observed as the wave cannot be coupled anymore through the mantle's edges (**Figs. A.27a** and **A.28a**). Even if the situation changed and the wave illuminated the CS from the top boundary (enabling again the wave to be coupled into the mantle), it is not expected to be waveguided inside the CS due to breaking the TIR conditions by having the substrate underneath, as mentioned in the previous subsection.

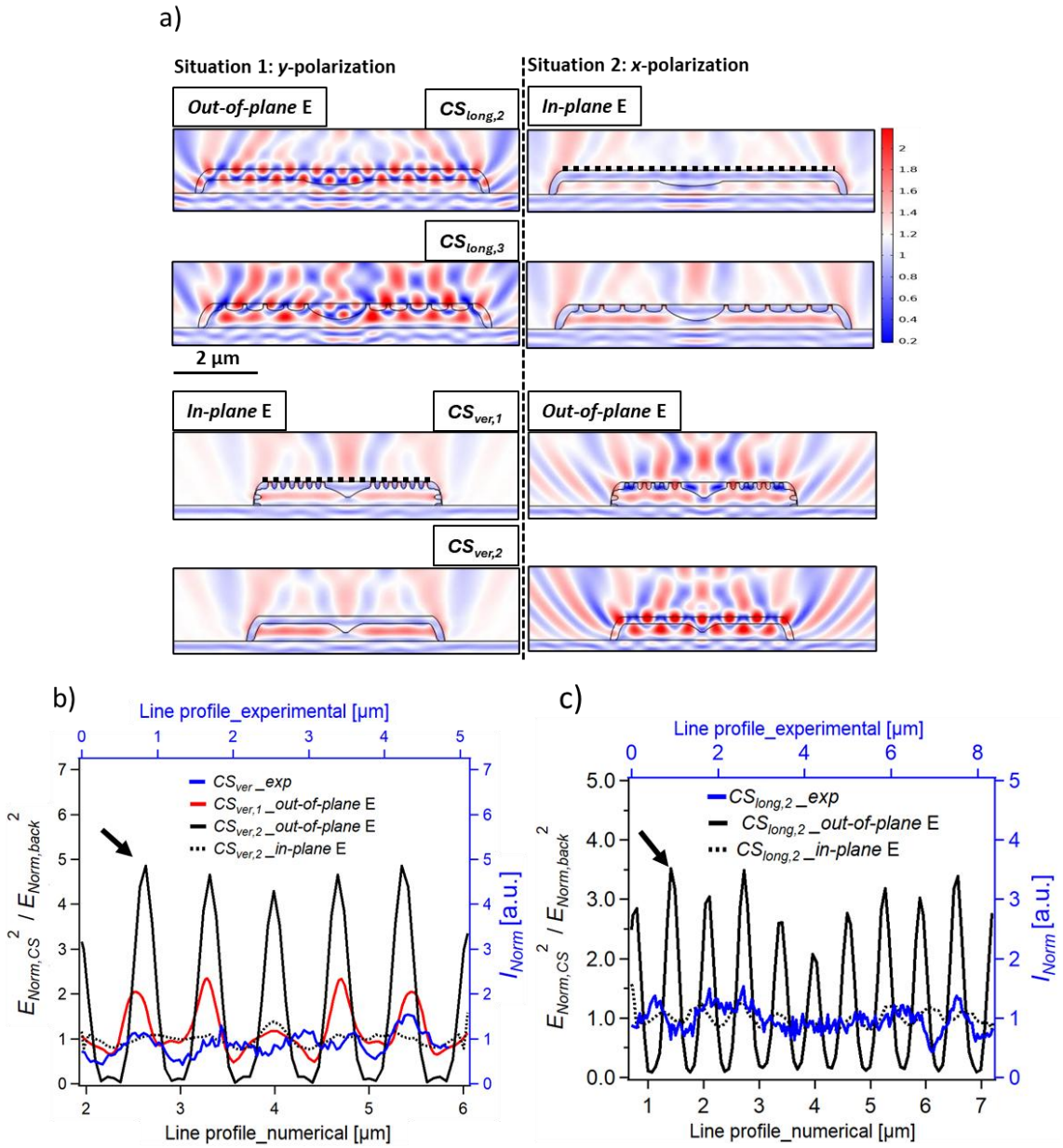

Fig. 6.7. (**a**) The 2D simulation results for the selected CSs (showing their **outer face upward**) at $\boldsymbol{\lambda_{vacc}}$ **= 808 nm** in air considering *y*-and *x*-polarizations. The color code is given in V/m. Comparing the normalized vertical (**b**) longitudinal (**c**) line profiles extracted from the experimental (blue trace on blue axes) and numerical data at comparable places in the valve at the optical near-field at λ_{vacc} = 808 nm. The black dashed lines in (**a**) indicate the position of the extracted line profiles from simulation domain. The black arrows indicate the peaks associated with the mantle-coupled guided waves.

Moreover, the PJ associated with the nodule and the sternum is observed in the relevant CSs, as expected. As also expected, neither the talbot interference pattern nor a grid-coupled GMR maximum is observed at λ_{vacc} 532 nm and 808 nm for the CSs having the grid-like element (**Fig. A.29**).

Some of the general trends observed in the simulations can be clearly seen in the experimental results of the collection mode, such as (i) showing more features per unit length at green laser compared to that at NIR (**Fig. 6.1c** *vs.* **e** and **6.3c** *vs.* **e**), (ii) the enhancement associated with PJ generated by the nodule and sternum (**Fig. 6.3c** and **e**), and (iii) the presence of dark/bright contours associated with some diffraction fringes. There was also no evidence for the presence of a Talbot pattern or GMR. The talbot pattern would appear as an enhancement associated with the valve's ribs at the optical near-field in the collection mode for wavelengths > 500 nm in air at normal incidence. The bright rings of subwavelength features observed in **Fig. 6.1c** may be evidence of the mantle-coupled guided waves (see also **Fig. A.30**, **Appendix A**). In contrast to simulation results, where the mantle-coupled guided waves appeared at both λ_{vacc} (see **Fig. 6.6a** and **6.7a**), this behavior was only clear at green laser (**Fig. 6.1c**) and not observed in the case of NIR laser (**Fig. 6.1e**).

As previously mentioned, the direct fitting of 2D simulation results to the experimental results is not straightforward. When the SNOM tip scans the valve surface in contact mode, it is not expected to be able to reveal all features and can only show the optical near-field. For example, the edge diffraction fringes outside the valve cannot be observed, as the tip returns to the gelatine substrate after passing the valve mantle, as demonstrated in **Fig. A.31** (**Appendix A**). Another example is when the outer valve face is upward, the enhancement associated with the PJ generated by the nodule is not expected to be observed exactly at the surface, as it started a bit above the surface (see, for example, the profiles extracted at the outer surface of $CS_{ver,1}$ and $CS_{ver,2}$ in **Fig. 6.6b**). These two examples match the experimental findings (see **Figs. 6.1c** and **e**). Additionally, both the propagating (including diffraction fringes) and non-propagating fields were collected together at the SNOM nanoaperture and were not emphasized.

Despite the challenges, the numerical results are—to a good extent—comparable in magnitude (sometimes also in shape) to the experimental results, especially for vertical CSs at λ_{vacc} = 532 nm (**Fig. 6.6b**). Such agreement is not observed in the case of *out-of-plane* **E** simulation results at λ_{vacc} = 808 nm, where the magnitude of the peaks associated with the evanescent component of the mantle-coupled guided waves was not observed in the experimental data (**Figs. 6.7b** and **c**). Despite that, a better agreement can be seen for the *in-plane* **E** simulation results. The *out-of-plane* **E** field numerical results were also able to a good extant expect the shape and magnitude of the PJ generated by the valve starting from the surface when its inner face is upward (see **Figs. A.27b** and **A.28b**). In all cases, the observed

discrepancy may be attributed to many factors, including the influence of SNOM tip shape and geometry, scan resolution, and the difference between 2D and 3D situations.

6.2. SNOM measurements of *Aula* valves

Fig. 6.8 shows the optical near-field interference patterns at the outer face of a selected *Aula* valve in illumination and collection modes **at green laser**. The ultrastructure of the valve face, including the areolae and spines, can be seen in the shear force image (**Fig. 6.8a**).

The SNOM optical images for the whole valve were unclear and showed almost the same interference pattern, with a distinctive bright circular area at the valve's center and a dark contour surrounding the valve (**Figs. 6.8b** and **c**). To disclose the finer features of the interference pattern, smaller areas of the valve were scanned separately at high resolution. By scanning the **spines area**, the dark contour was clearly revealed associated with the spines position (white arrows, **Fig. 6.8**, **spines**), while bright fringes were observed within the valve face (blue arrows, **Fig. 6.8**, **spines**). The other positions (**positions 2**, **3**, and **center**) showed subwavelength features (bright fringes alternative with darker ones) in the collection mode. It should be noted that the position of the observed bright/dark fringes did not follow the ultrastructure pattern. That was more evidenced at the **center**, where the defect observed in the shear force image (indicated by the yellow arrow in **Fig. 6.8**) did not influence the generated bright/dark fringes. While the illumination mode showed a hazy interference pattern of bright/dark areas, which may indicate the radiative modes at the valve face. These observations are similar to that of *GP* valve with its outer face upward (**Fig. 6.1**).

Fig. 6.9 shows the optical near-field interference patterns at the outer face of another selected *Aula* valve in illumination and collection modes **at NIR laser**. In this case, the dark contour associated with the spines was clearer and wider than that observed at the green laser. A few ring-shaped bright fringes alternative with darker ones were also observed within the valve face. A bright circular area (of reduced size compared to that at green laser) appeared approximately at the center of the valve face. Interestingly, these bright rings showed finer details in the collection mode (**Fig. 6.9c**).

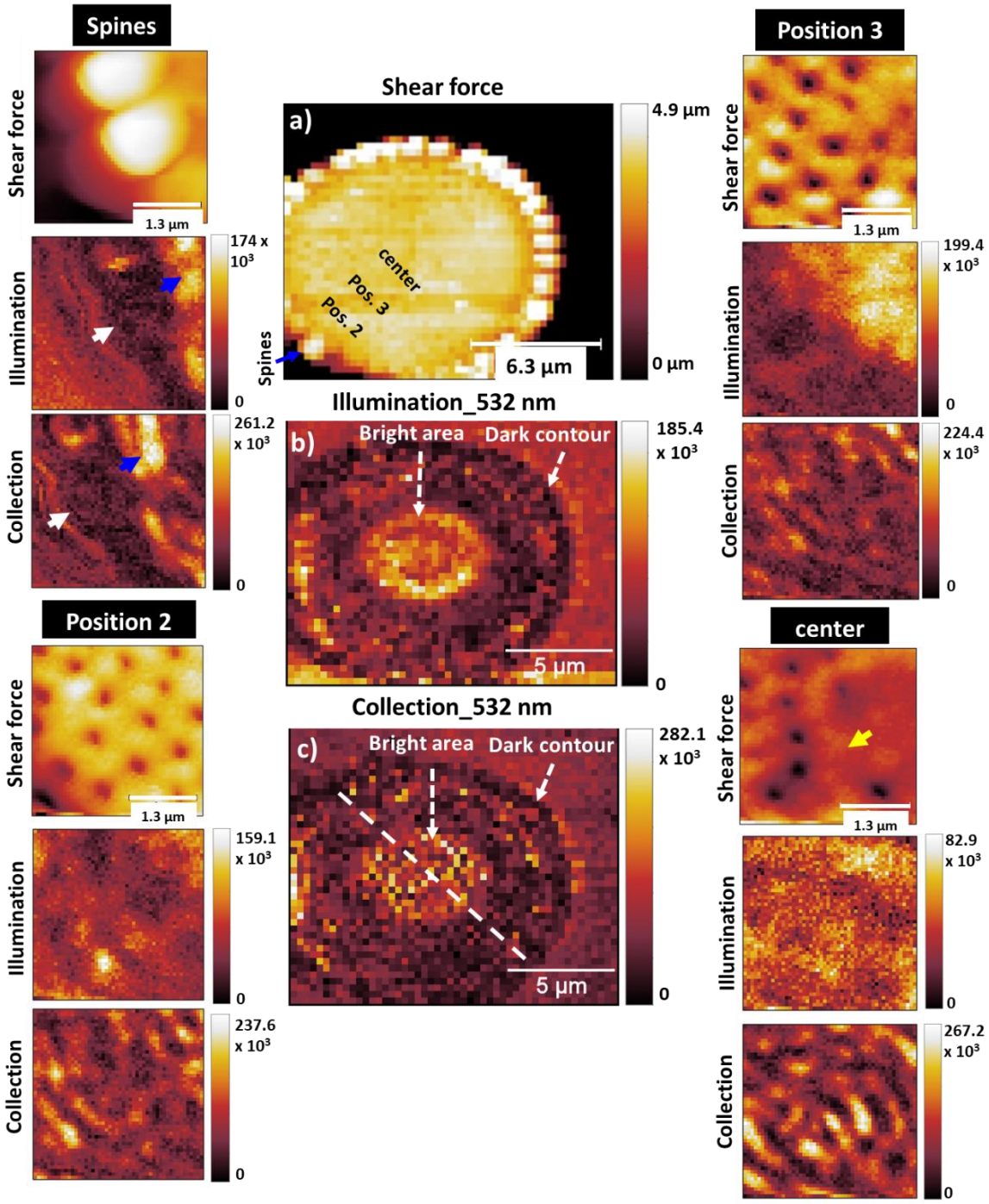

Fig. 6.8. SNOM shear-force image of an *Aula* valve showing its **outer face** upward (**a**). SNOM optical images showing the optical response of this valve **at green laser** in illumination (**b**) and collection (**c**) modes. The images at the right and the left showing the shear-force and the SNOM optical images of four selected smaller areas at the valve surface at green laser. The positions of these areas are indicated in (**a**). It should be noted that the Shear-force images show the actual scanned area for the illumination mode, while there was a slight shift in the case of collection mode (*e.g.*, the positions of white and blue arrows in **spines position**). The yellow arrow indicates the defect occur at the center of this valve. The intensity scales are given by integrated counts. The length scale bars have an estimated error up to ± 10%. The raw SNOM images were acquired by Professor Paul Fumagalli.

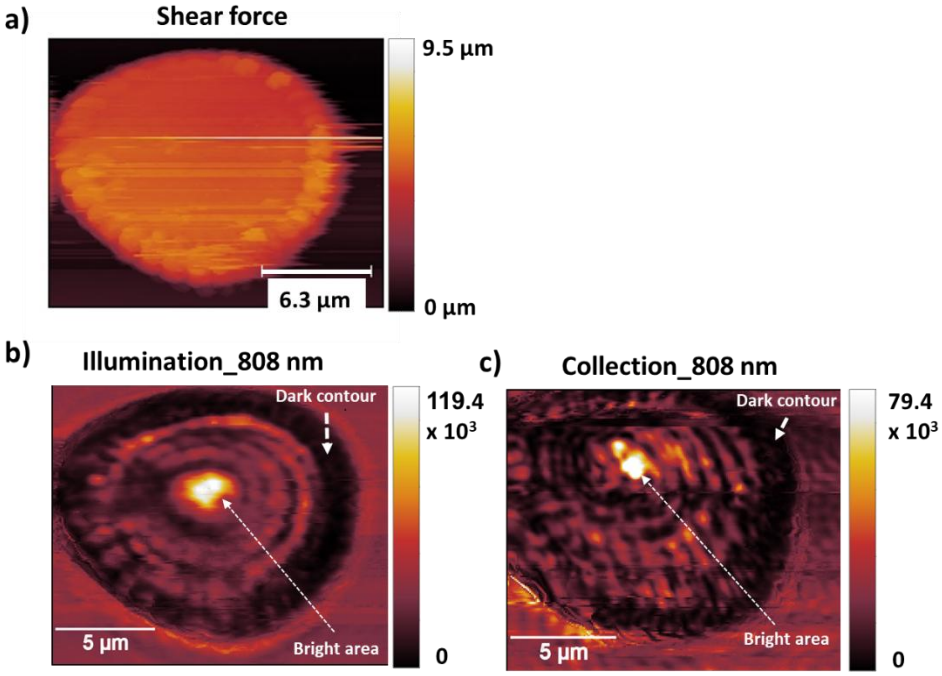

Fig. 6.9. SNOM shear-force image of an *Aula* valve showing its **outer face** upward (**a**). SNOM optical images showing the optical response of this valve **at NIR laser** in illumination (**b**) and collection (**c**) modes. The intensity scales are given by integrated counts. The length scale bars have an estimated error up to ± 10%. The raw SNOM images were acquired by Professor Paul Fumagalli.

6.2.1. Numerical analysis of the collection mode

In this subsection, the 2D simulations are compared to the experimental results to see how far the 2D simulations could predict and explain the experimentally observed features of *Aula* valves. **Fig. 6.10** illustrates the simulation results for the *Aula* longitudinal CSs, which show very complex interference patterns in the optical near-field. As illustrated in **section A.12** (**Appendix A**), such complex interference patterns can be explained by disassembling the distinct optical elements.

At λ_{vacc} = 532 nm, the fine interference pattern fringes, which appear at the outer face of $CS_{long,2}$, show contributions from the edge diffraction at its ringleist (indicated by the green arrows in **Fig. 6.10a**). The contribution from the grid-like element is also evidenced in $CS_{long,1}$, which shows a heavily deformed Talbot pattern (indicated by the black arrow in **Fig. 6.10a**). The deformation in the Talbot pattern is mainly attributed to the diffraction contributions from the ringleist. At λ_{vacc} = 808 nm, the grid-like element of $CS_{long,1}$ does not show the Talbot pattern anymore but likely approaches the bandwidth of its zero mode GMR (only for *out-of-plane* **E** wave). That is why a high intense $\mathbf{E_{Norm}}$ is observed inside the CS face and at its optical near-field in that case (indicated by the black arrow in **Fig. 6.10b**).

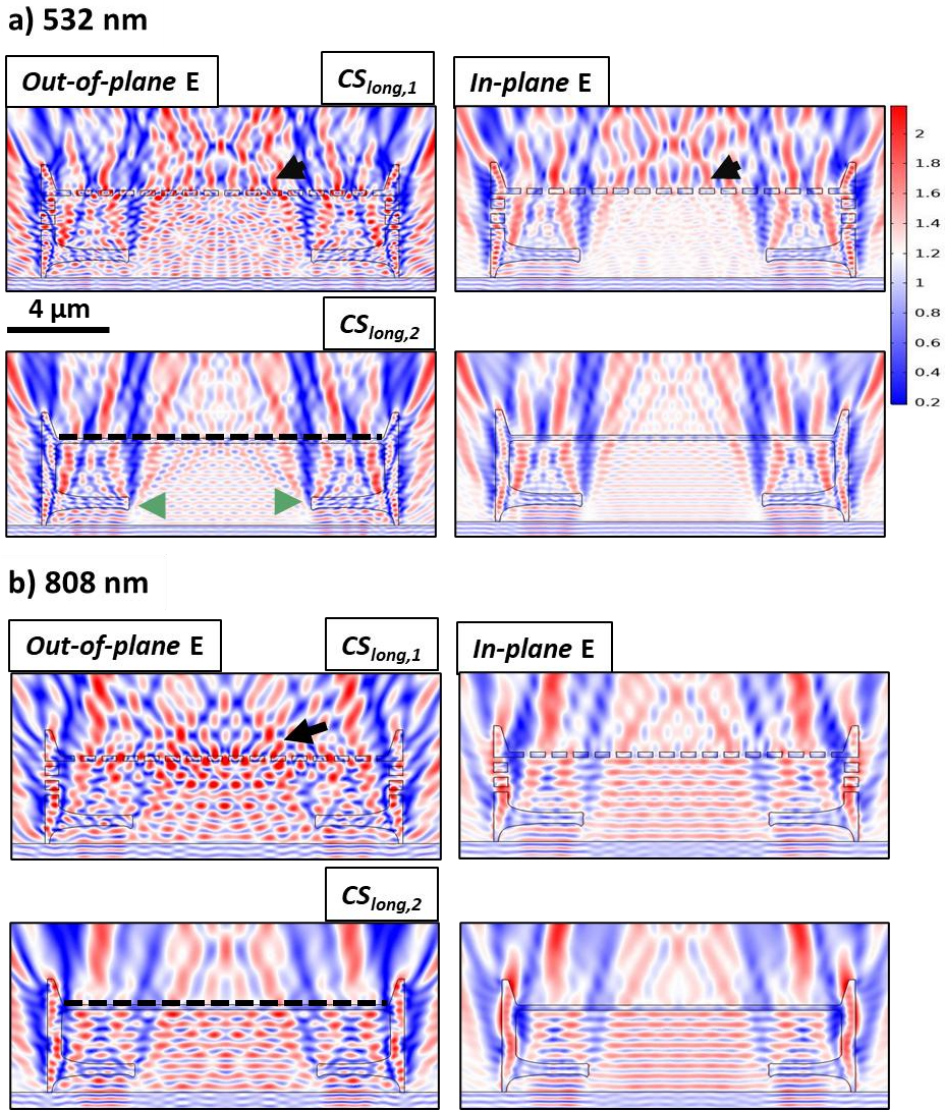

Fig. 6.10. The 2D simulation results for *Aula* longitudinal CSs (showing their **outer face upward**) at λ_{vacc} = 532 nm (**a**) and at λ_{vacc} = 808 nm (**b**) in air considering *y*-and *x*-polarizations. Unlike *GP* valve, there is no difference between *x*- and *y*-polarizations, due to the radial symmetry of the *Aula* valve. Therefore, the results here are shown for *out-of-plane* and *in-plane* **E**, without emphasizing the polarization state. The color code is given in V/m, and the white color indicates $\mathbf{E}_{\mathbf{background}}$ over gelatine substrate (= 1.187 V/m). The simulated wave was initiated from the bottom. The black dashed lines indicate the position of the extracted line profiles from the simulation domain.

Fig. 6.11a shows the comparison of the line profiles extracted from numerical and the experimental results at green laser at low resolution, which could only show that the normalized intensity magnitude of the experimentally obtained interference fringes is comparable to that of the numerical results. By increasing the scan resolution, some experimentally resolved features were to some extent comparable in shape and magnitude to the numerical results (**Fig. 6.11a**). Moreover, scanning smaller areas within the valve (with a higher resolution) shows a more interesting match (**Fig. 6.11b**). **Fig. 6.11c** shows the comparison of the numerical and

experimental results at NIR laser, where the normalized intensity magnitude of the brighter area at the valve center was comparable to that of simulation results.

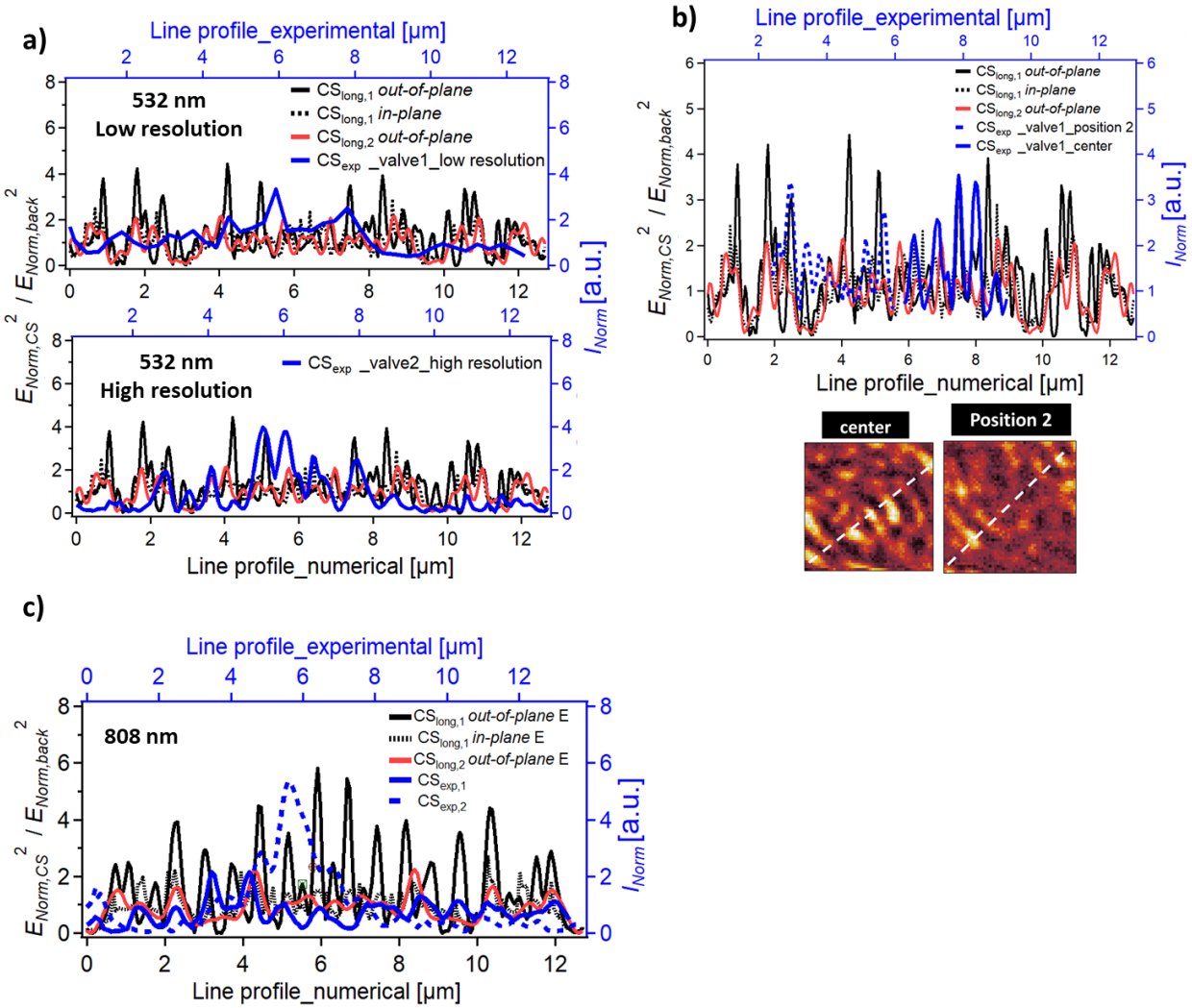

Fig. 6.11. (**a**) Comparing the normalized line profiles extracted from the numerical results at λ_{vacc} = 532 nm and the experimental data at green laser (blue trace on blue axes) for the complete valve at low resolution (extracted from **Fig. 6.8c**, the white dashed line) and at high resolution (extracted from **Fig. A.32b**). (**b**) Considering small areas of the valve face with high resolution gives a better match. The positions of the experimentally obtained lines profiles are illustrated below. (**c**) Considering the results at λ_{vacc} = 808 nm (extracted from **Fig. 6.9c**).

In general, the numerically obtained bright/dark interference fringes can be visually linked to the bright/dark areas (fringes) observed in the experimental results of the collection mode at both wavelengths (**Fig. 6.10** *vs.* **Figs. 6.8c** and **6.9c**). Moreover, the numerical results suggest that the subwavelength interference fringes observed at green laser, which forming the bright circular area appeared at the valve center (**Fig. 6.8c**, see also **center** position), may be attributed to the overlapping of talbot fringes (which will have 2D pattern, as the pore array of the *Aula* valve face occurs in 2D) and the inner diffraction fringes mainly generated from the ringleist.

However, the experimental results suggested that the pore array did not influence this interference pattern (**Fig. 6.8**, **center** position). Furthermore, the bright circular area appeared at NIR laser (**Fig. 6.9c**) may be attributed to approaching the zero GMR mode, as suggested by the simulations (**Fig. 6.10b** and **6.11c**). Further investigation to zoom-in on the valve at NIR laser with higher resolution is still required and left for future work.

6.3. Further discussions

In this chapter, the optical near-field of the *GP* and *Aula* valves was experimentally investigated for the first time using a-SNOM operated in transmission configuration. The experimental results shown here can be added to the far-field experimental results obtained for these valves in **Chapter 5** (see also **sections A.10** and **A.12**, **Appendix A**), which revealed the optical features at the Fresnel regime zone of these valves, to have a broader picture of their light modulation capabilities.

Although the illumination mode revealed some optical features of the studied valves, it cannot provide information on the non-propagating waves at the surface, as already explained in **section 2.5** (**Chapter 2**). The results of this mode are an addition to the previous efforts reported in literature for the valves of other diatom species; the pennate diatom *Nitzschia filiformis* [126] and the centric diatom *Cyclotella* sp. [307]. In addition to illumination mode, the collection mode was used for the **first time** in this chapter, which enabled revealing interesting features, as can be seen in **Figs. 6.1c**, **6.8** (clear in scanning the smaller areas), and **6.9**. These features included information on propagating (*e.g.*, inner diffraction fringes, diffraction-driven focusing spots, and PJ) and non-propagating (*i.e.*, evanescent component of guided waves) waves combined together.

The 2D simulation approach developed for simulating the collection mode showed to a good extent the ability to explain and predict the general trends observed in the experimental results, as shown for *GP* and *Aula* valves. Despite that, there were limitations to the direct fitting of experimental and numerical results and to predict the actual interference pattern obtained in 3D. Some of these limitations are related to the scanning area and the associated resolution, as confirmed in the case of *the Aula* valve (clearly illustrated in **Figs. 6.11a-b**).

Moreover, the results shown in this chapter offer interesting insights relevant to applications. Both valves were able to modulate light in the optical near-field and induce an enhancement in the local EM field (thus, higher $\mathbf{E_{loc}}$), which could be promising for photonic and optoelectronic applications. Such a conclusion, if extended to the valves of other species, might explain their successful applications reported in the literature (see **subsection 1.2.5**, **Chapter 1**). In the case of pennate valves of similar geometry to the *GP* valves, their orientation over the substrate

seems to be crucial in determining their light modulation capabilities. Having their outer valve face upward may be more promising for optoelectronic applications due to the ability to couple light into guided waves across the surface, which may lead to a great enhancement for their $\mathbf{E_{loc}}$, which will not be possible if the inner face is upward. Modifying the refractive index of the valve by doping/coating with other materials of higher refractive index could change this situation and enable waveguiding even if the inner valve face is upward (as shown in **Fig. A.26d**, **Appendix A**). Additionally, the illumination mode results also suggest that the light can be coupled and guided through a diatom valve if a nano-size local source illuminates the valves.

Furthermore, the collection mode results for the *GP* valve confirmed that the enhancement associated with the sternum and the nodules occurs starting from the valve's optical near-field. These results support the hypothetical photobiological relevance of these PJs discussed in **Chapter 5** (**subsection 5.4.2**). However, the intensity of the generated PJs is expected to become lower inside the complete frustule under water (as seen in **section 4.4**, **Chapter 4**), but could still influence the hypothetical plasma membrane proteins occurring adjacent to the valve (in its near-field).

Finally, the collection mode can be employed in future work to also study the interference patterns at the Fresnel regime zone of diatom valves with very high resolution better than the diffraction-limited far-field techniques employed in **Chapter 5**. This has been carried out in literature for artificial structures (see, *e.g.* [241,242]). This mode can also be used to study the waveguiding behavior and PC features of diatom valves/gridle bands.

7 Diatom valves for fabrication of SERS hybrid substrates

The results shown in this chapter have been published in:

Gilic, M.; **Ghobara, M.**; Reissig, L. Tuning SERS Signal via Substrate Structuring: Valves of Different Diatom Species with Ultrathin Gold Coating. Nanomaterials 2023, 13, 1594, https://doi.org/10.3390/nano13101594. Used here under the terms and conditions of the Creative Commons Attribution (CC BY 4.0) license (https://creativecommons.org/licenses/by/4.0/).

As already mentioned, employing diatom valves as substrates—after coating with a plasmonic material—for fabricating SERS-based sensors has already been investigated utilizing the valves of a few diatom species, mostly belonging to the genus *Pinnularia* [145,146]. Most of these studies focused on incorporating metallic nanoparticles (NPs) on top or within the pores of diatom valves. The achieved enhancement is often linked to the coupling of diatom valves' GMR and the SPR of metallic NPs (see, *e.g.*, **Fig. 2.13b**, **Chapter 2**). Fewer publications have considered metallic thin films to overcome some limitations of NPs [308,309]. The results of all studies are indeed promising. Still, more studies are needed to—among other tasks—understand the contribution of the valves' ultrastructure to SERS enhancement and enable the screening of structurally distinct valves to select the valve that could give the best performance.

In this chapter, the preliminary results reported in Gilic *et al.* [310] are summarized and discussed. In this paper, I prepared diatom samples and different SERS hybrid substrates (as described in **subsection 3.5.1**, **Chapter 3**). I also worked together with Dr. Martina Gilic to do the SERS measurements, mapping, and data analysis (see **subsection 3.5.3**). In this paper, three structurally distinct diatom valves (*GP*, *CR*, and *Aula*) were utilized to fabricate SERS hybrid substrates, which were compared under equal measuring conditions. These valves have already shown interesting light modulation capabilities in the previous chapters, especially *GP* and *Aula* valves. The utilization of metallic NPs as the plasmonic material—as has been done in most of the previous work [145]—was inappropriate in this study as it could create uncontrollable hot spots over diatom valves (resulting from the uncontrollable distribution of NPs), which may hamper revealing the SERS enhancement contributed by the valve ultrastructure. Therefore, a smooth ultrathin gold film—devoid of distinct NPs, islands, or voids as possible—was employed to

coat diatom valves (as described in **subsection 3.5.1**). It should be noted that optimizing and maximizing the SERS signal or fabricating an end-user sensor is not included here and is left for future work.

7.1. Characterization of the obtained ultrathin gold film

The obtained gold film over the reference substrate (*i.e.*, without diatom valves) showed smoothness, homogeneity, and continuity, as evident by SEM and AFM analysis (**Figs. 7.1a** and **b**, respectively). The AFM analysis showed that the film has a root-mean-square (RMS) roughness of 0.54 nm. The film also showed good electric conductivity and excellent adhesion to the glass substrate, as we could not peel it out of the glass substrate using scotch tape. These properties are associated with the special bonding between the thiol group (-SH) of MPTMS and gold atoms (Au), which not only act as nucleation sites but also create a strong bond [311].

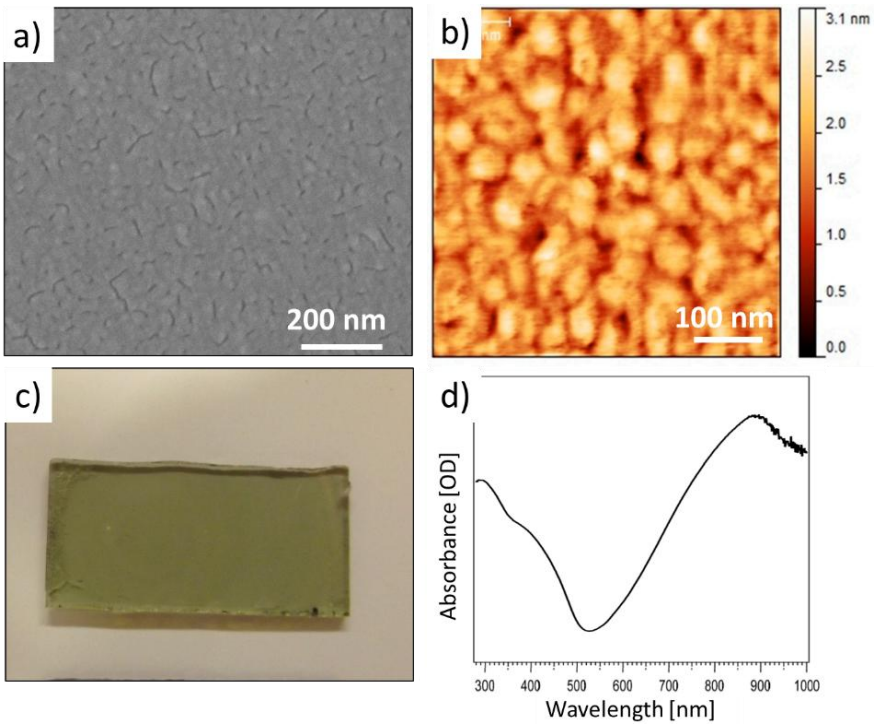

Fig. 7.1. (**a**) SEM and (**b**) AFM of the ultrathin gold film on the reference substrate. (**c**) the optical appearance of the film, and (**d**) its UV-Vis absorbance spectrum. The SEM was acquired by Dr. Martina Gilic, while the AFM as well as UV-Vis spectrum were obtained by Prof. Louisa Reissig and Dr. Martina Gilic together. This figure (except **c**) consists of modified and merged figures from Gilic *et al.* [310].

The obtained film is transparent with a greenish color (**Fig. 7.1c**). The UV-Vis absorbance spectrum of the reference substrate displays a minimum absorbance at 532 nm and a maximum at 890 nm (**Fig. 7.1d**); the latter is likely associated with the plasmonic resonance of the film [312].

Fig. 7.2 shows the gold film obtained on the three structurally distinct diatom valves. The valves' morphology and ultrastructure have been described in the previous chapters (see **Chapters 4** and **5**). These valves offered nanostructuring to the gold film associated with their ultrastructure, while the film roughness on top of the valves was kept as minimal as possible (lower than the gold film roughness reported in relevant literature [308]) thanks to the SAM layer introduced here. Most valves were coated homogeneously without blocking their nanofeatures. For instance, the fine ultrastructural features of *GP* valves—such as the crescent-like slit of pore occlusion—were preserved after depositing the gold film (**Fig. 7.2b**). Nevertheless, it should be noted that fewer valves showed imperfection in the gold film homogeneity (see, *e.g.*, the inset in **Fig. 7.2d**).

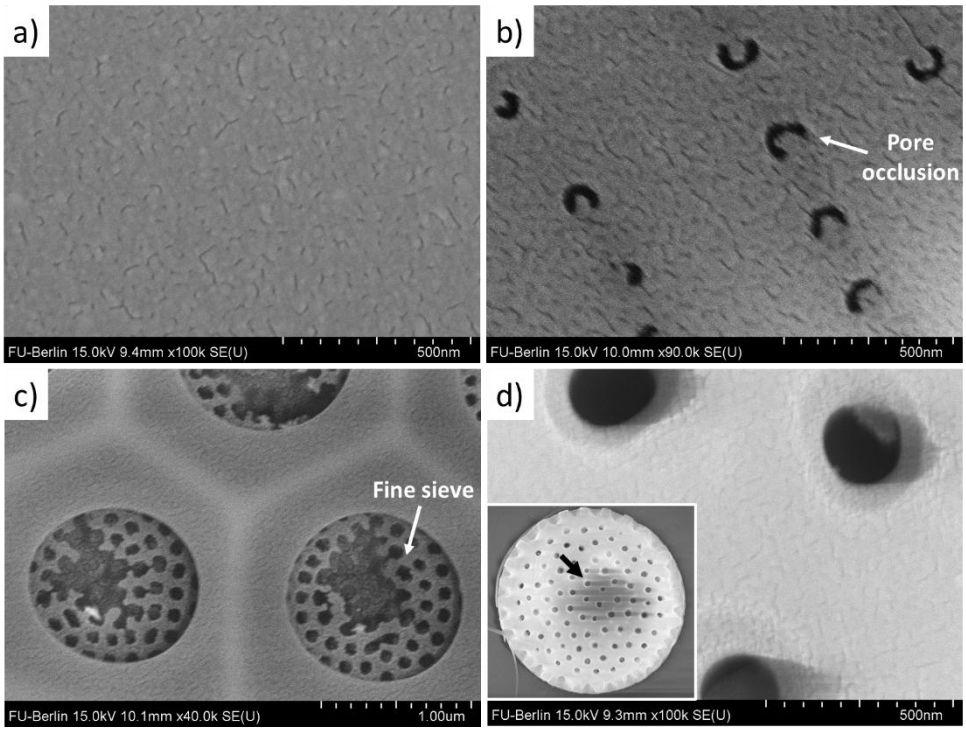

Fig. 7.2. SEMs show examples of the ultrathin gold film coating the structurally distinct valves compared to the reference substrate demonstrated in (**a**). The SEMs show a zoom in the gold film over *GP* (**b**), *CR* (**c**) and *Aula* valves (**d**). The inset in (**d**) shows a complete *Aula* valve with an inhomogeneity in the gold film thickness at its center, which is evident by the charging (indicated by the black arrow in the inset micrograph). The raw SEMs were acquired by Dr. Martina Gilic. This figure (except the inset in **d**) consists of merged modified figures from Gilic *et al.* [310].

7.2. Comparative analysis of the R6G SERS spectra obtained from the distinct substrates

The SERS spectra generally show the characteristic vibrational bands of R6G reported in the literature [313–318], including peaks at around 610, 770, 1187, 1312, 1360, 1508, 1600, and 1648 cm^{-1}. The peak at around 610 cm^{-1} stands for C-C-C (xanthene

ring) *in-plane* bending, the peak at 770 cm^{-1} stands for C-H *out-of-plane* bending, the peaks at 1124 and 1180 cm^{-1} are associated with C-H *in-plane* bending, while the peaks from 1314 cm^{-1} to 1648 cm^{-1} are associated with the aromatic C-C stretching [313]. Some of these peaks were insignificantly shifted between distinct substrates, as can be seen in **Fig. 7.3**.

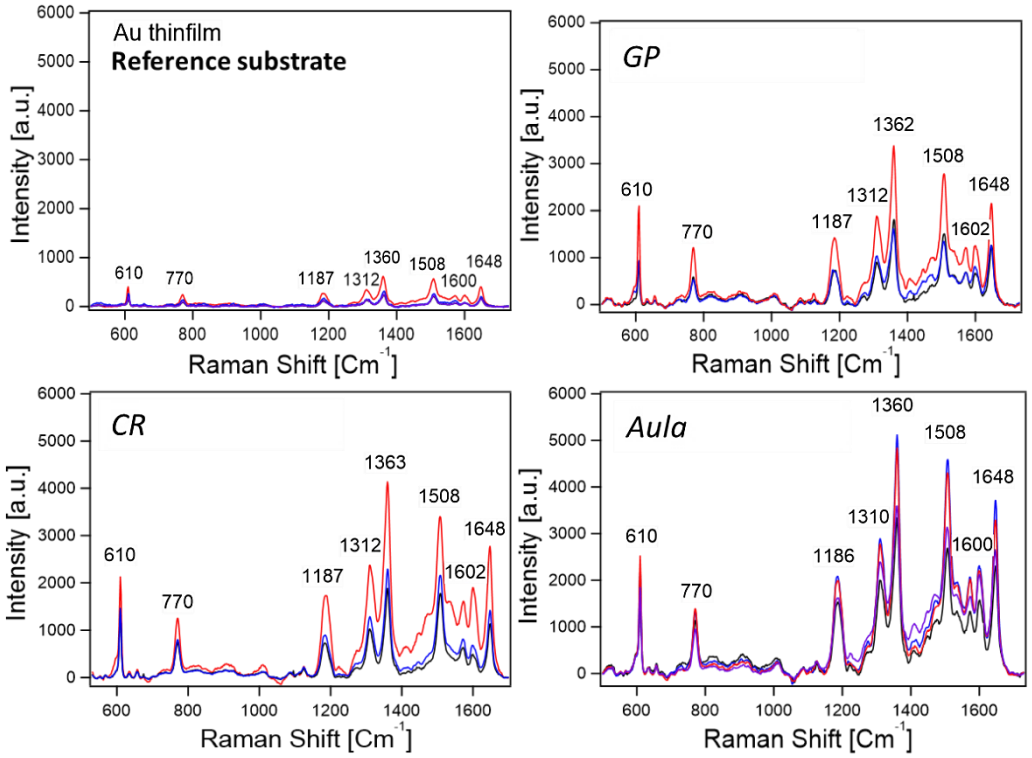

Fig. 7.3. SERS spectra of R6G molecules (10^{-3} M) on distinct substrates under equal measuring parameters (λ_{exc} = 638 nm). The different spectra shown for each substrate—having different colors—represent the reproducibility of the signal on different valves (or places in the case of the reference substrate). All spectra were acquired while the valve was at the best focus. In the case of diatom valves, the porous area was only considered for these measurements while avoiding the valves' mantle. This figure is modified from Gilic *et al.* [310].

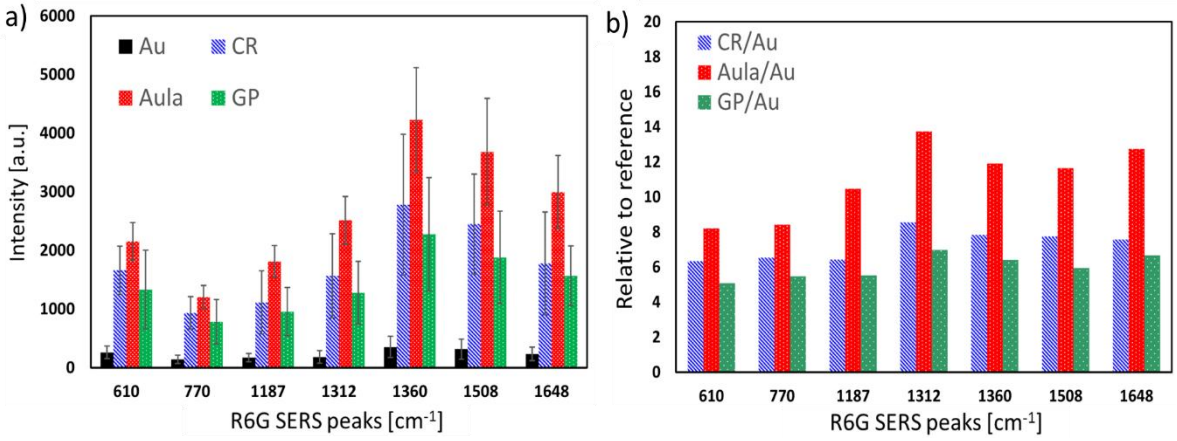

Fig. 7.4. (**a**) The average SERS signal intensity of different R6G peaks obtained on the distinct substrates, calculated based on the spectra shown in **Fig. 7.3**. The error bars in (**a**) are

associated with the standard deviation, which indicates the signal reproducibility range among the valves of the same species (or different places in the case of the reference substrate). (**b**) The relative enhancement (compared to the reference) of the characteristic peaks for each substrate, calculated by dividing the average intensity of each peak (shown in **Fig. 7.4a**) by the average intensity of the same peak in the reference substrate. This figure is modified from Gilic *et al.* [310].

Generally, all the substrates employed diatom valves significantly improved SERS signal compared to the reference substrate (**Fig. 7.3** and **7.4a**). Nevertheless, the magnitude of this enhancement is likely specific for each species, thus its valve ultrastructure. As can be determined from **Fig. 7.4a**, the enhancement obtained on the substrates containing *Aula* valves was significantly higher than the others. In all cases, the highest peaks were observed for the vibrational bands at around 1360 and 1508 Cm^{-1}. Considering the relative enhancement (compared to the reference) of all characteristic peaks (**Fig. 7.4b**), the substrates containing *GP*, *CR*, or *Aula* valves showed a relative enhancement range of 5-7, 6-8, or 8-14 folds, respectively.

7.3. The role of valve's ultrastructure

The substrate containing *Aula* valves showed a relatively uniform SERS signal magnitude over a large part of the valve face. While the substrate containing *GP* valves showed a very intense background associated with their mantle—despite applying the automatic flat correction—that obscured obtaining a good SERS signal at positions close to it. On the other hand, the substrate containing *CR* valves showed an apparent influence of their ultrastructure on the SERS signal magnitude, which was evident in their SERS maps. The periodic arrangement of areolae is—to some extent—preserved in the SERS maps, having the maximum enhancement emanating from the areolae (**Fig. 7.5**). Interestingly, inside the areolae—which can be considered as a chamber of an estimated depth ≈ 1 µm—there is a sieve of finer pores with diameters ranging from 50-100 nm. As illustrated in **Fig. 7.2c**, this sieve is also covered with the gold thin film that potentially may lead to stronger localized SPR and may explain the obtained result.

In literature, it is often assumed that the coupling of GMR and SPR is the reason for the enhancement obtained from diatom-based SERS hybrid substrates (*e.g.*, **Fig. 2.13b, Chapter 2**). As concluded from the previous chapters, the variation of valve ultrastructure could alter the associated light modulation capabilities, including $\lambda_{vacc,GMR}$ of grid-coupled GMR (see **subsection 4.3.7**, **Chapter 4**), thus the expected contribution to the SERS enhancement. When looking at the ultrastructural parameters of studied valves, such as the pore size and spacing (see **Table 4.1** for *GP*; **Table 5.1** for *CR*; **Table 5.2** for *Aula*), it can be logically concluded that at the same excitation laser λ_{exc}, these pore arrays cannot all support grid-coupled GMR (if can at all). Such a conclusion is supported by the 2D simulation results obtained by Dr.

Martina Gilic and demonstrated in Gilic *et al.* [310], which might partially explain the variability in the enhancement magnitude between distinct substrates. However, it should be noted that 3D simulations—considering the whole valve structure over the glass substrate—are required to approximate the actual $\lambda_{vacc,GMR}$ (and the associated bandwidth). We should also consider that the SERS measurements were carried out using a small laser spot (not a plane wave of larger diameter) illuminating a finite part of the valve, which could change $\lambda_{vacc,GMR}$, as can also be concluded from Ren *et al.* [319]. Therefore, in future work, the 3D numerical analysis of the actual situation is required to investigate whether the GMR (and/or other optical phenomena) contribute to the SERS enhancement of distinct hybrid substrates.

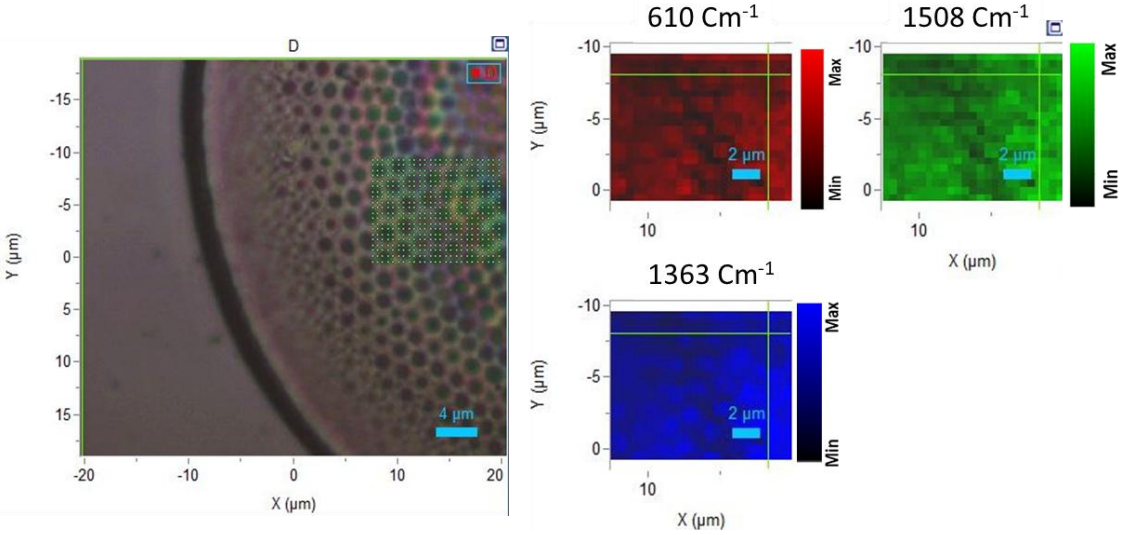

Fig. 7.5. A SERS mapping at three different intense R6G bands (at right) for a selected area of the hybrid substrate containing a *CR* valve, having its inner face fronting the objective (at left). This figure was acquired together with Dr. Martina Gilic.

Finally, it should be noted that whether the valve initiated GMR or not, the presence and the size of pores in the hybrid substrate (which can be seen as cavities introduced to the gold thin film by the valves) could contribute to the obtained SERS enhancement through inducing and enhancing localized SPR (specifically the fine pores, such as the sieve in *CR* valves). That is evident in previous work on porous metallic films (*e.g.* [320]). Further, the pores give a larger surface area (compared to the smooth film without diatoms), where more dye molecules could be absorbed leading to signal enhancement as a result of increasing analyte concentration. These two reasons might explain why we can get enhancement even if we don't initiate GMR and how this enhancement could be correlated to the valve's ultrastructure.

8 Summary and Conclusions

This thesis aims to expand previous efforts and deepen our understanding of how light interacts with diatom valves/frustules, influenced by their size, geometry, and ultrastructure. Most previous works investigated only a single optical feature of diatom valves/frustules, by looking, for example, at their pore arrays (approximating it as PC slab), at their diffraction-driven focusing behavior, or their far-field diffraction grating behavior [36,44]. That approach has made progress in the field and revealed some features; however, considering the valves'/frustules' structural complexity and the possible presence of other overlapped optical features is crucial for unveiling their limits in applications and their photobiological roles. Additionally, some studies only looked at the far-field light modulation abilities, while the most relevant phenomena to optoelectronic and photonic applications as well as photobiology are those occurring in the valve's/frustule's optical near-field and Fresnel regime.

Following these thoughts, a novel approach was developed in **Chapter 4**, successfully offering an analytical understanding of the complex interference pattern that can be induced by illuminating the small-size *GP* valve/frustule. By employing the 2D FEFD numerical analysis, the presence of distinct optical phenomena, influencing the valve's/frustule's optical near-field and Fresnel regime zone and correlated with the presence of distinct optical elements, was evident. The relevance of some optical phenomena, such as PJ generation and Talbot effect, to diatoms were discussed for the **first time**. In the 3D complex structure, these phenomena overlap and compete with each other, depending on the incident λ_{vacc} and Δn. Some of the observed optical phenomena have the potential to be employed in applications and might have photobiological relevance. At the end of this chapter, it can be realized that it is not only predicting light modulation abilities of *GP* valve/frustule (which was studied here for the **first time**) but also gives the potential to predict those of the valves/frustules of other structurally similar species and genera (*i.e.*, other small biraphid pennates). It may even be extended to analytically understand the light modulation abilities of the valves/frustules of other dissimilar pennates, as well as centrics, by dissembling their distinct optical components and determining the relevant optical phenomena in the light of their structural parameters.

In **Chapter 5** more attention was paid to the colligative diffraction-driven focusing abilities of diatom valves, which have been reported in literature only for a few species. By employing far-field optical microscopy techniques, this chapter successfully illustrated the valves' ability of a number of species of a wide range of geometries, ultrastructure, and sizes (some of which were studied here for the **first time**) to induce such behavior in their Fresnel regime zone. These findings confirmed the assumption that this phenomenon could be widespread among diatom species and genera. Through examining the trans-illumination results of *GP* valves, as well as other larger pennate valves, the analytical understanding reached in **Chapter 4** was supported. Interestingly, the comparison of the 2D FEFD simulations to the experimental results, as shown in the case of *GP* and *Aula* valves (**sections A.10** and **A.12**, respectively), illustrated that—despite the limitations—the 2D simulations can to a good extent predict the focusing behavior (including its magnitude) but may also predict other features of the interference pattern in the Fresnel zone, such as the destructive interference regions (see, *e.g.*, **Fig. A.17c**). This chapter also shows, for the **first time**, the ability of structurally distinct diatom valves to induce focusing when being illuminated from the side. In all cases, the observed focusing could be generated through the interference of multiple diffraction sources within the valves/frustules and may be influenced by the waveguiding behavior of the mantle/girdle bands (under transillumination) and of the valve face (under side-illumination). The photonic crystal features of the periodic pore arrays may further influence such focusing behavior, as shown in the case of *Aula* valves.

In **Chapter 6**, the interference pattern induced in the optical near-field of the *GP* and *Aula* valves was studied employing a-SNOM operating in trans-illumination configuration. Both illumination and collection modes were utilized in the study, the latter being used for the **first time**. The collection mode showed interesting subwavelength features in the *GP* valves at green laser, which may be attributed to mantle-coupled guided waves, observed in the 2D simulations of *out-of-plane* **E** wave propagation. The *Aula* valves also showed interesting subwavelength features in the collection mode that are not comparable in the illumination mode. In general, the 2D FEFD simulations showed an agreement with many features observed in the experimental results, while the discrepancies between the simulation and experimental results could be related to many factors, including the difference between 2D and 3D situations, the SNOM tip shape and geometry, the size and resolution of the scan (which was clear in **Fig. 6.11**, for *Aula* valves), and any structural variability between the simulation model and the measured valves.

The results from **Chapters 4**, **5**, and **6** highlight the importance of the thicker parts, such as the nodules, in photobiology. The generated PJs from these parts remain inside the frustule and may induce a light sensing mechanism that may explain phenomena, such as the phototactic in raphid pennates.

Moreover, when considering the pore arrays featuring the valves/girdle bands to investigate their possible PC features, many previous works assumed a specific lattice arrangement based on the bare-hand/-eye assignments, and often overlooking the structural complexity and the presence of additional periodicities and symmetries that could influence the associated PC features. For this, **Appendix B** offers a novel method to study the 2D periodicities and symmetries of pore arrays. By applying this method on a number of examples, the possible presence of distinct 2D Bravais lattices was also evident. From the study, it is clear that the valves of some diatoms cannot be simply approximated to a PC slab due to the presence of additional symmetries. Such valves then can be seen as a merge of distinct smaller PCs. Future developments for this method are recommended to enable judging the perfection level in a more precise way.

Furthermore, utilizing diatom valves in optical applications as an eco-friendly and likely cost-effective alternative to synthetic materials and structures can be seen as a major motivation to understand more about their light modulation capabilities. In this thesis, the incorporation of distinct diatom valves into optoelectronic and photonic devices has been preliminary investigated. In **Chapter 7**, a novel method has been developed to fabricate diatom-based SERS hybrid substrates with a smooth ultrathin gold film enabling study of the influence of the valves' ultrastructure on the SERS enhancement magnitude. In future, this method could enable screening different valve designs (belonging to distinct species), seeking the design that contributes the best SERS enhancement for fabricating efficient diatom-based SERS sensors for commercial use. Additionally, **Appendix C** shows a preliminary attempt to incorporate diatom valves into organic MISM photodetectors. Still, more efforts are needed to enhance the process and choose a better method to incorporate these valves into such complicated devices.

Finally, this thesis offers novel insights into understanding the light modulation capabilities of diatom valves/frustules, successfully answering some questions that have stood in the field for several years. The thesis also developed many novel numerical and experimental approaches that could facilitate future studies. The observations from both numerical analysis and experimental work raised many more questions. More understanding is still needed to complete the picture, prove the photobiology roles, and enable commercial optical applications based on diatom valves/girdle bands.

References

1. Jenkins, F.A.; White, H.E. *Fundamentals of Optics*; McGraw-Hill, 2001; ISBN 0072561912.
2. Saleh, B.; Teich, M. *Fundamentals of Photonics*; 3rd ed.; john Wiley & sons, 2019; ISBN 9780471213741.
3. Sukhoivanov, I.A.; Guryev, I. V. *Photonic Crystals: Physics and Practical Modeling*; Springer Berlin Heidelberg: Berlin, Heidelberg, 2009; Vol. 152; ISBN 978-3-642-02645-4.
4. Yang, Y.; Seong, J.; Choi, M.; Park, J.; Kim, G.; Kim, H.; Jeong, J.; Jung, C.; Kim, J.; Jeon, G.; et al. Integrated Metasurfaces for Re-Envisioning a near-Future Disruptive Optical Platform. *Light Sci Appl* **2023**, *12*, 152, doi:10.1038/s41377-023-01169-4.
5. Nogueras, J.M.D.T. *Nanofabrication: Nanolithography Techniques and Their Applications*; IOP Publishing Ltd, 2020; ISBN 9780750326087.
6. Gates, B.D.; Xu, Q.; Stewart, M.; Ryan, D.; Willson, C.G.; Whitesides, G.M. New Approaches to Nanofabrication: Molding, Printing, and Other Techniques. *Chem Rev* **2005**, *105*, 1171–1196, doi:10.1021/cr030076o.
7. Gould, S.J. The Evolution of Life on the Earth. *Sci Am* **1994**, *271*, 84–91.
8. Badarnah, L. Light Management Lessons from Nature for Building Applications. *Procedia Eng* **2016**, *145*, 595–602, doi:10.1016/j.proeng.2016.04.049.
9. Parker, A.R.; Townley, H.E. Biomimetics of Photonic Nanostructures. *Nat Nanotechnol* **2007**, *2*, 347–353, doi:10.1038/nnano.2007.152.
10. Vukusic, P.; Sambles, J.R. Photonic Structures in Biology. *Nature* **2003**, *424*, 852–855, doi:10.1038/nature01941.
11. Jacobs, M.; Lopez-Garcia, M.; Phrathep, O.-P.; Lawson, T.; Oulton, R.; Whitney, H.M. Photonic Multilayer Structure of Begonia Chloroplasts Enhances Photosynthetic Efficiency. *Nat Plants* **2016**, *2*, 16162, doi:10.1038/nplants.2016.162.
12. Vignolini, S.; Moyroud, E.; Glover, B.J.; Steiner, U. Analysing Photonic Structures in Plants. *J R Soc Interface* **2013**, *10*, 20130394, doi:10.1098/rsif.2013.0394.
13. Kolle, M.; Steiner, U. Structural Color in Animals. In *Encyclopedia of Nanotechnology*; Springer Netherlands: Dordrecht, 2012; pp. 2514–2527 ISBN 978-90-481-9751-4.
14. Himel, M.H.; Sikder, B.; Ahmed, T.; Choudhury, S.M. Biomimicry in Nanotechnology: A Comprehensive Review. *Nanoscale Adv* **2023**, *5*, 596–614, doi:10.1039/D2NA00571A.
15. Primrose, S.B. *Biomimetics: Nature-Inspired Design and Innovation*; Wiley-Blackwell, 2020; ISBN 9781119683322.
16. Bhushan, B. Biomimetics: Lessons from Nature–an Overview. *Philos Trans A Math Phys Eng Sci* **2009**, *367*, 1445–1486, doi:10.1098/rsta.2009.0011.
17. Round, F.E.; Crawford, R.M.; Mann, D.G. *Diatoms: Biology and Morphology of the Genera*; Cambridge university press, 1990; ISBN 0521363187.
18. von Quillfeldt, C.H. Common Diatom Species in Arctic Spring Blooms: Their Distribution and Abundance. *Bot Mar* **2000**, *43*, 499–516, doi:10.1515/BOT.2000.050.
19. Pumas, C.; Pruetiworanan, S.; Peerapornpisal, Y. Diatom Diversity in Some Hot Springs of Northern Thailand. *Botanica* **2018**, *24*, 69–86, doi:10.2478/botlit-2018-0007.
20. Fazlutdinova, A.; Gabidullin, Y.; Allaguvatova, R.; Gaysina, L. Diatoms in Kamchatka's Hot Spring Soils. *Diversity (Basel)* **2020**, *12*, 435, doi:10.3390/d12110435.
21. Poulíčková, A.; Hašler, P. Aerophytic Diatoms from Caves in Central Moravia (Czech Republic). *Preslia* **2007**, 185–204.
22. Prasetiya, F.S.; Foret, M.; Deschênes, J.-S.; Gastineau, R.; Mouget, J.-L.; Tremblay, R. Semi-Continuous System for Benthic Diatom Cultivation and Marennine Production. *Algal Res* **2022**, *62*, 102633, doi:10.1016/j.algal.2022.102633.
23. Wang, J.K.; Seibert, M. Prospects for Commercial Production of Diatoms. *Biotechnol Biofuels* **2017**, *10*, doi:10.1186/s13068-017-0699-y.
24. Matsumoto, M.; Nojima, D.; Nonoyama, T.; Ikeda, K.; Maeda, Y.; Yoshino, T.; Tanaka, T. Outdoor Cultivation of Marine Diatoms for Year-Round Production of Biofuels. *Mar Drugs* **2017**, *15*, 94, doi:10.3390/md15040094.
25. Marella, T.K.; Tiwari, A. Cultivation of Diatoms in Photobioreactors. In *Current Developments in Biotechnology and Bioengineering*; Elsevier, 2023; pp. 207–228.

26. Spaulding, S.A.; Potapova, M.G.; Bishop, I.W.; Lee, S.S.; Gasperak, T.S.; Jovanoska, E.; Furey, P.C.; Edlund, M.B. *Diatoms.Org* : Supporting Taxonomists, Connecting Communities. *Diatom Research* **2021**, *36*, 291–304, doi:10.1080/0269249X.2021.2006790.
27. Collier, A.; Murphy, A. Very Small Diatoms: Preliminary Notes and Description of *Chaetoceros Galvestonensis*. *Science (1979)* **1962**, *136*, 780–781, doi:10.1126/science.136.3518.780.
28. Kemp, A.E.S.; Pearce, R.B.; Grigorov, I.; Rance, J.; Lange, C.B.; Quilty, P.; Salter, I. Production of Giant Marine Diatoms and Their Export at Oceanic Frontal Zones: Implications for Si and C Flux from Stratified Oceans. *Global Biogeochem Cycles* **2006**, *20*, GB4S04, doi:10.1029/2006GB002698.
29. Round, F.E. Forms of the Giant Diatom Ethmodiscus from the Pacific and Indian Oceans. *Phycologia* **1980**, *19*, 307–316, doi:10.2216/i0031-8884-19-4-307.1.
30. Topal, E.; Rajendran, H.; Zgłobicka, I.; Gluch, J.; Liao, Z.; Clausner, A.; Kurzydłowski, K.; Zschech, E. Numerical and Experimental Study of the Mechanical Response of Diatom Frustules. *Nanomaterials* **2020**, *10*, 959, doi:10.3390/nano10050959.
31. Hamm, C.E.; Merkel, R.; Springer, O.; Jurkojc, P.; Maier, C.; Prechtel, K.; Smetacek, V. Architecture and Material Properties of Diatom Shells Provide Effective Mechanical Protection. *Nature* **2003**, *421*, 841–843, doi:10.1038/nature01416.
32. Soleimani, M.; van den Broek, S.J.J.; Joosten, R.R.M.; van Hazendonk, L.S.; Maddala, S.P.; van Breemen, L.C.A.; van Benthem, R.A.T.M.; Friedrich, H. Investigating the Morphology and Mechanics of Biogenic Hierarchical Materials at and below Micrometer Scale. *Nanomaterials* **2022**, *12*, 1549, doi:10.3390/nano12091549.
33. Cvjetinovic, J.; Luchkin, S.Yu.; Statnik, E.S.; Davidovich, N.A.; Somov, P.A.; Salimon, A.I.; Korsunsky, A.M.; Gorin, D.A. Revealing the Static and Dynamic Nanomechanical Properties of Diatom Frustules—Nature's Glass Lace. *Sci Rep* **2023**, *13*, 5518, doi:10.1038/s41598-023-31487-x.
34. Rosengarten, G.; Herringer, J.W. Interactions of Diatoms with Their Fluid Environment. In *Diatom Nanotechnology: Progress and Emerging Applications*; Losic, D., Ed.; The Royal Society of Chemistry, 2017; pp. 14–54.
35. Herringer, J.W.; Lester, D.; Dorrington, G.E.; Rosengarten, G. Can Diatom Girdle Band Pores Act as a Hydrodynamic Viral Defense Mechanism? *J Biol Phys* **2019**, *45*, 213–234, doi:10.1007/s10867-019-09525-5.
36. De Tommasi, E. Light Manipulation by Single Cells: The Case of Diatoms. *J spectrosc* **2016**, *2016*, 1–13, doi:10.1155/2016/2490128.
37. De Tommasi, E.; Congestri, R.; Dardano, P.; De Luca, A.C.; Managò, S.; Rea, I.; De Stefano, M. UV-Shielding and Wavelength Conversion by Centric Diatom Nanopatterned Frustules. *Sci Rep* **2018**, *8*, 16285, doi:10.1038/s41598-018-34651-w.
38. Malviya, S.; Scalco, E.; Audic, S.; Vincent, F.; Veluchamy, A.; Poulain, J.; Wincker, P.; Iudicone, D.; De Vargas, C.; Bittner, L.; et al. Insights into Global Diatom Distribution and Diversity in the World's Ocean. *Proc Natl Acad Sci U S A* **2016**, *113*, E1516–E1525, doi:10.1073/pnas.1509523113.
39. Sims, P.A.; Mann, D.G.; Medlin, L.K. Evolution of the Diatoms: Insights from Fossil, Biological and Molecular Data. *Phycologia* **2006**, *45*, 361–402, doi:10.2216/05-22.1.
40. Mann, D.G.; Crawford, R.M.; Round, F.E. Bacillariophyta. In *Handbook of the Protists*; Archibald, J.M., Simpson, A.G.B., Slamovits, C.H., Eds.; Springer International Publishing: Cham, 2017; pp. 205–266.
41. Losic, D.; Mitchell, J.G.; Lal, R.; Voelcker, N.H. Rapid Fabrication of Micro- and Nanoscale Patterns by Replica Molding from Diatom Biosilica. *Adv Funct Mater* **2007**, *17*, 2439–2446, doi:10.1002/adfm.200600872.
42. Fuhrmann, T.; Landwehr, S.; El Rharbi-Kucki, M.; Sumper, M. Diatoms as Living Photonic Crystals. *Appl Phys B* **2004**, *78*, 257–260, doi:10.1007/s00340-004-1419-4.
43. Goessling, J.W.; Santiago González, A.A.; Paul Raj, V.S.; Ashworth, M.P.; Manning, S.R.; Lopez-Garcia, M. Biosilica Slab Photonic Crystals as an Alternative to Cleanroom Nanofabrication? *Faraday Discuss* **2020**, *223*, 261–277, doi:10.1039/D0FD00031K.
44. Ghobara, M.M.; Mazumder, N.; Vinayak, V.; Reissig, L.; Gebeshuber, I.C.; Tiffany, M.A.; Gordon, R. On Light and Diatoms: A Photonics and Photobiology Review. In *Diatoms: Fundamentals and Applications*; Seckbach, J., Gordon, R., Eds.; Wiley-Scrivener, 2019; pp. 129–189.

45. Goessling, J.W.; Yanyan, S.; Kühl, M.; Ellegaard, M. Frustule Photonics and Light Harvesting Strategies in Diatoms. In *Diatom Morphogenesis*; Annenkov, V., Seckback, J., Gordon, R., Eds.; Wiley-Scrivener, 2021; pp. 269–300.
46. De Tommasi, E.; Rogato, A.; Caratelli, D.; Mescia, L.; Gielis, J. Following the Photons Route: Mathematical Models Describing the Interaction of Diatoms with Light. In *The Mathematical Biology of Diatoms*; Pappas, J.L., Ed.; Wiley-Scrivener, 2023; pp. 343–391.
47. Ruggiero, M.A.; Gordon, D.P.; Orrell, T.M.; Bailly, N.; Bourgoin, T.; Brusca, R.C.; Cavalier-Smith, T.; Guiry, M.D.; Kirk, P.M. A Higher Level Classification of All Living Organisms. *PLoS One* **2015**, *10*, e0119248, doi:10.1371/journal.pone.0119248.
48. Armbrust, E.V. The Life of Diatoms in the World's Oceans. *Nature* **2009**, *459*, 185–192, doi:10.1038/nature08057.
49. Smetacek, V. Making Sense of Ocean Biota: How Evolution and Biodiversity of Land Organisms Differ from That of the Plankton. *J Biosci* **2012**, *37*, 589–607, doi:10.1007/s12038-012-9240-4.
50. Chepurnov, V.A.; Mann, D.G.; Sabbe, K.; Vyverman, W. Experimental Studies on Sexual Reproduction in Diatoms. *Int Rev Cytol* **2004**, *237*, 91–154, doi:10.1016/S0074-7696(04)37003-8.
51. Poulíčková, A.; Mann, D.G. Diatom Sexual Reproduction and Life Cycles. In *Diatoms: Fundamentals and Applications*; Seckbach, J., Gordon, R., Eds.; Wiley-Scrivener, 2019; pp. 245–272.
52. Mann, D.G.; Vanormelingen, P. An Inordinate Fondness? The Number, Distributions, and Origins of Diatom Species. *J Eukaryot Microbiol* **2013**, *60*, 414–420, doi:10.1111/jeu.12047.
53. Mann, D.G.; Droop, S.J.M. 3. Biodiversity, Biogeography and Conservation of Diatoms. *Hydrobiologia* **1996**, *336*, 19–32, doi:10.1007/BF00010816.
54. Hohmann-Marriott, M.F.; Blankenship, R.E. Evolution of Photosynthesis. *Annu Rev Plant Biol* **2011**, *62*, 515–548, doi:10.1146/annurev-arplant-042110-103811.
55. Benoiston, A.S.; Ibarbalz, F.M.; Bittner, L.; Guidi, L.; Jahn, O.; Dutkiewicz, S.; Bowler, C. The Evolution of Diatoms and Their Biogeochemical Functions. *Philos Trans R Soc Lond B Biol Sci* **2017**, *372*, doi:10.1098/rstb.2016.0397.
56. Lazarus, D.; Barron, J.; Renaudie, J.; Diver, P.; Türke, A. Cenozoic Planktonic Marine Diatom Diversity and Correlation to Climate Change. *PLoS One* **2014**, *9*, e84857, doi:10.1371/journal.pone.0084857.
57. Tesson, B.; Hildebrand, M. Characterization and Localization of Insoluble Organic Matrices Associated with Diatom Cell Walls: Insight into Their Roles during Cell Wall Formation. *PLoS One* **2013**, *8*, e61675, doi:10.1371/journal.pone.0061675.
58. Cox, E.J. Diatom Identification in the Face of Changing Species Concepts and Evidence of Phenotypic Plasticity. *J Micropalaeontol* **2014**, *33*, 111–120, doi:10.1144/jmpaleo2014-014.
59. Cox, E.J. Girdle Band Structure in the Diatom Genus Proschkinia (Bacillariophyta)—Another Potential Adaptation to Stabilise a Deep Cingulum? *Diversity (Basel)* **2023**, *15*, 734, doi:10.3390/d15060734.
60. Ghobara, M.M.; Gordon, R.; Reissig, L. The Mesopores of Raphid Pennate Diatoms: Toward Natural Controllable Anisotropic Mesoporous Silica Microparticles. In *Diatom morphogenesis*; Annenkov, V., Seckback, J., Gordon, R., Eds.; Wiley-Scrivener, 2021; pp. 383–409.
61. Losic, D.; Rosengarten, G.; Mitchell, J.G.; Voelcker, N.H. Pore Architecture of Diatom Frustules: Potential Nanostructured Membranes for Molecular and Particle Separations. *J Nanosci Nanotechnol* **2006**, *6*, 982–989, doi:10.1166/jnn.2006.174.
62. Jantschke, A.; Fischer, C.; Hensel, R.; Braun, H.-G.; Brunner, E. Directed Assembly of Nanoparticles to Isolated Diatom Valves Using the Non-Wetting Characteristics after Pyrolysis. *Nanoscale* **2014**, *6*, 11637–11645, doi:10.1039/C4NR02662D.
63. Babenko, I.; Friedrich, B.M.; Kröger, N. Structure and Morphogenesis of the Frustule. In *The Molecular Life of Diatoms*; Falciatore, A., Mock, T., Eds.; Springer International Publishing: Cham, 2022; pp. 287–312.
64. Zurzolo, C. Exploring Bioinorganic Pattern Formation in Diatoms. A Story of Polarized Trafficking. *Plant Physiol* **2001**, *127*, 1339–1345, doi:10.1104/pp.127.4.1339.
65. Annenkov, V.; Seckback, J.; Gordon, R. *Diatom Morphogenesis*; Wiley-Scrivener, 2021; ISBN 9781119487951.
66. Gordon, R.; Drum, R.W. The Chemical Basis of Diatom Morphogenesis. *Int rev cytol* **1994**, *150*, 243–372, doi:10.1016/S0074-7696(08)61544-2.

67. Kolbe, F.; Brunner, E. Silicic Acid Uptake and Storage by Diatoms. In *The Molecular Life of Diatoms*; Falciatore, A., Mock, T., Eds.; Springer International Publishing: Cham, 2022; pp. 345–365.
68. Hildebrand, M.; Lerch, S.J.L.; Shrestha, R.P. Understanding Diatom Cell Wall Silicification—Moving Forward. *Front Mar Sci* **2018**, *5*, 1–19, doi:10.3389/fmars.2018.00125.
69. Kröger, N. Biomolecules Involved in Frustule Biogenesis and Function. In *The Molecular Life of Diatoms*; Falciatore, A., Mock, T., Eds.; Springer International Publishing: Cham, 2022; pp. 313–343.
70. Kröger, N.; Poulsen, N. Biosilica Nanofabrication in Diatoms: The Structures and Properties of Regulatory Silaffins. *MRS Proceedings* **2005**, *873*, K1.2, doi:10.1557/PROC-873-K1.2.
71. Tesson, B.; Hildebrand, M. Extensive and Intimate Association of the Cytoskeleton with Forming Silica in Diatoms: Control over Patterning on the Meso- and Micro-Scale. *PLoS One* **2010**, *5*, e14300, doi:10.1371/journal.pone.0014300.
72. Parkinson, J.; Brechet, Y.; Gordon, R. Centric Diatom Morphogenesis: A Model Based on a DLA Algorithm Investigating the Potential Role of Microtubules. *Biochimica et Biophysica Acta (BBA) - Molecular Cell Research* **1999**, *1452*, 89–102, doi:10.1016/S0167-4889(99)00116-0.
73. Yekaterina, B.; Ksenia, G.; Maria, P.; Alexey, M.; Yelena, L. Anomalies in the Valve Morphogenesis of the Centric Diatom Alga *Aulacoseira Islandica* Caused by Microtubule Inhibitors. *Biol Open* **2018**, bio035519, doi:10.1242/bio.035519.
74. Tesson, B.; Lerch, S.J.L.; Hildebrand, M. Characterization of a New Protein Family Associated With the Silica Deposition Vesicle Membrane Enables Genetic Manipulation of Diatom Silica. *Sci Rep* **2017**, *7*, 13457, doi:10.1038/s41598-017-13613-8.
75. Flower, R.J. Diatomites: Their Formation, Distribution, and Uses. In *Encyclopedia of Quaternary Science: Second Edition*; Elsevier Inc., 2013; pp. 501–506 ISBN 9780444536433.
76. Galal Mors, H.E. Diatomite: Its Characterization, Modifications and Applications. *Asian J Mater Sci* **2010**, *2*, 121–136, doi:10.3923/ajmskr.2010.121.136.
77. Ghobara, M.M.; Mohamed, A. Diatomite in Use: Nature, Modifications, Commercial Applications and Prospective Trends. In *Diatoms: Fundamentals and Applications*; Seckbach, J., Gordon, R., Eds.; Wiley-Scrivener, 2019; pp. 471–509.
78. Dolley, T.; Moyle, P. History and Overview of the U.S. Diatomite Mining Industry, with Emphasis on the Western United States. In *Contributions to Industrial-Minerals Research*; Bliss, J.D., Moyle, P.R., Long, K.R., Eds.; U.S. Geological Survey Bulletin 2209, 2003; pp. E1–E8.
79. Harwood, D.M. Diatomite. In *The Diatoms: Applications for the Environmental and Earth Sciences*; Smol, J.P., Stoermer, E.F., Eds.; Cambridge University Press, 2010; pp. 570–574.
80. Dolley, T.P. Diatomite. In *U.S. Geological Survey Minerals Yearbook*; U. S. Geological Survey, 2000; Vol. 25, pp. 1–6.
81. Crangle, R.D. Diatomite. In *2018 Minerals yearbook*; U.S. Geological Survey, 2018; Vol. 22, pp. 1–6.
82. Smol, J.P.; Stoermer, E.F. *The Diatoms: Applications for the Environmental and Earth Sciences*; 2nd ed.; Cambridge University Press, 2010; ISBN 9781107564961.
83. Mishra, M.; Singh, S.K.; Bhardwaj, A.; Kumar, L.; Singh, M.K.; Sundaram, S. Development of a Diatom-Based Photoluminescent Immunosensor for the Early Detection of Karnal Bunt Disease of Wheat Crop. *ACS Omega* **2020**, *5*, 8251–8257, doi:10.1021/acsomega.0c00551.
84. Selvaraj, V.; Thomas, N.; Anthuvan, A.J.; Nagamony, P.; Chinnuswamy, V. Amine-Functionalized Diatom Frustules: A Platform for Specific and Sensitive Detection of Nitroaromatic Explosive Derivative. *Environ Sci Pollut Res* **2018**, *25*, 20540–20549, doi:10.1007/s11356-017-0916-z.
85. Kong, X.; Chong, X.; Squire, K.; Wang, A.X. Microfluidic Diatomite Analytical Devices for Illicit Drug Sensing with Ppb-Level Sensitivity. *Sens Actuators B Chem* **2018**, *259*, 587–595, doi:10.1016/j.snb.2017.12.038.
86. Lin, K.-C.; Kunduru, V.; Bothara, M.; Rege, K.; Prasad, S.; Ramakrishna, B.L. Biogenic Nanoporous Silica-Based Sensor for Enhanced Electrochemical Detection of Cardiovascular Biomarkers Proteins. *Biosens Bioelectron* **2010**, *25*, 2336–2342, doi:10.1016/j.bios.2010.03.032.
87. Wang, Z.; Gong, D.; Cai, J. Diatom Frustule Array for Flow-through Enhancement of Fluorescent Signal in a Microfluidic Chip. *Micromachines (Basel)* **2021**, *12*, 1017, doi:10.3390/mi12091017.

88. Gannavarapu, K.P.; Ganesh, V.; Thakkar, M.; Mitra, S.; Dandamudi, R.B. Nanostructured Diatom-ZrO2 Composite as a Selective and Highly Sensitive Enzyme Free Electrochemical Sensor for Detection of Methyl Parathion. *Sens Actuators B Chem* **2019**, *288*, 611–617, doi:10.1016/j.snb.2019.03.036.
89. Garapati, M.S.; Vijaya Kumar Saroja, A.P.; Sundara, R. Diatom-Frustule Catalyst Supported Multiwalled Carbon Nanotubes: Scalable and Cost-Effective Synthesis and Stable Anode for Lithium-Ion Battery. *Mater Sci Eng B* **2020**, *261*, 114695, doi:10.1016/j.mseb.2020.114695.
90. Mina-Villarreal, M.C.; Briceño, S.; Vizuete, K.; Debut, A.; González, G. Growth of Carbon Nanotubes and Carbon Spheres on Diatoms. *J Porous Mater* **2022**, *30*, 343–349, doi:10.1007/s10934-022-01345-8.
91. Davis, S.C.; Sheppard, V.C.; Begum, G.; Cai, Y.; Fang, Y.; Berrigan, J.D.; Kröger, N.; Sandhage, K.H. Rapid Flow-Through Biocatalysis with High Surface Area, Enzyme-Loaded Carbon and Gold-Bearing Diatom Frustule Replicas. *Adv Funct Mater* **2013**, *23*, 4611–4620, doi:10.1002/adfm.201203758.
92. Kumari, S.; Min, K.H.; Kanth, B.K.; Jang, E.K.; Pack, S.P. Production of TiO2-Deposited Diatoms and Their Applications for Photo-Catalytic Degradation of Aqueous Pollutants. *Biotechnol Bioprocess Eng* **2020**, *25*, 758–765, doi:10.1007/s12257-020-0019-4.
93. Ouwehand, J.; van Eynde, E.; de Canck, E.; Lenaerts, S.; Verberckmoes, A.; van der Voort, P. Titania-Functionalized Diatom Frustules as Photocatalyst for Indoor Air Purification. *Appl Catal B* **2018**, *226*, 303–310, doi:10.1016/j.apcatb.2017.12.063.
94. Kim, K.; Liang, Z.; Liu, M.; Fan, D.E. Biobased High-Performance Rotary Micromotors for Individually Reconfigurable Micromachine Arrays and Microfluidic Applications. *ACS Appl Mater Interfaces* **2017**, *9*, 6144–6152, doi:10.1021/acsami.6b13997.
95. Guo, J.; Liang, Z.; Huang, Y.; Kim, K.; Vandeventer, P.; Fan, D. Acceleration of Biomolecule Enrichment and Detection with Rotationally Motorized Opto-Plasmonic Microsensors and the Working Mechanism. *ACS Nano* **2020**, *14*, 15204–15215, doi:10.1021/acsnano.0c05429.
96. Oliveira, N.M.; Reis, R.L.; Mano, J.F. Superhydrophobic Surfaces Engineered Using Diatomaceous Earth. *ACS Appl Mater Interfaces* **2013**, *5*, 4202–4208, doi:10.1021/am4003759.
97. Li, F.; Xing, Y.; Huang, M.; Li, K.L.; Yu, T.T.; Zhang, Y.X.; Losic, D. MnO_2 Nanostructures with Three-Dimensional (3D) Morphology Replicated from Diatoms for High-Performance Supercapacitors. *J Mater Chem A Mater* **2015**, *3*, 7855–7861, doi:10.1039/C5TA00634A.
98. Jeffryes, C.; Campbell, J.; Li, H.; Jiao, J.; Rorrer, G. The Potential of Diatom Nanobiotechnology for Applications in Solar Cells, Batteries, and Electroluminescent Devices. *Energy Environ Sci* **2011**, *4*, 3930, doi:10.1039/c0ee00306a.
99. Terracciano, M.; De Stefano, L.; Rea, I. Diatoms Green Nanotechnology for Biosilica-Based Drug Delivery Systems. *Pharmaceutics* **2018**, *10*, 242, doi:10.3390/pharmaceutics10040242.
100. Phogat, S.; Saxena, A.; Kapoor, N.; Aggarwal, C.; Tiwari, A. Diatom Mediated Smart Drug Delivery System. *J Drug Deliv Sci Technol* **2021**, *63*, 102433, doi:10.1016/j.jddst.2021.102433.
101. Losic, D. *Diatom Nanotechnology: Progress and Emerging Applications*; Royal Society of Chemistry: Cambridge, 2017; ISBN 978-1-78262-932-0.
102. Reissig, L.; Ghobara, M.; Maibohm, C.; Goessling, J. A Journey to Mars with Diatoms on Board. In *Diatom Photosynthesis: From Primary Production to High-Value Molecules*; Goessling, J.W., Serôdio, J., Lavaud, J., Eds.; Wiley-Scrivener, 2024; pp. 551–581.
103. Beninger, P.G. What Makes Diatoms Attractive for Suspensivores? The Organic Casing and Associated Organic Molecules of Coscinodiscus Perforatus Are Quality Cues for the Bivalve Pecten Maximus. *J Plankton Res* **2004**, *27*, 11–17, doi:10.1093/plankt/fbh156.
104. Wang, Y.; Cai, J.; Jiang, Y.; Jiang, X.; Zhang, D. Preparation of Biosilica Structures from Frustules of Diatoms and Their Applications: Current State and Perspectives. *Appl Microbiol Biotechnol* **2013**, *97*, 453–460, doi:10.1007/s00253-012-4568-0.
105. Su, Y.; Lundholm, N.; Ellegaard, M. Effects of Abiotic Factors on the Nanostructure of Diatom Frustules—Ranges and Variability. *Appl Microbiol Biotechnol* **2018**, *102*, 5889–5899, doi:10.1007/s00253-018-9087-1.
106. Reid, A.; Buchanan, F.; Julius, M.; Walsh, P.J. A Review on Diatom Biosilicification and Their Adaptive Ability to Uptake Other Metals into Their Frustules for Potential Application in Bone Repair. *J Mater Chem B* **2021**, *9*, 6728–6737, doi:10.1039/d1tb00322d.

107. Brzozowska, W.; Sprynskyy, M.; Wojtczak, I.; Dabek, P.; Witkowski, A.; Buszewski, B. “Outsourcing” Diatoms in Fabrication of Metal-Doped 3D Biosilica. *Materials* **2020**, *13*, 2576, doi:10.3390/ma13112576.
108. Butcher, K.S.A.; Ferris, J.M.; Phillips, M.R.; Wintrebert-Fouquet, M.; Jong Wah, J.W.; Jovanovic, N.; Vyverman, W.; Chepurnov, V.A. A Luminescence Study of Porous Diatoms. *Mater Sci Eng C* **2005**, *25*, 658–663, doi:10.1016/j.msec.2005.06.049.
109. Arteaga-Larios, N. V.; Nahmad, Y.; Navarro-Contreras, H.R.; Encinas, A.; Viridiana García-Meza, J. Photoluminescence Shift in Frustules of Two Pennate Diatoms and Nanostructural Changes to Their Pores. *Luminescence* **2014**, *29*, 969–976, doi:10.1002/bio.2646.
110. Mazumder, N.; Gogoi, A.; Kalita, R.D.; Ahmed, G.A.; Buragohain, A.K.; Choudhury, A. Luminescence Studies of Fresh Water Diatom Frustules. *Indian Journal of Physics* **2010**, *84*, 665–669, doi:10.1007/s12648-010-0068-1.
111. De Stefano, L.; Rendina, I.; De Stefano, M.; Bismuto, A.; Maddalena, P. Marine Diatoms as Optical Chemical Sensors. *Appl Phys Lett* **2005**, *87*, 233902, doi:10.1063/1.2140087.
112. Colder, A.; Huisken, F.; Trave, E.; Ledoux, G.; Guillois, O.; Reynaud, C.; Hofmeister, H.; Pippel, E. Strong Visible Photoluminescence from Hollow Silica Nanoparticles. *Nanotechnology* **2004**, *15*, L1–L4, doi:10.1088/0957-4484/15/3/L01.
113. Glinka, Y.D.; Lin, S.-H.; Hwang, L.-P.; Chen, Y.-T. Photoluminescence Spectroscopy of Silica-Based Mesoporous Materials. *J Phys Chem B* **2000**, *104*, 8652–8663, doi:10.1021/jp0009599.
114. Gale, D.K.; Jeffryes, C.; Gutu, T.; Jiao, J.; Chang, C.; Rorrer, G.L. Thermal Annealing Activates Amplified Photoluminescence of Germanium Metabolically Doped in Diatom Biosilica. *J Mater Chem* **2011**, *21*, 10658–10665, doi:10.1039/c1jm10861a.
115. Ragni, R.; Scotognella, F.; Vona, D.; Moretti, L.; Altamura, E.; Ceccone, G.; Mehn, D.; Cicco, S.R.; Palumbo, F.; Lanzani, G.; et al. Hybrid Photonic Nanostructures by In Vivo Incorporation of an Organic Fluorophore into Diatom Algae. *Adv Funct Mater* **2018**, *28*, 1706214, doi:10.1002/adfm.201706214.
116. Townley, H.E.; Woon, K.L.; Payne, F.P.; White-Cooper, H.; Parker, A.R. Modification of the Physical and Optical Properties of the Frustule of the Diatom *Coscinodiscus Wailesii* by Nickel Sulfate. *Nanotechnology* **2007**, *18*, 295101, doi:10.1088/0957-4484/18/29/295101.
117. Sukhoivanov, I.A.; Guryev, I. V. *Photonic Crystals: Physics and Practical Modeling*; Springer Berlin Heidelberg: Berlin, Heidelberg, 2009; ISBN 978-3-642-02645-4.
118. Joannopoulos, J.D.; Villeneuve, P.R.; Fan, S. Photonic Crystals: Putting a New Twist on Light. *Nature* **1997**, *386*, 143–149, doi:10.1038/386143a0.
119. Gangwar, R.K.; Pathak, A.K.; Kumar, S. Recent Progress in Photonic Crystal Devices and Their Applications: A Review. *Photonics* **2023**, *10*, 1199, doi:10.3390/photonics10111199.
120. Joannopoulos, J.D.; Johnson, S.G.; Winn, J.N.; Meade, R.D. *Photonic Crystals: Molding the Flow of Light*; Second.; Princeton University Press, 2008; ISBN 978-0691124568.
121. Vigneron, J.P.; Simonis, P. Natural Photonic Crystals. *Physica B Condens Matter* **2012**, *407*, 4032–4036, doi:10.1016/j.physb.2011.12.130.
122. Pappas, J.L.; Tiffany, M.A.; Gordon, R. The Uncanny Symmetry of Some Diatoms and Not of Others: A Multi-Scale Morphological Characteristic and a Puzzle for Morphogenesis. In *Diatom Morphogenesis*; Annenkov, V., Seckback, J., Gordon, R., Eds.; Wiley-Scrivener, 2021; pp. 19–67.
123. Ghobara, M.M.; Tiffany, M.A.; Gordon, R.; Reissig, L. Diatom Pore Arrays’ Periodicities and Symmetries in the Euclidean Plane: Nature Between Perfection and Imperfection. In *Diatom Morphogenesis*; Annenkov, V., Seckback, J., Gordon, R., Eds.; Wiley-Scrivener, 2021; pp. 117–158.
124. Yamanaka, S.; Yano, R.; Usami, H.; Hayashida, N.; Ohguchi, M.; Takeda, H.; Yoshino, K. Optical Properties of Diatom Silica Frustule with Special Reference to Blue Light. *J Appl Phys* **2008**, *103*, 074701, doi:10.1063/1.2903342.
125. Goessling, J.W.; Wardley, W.P.; Lopez-Garcia, M. Highly Reproducible, Bio-Based Slab Photonic Crystals Grown by Diatoms. *Adv Sci* **2020**, *7*, 1903726, doi:10.1002/advs.201903726.
126. D’Mello, Y.; Bernal, S.; Petrescu, D.; Skoric, J.; Andrews, M.; Plant, D. V. Solar Energy Harvesting Mechanisms of the Frustules of Nitzschia Filiformis Diatoms. *Opt Mater Express* **2022**, *12*, 4665–4681, doi:10.1364/OME.473109.

127. Kieu, K.; Li, C.; Fang, Y.; Cohoon, G.; Herrera, O.D.; Hildebrand, M.; Sandhage, K.H.; Norwood, R.A. Structure-Based Optical Filtering by the Silica Microshell of the Centric Marine Diatom Coscinodiscus Wailesii. *Opt Express* **2014**, *22*, 15992–15999, doi:10.1364/OE.22.015992.
128. Noyes, J.; Sumper, M.; Vukusic, P. Light Manipulation in a Marine Diatom. *J Mater Res* **2008**, *23*, 3229–3235, doi:10.1557/JMR.2008.0381.
129. De Stefano, L.; Rea, I.; Rendina, I.; De Stefano, M.; Moretti, L. Lensless Light Focusing with the Centric Marine Diatom Coscinodiscus Walesii. *Opt Express* **2007**, *15*, 18082–18088, doi:10.1364/OE.15.018082.
130. De Tommasi, E.; Rea, I.; De Stefano, L.; Dardano, P.; Di Caprio, G.; Ferrara, M.A.; Coppola, G. Optics with Diatoms: Towards Efficient, Bioinspired Photonic Devices at the Micro-Scale. In Proceedings of the Optical Methods for Inspection, Characterization, and Imaging of Biomaterials; 2013; p. 87920O.
131. Ferrara, M.A.; Dardano, P.; De Stefano, L.; Rea, I.; Coppola, G.; Rendina, I.; Congestri, R.; Antonucci, A.; De Stefano, M.; De Tommasi, E. Optical Properties of Diatom Nanostructured Biosilica in Arachnoidiscus Sp: Micro-Optics from Mother Nature. *PLoS One* **2014**, *9*, e103750, doi:10.1371/journal.pone.0103750.
132. De Tommasi, E.; De Luca, A.C.; Lavanga, L.; Dardano, P.; De Stefano, M.; De Stefano, L.; Langella, C.; Rendina, I.; Dholakia, K.; Mazilu, M. Biologically Enabled Sub-Diffractive Focusing. *Opt Express* **2014**, *22*, 27214–27227, doi:10.1364/OE.22.027214.
133. Maibohm, C.; Friis, S.M.M.; Ellegaard, M.; Rottwitt, K. Interference Patterns and Extinction Ratio of the Diatom Coscinodiscus Granii. *Opt Express* **2015**, *23*, 9543–9548, doi:10.1364/OE.23.009543.
134. Maibohm, C.; Friis, S.M.M.; Su, Y.; Rottwitt, K. Comparing Optical Properties of Different Species of Diatoms. In Proceedings of the Proceedings Volume 9360, Organic Photonic Materials and Devices XVII; 2015; p. 93600B.
135. Romann, J.; Valmalette, J.-C.; Røyset, A.; Einarsrud, M.-A. Optical Properties of Single Diatom Frustules Revealed by Confocal Microspectroscopy. *Opt Lett* **2015**, *40*, 740–743, doi:10.1364/OL.40.000740.
136. Romann, J.; Valmalette, J.-C.; Chauton, M.S.; Tranell, G.; Einarsrud, M.-A.; Vadstein, O. Wavelength and Orientation Dependent Capture of Light by Diatom Frustule Nanostructures. *Sci Rep* **2015**, *5*, 17403, doi:10.1038/srep17403.
137. Hsu, S.-H.; Paoletti, C.; Torres, M.; Ritchie, R.J.; Larkum, A.W.D.; Grillet, C. Light Transmission of the Marine Diatom Coscinodiscus Wailesii. In Proceedings of the Proceedings Volume 8339, Bioinspiration, Biomimetics, and Bioreplication; 2012; p. 83390F.
138. De Tommasi, E.; Rea, I.; Ferrara, M.A.; De Stefano, L.; De Stefano, M.; Al-Handal, A.Y.; Stamenković, M.; Wulff, A. Multiple-Pathways Light Modulation in Pleurosigma Strigosum Bi-Raphid Diatom. *Sci Rep* **2024**, *14*, 6476, doi:10.1038/s41598-024-56206-y.
139. De Tommasi, E.; Rea, I.; Ferrara, M.A.; De Stefano, L.; De Stefano, M.; Al-Handal, A.Y.; Stamenković, M.; Wulff, A. Underwater Light Manipulation by the Benthic Diatom Ctenophora Pulchella: From PAR Efficient Collection to UVR Screening. *Nanomaterials* **2021**, *11*, 2855, doi:10.3390/nano11112855.
140. De Tommasi, E.; Rea, I.; Mocella, V.; Moretti, L.; De Stefano, M.; Rendina, I.; De Stefano, L. Multi-Wavelength Study of Light Transmitted through a Single Marine Centric Diatom. *Opt Express* **2010**, *18*, 12203–12212, doi:10.1364/OE.18.012203.
141. Di Caprio, G.; Coppola, G.; Stefano, L. De; Stefano, M. De; Antonucci, A.; Congestri, R.; Tommasi, E. De Shedding Light on Diatom Photonics by Means of Digital Holography. *J Biophotonics* **2014**, *7*, 341–350, doi:10.1002/jbio.201200198.
142. Bismuto, A.; Setaro, A.; Maddalena, P.; De Stefano, L.; De Stefano, M. Marine Diatoms as Optical Chemical Sensors: A Time-Resolved Study. *Sens Actuators B Chem* **2008**, *130*, 396–399, doi:10.1016/j.snb.2007.09.012.
143. Wang, Z.; Gong, D.; Cai, J. Diatom Frustule Array for Flow-Through Enhancement of Fluorescent Signal in a Microfluidic Chip. *Micromachines (Basel)* **2021**, *12*, 1017, doi:10.3390/mi12091017.
144. Squire, K.; Kong, X.; LeDuff, P.; Rorrer, G.L.; Wang, A.X. Photonic Crystal Enhanced Fluorescence Immunoassay on Diatom Biosilica. *J Biophotonics* **2018**, *11*, e201800009, doi:10.1002/jbio.201800009.

145. De Tommasi, E.; De Luca, A.C. Diatom Biosilica in Plasmonics: Applications in Sensing, Diagnostics and Therapeutics [Invited]. *Biomed Opt Express* **2022**, *13*, 3080–3101, doi:10.1364/BOE.457483.
146. Biswas, R.; Biswas, S. Diatom Assisted SERS. In *Diatom Microscopy*; Mazumder, N., Gordon, R., Eds.; Wiley-Scrivener, 2022; pp. 237–249.
147. Zaman, S.; Hassan, M.M.; Hasanuzzaman, M.; Baten, M.Z. Coscinodiscus Diatom Inspired Bi-Layered Photonic Structures with near-Perfect Absorptance Accompanied by Tunable Absorption Characteristics. *Opt Express* **2020**, *28*, 25007–25021, doi:10.1364/OE.399505.
148. Chen, X.; Wang, C.; Baker, E.; Sun, C. Numerical and Experimental Investigation of Light Trapping Effect of Nanostructured Diatom Frustules. *Sci Rep* **2015**, *5*, 11977, doi:10.1038/srep11977.
149. Chen, X.; Wang, C.; Baker, E.; Wang, J.; Sun, C. Understanding the Nanophotonic Light-Trapping Structure of Diatom Frustule for Enhanced Solar Energy Conversion: A Theoretical and Experimental Study. In Proceedings of the Proceedings Volume 8958, Bioinspired, Biointegrated, Bioengineered Photonic Devices II; 2014; p. 89580I.
150. Bandara, T.M.W.J.; Furlani, M.; Albinsson, I.; Wulff, A.; Mellander, B.-E. Diatom Frustules Enhancing the Efficiency of Gel Polymer Electrolyte Based Dye-Sensitized Solar Cells with Multilayer Photoelectrodes. *Nanoscale Adv* **2020**, *2*, 199–209, doi:10.1039/C9NA00679F.
151. McMillon-Brown, L.; Mariano, M.; Lin, Y.L.; Li, J.; Hashmi, S.M.; Semichaevsky, A.; Rand, B.P.; Taylor, A.D. Light-Trapping in Polymer Solar Cells by Processing with Nanostructured Diatomaceous Earth. *Org Electron* **2017**, *51*, 422–427, doi:10.1016/j.orgel.2017.09.009.
152. Su, Y.; Lenau, T.A.; Gundersen, E.; Kirkensgaard, J.J.K.; Maibohm, C.; Pinti, J.; Ellegaard, M. The UV Filtering Potential of Drop-Casted Layers of Frustules of Three Diatom Species. *Sci Rep* **2018**, *8*, 959, doi:10.1038/s41598-018-19596-4.
153. Hall, D.O.; Rao, K.K. *Photosynthesis*; 6th edition.; Cambridge University Press: Cambridge, UK, 1999; ISBN 978-0521428064.
154. Morelle, J.; Bastos, A.; Frankenbach, S.; Frommlet, J.C.; Campbell, D.A.; Lavaud, J.; Serôdio, J. The Photoprotective Behavior of a Motile Benthic Diatom as Elucidated from the Interplay Between Cell Motility and Physiological Responses to a Light Microgradient Using a Novel Experimental Setup. *Microb Ecol* **2024**, *87*, 40, doi:10.1007/s00248-024-02354-7.
155. Furukawa, T.; Watanabe, M.; Shihira-Ishikawa, I. Green- and Blue-Light-Mediated Chloroplast Migration in the Centric DiatomPleurosira Laevis. *Protoplasma* **1998**, *203*, 214–220, doi:10.1007/BF01279479.
156. Aguirre, L.E.; Ouyang, L.; Elfwing, A.; Hedblom, M.; Wulff, A.; Inganäs, O. Diatom Frustules Protect DNA from Ultraviolet Light. *Sci Rep* **2018**, *8*, 5138, doi:10.1038/s41598-018-21810-2.
157. Depauw, F.A.; Rogato, A.; Ribera d'Alcala, M.; Falciatore, A. Exploring the Molecular Basis of Responses to Light in Marine Diatoms. *J Exp Bot* **2012**, *63*, 1575–1591, doi:10.1093/jxb/ers005.
158. Fleisch, D. *A Student's Guide to Maxwell's Equations.*; Cambridge University Press, 2008; ISBN 978-0521701471.
159. Grynberg, G.; Aspect, A.; Fabre, C.; Cohen-Tannoudji, C. *Introduction to Quantum Optics*; Cambridge University Press, 2010; ISBN 9780521551120.
160. Kong, J.A. *Electromagnetic Wave Theory*; Wiley: New York, 1986; ISBN 978-0471828235.
161. Gernot Zimmer *Electromagnetic Field Theory*; Fachhochschule Frankfurt am Main - Fachbereich Informatik und Ingenieurwissenschaften - Information Technology;
162. Keller, R.B. Electromagnetic Fields. In *Design for Electromagnetic Compatibility--In a Nutshell*; Keller, R.B., Ed.; Springer International Publishing: Cham, 2023; pp. 95–109.
163. Zappe, H. Diffractive Micro-Optics. In *Fundamentals of Micro-Optics*; Cambridge University Press, 2010; pp. 265–320.
164. Paschotta, R. Fresnel Number - an Encyclopedia Article Available online: https://www.rp-photonics.com/fresnel_number.html.
165. Zappe, H. *Fundamentals of Micro-Optics*; Cambridge University Press, 2010; ISBN 9780521895422.
166. Lahiri, A. Diffraction and Scattering. In *Basic Optics: Principles and Concepts*; Lahiri, A., Ed.; Elsevier, 2016; pp. 385–537 ISBN 978-0128053577.
167. Serway, R.; Jewett, J. *Physics for Scientists and Engineers with Modern Physics*; Seventh Edition.; Thomson Learning, 2008; ISBN 978-0-495-11245-7.

168. Kinoshita, S. Fundamentals of Structural Coloration. In *Structural Colors in the Realm of Nature*; Kinoshita, S., Ed.; WORLD SCIENTIFIC, 2008; pp. 7–42 ISBN 978-981-270-975-2.
169. Yuan, W.; Li, L.-H.; Lee, W.-B.; Chan, C.-Y. Fabrication of Microlens Array and Its Application: A Review. *Chin J Mech Eng* **2018**, *31*, 16, doi:10.1186/s10033-018-0204-y.
170. Pan, M.; Fu, Y.; Zheng, M.; Chen, H.; Zang, Y.; Duan, H.; Li, Q.; Qiu, M.; Hu, Y. Dielectric Metalens for Miniaturized Imaging Systems: Progress and Challenges. *Light Sci Appl* **2022**, *11*, 195, doi:10.1038/s41377-022-00885-7.
171. He, Y.; Song, B.; Tang, J. Optical Metalenses: Fundamentals, Dispersion Manipulation, and Applications. *Front Optoelectron* **2022**, *15*, 24, doi:10.1007/s12200-022-00017-4.
172. Wang, P.; Mohammad, N.; Menon, R. Chromatic-Aberration-Corrected Diffractive Lenses for Ultra-Broadband Focusing. *Sci Rep* **2016**, *6*, 21545, doi:10.1038/srep21545.
173. Liu, C.-Y.; Lin, F.-C. Geometric Effect on Photonic Nanojet Generated by Dielectric Microcylinders with Non-Cylindrical Cross-Sections. *Opt Commun* **2016**, *380*, 287–296, doi:10.1016/j.optcom.2016.06.021.
174. Benincasa, D.S.; Barber, P.W.; Zhang, J.-Z.; Hsieh, W.-F.; Chang, R.K. Spatial Distribution of the Internal and Near-Field Intensities of Large Cylindrical and Spherical Scatterers. *Appl Opt* **1987**, *26*, 1348–1356, doi:10.1364/AO.26.001348.
175. Chen, Z.; Taflove, A.; Backman, V. Photonic Nanojet Enhancement of Backscattering of Light by Nanoparticles: A Potential Novel Visible-Light Ultramicroscopy Technique. *Opt Express* **2004**, *12*, 1214–1220, doi:10.1364/OPEX.12.001214.
176. Heifetz, A.; Huang, K.; Sahakian, A. v.; Li, X.; Taflove, A.; Backman, V. Experimental Confirmation of Backscattering Enhancement Induced by a Photonic Jet. *Appl Phys Lett* **2006**, *89*, 221118, doi:10.1063/1.2398907.
177. Ferrand, P.; Wenger, J.; Devilez, A.; Pianta, M.; Stout, B.; Bonod, N.; Popov, E.; Rigneault, H. Direct Imaging of Photonic Nanojets. *Opt Express* **2008**, *16*, 6930–6940, doi:10.1364/OE.16.006930.
178. Heifetz, A.; Kong, S.-C.; Sahakian, A. V.; Taflove, A.; Backman, V. Photonic Nanojets. *J Comput Theor Nanosci* **2009**, *6*, 1979–1992, doi:10.1166/jctn.2009.1254.
179. Salhi, M.; Evans, P.G. Photonic Nanojet as a Result of a Focused Near-Field Diffraction. *J opt soc am B* **2019**, *36*, 1031–1036, doi:10.1364/JOSAB.36.001031.
180. Darafsheh, A.; Bollinger, D. Systematic Study of the Characteristics of the Photonic Nanojets Formed by Dielectric Microcylinders. *Opt Commun* **2017**, *402*, 270–275, doi:10.1016/j.optcom.2017.06.004.
181. Darafsheh, A. Photonic Nanojets and Their Applications. *JPhys Photonics* **2021**, *3*, 022001, doi:10.1088/2515-7647/abdb05.
182. Luk'yanchuk, B.S.; Paniagua-Domínguez, R.; Minin, I.; Minin, O.; Wang, Z. Refractive Index Less than Two: Photonic Nanojets Yesterday, Today and Tomorrow [Invited]. *Opt Mater Express* **2017**, *7*, 1820, doi:10.1364/OME.7.001820.
183. Minin, I. V.; Minin, O. V.; Geints, Y.E. Localized EM and Photonic Jets from Non-spherical and Non-symmetrical Dielectric Mesoscale Objects: Brief Review. *Ann Phys* **2015**, *527*, 491–497, doi:10.1002/andp.201500132.
184. Du, B.; Xia, J.; Wu, J.; Zhao, J.; Zhang, H. Switchable Photonic Nanojet by Electro-Switching Nematic Liquid Crystals. *Nanomaterials* **2019**, *9*, 72, doi:10.3390/nano9010072.
185. Hengyu, Z.; Zaichun, C.; Chong, C.T.; Minghui, H. Photonic Jet with Ultralong Working Distance by Hemispheric Shell. *Opt Express* **2015**, *23*, 6626–6633, doi:10.1364/OE.23.006626.
186. Wang, H.; Zhang, J.; Wu, X.; Shen, D. On-Resonance Photonic Nanojets for Nanoparticle Trapping. *Opt Express* **2019**, *27*, 10472–10481, doi:10.1364/OE.27.010472.
187. Geints, Y.E.; Zemlyanov, A.A.; Panina, E.K. Photonic Jets from Resonantly Excited Transparent Dielectric Microspheres. *J Opt Soc Am B* **2012**, *29*, 758–762, doi:10.1364/JOSAB.29.000758.
188. Yue, L.; Minin, O. V.; Wang, Z.; Monks, J.N.; Shalin, A.S.; Minin, I. V. Photonic Hook: A New Curved Light Beam. *Opt Lett* **2018**, *43*, 771–774, doi:10.1364/OL.43.000771.
189. Zhu, J.; Goddard, L.L. All-Dielectric Concentration of Electromagnetic Fields at the Nanoscale: The Role of Photonic Nanojets. *Nanoscale Adv* **2019**, *1*, 4615–4643, doi:10.1039/C9NA00430K.
190. Darafsheh, A. Microsphere-Assisted Microscopy. *J Appl Phys* **2022**, *131*, 031102, doi:10.1063/5.0068263.

191. Wang, Z.; Guo, W.; Li, L.; Luk'yanchuk, B.; Khan, A.; Liu, Z.; Chen, Z.; Hong, M. Optical Virtual Imaging at 50 Nm Lateral Resolution with a White-Light Nanoscope. *Nat Commun* **2011**, *2*, 218, doi:10.1038/ncomms1211.
192. Lecler, S.; Perrin, S.; Leong-Hoi, A.; Montgomery, P. Photonic Jet Lens. *Sci Rep* **2019**, *9*, 4725, doi:10.1038/s41598-019-41193-2.
193. Jacassi, A.; Tantussi, F.; Dipalo, M.; Biagini, C.; Maccaferri, N.; Bozzola, A.; De Angelis, F. Scanning Probe Photonic Nanojet Lithography. *ACS Appl Mater Interfaces* **2017**, *9*, 32386–32393, doi:10.1021/acsami.7b10145.
194. Ranha Neves, A.A.; Cesar, C.L. Analytical Calculation of Optical Forces on Spherical Particles in Optical Tweezers: Tutorial. *J Opt Soc Am B* **2019**, *36*, 1525–1537, doi:10.1364/JOSAB.36.001525.
195. Patel, H.S.; Kushwaha, P.K.; Swami, M.K. Photonic Nanojet Assisted Enhancement of Raman Signal: Effect of Refractive Index Contrast. *J Appl Phys* **2018**, *123*, 023102, doi:10.1063/1.4994944.
196. Gašparić, V.; Taccheo, S.; Gebavi, H.; Ristić, D.; Ivanda, M. Photonic Nanojet Mediated Raman Enhancement: Vertical Raman Mapping and Simple Ray Matrix Analysis. *J Raman Spectrosc* **2020**, *51*, 165–175, doi:10.1002/jrs.5747.
197. Gérard, D.; Wenger, J.; Devilez, A.; Gachet, D.; Stout, B.; Bonod, N.; Popov, E.; Rigneault, H. Strong Electromagnetic Confinement near Dielectric Microspheres to Enhance Single-Molecule Fluorescence. *Opt Express* **2008**, *16*, 15297–15303, doi:10.1364/OE.16.015297.
198. Loewen, E.G.; Popov, E. *Diffraction Gratings and Applications*; CRC Press, 2018; ISBN 9781315214849.
199. Talbot, H.F. LXXVI. *Facts Relating to Optical Science. No. IV*. *London Edinburgh Philos Mag & J Sci* **1836**, *9*, 401–407, doi:10.1080/14786443608649032.
200. Rayleigh, Lord XXV. On Copying Diffraction-Gratings, and on Some Phenomena Connected Therewith . *London Edinburgh Philos Mag & J Sci* **1881**, *11*, 196–205, doi:10.1080/14786448108626995.
201. Mansuripur, M. The Talbot Effect. In *Classical Optics and its Applications*; Mansuripur, M., Ed.; Cambridge University Press, 2011; pp. 367–378 ISBN 9780511803796.
202. Kim, M.-S.; Scharf, T.; Menzel, C.; Rockstuhl, C.; Herzig, H.P. Talbot Images of Wavelength-Scale Amplitude Gratings. *Opt Express* **2012**, *20*, 4903–4920, doi:10.1364/OE.20.004903.
203. Fang, Y.; Tan, Q.; Zhang, M.; Jin, G. Quasi-Fractional Talbot Effect of Resonant Diffraction Grating. *Opt Commun* **2012**, *285*, 4161–4165, doi:10.1016/j.optcom.2012.06.073.
204. Hua, Y.; Suh, J.Y.; Zhou, W.; Huntington, M.D.; Odom, T.W. Talbot Effect beyond the Paraxial Limit at Optical Frequencies. *Opt Express* **2012**, *20*, 14284–14291, doi:10.1364/OE.20.014284.
205. Lu, Y.; Zhou, C.; Wang, S.; Wang, B. Polarization-Dependent Talbot Effect. *J Opt Soc Am A* **2006**, *23*, 2154–2160, doi:10.1364/JOSAA.23.002154.
206. Luo, H.; Zhou, C.; Zou, H.; Lu, Y. Talbot-SNOM Method for Non-Contact Evaluation of High-Density Gratings. *Opt Commun* **2005**, *248*, 97–103, doi:10.1016/j.optcom.2004.12.004.
207. Coulon, P.-M.; Damilano, B.; Alloing, B.; Chausse, P.; Walde, S.; Enslin, J.; Armstrong, R.; Vézian, S.; Hagedorn, S.; Wernicke, T.; et al. Displacement Talbot Lithography for Nano-Engineering of III-Nitride Materials. *Microsyst Nanoeng* **2019**, *5*, 52, doi:10.1038/s41378-019-0101-2.
208. Isoyan, A.; Jiang, F.; Cheng, Y.C.; Cerrina, F.; Wachulak, P.; Urbanski, L.; Rocca, J.; Menoni, C.; Marconi, M. Talbot Lithography: Self-Imaging of Complex Structures. *J Vac Sci Technol B* **2009**, *27*, 2931–2937, doi:10.1116/1.3258144.
209. Sun, Y.; Pang, S. Fluorescence Talbot Microscope Using Incoherent Source. *J Biomed Opt* **2016**, *21*, 086003, doi:10.1117/1.JBO.21.8.086003.
210. Wang, A.; Gill, P.; Molnar, A. Light Field Image Sensors Based on the Talbot Effect. *Appl Opt* **2009**, *48*, 5897–5905, doi:10.1364/AO.48.005897.
211. Ye, E.; Atabaki, A.H.; Han, N.; Ram, R.J. Miniature, Sub-Nanometer Resolution Talbot Spectrometer. *Opt Lett* **2016**, *41*, 2434–2437, doi:10.1364/OL.41.002434.
212. Zappe, H. Guided-Wave Micro-Optics. In *Fundamentals of Micro-Optics*; Zappe, H., Ed.; Cambridge University Press, 2010; pp. 321–392.
213. Wu, X.; Tong, L. Optical Microfibers and Nanofibers. *Nanophotonics* **2013**, *2*, 407–428, doi:10.1515/nanoph-2013-0033.

214. Zhang, L.; Tang, Y.; Tong, L. Micro-/Nanofiber Optics: Merging Photonics and Material Science on Nanoscale for Advanced Sensing Technology. *iScience* **2020**, *23*, 100810, doi:10.1016/j.isci.2019.100810.
215. Buck, J.A. *Fundamentals of Optical Fibers*; 2nd Edition.; Wiley, 2004; ISBN 978-0-471-22191-3.
216. Wang, S.S.; Magnusson, R. Theory and Applications of Guided-Mode Resonance Filters. *Appl Opt* **1993**, *32*, 2606–2613, doi:10.1364/AO.32.002606.
217. Quaranta, G.; Basset, G.; Martin, O.J.F.; Gallinet, B. Recent Advances in Resonant Waveguide Gratings. *Laser Photon Rev* **2018**, *12*, 1800017, doi:10.1002/lpor.201800017.
218. Drayton, A.; Barth, I.; Krauss, T.F. Guided Mode Resonances and Photonic Crystals for Biosensing and Imaging. *Semiconductors and Semimetals* **2019**, *100*, 115–148, doi:10.1016/bs.semsem.2019.01.002.
219. Fan, S.; Joannopoulos, J.D. Analysis of Guided Resonances in Photonic Crystal Slabs. *Phys Rev B* **2002**, *65*, 235112, doi:10.1103/PhysRevB.65.235112.
220. Collin, S. Nanostructure Arrays in Free-Space: Optical Properties and Applications. *Rep Prog Phys* **2014**, *77*, 126402, doi:10.1088/0034-4885/77/12/126402.
221. Wang, S.S.; Magnusson, R.; Bagby, J.S.; Moharam, M.G. Guided-Mode Resonances in Planar Dielectric-Layer Diffraction Gratings. *J Opt Soc Am A* **1990**, *7*, 1470–1474, doi:10.1364/JOSAA.7.001470.
222. Tibuleac, S.; Magnusson, R. Reflection and Transmission Guided-Mode Resonance Filters. *J Opt Soc Am A* **1997**, *14*, 1617–1626, doi:10.1364/josaa.14.001617.
223. Guo, T.; Evans, J.; Wang, N.; Jin, Y.; He, J.; Sun, Y. Guided Mode Resonance in a Low-Index Waveguide Layer. *Applied Sciences (Switzerland)* **2021**, *11*, 3312, doi:10.3390/app11083312.
224. Chu, A.; Gréboval, C.; Goubet, N.; Martinez, B.; Livache, C.; Qu, J.; Rastogi, P.; Bresciani, F.A.; Prado, Y.; Suffit, S.; et al. Near Unity Absorption in Nanocrystal Based Short Wave Infrared Photodetectors Using Guided Mode Resonators. *ACS Photonics* **2019**, *6*, 2553–2561, doi:10.1021/acsphotonics.9b01015.
225. Sadiku, M.N.O. Finite Element Method. In *Numerical Techniques in Electromagnetics*; Sadiku, M.N.O., Ed.; CRC Press, 2000; p. 90 ISBN 9780429196089.
226. Sadiku, M.N.O. *Numerical Techniques in Electromagnetics*; 2nd ed.; CRC Press: Boca Raton, 2000; ISBN 9780429196089.
227. COMSOL Multiphysics The Wave Optics Module User's Guide. *https://doc.comsol.com/5.4/doc/com.comsol.help.woptics/WaveOpticsModuleUsersGuide.pdf* 2021.
228. Murphy, D.B.; Davidson, M.W. *Fundamentals of Light Microscopy and Electronic Imaging*; 2nd ed.; Wiley-Blackwell: UK, 2012; ISBN 9780471692140.
229. Bond, C.; Santiago-Ruiz, A.N.; Tang, Q.; Lakadamyali, M. Technological Advances in Super-Resolution Microscopy to Study Cellular Processes. *Mol Cell* **2022**, *82*, 315–332, doi:10.1016/j.molcel.2021.12.022.
230. Bian, K.; Gerber, C.; Heinrich, A.J.; Müller, D.J.; Scheuring, S.; Jiang, Y. Scanning Probe Microscopy. *Nat Rev Methods Primers* **2021**, *1*, 36, doi:10.1038/s43586-021-00033-2.
231. Courjon, D.; Bainier, C. Near Field Microscopy and near Field Optics. *Rep Prog Phys* **1994**, *57*, 989–1028, doi:10.1088/0034-4885/57/10/002.
232. Fisher, A.J. Scanning Probe Microscopy, Theory. In *Encyclopedia of Spectroscopy and Spectrometry*; Lindon, C.J., Tranter, G.E., Koppenaal, D.W., Eds.; Elsevier, 2017; pp. 23–28.
233. Song, M.; Fumagalli, P.; Schmid, M. Scanning Near-Field Optical Microscopy Measurements and Simulations of Regularly Arranged Silver Nanoparticles. *Nanotechnology* **2024**, *35*, 065702, doi:10.1088/1361-6528/ad0a0e.
234. Rousso, I.; Deshpande, A. Applications of Atomic Force Microscopy in HIV-1 Research. *Viruses* **2022**, *14*, 648, doi:10.3390/v14030648.
235. Florea, C.; Dreucean, M.; Laasanen, M.S.; Halvari, A. Determination of Young's Modulus Using AFM Nanoindentation. Applications on Bone Structures. In Proceedings of the 2011 E-Health and Bioengineering Conference (EHB); IEEE: Romania, 2011; pp. 1–4.
236. Dzedzickis, A.; Rožėnė, J.; Bučinskas, V.; Viržonis, D.; Morkvėnaitė-Vilkončienė, I. Characteristics and Functionality of Cantilevers and Scanners in Atomic Force Microscopy. *Materials* **2023**, *16*, 6379, doi:10.3390/ma16196379.
237. Bozhevolnyi, S.I.; Kuipers, L. Near-Field Characterization of Photonic Crystal Waveguides. *Semicond Sci Technol* **2006**, *21*, R1–R16, doi:10.1088/0268-1242/21/5/R01.

238. Vo, T.-P.; Rahmani, A.; Belarouci, A.; Seassal, C.; Nedeljkovic, D.; Callard, S. Near-Field and Far-Field Analysis of an Azimuthally Polarized Slow Bloch Mode Microlaser. *Opt Express* **2010**, *18*, 26879–26886, doi:10.1364/OE.18.026879.
239. Tsuruoka, T.; Liang, C.H.; Terabe, K.; Hasegawa, T. Optical Waveguide Properties of Single Indium Oxide Nanofibers. *J Opt A: Pure Appl Opt* **2008**, *10*, 055201, doi:10.1088/1464-4258/10/5/055201.
240. Itoh, T.; Natsuhara, H.; Nonomura, S. Local Photovoltaic Characterization for Silicon Thin Film Solar Cells Using a Scanning Probe Microscope. *J Phys Conf Ser* **2012**, *379*, 012003, doi:10.1088/1742-6596/379/1/012003.
241. Alferov, S. V.; Khonina, S.N.; Savelyev, D.A.; Savelyev, D.A. Experimental Generation of the Longitudinal Electric Field Component on the Optical Axis with High-Numerical-Aperture Binary Axicons. In Proceedings of the Proceedings Volume 9533, Optical Technologies for Telecommunications; 2015; Vol. 15, p. 95330D.
242. Mote, R.G.; Yu, S.F.; Kumar, A.; Zhou, W.; Li, X.F. Experimental Demonstration of Near-Field Focusing of a Phase Micro-Fresnel Zone Plate (FZP) under Linearly Polarized Illumination. *Appl Phys B* **2011**, *102*, 95–100, doi:10.1007/s00340-010-4210-8.
243. Smith, E.; Dent, G. *Modern Raman Spectroscopy: A Practical Approach*; Wiley, 2019; ISBN 9781119440550.
244. Long, D.A. *The Raman Effect*; Wiley, 2002; ISBN 9780471490289.
245. Dey, T. Microplastic Pollutant Detection by Surface Enhanced Raman Spectroscopy (SERS): A Mini-Review. *Nanotechnology for Environmental Engineering* **2023**, *8*, 41–48, doi:10.1007/s41204-022-00223-7.
246. Kraai, J.A.; Wang, A.X.; Rorrer, G.L. Photonic Crystal Enhanced SERS Detection of Analytes Separated by Ultrathin Layer Chromatography Using a Diatom Frustule Monolayer. *Adv Mater Interfaces* **2020**, *7*, 2000191, doi:10.1002/admi.202000191.
247. Jones, R.R.; Hooper, D.C.; Zhang, L.; Wolverson, D.; Valev, V.K. Raman Techniques: Fundamentals and Frontiers. *Nanoscale Res Lett* **2019**, *14*, 231, doi:10.1186/s11671-019-3039-2.
248. Langer, J.; Jimenez de Aberasturi, D.; Aizpurua, J.; Alvarez-Puebla, R.A.; Auguié, B.; Baumberg, J.J.; Bazan, G.C.; Bell, S.E.J.; Boisen, A.; Brolo, A.G.; et al. Present and Future of Surface-Enhanced Raman Scattering. *ACS Nano* **2020**, *14*, 28–117, doi:10.1021/acsnano.9b04224.
249. Fleischmann, M.; Hendra, P.J.; McQuillan, A.J. Raman Spectra of Pyridine Adsorbed at a Silver Electrode. *Chem Phys Lett* **1974**, *26*, 163–166, doi:10.1016/0009-2614(74)85388-1.
250. Tim, B.; Błaszkiewicz, P.; Kotkowiak, M. Recent Advances in Metallic Nanoparticle Assemblies for Surface-Enhanced Spectroscopy. *Int J Mol Sci* **2021**, *23*, 291, doi:10.3390/ijms23010291.
251. Lee, C.; Robertson, C.S.; Nguyen, A.H.; Kahraman, M.; Wachsmann-Hogiu, S. Thickness of a Metallic Film, in Addition to Its Roughness, Plays a Significant Role in SERS Activity. *Sci Rep* **2015**, *5*, 11644, doi:10.1038/srep11644.
252. Kumar, S.; Gahlaut, S.K.; Singh, J.P. Sculptured Thin Films: Overcoming the Limitations of Surface-Enhanced Raman Scattering Substrates. *Appl Surf Sci Adv* **2022**, *12*, 100322, doi:10.1016/j.apsadv.2022.100322.
253. Kneipp, K.; Moskovits, M.; Kneipp, H. *Surface-Enhanced Raman Scattering*; Kneipp, K., Moskovits, M., Kneipp, H., Eds.; Springer Berlin Heidelberg, 2006; Vol. 103; ISBN 978-3-540-33566-5.
254. Wang, A.; Kong, X. Review of Recent Progress of Plasmonic Materials and Nano-Structures for Surface-Enhanced Raman Scattering. *Materials* **2015**, *8*, 3024–3052, doi:10.3390/ma8063024.
255. Xu, X.; Hasan, D.; Wang, L.; Chakravarty, S.; Chen, R.T.; Fan, D.L.; Wang, A.X. Guided-Mode-Resonance-Coupled Plasmonic-Active SiO2 Nanotubes for Surface Enhanced Raman Spectroscopy. *Appl Phys Lett* **2012**, *100*, 191114, doi:10.1063/1.4714710.
256. Sabri, L.; Shahabadi, M.; Forooraghi, K.; Ghaffari-Miab, M. Interaction of Two Guided-Mode Resonances in an All-Dielectric Photonic Crystal for Uniform SERS. *Opt Express* **2020**, *28*, 10467–10476, doi:10.1364/OE.389524.
257. Hu, M.; Fattal, D.; Li, J.; Li, X.; Li, Z.; Williams, R.S. Optical Properties of Sub-Wavelength Dielectric Gratings and Their Application for Surface-Enhanced Raman Scattering. *Appl Phys A* **2011**, *105*, 261–266, doi:10.1007/s00339-011-6613-8.

258. Ghobara, M. Studies on the Frustules of Some Diatom Species and Its Applications in Nanotechnology. Master thesis, Botany department, Faculty of science, Tanta university: Tanta, 2016.
259. Blanco, S.; Álvarez, I.; Cejudo, C. A Test on Different Aspects of Diatom Processing Techniques. *J Appl Phycol* **2008**, *20*, 445–450, doi:10.1007/s10811-007-9292-2.
260. Goren, R.; Baykara, T.; Marsoglu, M. A Study on the Purification of Diatomite in Hydrochloric Acid. *Scand J Metall* **2002**, *31*, 115–119, doi:10.1034/j.1600-0692.2002.310205.x.
261. Ghobara, M.; Oschatz, C.; Fratzl, P.; Reissig, L. Numerical Analysis of the Light Modulation by the Frustule of Gomphonema Parvulum: The Role of Integrated Optical Components. *Nanomaterials* **2022**, *13*, 113, doi:10.3390/nano13010113.
262. COMSOL. Focusing Lens Available online: https://www.comsol.com/model/focusing-lens-57621.
263. Soto, J.M.; Rodrigo, J.A.; Alieva, T. Refractive Index Tomography for Diatom Analysis. In *Diatom Microscopy*; Mazumder, N., Gordon, R., Eds.; Wiley-Scrivener, 2022; pp. 111–137 ISBN 9781119711568.
264. ARTRAY CO. USB2.0 CMOS CAMERA ARTCAM-MI-WOM Series INSTRUCTION BOOKLET Available online: http://www.artray.us/download/pmanual/INTRDUCTION_ARTCAM-MI-WOM_220826_V133.pdf.
265. Beléndez, A.; Beléndez, T.; Neipp, C.; Pascual, I. Determination of the Refractive Index and Thickness of Holographic Silver Halide Materials by Use of Polarized Reflectances. *Appl Opt* **2002**, *41*, 6802–6808, doi:10.1364/AO.41.006802.
266. Murphy, D.B.; Davidson, M.W. *Fundamentals of Light Microscopy and Electronic Imaging.*; 2nd ed.; Wiley-Blackwell: UK, 2012; ISBN 9781118382905.
267. McCloskey, D.; Wang, J.J.; Donegan, J.F. Low Divergence Photonic Nanojets from Si_3N_4 Microdisks. *Opt Express* **2012**, *20*, 128–140, doi:10.1364/OE.20.000128.
268. Liu, C.-Y.; Chen, C.-J. Characterization of Photonic Nanojets in Dielectric Microdisks. *Physica E Low Dimens Syst Nanostruct* **2015**, *73*, 226–234, doi:10.1016/j.physe.2015.06.005.
269. Liu, C.Y.; Lin, F.C. Geometric Effect on Photonic Nanojet Generated by Dielectric Microcylinders with Non-Cylindrical Cross-Sections. *Opt Commun* **2016**, *380*, 287–296, doi:10.1016/j.optcom.2016.06.021.
270. Li, Y.; Liu, X.; Li, B. Single-Cell Biomagnifier for Optical Nanoscopes and Nanotweezers. *Light Sci Appl* **2019**, *8*, 61, doi:10.1038/s41377-019-0168-4.
271. Lin, C.-B.; Lin, Y.-H.; Chen, W.-Y.; Liu, C.-Y. Photonic Nanojet Modulation Achieved by a Spider-Silk-Based Metal–Dielectric Dome Microlens. *Photonics* **2021**, *8*, 334, doi:10.3390/photonics8080334.
272. Andrä, P. Optische Untersuchung von Nanostrukturen Zur Gesteigerten Lichtabsorption in Solarzellen. PhD dissertation, Physics department, Freie Universität Berlin: Berlin, 2015.
273. Stec, H.M.; Williams, R.J.; Jones, T.S.; Hatton, R.A. Ultrathin Transparent Au Electrodes for Organic Photovoltaics Fabricated Using a Mixed Mono-Molecular Nucleation Layer. *Adv Funct Mater* **2011**, *21*, 1709–1716, doi:10.1002/adfm.201002021.
274. Kermarrec, L.; Bouchez, A.; Rimet, F.; Humbert, J.-F. First Evidence of the Existence of Semi-Cryptic Species and of a Phylogeographic Structure in the Gomphonema Parvulum (Kützing) Kützing Complex (Bacillariophyta). *Protist* **2013**, *164*, 686–705, doi:10.1016/j.protis.2013.07.005.
275. Abarca, N.; Jahn, R.; Zimmermann, J.; Enke, N. Does the Cosmopolitan Diatom Gomphonema Parvulum (Kützing) Kützing Have a Biogeography? *PLoS One* **2014**, *9*, e86885, doi:10.1371/journal.pone.0086885.
276. filmetrics company Spectral Reflectance Calculator Available online: https://www.filmetrics.com/reflectance-calculator.
277. Salvdari, H.; Taghi Tavassoly, M. Fresnel Diffraction from the Edge of a Transparent Plate in the General Case. *j opt soc am A* **2018**, *35*, 496–503, doi:10.1364/josaa.35.000496.
278. Santhanakrishnan, T.; Rajesh, R.; Awasthi, R.L.; Sreehari, C. V. Optical Diffraction Phenomena around the Edges of Photodetectors: A Simplified Method for Metrological Applications. *Sci Rep* **2019**, *9*, 3397, doi:10.1038/s41598-019-40270-w.
279. Salhi, M.; Evans, P.G. Photonic Nanojet as a Result of a Focused Near-Field Diffraction. *j opt soc am B* **2019**, *36*, 1031–1036, doi:10.1364/josab.36.001031.

280. Quinten, M. Propagation of Light and Other Electromagnetic Waves. In *A Practical Guide to Optical Metrology for Thin Films*; Quinten, M., Ed.; Wiley-VCH Verlag GmbH & Co. KGaA: Weinheim, 2012; pp. 7–57 ISBN 9783527664344.
281. Spagnolo, G.S.; Ambrosini, D. Talbot Effect Application: Measurement of Distance with a Fourier-Transform Method. *Meas. Sci. Technol* **2000**, *11*, 77–82, doi:10.1088/0957-0233/11/1/312.
282. De Stefano, L.; De Stefano, M.; Maddalena, P.; Moretti, L.; Rea, I.; Mocella, V.; Rendina, I. Playing with Light in Diatoms: Small Water Organisms with a Natural Photonic Crystal Structure. In Proceedings of the Proceedings Volume 6593, Photonic Materials, Devices, and Applications II; 2007; p. 659313.
283. Zhu, J.; Goddard, L.L. All-Dielectric Concentration of Electromagnetic Fields at the Nanoscale: The Role of Photonic Nanojets. *Nanoscale Adv* **2019**, *1*, 4615–4643, doi:10.1039/c9na00430k.
284. Mansuripur, M. The Talbot Effect. In *Classical Optics and its Applications*; Mansuripur, M., Ed.; Cambridge University Press, 2011; pp. 367–378 ISBN 9780511803796.
285. Pang, S.; Han, C.; Kato, M.; Sternberg, P.W.; Yang, C. Wide and Scalable Field-of-View Talbot-Grid-Based Fluorescence Microscopy. *Opt Lett* **2012**, *37*, 5018–5020, doi:10.1364/OL.37.005018.
286. Sun, Y.; Pang, S. Fluorescence Talbot Microscope Using Incoherent Source. *J Biomed Opt* **2016**, *21*, 86003, doi:10.1117/1.JBO.21.8.086003.
287. Solak, H.H.; Dais, C.; Clube, F. Displacement Talbot Lithography: A New Method for High-Resolution Patterning of Large Areas. *Opt Express* **2011**, *19*, 10686–10691, doi:10.1364/OE.19.010686.
288. Chausse, P.J.P.; Le Boulbar, E.D.; Lis, S.D.; Shields, P.A. Understanding Resolution Limit of Displacement Talbot Lithography. *Opt Express* **2019**, *27*, 5918–5930, doi:10.1364/OE.27.005918.
289. Wang, A.; Gill, P.; Molnar, A. Light Field Image Sensors Based on the Talbot Effect. *Appl Opt* **2009**, *48*, 5897–5905, doi:10.1364/AO.48.005897.
290. Li, A.; Zhang, W.; Ghaffarivardavagh, R.; Wang, X.; Anderson, S.W.; Zhang, X. Towards Uniformly Oriented Diatom Frustule Monolayers: Experimental and Theoretical Analyses. *Microsyst Nanoeng* **2016**, *2*, 16064, doi:10.1038/micronano.2016.64.
291. Aguirre, L.E.; Ouyang, L.; Elfwing, A.; Hedblom, M.; Wulff, A.; Inganäs, O. Diatom Frustules Protect DNA from Ultraviolet Light. *Sci Rep* **2018**, *8*, 5138, doi:10.1038/s41598-018-21810-2.
292. Cox, E.J.; Williams, D.M. Systematics of Naviculoid Diatoms (Bacillariophyta): A Preliminary Analysis of Protoplast and Frustule Characters for Family and Order Level Classification. *Syst Biodivers* **2006**, *4*, 385–399, doi:10.1017/S1477200006001940.
293. Schuergers, N.; Lenn, T.; Kampmann, R.; Meissner, M. V; Esteves, T.; Temerinac-Ott, M.; Korvink, J.G.; Lowe, A.R.; Mullineaux, C.W.; Wilde, A. Cyanobacteria Use Micro-Optics to Sense Light Direction. *Elife* **2016**, *5*, e12620, doi:10.7554/eLife.12620.001.
294. Nilsson, D.-E.; Colley, N.J. Comparative Vision: Can Bacteria Really See? *Curr Biol* **2016**, *26*, R369–R371, doi:10.1016/j.cub.2016.03.025.
295. Bicudo, D.C.; Tremarin, P.I.; Almeida, P.D.; Zorzal-Almeida, S.; Wengrat, S.; Faustino, S.B.; Costa, L.F.; Bartozek, E.C.R.; Rocha, A.C.R.; Bicudo, C.E.M.; et al. Ecology and Distribution of *Aulacoseira* Species (Bacillariophyta) in Tropical Reservoirs from Brazil. *Diatom Research* **2016**, *31*, 199–215, doi:10.1080/0269249X.2016.1227376.
296. Toster, J.; Iyer, K.S.; Xiang, W.; Rosei, F.; Spiccia, L.; Raston, C.L. Diatom Frustules as Light Traps Enhance DSSC Efficiency. *Nanoscale* **2013**, *5*, 873–876, doi:10.1039/C2NR32716C.
297. Liu, C.-Y.; Chang, L.-J. Photonic Nanojet Modulation by Elliptical Microcylinders. *Optik (Stuttg)* **2014**, *125*, 4043–4046, doi:10.1016/j.ijleo.2014.01.116.
298. Liu, C.-Y.; Yeh, M.-J. Experimental Verification of Twin Photonic Nanojets from a Dielectric Microcylinder. *Opt Lett* **2019**, *44*, 3262–3265, doi:10.1364/OL.44.003262.
299. Darafsheh, A.; Bollinger, D. Systematic Study of the Characteristics of the Photonic Nanojets Formed by Dielectric Microcylinders. *Opt Commun* **2017**, *402*, 270–275, doi:10.1016/j.optcom.2017.06.004.
300. Missinne, J.; Verplancke, R.; Chang, Y.-T.; Van Asch, J.; Kannojia, H.; Geudens, V.; Kyriazis, A.; Van Steenberge, G. Microlens Integration on Photonic Integrated Circuits: A Platform for Achieving Relaxed Packaging Tolerances and Hybrid Integration of External Functionality. In Proceedings of the Proceedings Volume 12891, Silicon Photonics XIX; 2024; p. 27.

301. Falciatore, A.; Mock, T. *The Molecular Life of Diatoms*; Springer International Publishing: Cham, 2022; ISBN 978-3-030-92499-7.
302. Jaubert, M.; Duchêne, C.; Kroth, P.G.; Rogato, A.; Bouly, J.-P.; Falciatore, A. Sensing and Signalling in Diatom Responses to Abiotic Cues. In *The Molecular Life of Diatoms*; Falciatore, A., Mock, T., Eds.; Springer International Publishing: Cham, 2022; pp. 607–639 ISBN 978-3-030-92499-7.
303. Poulsen, N.; Davutoglu, M.G.; Zackova Suchanova, J. Diatom Adhesion and Motility. In *The Molecular Life of Diatoms*; Springer International Publishing: Cham, 2022; pp. 367–393.
304. Cohn, S.; Manoylov, K.; Gordon, R. *Diatom Gliding Motility*; Cohn, S., Manoylov, K., Gordon, R., Eds.; Wiley, 2021; ISBN 9781119526353.
305. D'Mello, Y.; Petrescu, D.; Skoric, J.; Campbell, M.; Andrews, M.; Plant, D. Characterization of the Photonic Response in Nitzschia Filiformis Phytoplankton. In Proceedings of the Conference on Lasers and Electro-Optics (CLEO); 2018; pp. 1–2.
306. D'Mello, Y.; Bernal, S.; Skoric, J.; Petrescu, D.; Andrews, M.; Plant, D. V Photonic Crystal Behavior of Nitzschia Filiformis Phytoplankton for Chlorophyll A Photosynthesis. In Proceedings of the Conference on Lasers and Electro-Optics (CLEO); 2019; pp. 1–2.
307. Bernal, S.; D'Mello, Y.; Petrescu, D.; Andrews, M.; Plant, D. V Optical Response of the Centric Valve in Cyclotella Quillensis Diatoms. In Proceedings of the Conference on Lasers and Electro-Optics (CLEO); 2020; pp. 1–2.
308. Managò, S.; Zito, G.; Rogato, A.; Casalino, M.; Esposito, E.; De Luca, A.C.; De Tommasi, E. Bioderived Three-Dimensional Hierarchical Nanostructures as Efficient Surface-Enhanced Raman Scattering Substrates for Cell Membrane Probing. *ACS Appl Mater Interfaces* **2018**, *10*, 12406–12416, doi:10.1021/acsami.7b19285.
309. Payne, E.K.; Rosi, N.L.; Xue, C.; Mirkin, C.A. Sacrificial Biological Templates for the Formation of Nanostructured Metallic Microshells. *Angew Chem Int Ed* **2005**, *44*, 5064–5067, doi:10.1002/anie.200500988.
310. Gilic, M.; Ghobara, M.; Reissig, L. Tuning SERS Signal via Substrate Structuring: Valves of Different Diatom Species with Ultrathin Gold Coating. *Nanomaterials* **2023**, *13*, 1594, doi:10.3390/nano13101594.
311. Xue, Y.; Li, X.; Li, H.; Zhang, W. Quantifying Thiol–Gold Interactions towards the Efficient Strength Control. *Nat Commun* **2014**, *5*, 4348, doi:10.1038/ncomms5348.
312. Rai, V.N.; Srivastava, A.K. Correlation Between Optical and Morphological Properties of Nanostructured Gold Thin Film. *JSM Nanotechnology & Nanomedicine* **2016**, *4*, 1039.
313. Vosgröne, T.; Meixner, A.J. Surface- and Resonance-Enhanced Micro-Raman Spectroscopy of Xanthene Dyes: From the Ensemble to Single Molecules. *Chem Phys Chem* **2005**, *6*, 154–163, doi:10.1002/cphc.200400395.
314. Sil, S.; Kuhar, N.; Acharya, S.; Umapathy, S. Is Chemically Synthesized Graphene "Really" a Unique Substrate for SERS and Fluorescence Quenching? *Sci Rep* **2013**, *3*, 3336, doi:10.1038/srep03336.
315. Kirubha, E.; Palanisamy, P.K. Green Synthesis, Characterization of Au-Ag Core-Shell Nanoparticles Using Gripe Water and Their Applications in Nonlinear Optics and Surface Enhanced Raman Studies. *Adv Nat Sci Nanosci Nanotechnol* **2014**, *5*, 045006, doi:10.1088/2043-6262/5/4/045006.
316. Zhang, Y.X.; Zheng, J.; Gao, G.; Kong, Y.F.; Zhi, X.; Wang, K.; Zhang, X.Q.; Cui, D.X. Biosynthesis of Gold Nanoparticles Using Chloroplasts. *Int J Nanomedicine* **2011**, *6*, 2899–2906, doi:10.2147/ijn.s24785.
317. He, X.N.; Gao, Y.; Mahjouri-Samani, M.; Black, P.N.; Allen, J.; Mitchell, M.; Xiong, W.; Zhou, Y.S.; Jiang, L.; Lu, Y.F. Surface-Enhanced Raman Spectroscopy Using Gold-Coated Horizontally Aligned Carbon Nanotubes. *Nanotechnology* **2012**, *23*, 205702, doi:10.1088/0957-4484/23/20/205702.
318. Ma, Y.; Hu, W.; Song, X.; Wang, C. Density Functional Theory Study on Raman Spectra of Rhodamine Molecules in Different Forms. *Chin J Chem Phys* **2014**, *27*, 291–296, doi:10.1063/1674-0068/27/03/291-296.
319. Ren, F.; Campbell, J.; Hasan, D.; Wang, X.; Rorrer, G.L.; Wang, A.X. Surface-Enhanced Raman Scattering on Diatom Biosilica Photonic Crystals. In Proceedings of the Proceedings Volume 8598, Bioinspired, Biointegrated, Bioengineered Photonic Devices; 2013; p. 85980N.

320. Zhang, X.; Zheng, Y.; Liu, X.; Lu, W.; Dai, J.; Lei, D.Y.; MacFarlane, D.R. Hierarchical Porous Plasmonic Metamaterials for Reproducible Ultrasensitive Surface-Enhanced Raman Spectroscopy. *Adv Mater* **2015**, *27*, 1090–1096, doi:10.1002/adma.201404107.
321. Manoylov, K.; Ghobara, M. Introduction for a Tutorial on Diatom Morphology. In *Diatom Morphogenesis*; Annenkov, V., Seckback, J., Gordon, R., Eds.; Wiley-Scrivener, 2021; pp. 1–18.
322. Anonymous Two Letters from a Gentleman in the Country, Relating to Mr Leuwenhoeck's Letter in Transaction. *Philosophical Transactions* **1703**, *23*, 1494–1501.
323. Krause, F. Elektronoptische Aufnahmen von Diatomeen Mit Dem Magnetischen Elektronenmikroskop. *Zeitschrift für Physik* **1936**, *102*, 417–422.
324. Hasle, G.R.; Fryxell, G.A. Diatoms: Cleaning and Mounting for Light and Electron Microscopy. *Trans Am Microsc Soc* **1970**, *89*, 469–474, doi:10.2307/3224555.
325. Linder, A.; Colchero, J.; Apell, H.-J.; Marti, O.; Mlynek, J. Scanning Force Microscopy of Diatom Shells. *Ultramicroscopy* **1992**, *42–44*, 329–332, doi:10.1016/0304-3991(92)90287-T.
326. Suzuki, H.; Tanaka, J.; Nagumo, T. MORPHOLOGY OF THE MARINE DIATOM *COCCONEIS PSEUDOMARGINATA* GREGORY VAR. *INTERMEDIA* GRUNOW. *Diatom Research* **2001**, *16*, 93–102, doi:10.1080/0269249X.2001.9705511.
327. van Putten, E.G.; Akbulut, D.; Bertolotti, J.; Vos, W.L.; Lagendijk, A.; Mosk, A.P. Scattering Lens Resolves Sub-100 Nm Structures with Visible Light. *Phys Rev Lett* **2011**, *106*, 193905, doi:10.1103/PhysRevLett.106.193905.
328. Erni, R.; Rossell, M.D.; Kisielowski, C.; Dahmen, U. Atomic-Resolution Imaging with a Sub-50-Pm Electron Probe. *Phys Rev Lett* **2009**, *102*, 096101, doi:10.1103/PhysRevLett.102.096101.
329. Roussel, L.Y.; Stokes, D.J.; Gestmann, I.; Darus, M.; Young, R.J. Extreme High Resolution Scanning Electron Microscopy (XHR SEM) and Beyond. In Proceedings of the Proceedings Volume 7378, Scanning Microscopy; 2009; p. 73780W.
330. De Hann, A.B.; Eral, H.B.; Schuur, B. Chapter 9. Sedimentation and Settling. In *Industrial Separation Processes*; De Hann, A.B., Eral, H.B., Schuur, B., Eds.; De Gruyter, 2020; pp. 289–324 ISBN 9783110654806.
331. Zhang, D.; Wang, Y.; Pan, J.; Cai, J. Separation of Diatom Valves and Girdle Bands from Coscinodiscus Diatomite by Settling Method. *J Mater Sci* **2010**, *45*, 5736–5741, doi:10.1007/s10853-010-4642-x.
332. Garello, R. *Two-Dimensional Signal Analysis*; Wiley, 2008; ISBN 9781848210189.
333. Pfleiderer, S.; Ball, D.G.A.; Bailey, R.C. AUTO: A Computer Program for the Determination of the Two-Dimensional Autocorrelation Function of Digital Images. *Comput Geosci* **1993**, *19*, 825–829, doi:10.1016/0098-3004(93)90053-8.
334. Lee, J.J.; Garinis, D.; Frost, D.L.; Lee, J.H.S.; Knystautas, R. Two-Dimensional Autocorrelation Function Analysis of Smoked Foil Patterns. *Shock Waves* **1995**, *5*, 169–174, doi:10.1007/BF01435524.
335. Schneider, C.A.; Rasband, W.S.; Eliceiri, K.W. NIH Image to ImageJ: 25 Years of Image Analysis. *Nat Methods* **2012**, *9*, 671–675, doi:10.1038/nmeth.2089.
336. Taylor, J.R. *Introduction To Error Analysis: The Study of Uncertainties in Physical Measurements*; University Science Books: California, USA, 1997; ISBN 978-0935702750.
337. Klapetek, K.; Necas, D.; Anderson, C. Gwyddion User Guide, Feature Measurement, in Chapter 4: Data Processing and Analysis Available online: http://gwyddion.net/documentation/user-guide-en/feature-measurement.html.
338. Goessling, J.; Frankenbach, S.; Ribeiro, L.; Serôdio, J.; Kühl, M. Modulation of the Light Field Related to Valve Optical Properties of Raphid Diatoms: Implications for Niche Differentiation in the Microphytobenthos. *Mar Ecol Prog Ser* **2018**, *588*, 29–42, doi:10.3354/meps12456.
339. Tung, R.T. The Physics and Chemistry of the Schottky Barrier Height. *Appl Phys Rev* **2014**, *1*, 011304, doi:10.1063/1.4858400.
340. Özerden, E.; Özden, P.; Afşin Kariper, İ.; Pakma, O. The Electrical Characterization of Metal–Insulator–Semiconductor Device with β-Naphthol Orange Interface. *J Mater Sci: Mater Electron* **2022**, *33*, 20900–20910, doi:10.1007/s10854-022-08897-0.
341. Jeon, W.; Kim, Y.; An, C.H.; Hwang, C.S.; Gonon, P.; Vallee, C. Demonstrating the Ultrathin Metal–Insulator– Metal Diode Using TiN/ZrO_2–Al_2O_3–ZrO_2 Stack by Employing RuO_2 Top Electrode. *IEEE Trans Electron Devices* **2018**, *65*, 660–666, doi:10.1109/TED.2017.2785120.
342. Al-Ahmadi, N.A. Metal Oxide Semiconductor-Based Schottky Diodes: A Review of Recent Advances. *Mater Res Express* **2020**, *7*, 032001, doi:10.1088/2053-1591/ab7a60.

343. Chow, P.C.Y.; Someya, T. Organic Photodetectors for Next-Generation Wearable Electronics. *adv mater* **2020**, *32*, 1902045, doi:10.1002/adma.201902045.
344. Reissig, L.; Dalgleish, S.; Awaga, K. A Differential Photodetector: Detecting Light Modulations Using Transient Photocurrents. *AIP Adv* **2016**, *6*, 015306, doi:10.1063/1.4939921.
345. Reissig, L.; Mori, K.; Treadwell, R.; Dalgleish, S.; Awaga, K. Factors Affecting the Polarity and Magnitude of Photoresponse of Transient Photodetectors. *Phys Chem Chem Phys* **2016**, *18*, 6821–6830, doi:10.1039/C6CP00093B.
346. Ahmad, S. Organic Semiconductors for Device Applications: Current Trends and Future Prospects. *Polym Sci Eng* **2014**, *34*, 279–338, doi:10.1515/polyeng-2013-0267.
347. Wang, S.; Peng, L.; Sun, H.; Huang, W. The Future of Solution Processing toward Organic Semiconductor Devices: A Substrate and Integration Perspective. *J Mater Chem C Mater* **2022**, *10*, 12468–12486, doi:10.1039/D2TC02316D.
348. Hu, L.; Iwasaki, A.; Suizu, R.; Yoshikawa, H.; Awaga, K.; Ito, H. Highly Efficient Alternating Photocurrent from Interactive Organic–Radical Dimers: A Novel Light-Harvesting Mechanism for Optoelectronic Conversion. *Chem Phys Lett* **2010**, *484*, 177–180, doi:10.1016/j.cplett.2009.11.013.
349. Hu, L.; Iwasaki, A.; Suizu, R.; Noda, Y.; Li, B.; Yoshikawa, H.; Matsushita, M.M.; Awaga, K.; Ito, H. Effect of Photoinduced Charge Displacement on Organic Optoelectronic Conversion. *Phys Rev B* **2011**, *84*, 205329, doi:10.1103/PhysRevB.84.205329.
350. Hu, L.; Noda, Y.; Ito, H.; Kishida, H.; Nakamura, A.; Awaga, K. Optoelectronic Conversion by Polarization Current, Triggered by Space Charges at Organic-Based Interfaces. *Appl Phys Lett* **2010**, *96*, 243303, doi:10.1063/1.3454915.
351. Mori, K. Anomalous Transient Photocurrents Using P3HT:PCBM. Bachelor thesis, department of Chemistry, Nagoya, Japan, 2014.
352. Dalgleish, S.; Reissig, L.; Hu, L.; Matsushita, M.M.; Sudo, Y.; Awaga, K. Factors Affecting the Stability and Performance of Ionic Liquid-Based Planar Transient Photodetectors. *Langmuir* **2015**, *31*, 5235–5243, doi:10.1021/la504972q.
353. Li, B.; Noda, Y.; Hu, L.; Yoshikawa, H.; Matsushita, M.M.; Awaga, K. Highly Efficient Organic Optoelectronic Conversion Induced by Electric Double Layers in Ionic Liquids. *Appl Phys Lett* **2012**, *100*, 163304, doi:10.1063/1.3697988.
354. Reissig, L.; Dalgleish, S.; Awaga, K. Towards High-Bandwidth Organic Photodetection Based on Pure Active Layer Polarization. *Sci Rep* **2018**, *8*, 15415, doi:10.1038/s41598-018-33822-z.
355. Dalgleish, S.; Reissig, L.; Sudo, Y.; Awaga, K. On-Tip Photodetection: A Simple and Universal Platform for Optoelectronic Screening. *Chemical Communications* **2015**, *51*, 16401–16404, doi:10.1039/C5CC06237C.
356. Tomimatsu, A.; Yokokura, S.; Reissig, L.; Dalgleish, S.; Matsushita, M.M.; Awaga, K. Rate-Determining Process in MISIM Photocells for Optoelectronic Conversion Using Photo-Induced Pure Polarization Current without Carrier Transfer across Interfaces. *Physical Chemistry Chemical Physics* **2019**, *21*, 13440–13445, doi:10.1039/C9CP01221D.
357. Gombos, A.M. Late Neogene Diatoms and Diatom Oozes in the Central South Atlantic. *Initial Reports of the Deep Sea Drilling Project* **1984**, *73*, doi:10.2973/dsdp.proc.73.115.1984.

Appendix A: supplementary information

A.1. Tools to study the morphology and ultrastructure of diatoms

Table A.1. Major tools utilized to study diatom frustule morphology and ultrastructure. This table is modified from Manoylov and Ghobara [321].

	LM	TEM	SEM	AFM	FIB-SEM
Applied on diatoms since	The 1700s [322]	The 1930s [323,324]	The 1960s [324]	The 1990s [325]	The 2000s [326]
Possible lateral resolution	Abbe diffraction limit. Utilizing special kinds of lenses can enhance the resolution (*e.g.*, down to 97 nm [327]).	The resolution can reach below 1 Å (= 0.1 nm) or even lower [328].	Details less than 10 nm are often not resolved under most SEMs. Recently, an outbreak has been achieved to obtain a resolution below 1 nm [329].	The resolution typically reaches below 1 nm.	The resolution is dependent on the SEM and the ion beam in use.
When should we use it?	Observing the presence or absence of diatoms in a sample. Observing the general morphology of diatom valves/frustules. Identification of diatoms on the genus level.	Observing fine ultrastructure (*e.g.*, diatom mesopores [60]). Observing of thin cross-sections in valves/frustules.	Observing the outer ultrastructure including most porosity. Observing the overall 3D geometry and ultrastructure of valves/frustules. Identification at the species and subspecies level.	Observing the 3D topology of diatom valves/frustules with a nano-resolution.	Understanding the inner ultrastructure of diatom valves/frustules by cutting cross-sections through it. Observation of the siliceous elements structural relations within the frustule. Observation of the whole 3D ultrastructure of the frustule via the 3D reconstruction
The Limitations	Fine ultrastructure, below the diffraction limit, cannot be observed. The complex 3D structure often cannot be revealed (either the girdle or	In some cases, the high energy electron beam may damage some sensitive samples. The electron beam cannot penetrate thicker parts in the valve, thus	The samples must be coated with a conductive layer, which in turn could change the texture of the frustule silica and probably pore sizes. In some cases, the high energy electron beam may	The frustules must be fixed to the substrate before measuring. A very sensitive tool with complicated precautions to be followed to get the desired	The required device is not available for all diatom research groups. In some cases, this technique requires more sophisticated steps for

	valve view is obtainable).	only the thinner parts can be revealed. The complex 3D structure cannot be revealed	damage some sensitive samples. Structures below the resolution limits cannot be observed, such as the very fine pore occlusions (below 10 nm).	results.	samples preparation and more sophisticated work to reconstruct the frustule or its parts.

A.2. Sample processing:

A.2.1. Hydrogen proxide (H_2O_2) treatment

Hydrogen peroxide is often used by diatomists to gently digest the organic matter in living diatom samples [104,258,259]. Before the treatment, the diatom culture (containing diatom living cells) was ultrasonicated in an ultrasonic bath for 3 min to disperse living cells. Then, the suspension was treated with about the same volume (1:1) of hydrogen peroxide (Carl Roth, 30%). The mixture was left boiling on a hot plate—covered with a petri dish to enable simple refluxing—in a fume hood for about 1 hour, and then it was left to calm down overnight to continue the digestion of organic materials. After that, the diatom siliceous parts were collected by centrifugation (rpm and time were variable depending on the sample). The collected sample was washed with deionized water and recollected by centrifugation several times until the pH became neutral. Finally, the concentrated clean sample (suspended in deionized water) was stored until further use.

A.2.2. Hydrochloric acid (HCl) treatment

Diatomists generally use Hydrochloric acid to remove inorganic oxides (such as calcite) and the organic residue associated with the siliceous content of the natural grade diatomite samples [104,258,260]. About 0.5 g of diatomite sample was added to 30 ml of deionized water and then ultrasonicated for 5 minutes to disperse the diatomite particles. About 24.6 ml of hydrochloric acid (Carl Roth, 37%) was added slowly to the diatomite suspension; then, the total volume was increased to 100 ml using deionized water to obtain 3N HCL. Following that, the suspension was left under ambient conditions for 48 hours. Thereafter, the diatomite was collected by centrifugation for 2 min at 5800 rpm. The collected sample was washed with deionized water and recollected by centrifugation several times until the pH became neutral. Finally, the concentrated clean sample (suspended in deionized water) was stored until further use.

A.2.3. Settling

Settling under gravity is a well-known separation technique used to separate particles of different sizes/densities in a fluid column [330]. Diatomists also use this technique to separate the coarse grains (such as sand particles in deposits samples) from the siliceous parts (valves/girdle bands) and purify the samples from debris. Interestingly, the settling method was recently used to separate the valves of *Coscinodiscus* sp. from their girdle bands, which have similar size but different geometry and sectional area [331]. Here, this method was applied to the Celatom sample—after the HCl treatment—to remove the siliceous debris and minimize the large variation of *Aula* valves' size found in the sample, probably associated with the presence of valves belonging to more than one species.

First, the method described by Zhang *et al.* [331] was adapted and optimized for the Celatom sample. The best separation result was reached by letting the *Aula* valves (suspended in deionized water after ultrasonicated for 5 min in an ultrasonic bath) settle down under gravity for 30 min in a 50 ml falcon tube. Then, about ≈ 35 ml of the suspension was carefully removed using a Pasteur pipette, leaving only ≈ 15 ml at the bottom. Thereby, the 15 ml fraction at the bottom had mainly valves of larger sizes and was devoid of the fine debris. The process was repeated by refilling the tube—containing the 15 ml bottom fraction—with deionized water and repeating the settling two more times to ensure the separation of the larger valves at the bottom fraction. Following the separation, most valves in the bottom fraction (the obtained sample) are of diameters ≥ 6 µm with a weighted mean value of 13.9 µm. **Fig. A.1** shows the difference between the natural and processed sample under SEM.

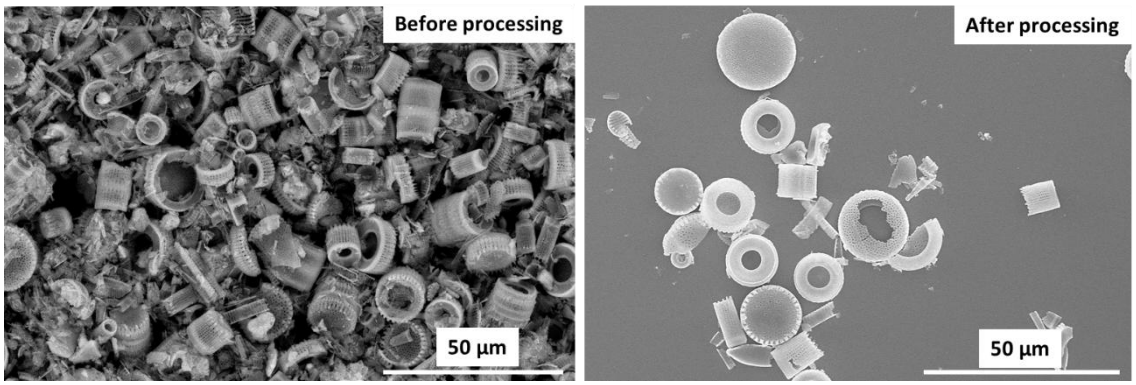

Fig. A.1. The SEM at the left shows the natural grade Celatom sample before processing, having a wide range of valve sizes and a considerable amount of debris. The SEM at the right shows the Celatom sample after processing (the bottom fraction), being cleaner and more homogenous. The SEM on the right was acquired by Dr. Martina Gilic.

A.2.4. Arranged clean valves on a substrate

As mentioned in **Table 3.1**, some of the studied clean valves (shown in **Fig. A.2**) were kindly provided by **Mr. Emiliano Bellotti** (Italy). He arranged these clean valves on a glass substrate covered by a thin layer of transparent glue with the help of an optical microscope and a mechanical micromanipulator. The glue helps to adhere the valves to the substrate while keeping them immersed in the air without sinking into the glue or blocking their pores, thus not changing the refractive index contrast. With this approach, one can study the light modulation behavior of these valves, and then investigate the ultrastructure of the same valves using SEM. The SEM analysis for these valves was carried out—after performing the trans-illumination study—by Mohamed Ghobara (myself) using **Zeiss Sigma 300 VP** (FE-SEM) located at the Institute of Geological Sciences (Mineralogy-Petrology division), FU berlin.

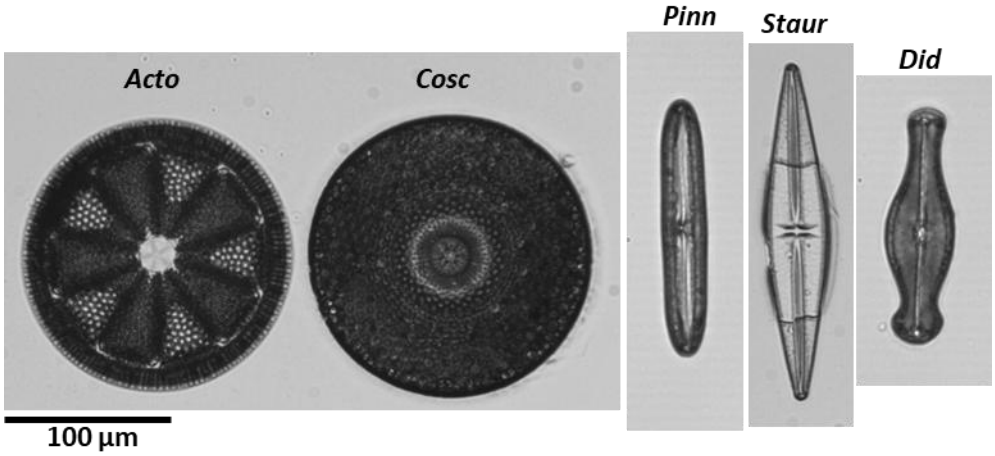

Fig. A.2. The studied arranged clean valves.

A.3. Preparation of clean glass substrates

Glass substrates of dimensions 10 x 26 mm (unless otherwise stated) were cut using a diamond cutter from a microscope glass slide (of dimensions 76 x 26 mm and thickness 1 mm), wiped (with ethanol), and arranged on a Teflon holder for cleaning. Thereafter, the Teflon holder was immersed in an aqueous solution of 0.5% Hellmanex^{TM}III (Sigma–Aldrich) and ultrasonicated for 10 min. This was followed by rinsing the substrates three times in deionized water until traces of the detergent were removed. Afterwards, the Teflon holder was immersed in acetone (Carl Roth, ≥ 99.5%), ultrasonicated for 10 min, and then disposed of. The latter step was repeated but using 2-propanol (Carl Roth, ≥ 99.5%). Finally, the substrates were carefully removed from the Teflon holder, and the excess of 2-Propanol was gently removed via air blowing.

A.4. The optimized film of *Ethmo* valves for the fabrication of $S_{PP}M_{Au+Ethmo}$ photoactive electrode

Fig. A.3 shows an example of the optimized film containing *Ethmo* valves.

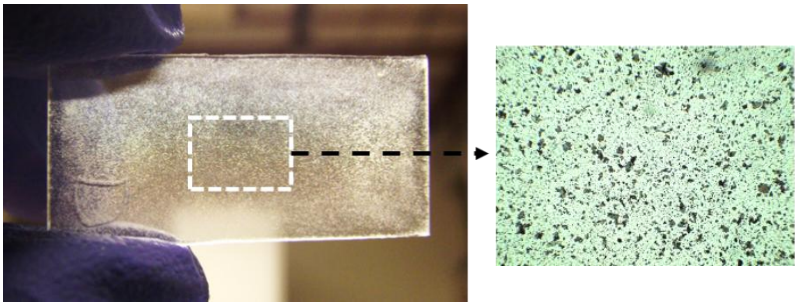

Fig. A.3. An optical image of a uniform film of *Ethmo* valves alongside an optical micrograph showing the cracks of *Ethmo* valves within the film under 4x objective.

A.5. Changing exposure in trans-illumination:

The camera exposure was adjusted depending on the species to avoid saturation at the focusing spots as possible, which can lead to inaccurate results (*e.g.*, defining the focusing maximum at the wrong distance above the valve). It should be noted that once the best exposure for each species was optimized, all parameters (including exposure) were fixed for each ***z***-scan.

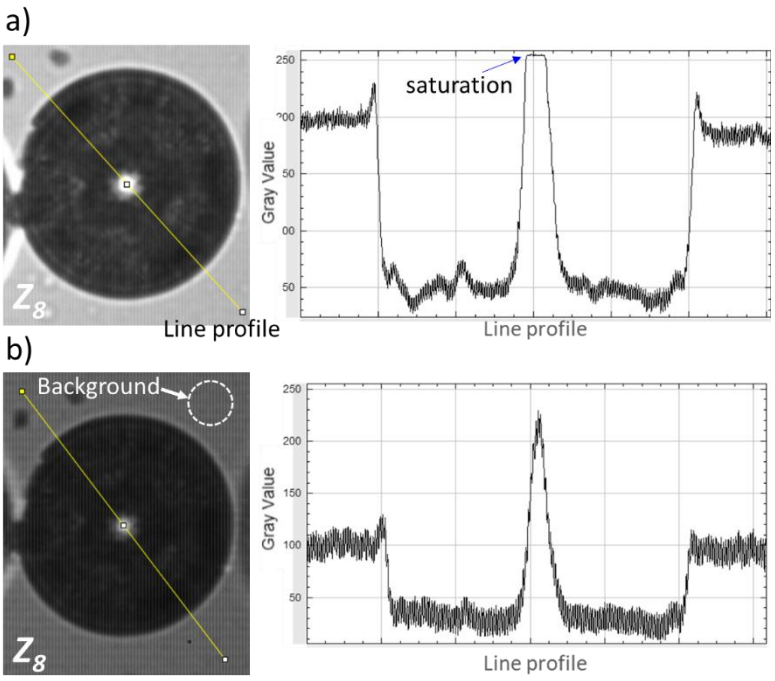

Fig. A.4. (**a**) ***Acto*** valve under trans-illumination using 10x objective (at left) showing a saturation of the focusing spot appeared at the center, as indicated from the extracted line profile (at right). (**b**) The exposure was decreased to half to reveal the maximum gray scale

value of the focusing spot. The dashed circle in (**b**) indicates an example of the areas from which the background's grayscale value was extracted. Each step on the **z**-axis is ≈ 7 µm ± 0.5 µm.

A.6. Validation of the side-illumination experimental setup

A typical PJ generator—artificial solid silica microspheres (diameter ≈ 5 µm, Sigma-Aldrich)—was used to investigate whether the side-illumination experimental setup could disclose the diffraction-driven light-focusing behavior. By examining the silica microspheres using the setup, the expected PJ beam was observed at their rear side (**Fig. A.5c**), alongside a pronounced bright spot (likely a backscattering) at the front side. The experimental results are comparable to the numerical analysis results obtained via the 2D FEFD simulations (**Fig. A.5c** *vs.* **d**). However, it should also be noted that the experimentally observed backscattering spot is not observed in the 2D simulations.

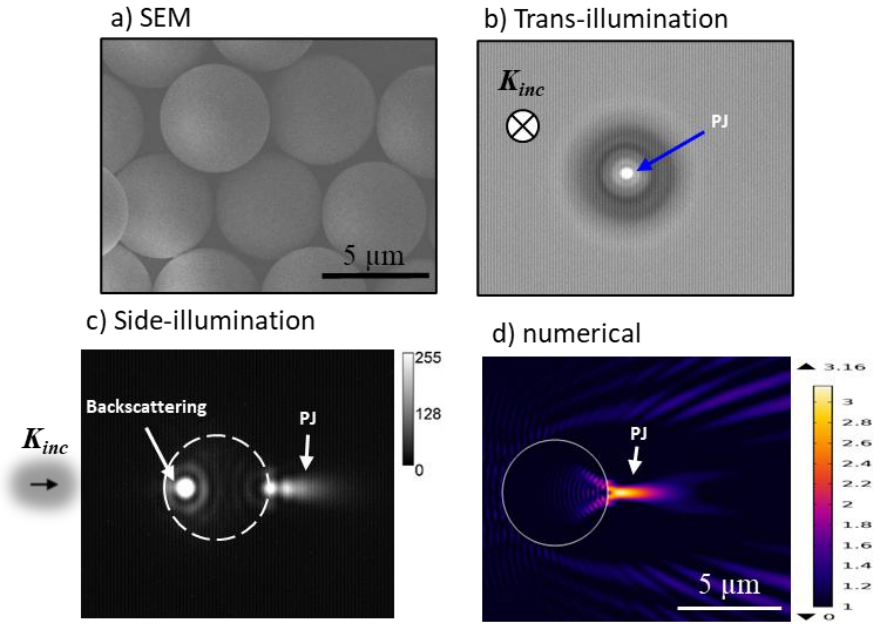

Fig. A.5. (**a**) SEM of silica microspheres. A microsphere under trans-illumination (**b**) and side-illumination (**c**), as appeared under the 40x objective. In the side-illumination setup, the microsphere was illuminated from the *left-hand side* by a red LED (λ_{max} = 660 nm), yielding a PJ beam at the rear side, besides a backscattering spot on the front side. The intensity scale in (**c**) is a greyscale value. (**d**) The 2D simulation results for the wave propagation (*in-plane* **E** field) across 5 µm circle (represents 2D CS in the 3D sphere) at the same wavelength (λ_{vacc} = 660 nm), where n_{sphere} = 1.46 and n_{medium} = 1. The color code ranges from 1 V/m ($\mathbf{E_{input}}$) to 3.16 V/m ($\mathbf{E_{max}}$). The SEM (**a**) was obtained by Dr. Martina Gilic.

A.7. The influence of D_{sl}, n_v, and n_m on reflectance and transmittance (thin-film interference)

As can be seen in **Fig. A.6**, the λ_{vacc} value, associated with the maximal reflectance or transmittance, shifts towards a longer wavelength by increasing the slab thickness D_{sl} ($n_{sl} = n_v = 1.46$, $n_m = 1.00$). At the same time, the associated changes in the maximal or minimal intensity values were negligible. This shift leads to the observation of more oscillations in the case of thicker slabs in our region of interest; as in all cases, the oscillations increase in density with decreasing λ_{vacc}.

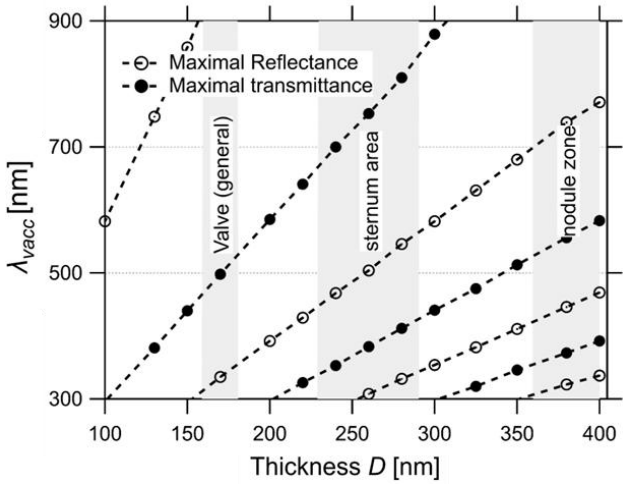

Fig. A.6. The dependency of λ_{vacc} value of the constructive interference maxima on D_{sl}. The grey-shaded areas indicate the significant error in the thickness of different valve parts (**Table 4.1**). This Figure is modified from Ghobara *et al.* [261].

Neither the positions of the maxima and minima in the interference pattern nor its shape depend on the refractive index of the medium n_m surrounding the thin slab when calculated relative to λ_{vacc} (**Fig. A.7b**, left). However, the obtained magnitude of the reflected light or the total attenuation of the transmitted light at a specific λ_{vacc} decreases quadratically when n_m approaches n_v (**Fig. A.7a**, left). Thus, the observed effect is strongly attenuated in water when compared to air.

In contrast to n_m, the refractive index of the thin-slab element n_v strongly influences the position of the spectrum, leading to a red shift in the spectra, as seen in **Fig. A.7b** (right), similar to an increase in D_{sl} but with a simultaneous rise in magnitude. Therefore, in the simulations, while changing n_v (for the same D_{sl} and n_m at specific λ_{vacc}), the intensity of the reflectance and transmittance changed accordingly, as can be seen in **Fig. A.7a** (right).

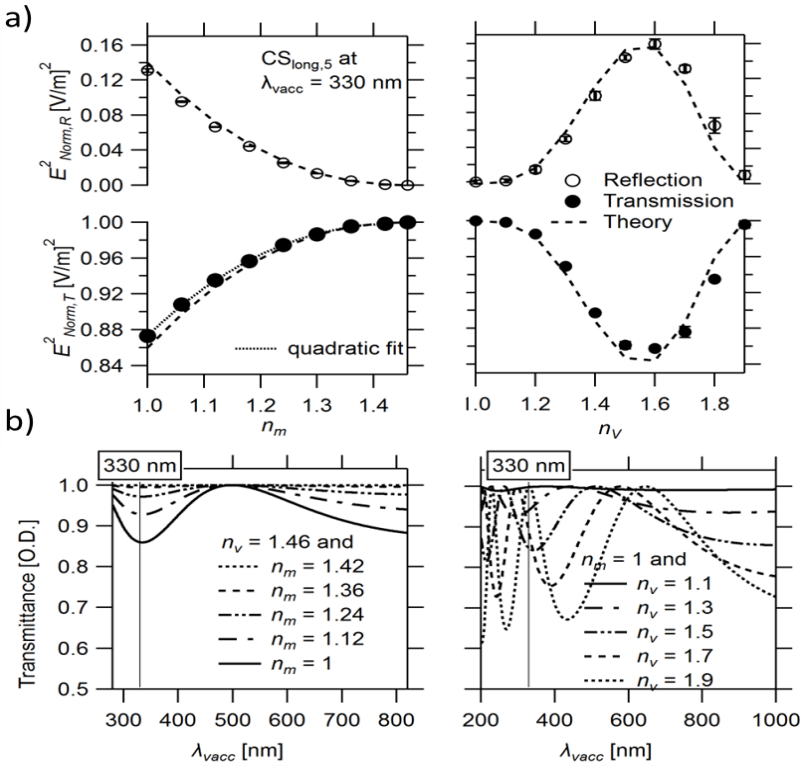

Fig. A.7. (**a**) The change of $\mathbf{E^2_{Norm}}$ (*i.e.*, intensity) of the reflected and transmitted wave by $CS_{long,5}$ at λ_{vacc} = 330 nm when changing n_m (for n_v = 1.46, at left) or changing n_v (for n_m = 1.00, at right) compared to theoretical calculations. (**b**) The change of transmission spectra when changing n_m (at left) or n_v (at right), based on theoretical calculations. This Figure is reproduced from Ghobara *et al.* [261].

A.8. The dependency of edge diffraction fringes on λ_{vacc}

Fig. A.8 shows the λ_{vacc}-dependency of edge diffraction fringes. The mantle in $CS_{long,5}$ spatially delays the 1st and 2nd diffraction fringes inside if compared to $S_{ana,long5}$.

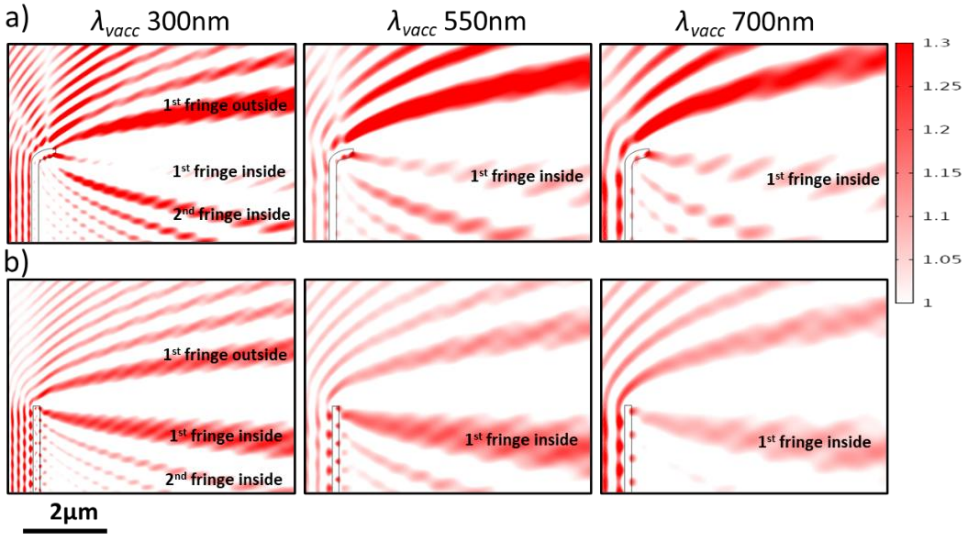

Fig. A.8. The dependency of edge diffraction fringes on λ_{vacc} in $CS_{long,5}$ (**a**) and $S_{ana,long5}$ (**b**) in the air. The color code emphasizes $\mathbf{E_{Norm}}$ enhancement in red ($\mathbf{E_{Norm}}$ > 1 V/m) while keeping both $\mathbf{E_{input}}$ and $\mathbf{E_{Norm}}$ reduction in white ($\mathbf{E_{Norm}}$ ≤ 1 V/m), not emphasized. This Figure is reproduced from Ghobara *et al.* [1].

A.9. The dependency of diffraction-driven focusing spots on λ_{vacc}

Fig. A.9 shows an example of the dependency of diffraction-driven focusing spots on λ_{vacc}. With increasing λ_{vacc}, the spots move toward the CS, decreasing Z_f and L_f and fading in intensity. All spots follow the same trend, even the spots that result from the interference with the so-called photonic jet, *e.g.*, spots 1 and 3.

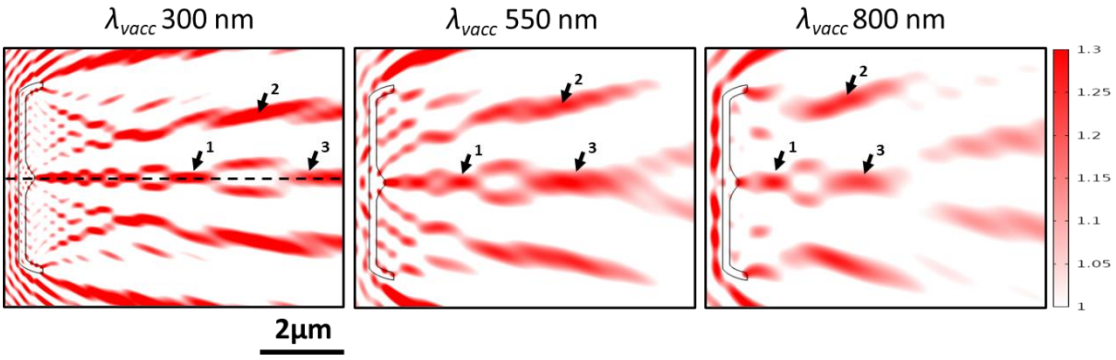

Fig. A.9. Tracking different focusing spots generated by $CS_{ver,2}$ while increasing λ_{vacc} in air. This Figure is modified from Ghobara *et al.* [261].

A.10. Diffraction-driven focusing by *GP* valves under trans-illumination

The *GP* valves utilized in the experimental studies conducted in **Chapter 5** (as well as **Chapters 6** and **7**) were a subculture of the same *GP* strain numerically analyzed in **Chapter 4**. The SEM analysis showed no statistically significant changes in the structural parameters of the valves extracted from the subculture compared to these studied in **Chapter 4**. That means the structural parameters were not only built precisely (as demonstrated in **Chapter 4**) but also were preserved over several generations. It should also be noted that some valves were still connected to a girdle band even after the cleaning procedures, along with the presence of some organic debris (**Fig. A.10**).

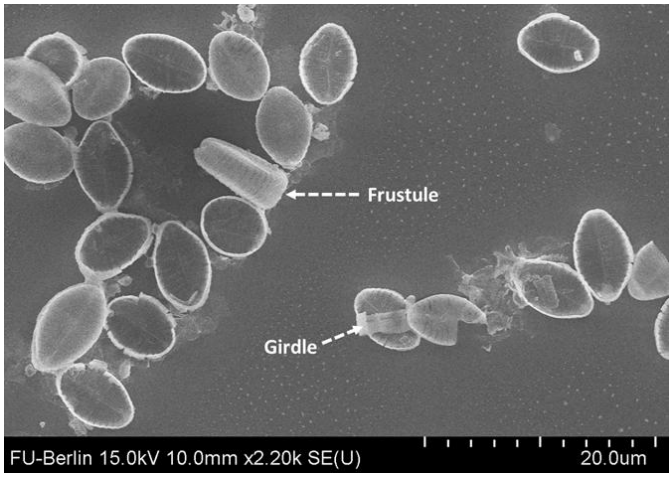

Fig. A.10. SEM show *GP* valves extracted from the subculture. This SEM was captured by Dr. Martina Gilic.

To investigate how much the *GP* 2D simulations could predict the experimental results demonstrated in **Fig. 5.4**, the numerical analysis approach described in **subsection 3.2.4** (**Chapter 3**) was followed. The analysis was carried out for selected 2D CSs, where the central nodule is apparent (see the sketch in **Fig. A.11a**, at left). As the trans-illumination was unpolarized, the situation of both *y*-polarized and *x*-polarized waves (for the light waves propagating on the ***z***-axis) were considered, as demonstrated in **Fig. A.11a**. For the *y*-polarized plane wave, the electric field oscillates *out-of-plane* the longitudinal CSs and *in-plane* the vertical CSs. While for the *x*-polarized plane wave, the electric field oscillates *in-plane* the longitudinal CSs and *out-of-plane* the vertical CSs.

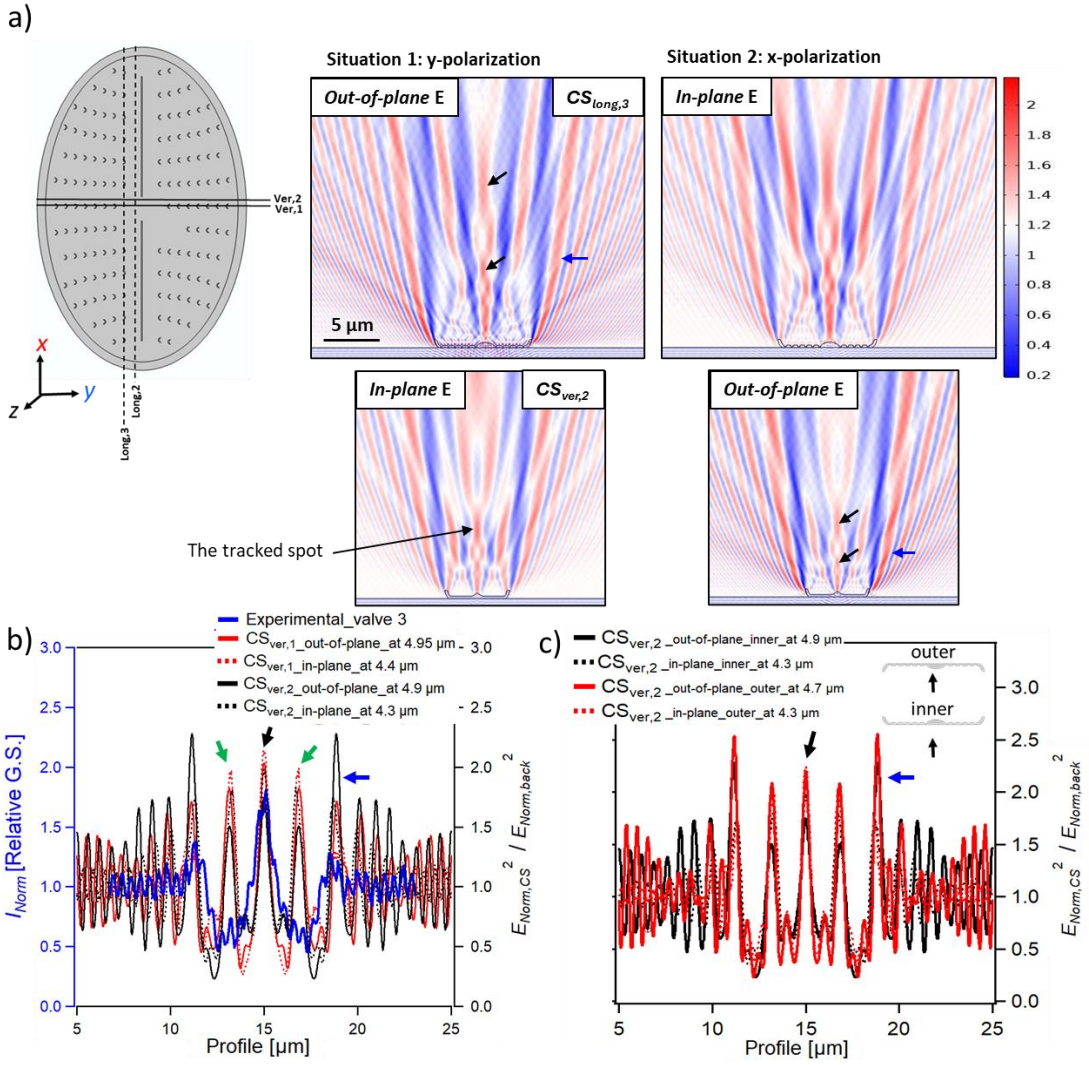

Fig. A.11. (**a**) The 2D simulation results for selected CSs (showing their inner face upward) at λ_{vacc} = 500 nm on the glass substrate in air considering *y*-and *x*-polarizations. The color code aims to only emphasize the enhanced $\mathbf{E_{Norm}}$. The simulated wave ($\mathbf{E_{input}}$ = 1 V/m) was initiated from the bottom. (**b**) Comparing the normalized vertical line profile extracted from valve 3 at z_4 (**Fig. 5.4**) and the vertical profiles extracted from the simulation domain of vertical CSs at maximum $\mathbf{E_{Norm,f}}$ (for the spot indicated in (**a**)) at λ_{vacc} = 500 nm in air at both polarizations. (**c**) Comparison of the vertical profiles when having the inner or outer face upward at both

polarizations. The black and blue arrows indicate diffraction-driven focusing spots and the outside edge diffraction fringes, respectively.

The selected CSs show $\mathbf{E_{Norm}}$ enhancement in transmittance behind the nodule position similar to the experimental observations, where the I_{Norm} enhancement associated with the nodule position was observed starting from $\boldsymbol{z_0}$ (**Fig. 5.4a**). A number of constructive spots were observed along the optical axis of the CSs (see, *e.g.*, the spots indicated by the black arrows in **Fig. A.11a**), which result from the overlay of the PJ generated by the nodule and the inner edge diffraction fringes of the CS (as explained in **Chapter 4**) and was not observed in the experimental results. Interestingly, at λ_{vacc} = 500 nm, the maximum of a major constructive interference spot of vertical CSs (indicated as the tracked spot in **Fig. A.11a**) occurred at a position ranging from 4.30 to 4.95 μm behind the CS (depending on the polarization) comparable to the experimentally observed focusing $I_{Norm,max}$ ($\boldsymbol{z_4}$ ≈ 5.6 ± 0.4 μm). The magnitude of the tracked spot is also comparable to the magnitude of the experimentally observed focusing spot, as demonstrated in **Fig. A.11b**. Moreover, the numerically observed two additional peaks associated with the interference pattern splitting (see **subsection 4.3.4**, **Chapter 4**), indicated by the green arrows in **Fig. A.11b**, are not observed in the experimental results. The outer edge diffraction fringes are also diminished in the experimental results compared to the simulations (**Fig. A.11b**), but its maximum fringe is still observed adjacent to the valve (blue arrows in **Fig. 5.4a**). The simulation results of *x*- and *y*-polarizations show relatively slight variations in $\mathbf{E^2_{Norm,f}}$ amplitude and the position of the tracked spot, as demonstrated in **Fig. A.11b**. Furthermore, when the orientation of the CS is changed, the same behavior is still observed; however, the CS having its outer face upward shows a slightly higher $\mathbf{E^2_{Norm,f}}$ amplitude and the focusing maximum occurs slightly closer to the CS (**Fig. A.11c**).

At this point, if we recall the fact that the CMOS camera used is greyscale and the spectral width of the halogen lamp is larger than the camera's spectral sensitivity. That could partially explain the discrepancy between the obtained experimental results and simulations. For instance, the multiple maxima/minima interference spots that are observed at the longitudinal profile along the optical axis behind the nodule of $CS_{ver,2}$ (see, *e.g.*, the blue arrows in **Fig. A.12a** for λ_{vacc} = 400 nm), will be spatially overlapped (and averaged) across the different wavelengths that can be detected by the camera (as for example illustrated for only four wavelengths in **Fig. A.12a**). That may explain the inability to experimentally detect intensity oscillations at different focal planes (due to averaging). Such oscillations could be revealed if a monochromatic light source is used as an alternative to the Halogen lamp and the system resolution is sufficient to reveal such features. Moreover, the extracted vertical line profiles at 5.6 μm from the CS at different λ_{vacc} (indicated as a black dashed line in **Fig. A.12a**, and equivalent to the distance of the

experimentally observed focusing maximum from the valve) give an idea of how the overlapping across different wavelengths could affect the pattern and magnitude of the experimentally yielded focusing spot as well as other interference features.

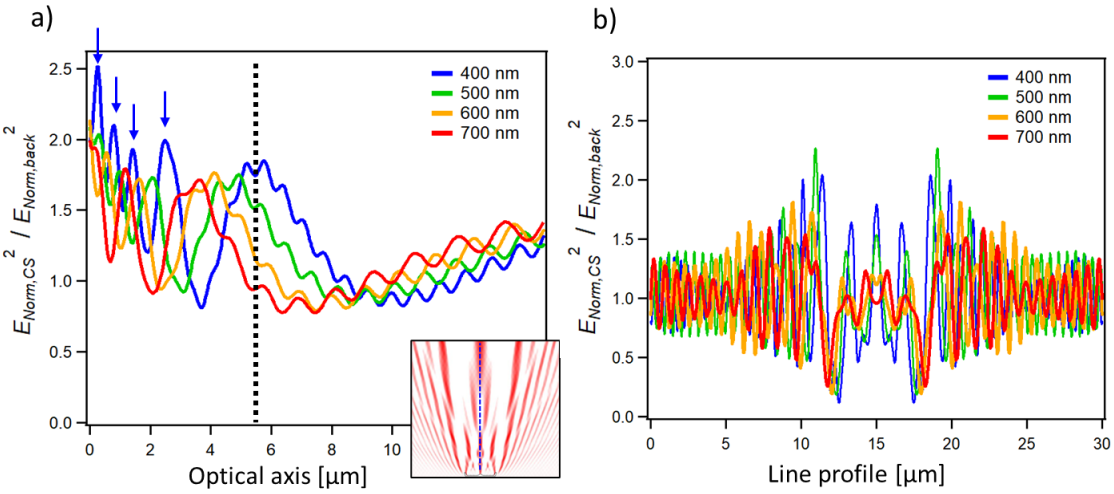

Fig. A.12. (**a**) Longitudinal profiles extracted at the optical axis of $CS_{ver,2}$ (with inner face upward) at different λ_{vacc} in air (*out-of-plane* **E** field). (**b**) Vertical line profiles extracted at the black dashed line (5.6 µm from the CS) indicated at the optical axis in (**a**).

In sum, the 2D simulation results could predict and explain—to a good extent—the experimentally obtained diffraction-driven focusing behavior and estimate the focusing magnitude that could be reached.

A.11. Diffraction-driven focusing induced by integrated mesosize structures

By merging a small silica slab (**Fig. A.13b**, which induces a PJ beam) and a larger slab (**Fig. A.13a**), the transmittance interference pattern of the large slab will be significantly influenced, as can be seen in **Fig. A.13c**. After merging, the PJ induced by the small slab is still observed associated with its position, while the interference pattern of the large slab is split (**Fig. A.13c**).

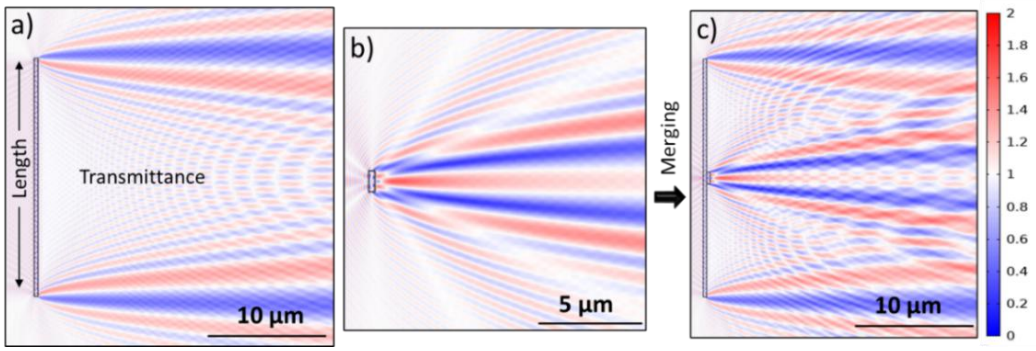

Fig. A.13. (**a**) a slab of silica (n_s = 1.46, L_s = 20.0 µm, D_s = 0.3 µm) impeded in air at λ_{vacc} = 470 nm. (**b**) a slab of reduced length (L_s = 1.0 µm). (**c**) merging the two slabs into a single

structure. The color code is given in V/m, and the simulated wave ($\mathbf{E_{input}}$ = 1 V/m, *out-of-plane* **E** field) was initiated from the *left-hand* side.

Interestingly, such behavior could occur regardless of the geometry of the small slab, where only dimensions matter (**Fig. A.14**).

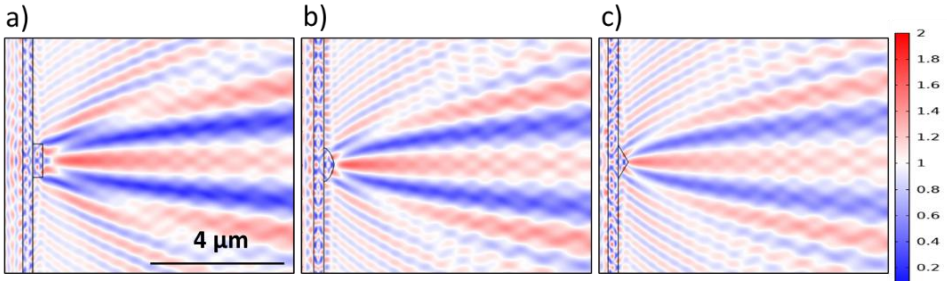

Fig. A.14. The mesosize merged structure can be rectangle, lens, triangle, *etc*. Simulations carried out using the same conditions used in **Fig. A.13** (in air at λ_{vacc} = 470 nm).

A.12. Diffraction-driven focusing by *Aula* valves under trans-illumination

The 2D numerical analysis for the wave propagation across *Aula* Longitudinal CSs demonstrates an ability to induce a diffraction-driven focusing behavior in transmittance when illuminated normally to their face (**Figs. A.15** and **A.16**).

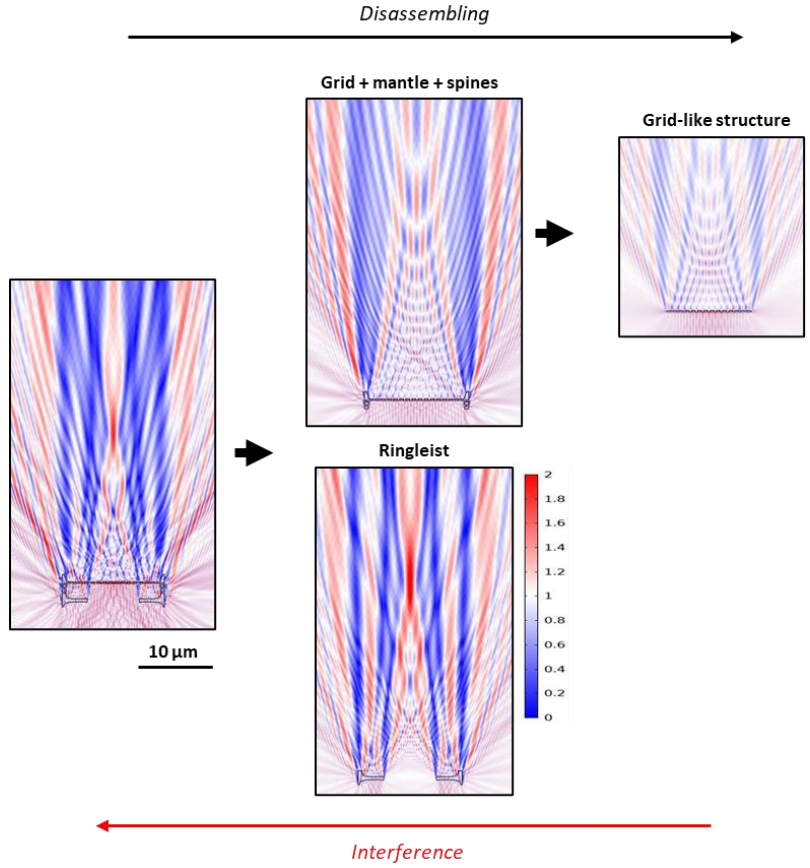

Fig. A.15. The complex interference pattern induced by $CS_{long,1}$ at λ_{vacc}= 500 nm in the air at the left. The disassembling of its distinct structural components shows the contribution of

each element to the interference pattern. The color code is given in V/m, and the simulated wave ($\mathbf{E_{input}}$ = 1 V/m, *out-of-plane* **E** field) was initiated from the bottom.

By disassembling the complex structure of $CS_{long,1}$ (the same approach followed in **Chapter 4** for *GP* CSs), the contribution of different components to the observed focusing behavior was evident (**Fig. A.15**). Interestingly, the interference pattern induced by only the **ringleist** showed a comparable diffraction-driven focusing behavior to the intact $CS_{long,1}$ (**Fig. A.15**), indicating its major contribution to this behavior. The induced interference pattern by the ringleist is attributed to the interference of the waves passed through its opening, the transmitted waves across it, and the diffracted waves at its edges. The presence of other components in $CS_{long,1}$ modulates such interference pattern (**Fig. A.15**).

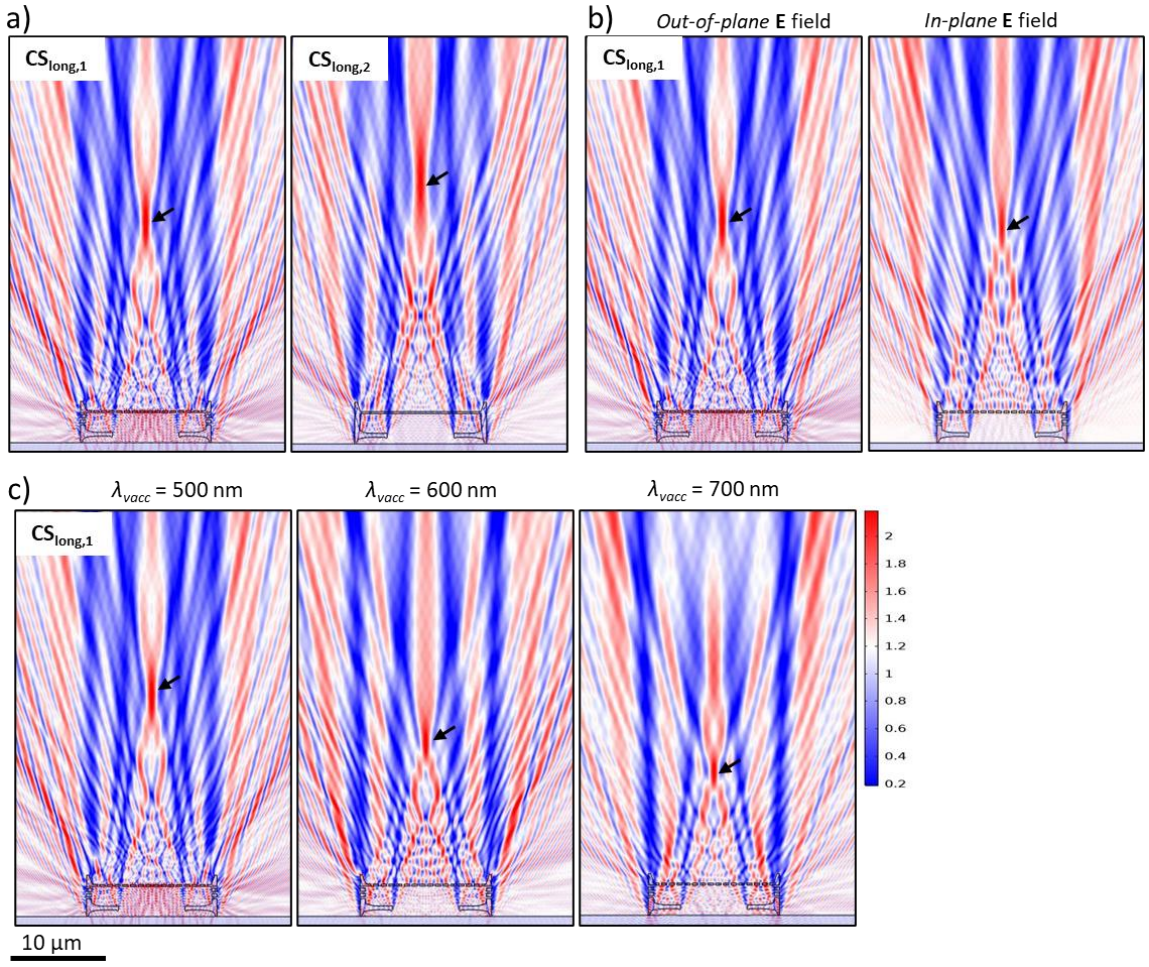

Fig. A.16. (**a**) The 2D simulation results of $CS_{long,1}$ and $CS_{long,2}$ (showing their inner face upward) reveal the diffraction-driven focusing behavior at λ_{vacc} = 500 nm in air on a glass substrate. (**b**) Comparison of the interference pattern of $CS_{long,1}$ at *out-of-plane* and *in-plane* **E** field at λ_{vacc} = 500 nm in air on a glass substrate. (**c**) the wavelength-dependency. The color code is given in V/m, and the white color indicates $\mathbf{E_{background}}$ over glass substrate (≈ 1.185 V/m). The simulated wave was initiated from the bottom. The black arrows indicate a major tracked focusing spot.

The focusing behavior is observed in the simulation results whether the CS has its outer or inner face upward. By laying the *Aula* Longitudinal CSs over a glass substrate, similar to the experiment, the focusing behavior is still observed (see, *e.g.*, **Fig. A.16a**). The simulations results show that the interference pattern (including the position and amplitude of diffraction driven focusing spots) is changed depending on the wave polarization (*e.g.*, **Fig. A.16b**), λ_{vacc} (**Fig. A.16c**), and valve diameter ($2r_v$). By increasing λ_{vacc}, all diffraction-driven focusing spots move toward the CSs (**Fig. A.16c**), similar to *GP* CSs. Increasing $2r_v$ would increase the distance between the ringleist's edges, which will lead to further changes, as can be seen by comparing, for example, **Fig. A.16a** *vs.* **A.17b**.

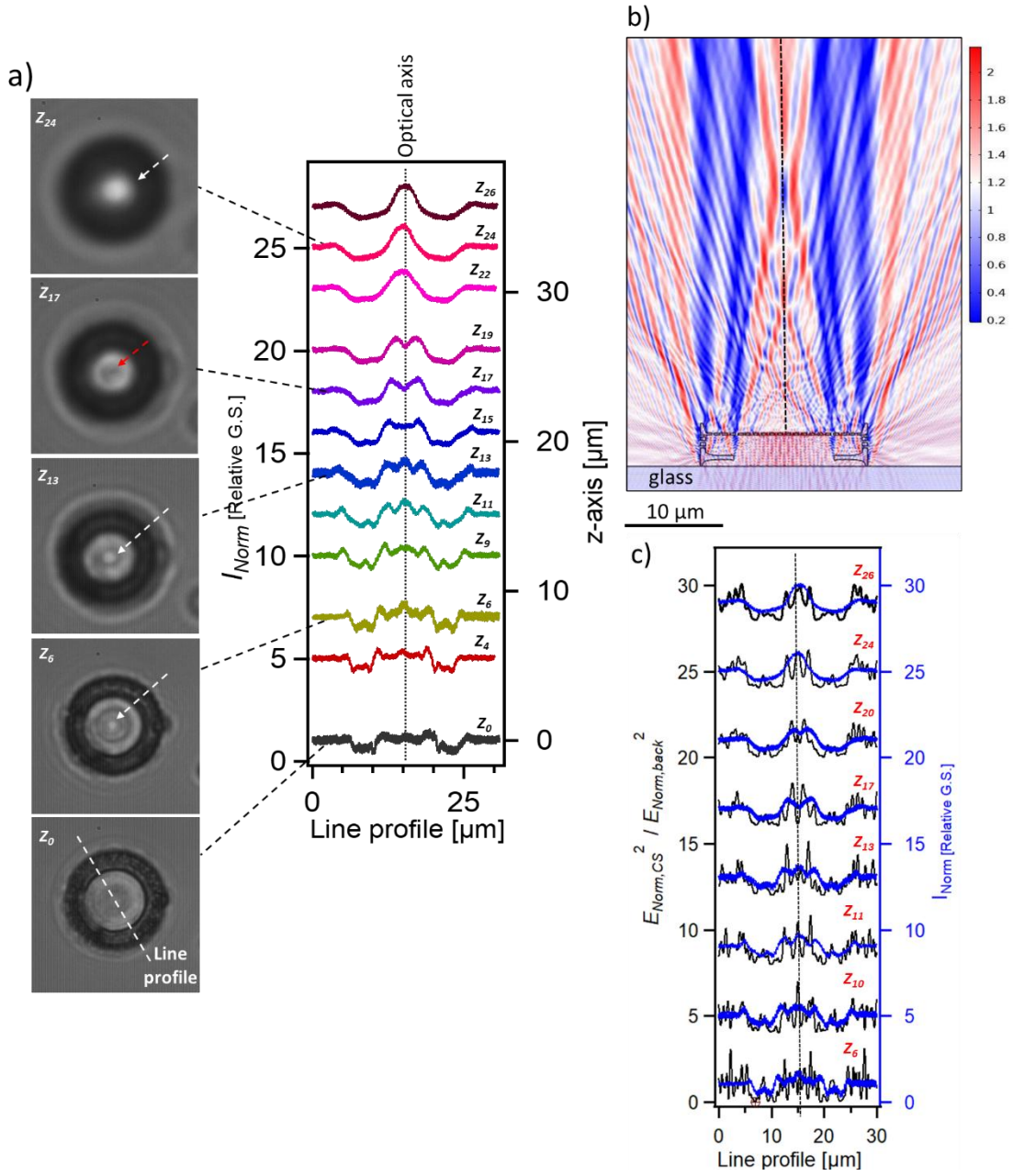

Fig. A.17. An *Aula* valve—showing its outer face upward, of diameter ≈ 17 µm—observed under 40x objective at different focal planes z_i, along with the normalized line profiles

extracted at selected focal planes along the valve's optical axis. Each step on the ***z***-axis is ≈ 1.4 ± 0.1 µm. In this figure, the brightness and contrast of the raw optical micrographs were enhanced to visualize the valve. (**b**) The interference pattern of a modified $CS_{long,1}$ (of diameter ≈ 17 µm) at λ_{vacc} = 500 nm in air on a glass substrate. The color code is given in V/m, and the white color indicates $\mathbf{E_{background}}$ over glass substrate (≈ 1.185 V/m). The simulated wave was initiated from the bottom, *out-of-plane* **E** field. (**c**) Comparing the normalized vertical line profile extracted at selected focal planes from (**a**) and the profiles extracted from the simulation domain in (**b**) at equivalent distance to the experimental focal planes at λ_{vacc} = 500 nm in air. In (**c**) the experimental results are in blue, while the numerical analysis results are in black. Different traces in (**c**), representing different focal planes, were shifted on the *y*-axis by 4 units for each to distinguish them. The dashed lines indicate the optical axis of the valve and the CS in transmittance.

The experimental results obtained for *Aula* valves have shown two focusing spots at distinct focal planes, separated by a dip in intensity, as demonstrated in **Fig. A.17a** (and also **Fig. 5.8**). In contrast, the simulation results show a more complex interference pattern with finer features especially close to the valve, which likely cannot be all observed using the experimental setup. Interestingly, **Fig. A.17c** shows that the simulation result of a modified $CS_{long,1}$ (of diameter and rignleist opening similar to the valve shown in **Fig. A.17a**), demonstrated in **Fig. A.17b**, explains to a good extent the experimentally observed behavior. Still, the discrepancy between the experimental and simulation results could be attributed to the same considerations discussed for the *GP* valve (**section A.10**).

A.13. Diffraction-driven focusing by *CR* valve under trans-illumination

Fig. A.18a shows a *CR* valve (of a diameter ≈ 81 µm and a hyaline area diameter ≈ 6.7 µm), which focused the light into a small spot for a specific distance in the vicinity of transmittance beyond the central hyaline area, reaching its minimum waist (FWHM ≈ 6 µm) and maximum normalized intensity ($I_{Norm,max}$) at $\boldsymbol{z_8}$ (≈ 56 ± 4 µm above the valve) before it started diverging and vanishing. A ring of enhanced intensity was also observed surrounding the central spot in **Fig. A.18a** ($\boldsymbol{z_8}$). Although the observed focusing is of a small magnitude, it was still observed and reproducible between different *CR* valves. This focusing (results from the constructive interference) was accompanied by a pronounced dip in the intensity, especially at the valve's outer rim, as seen in the extracted line profile (**Fig. A.18c**). These findings are similar to previous work on the valves of *Coscinodiscus* spp. [135,137].

An example of a *CR* girdle band (of a diameter ≈ 88 µm) is demonstrated in **Fig. A.18b**, which focused light into a spot, reaching its minimum waist (≈ 10 µm) and $I_{Norm,max}$ at $\boldsymbol{z_{11}}$ (≈ 77.0 µm ± 5.5 µm). At the maximum focus, the observed spot had a larger waist and occurred at a larger distance compared to that of the valve. Such

behavior could be linked to the interference of the light diffracted at the girdle band's edges and the incident light.

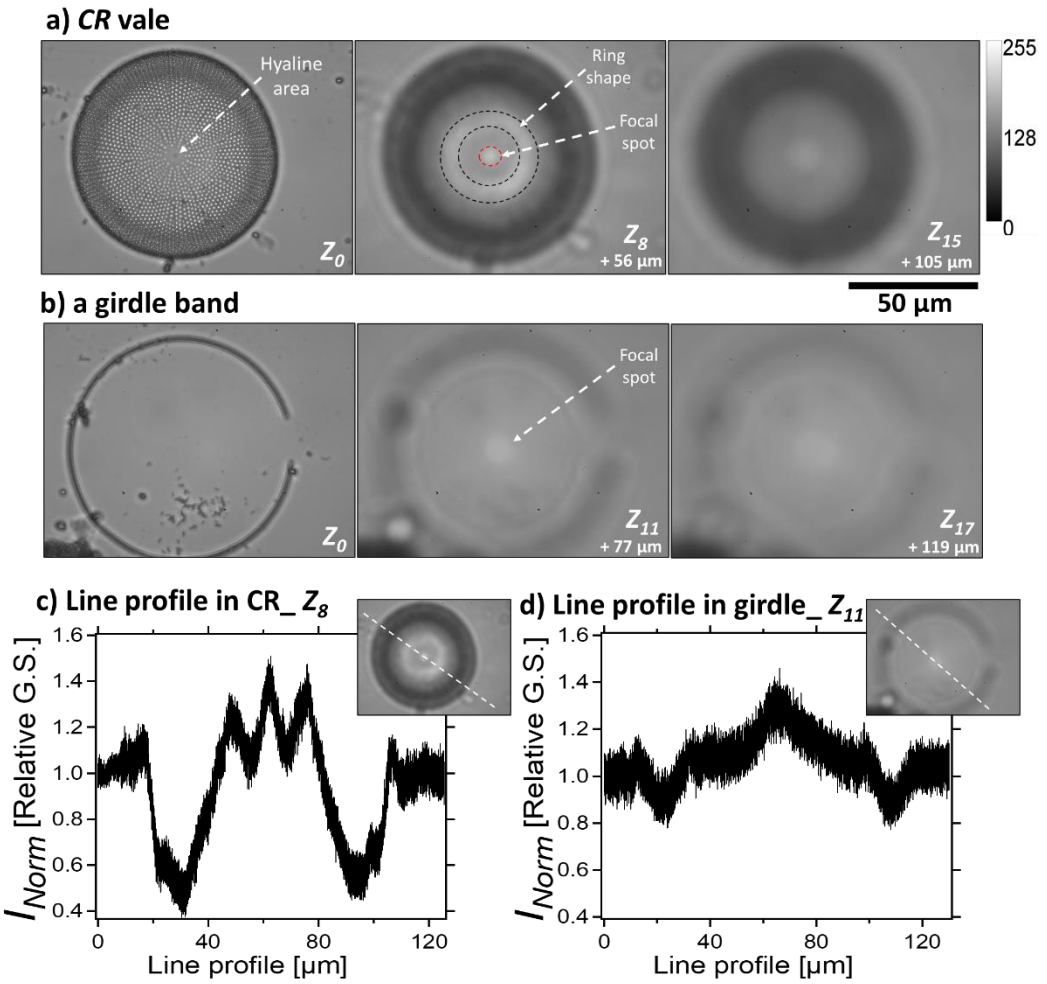

Fig. A.18. A *CR* valve (**a**) and a girdle (**b**) observed under 40X objective at different focal planes z_i, achieved by defocusing. Each step on the z-axis is ≈ 7 ± 0.5 µm. The intensity scale is a grayscale value. The normalized line profiles across the valve (**c**) and the girdle (**d**) at the maximum focus. In the line profiles, the input light intensity $I_{Norm,input}$ = 1, I_{Norm} < 1 indicates attenuation in transmission, while I_{Norm} > 1 indicates enhancement in transmission. The noise in the extracted line profiles represents the error range that is associated with the camera and the optical system.

A.14. Diffraction-driven focusing by *Cosc* valve under trans-illumination

Fig. A.19 shows the light modulation by the ***Cosc*** valve, which dramatically attenuated the transmitted light intensity. Nevertheless, a focusing spot of a relatively enhanced I_{Norm} (compared to the rest of the valve) was observed close to the valve surface (≈ z_0, where FWHM ≈ 2 µm) in the transmittance beyond its hyaline area (of a diameter ≈ 3 µm, see **Fig. 5.2a**), which diverged and vanished by defocusing. A ring of an enhanced intensity was also observed at z_0 (**Fig. A.19**) at the

boundary between the central and outer parts of the valve, where the transition between the two distinct porosity patterns occurs (see **Fig. 5.2a** and **Table 5.1**).

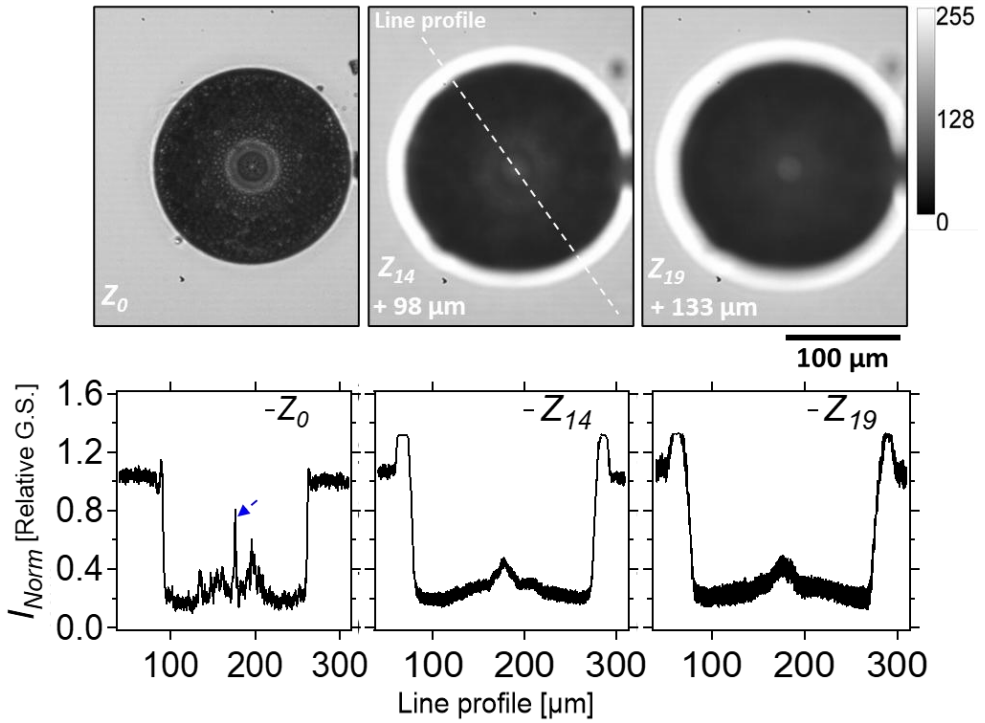

Fig. A.19. The studied *Cosc* valve—which shows its inner face upward—as observed under 10X objective at different focal planes z_i (at the top), along with their normalized line profiles (at the bottom). Each step on the z-axis is ≈ 7 ± 0.5 µm. The blue arrow indicates the focal spot.

A.15. Supplementary to the side-illumination results

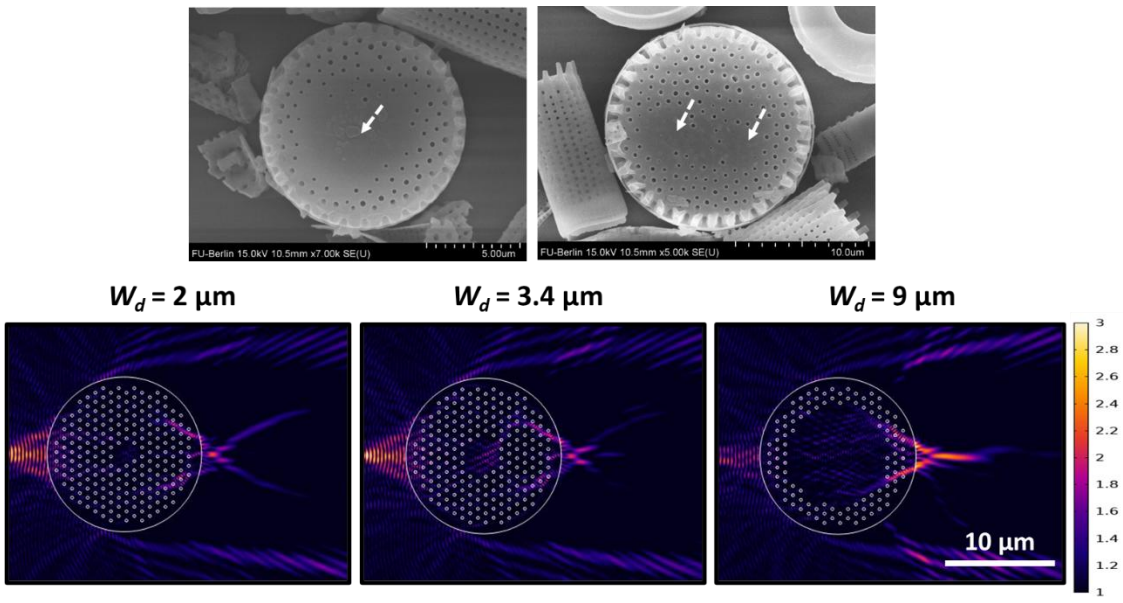

Fig. A.20. SEMs show *Aula* valves with defects indicated by white arrows (at the top). Simulation results show the influence of the presence of a defect in the hexagonal lattice of

$CS_{hor,1}$ and its width $\boldsymbol{W_d}$ on the generated PJ at λ_{vacc} 660 nm in air at rotational angle = 0 degree (at the bottom). At a small defect width, the PJ is still mainly generated at reflectance. In contrast, at a large defect width, the generated PJ beam is largely restored in the transmittance again. The color code is given in V/m, and the simulated wave ($\mathbf{E_{input}}$ = 1 V/m, *in-plane* **E** field) was initiated from the *left-hand* side.

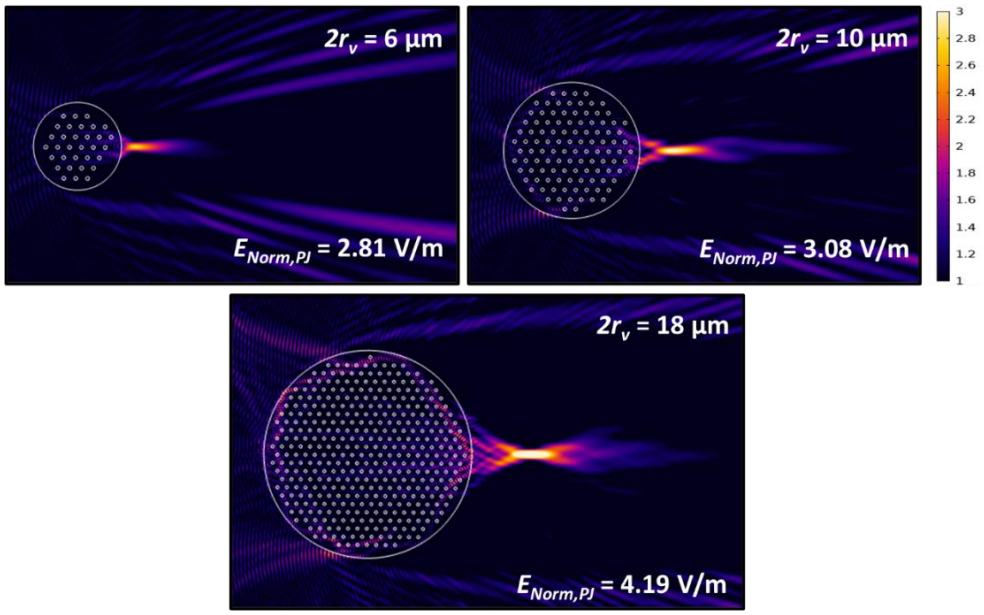

Fig. A.21. Simulation results show the influence of valve diameter $\boldsymbol{2r_v}$ on the generated PJ beam at λ_{vacc} 660 nm in air. By increasing $\boldsymbol{2r_v}$ of $CS_{hor,1}$, the $\mathbf{E_{Norm,PJ}}$ increases. The color code is given in V/m, and the simulated wave ($\mathbf{E_{input}}$ = 1 V/m, *in-plane* **E** field) was initiated from the *left-hand* side.

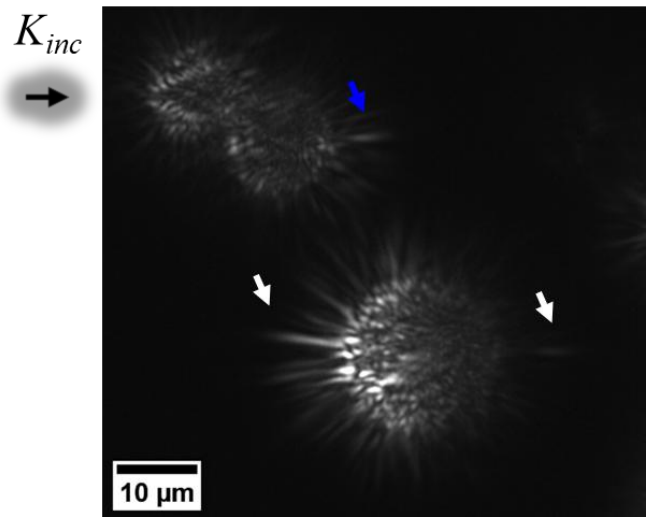

Fig. A.22. Anomalous experimental observation at λ_{max} = 660 nm. An *Aula* valve (at the bottom) shows what seems to be pronounced PJ at the front side (to occur in reflectance) and another PJ at the rear side but of much weaker strength. Another *Aula* valve (at the top) shows a normal PJ generated at the rear side above an *Aula* valve, indicated by the blue arrow.

A.16. Diffraction-driven focusing behavior underwater: photobiology relevance

By immersing the merged two slabs from **Fig. A.13c** underwater, the $\mathbf{E_{Norm}}$ strength of the whole interference pattern, including the induced PJ by the small slab, is reduced dramatically at the visible spectral range, as demonstrated in **Fig. A.23**. Interestingly, the PJ strength of the small slab can be increased underwater by increasing its thickness, as demonstrated in **Fig. A.24**, and a comparable strength could be obtained at higher wavelengths by further increasing the thickness (but keeping it relative to λ_{vacc}).

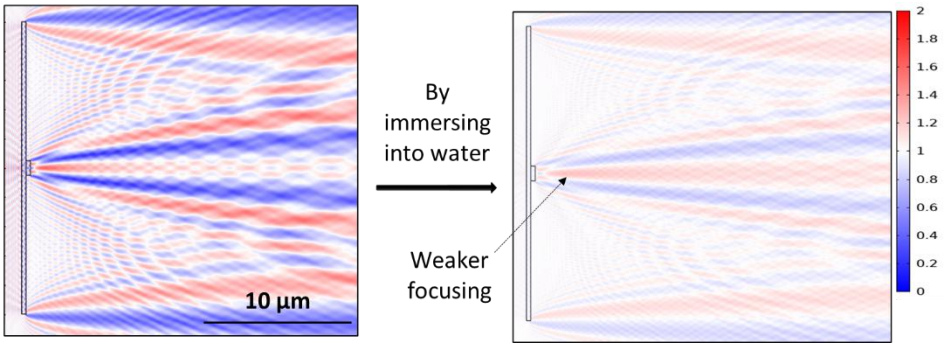

Fig. A.23. The merged two slabs from **Fig. A.13c** immersed in air vs. in water at λ_{vacc} = 470 nm. The color code is given in V/m, and the simulated wave ($\mathbf{E_{input}}$ = 1 V/m, *out-of-plane* **E** field) was initiated from the *left-hand* side.

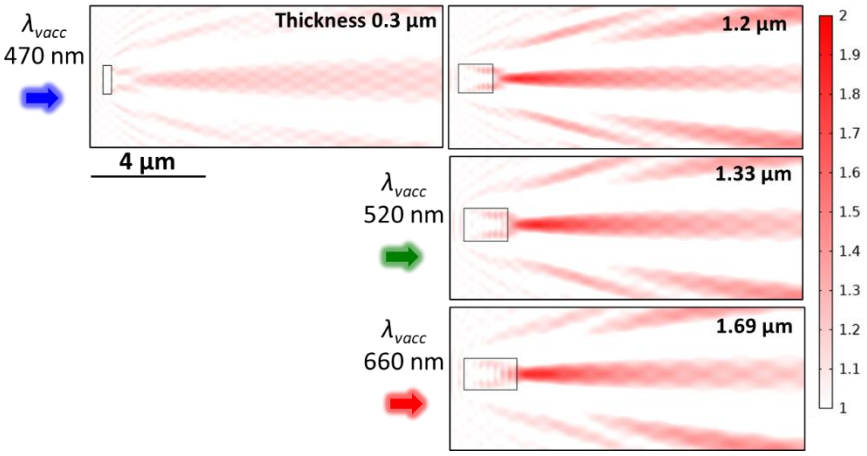

Fig. A.24. By increasing the thickness of the small slab, the PJ strength increased at λ_{vacc} = 470 nm in water (at top). By increasing the thickness slightly, comparable PJ strength obtained at higher wavelengths. The ratio of thickness/λ_{vacc} was kept about 2.6. The color code aims to only emphasize the enhanced $\mathbf{E_{Norm}}$ and the simulated wave ($\mathbf{E_{input}}$ = 1 V/m, *out-of-plane* **E** field) was initiated from the *left-hand* side.

A.17. supplementary information for the SNOM results

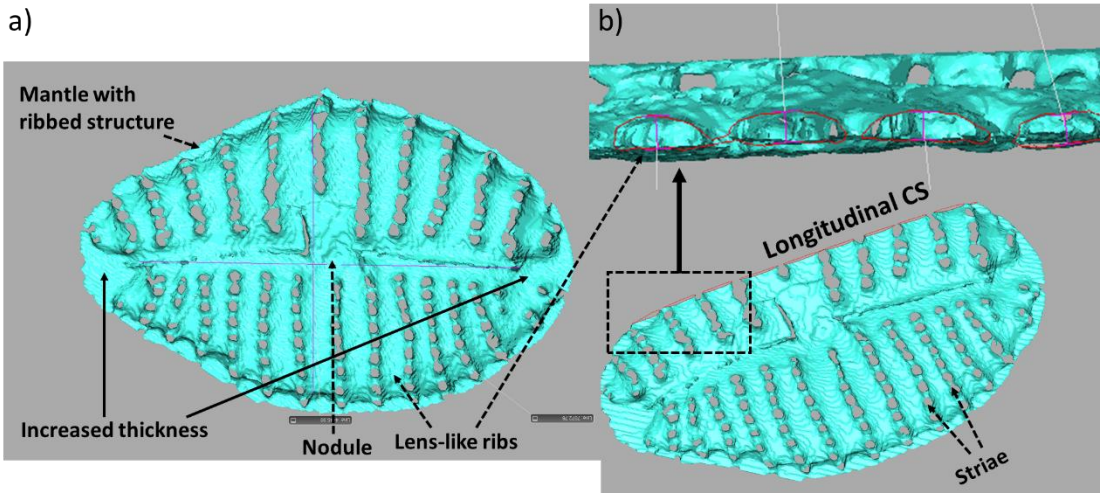

Fig. A.25. (**a**) A 3D constructed *GP* valve shows different parts of the valve. (**b**) Longitudinal CS across the reconstructed valve to show the lens-like ribs. The 3D reconstructed valve images were kindly provided by Dr. Cathleen Oschatz.

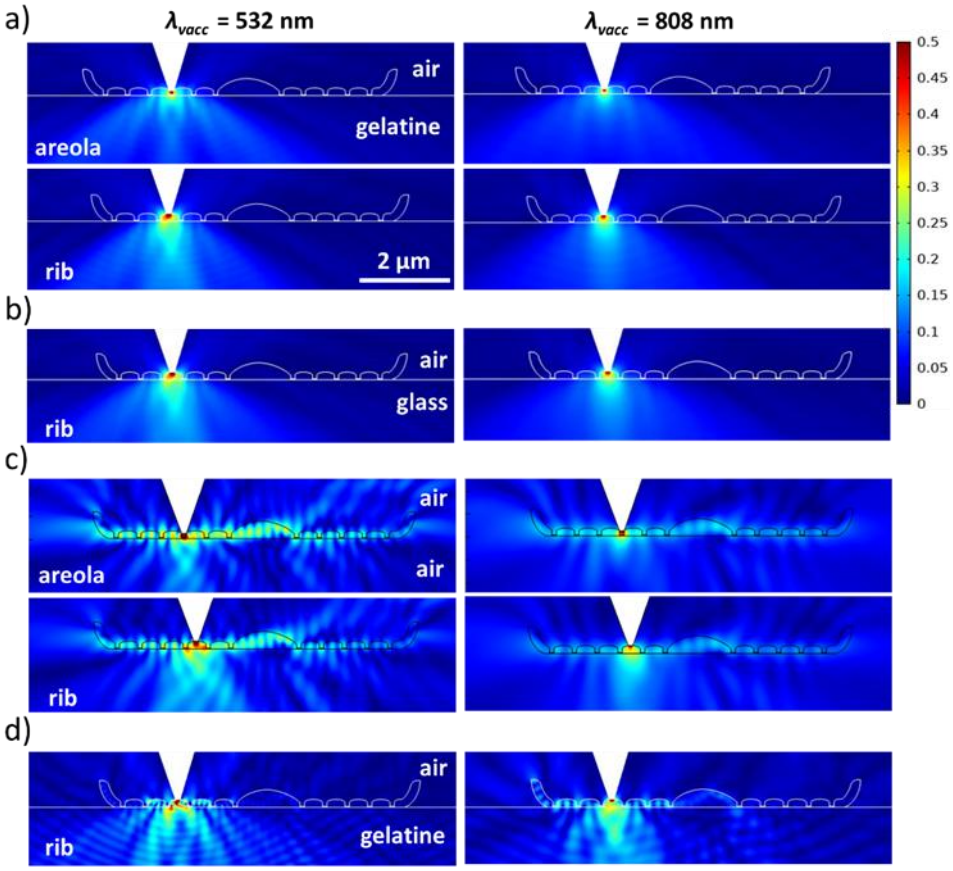

Fig. A.26. The interaction of the local illumination source (of an *out-of-plane* **E** field) with $CS_{long,3}$ showing its inner face upward while laying on a gelatine substrate (**a**), a glass substrate (**b**), or being suspended in air (**c**). (**d**) showing the influence of changing n_v (= 2.6) on the coupling and waveguiding behavior of $CS_{long,3}$ over a gelatine substrate. The color code is given in V/m units.

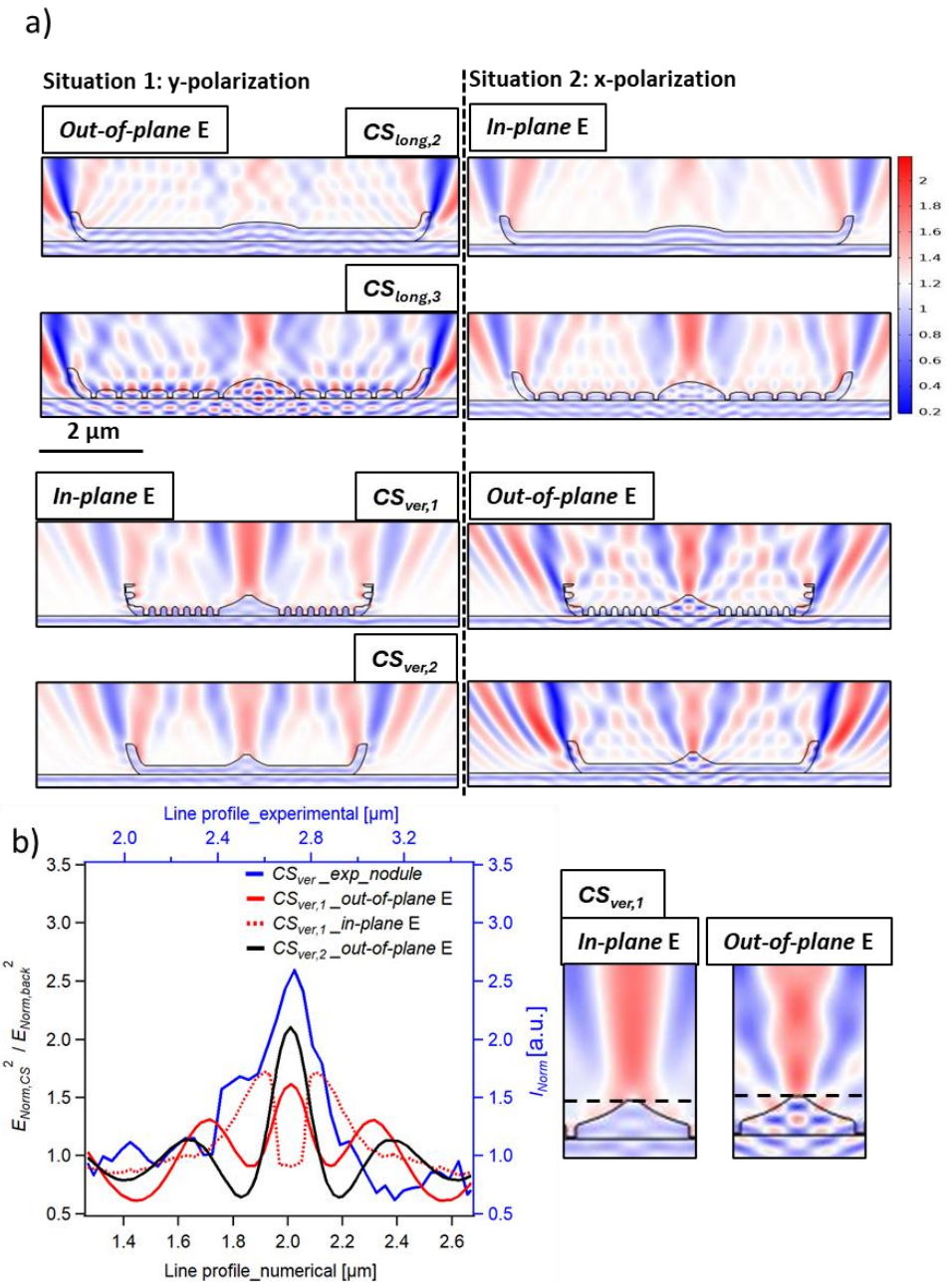

Fig. A.27. (**a**) The 2D simulation results for the selected CSs (showing their **inner face upward**) at $\boldsymbol{\lambda_{vacc}}$ **= 532 nm** in air considering *y*-and *x*-polarizations. The color code is given in V/m. The simulated wave was initiated from the bottom. (**b**) Comparing the normalized vertical line profiles extracted from the experimental (blue trace on blue axes) and numerical data at comparable places in the valve at the optical near-field at λ_{vacc} = 532 nm. The figures in (**b**) at the right demonstrate the exact position of the line profile extracted from the simulation domain, which explains why for the *in-plane* **E**, a dip in intensity is observed in the middle (see the red dashed trace in (**b**)). This is because the PJ is started a bit higher from the CS for the *in-plane* **E** results, which is not the case for *out-of-plane* **E** results.

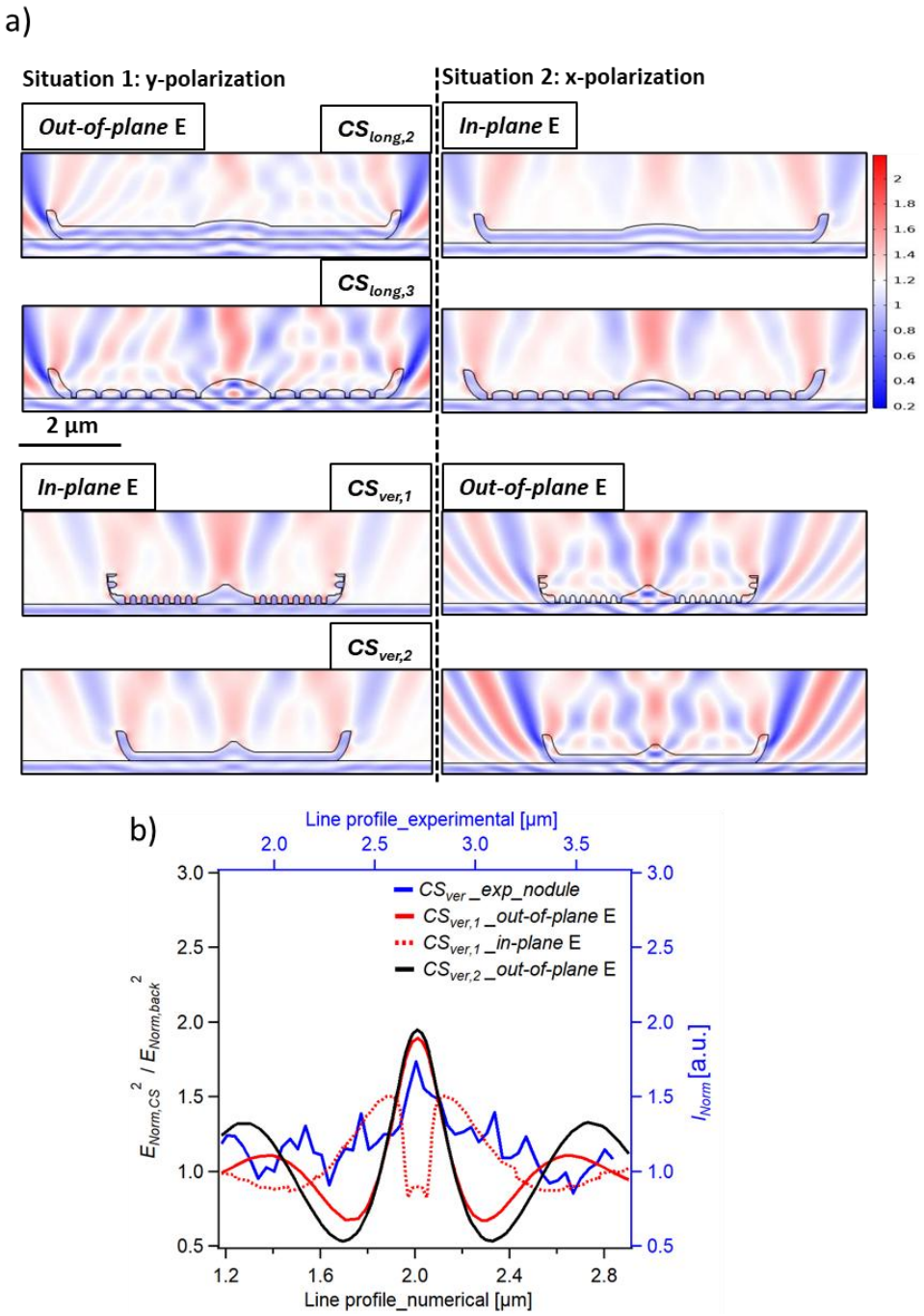

Fig. A.28. (**a**) The 2D simulation results for the selected CSs (showing their **inner face upward**) at $\boldsymbol{\lambda_{vacc}}$ **= 808 nm** in air considering *y*-and *x*-polarizations. The color code is given in V/m. (**b**) Comparing the normalized vertical line profiles extracted from the experimental (blue trace on blue axes) and numerical data at comparable places in the valve at the optical near-field at λ_{vacc} = 532 nm.

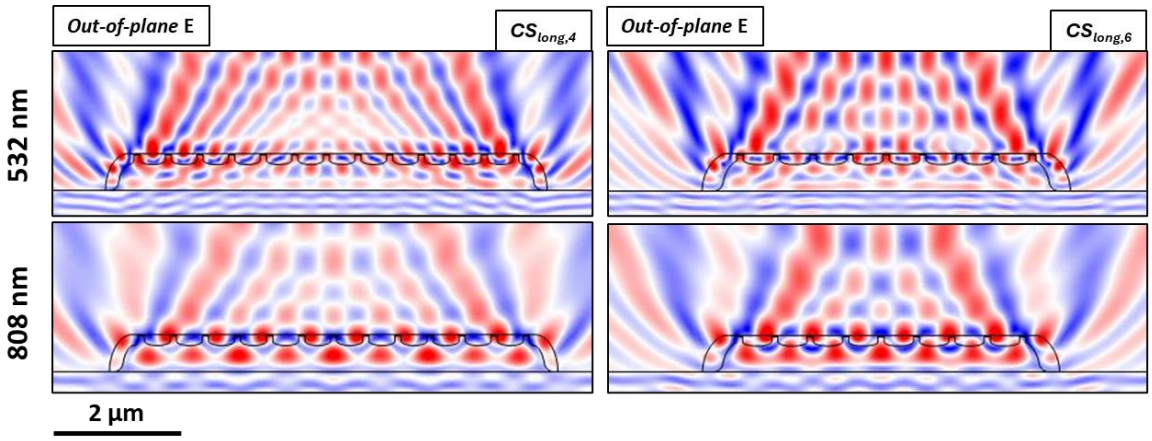

Fig. A.29. The 2D simulation results for GP CSs with grid-like element (showing their **outer face upward**) in air. No GMR or Talbot pattern was observed. Only the mantle-coupled guided waves were observed. The color code is given in V/m.

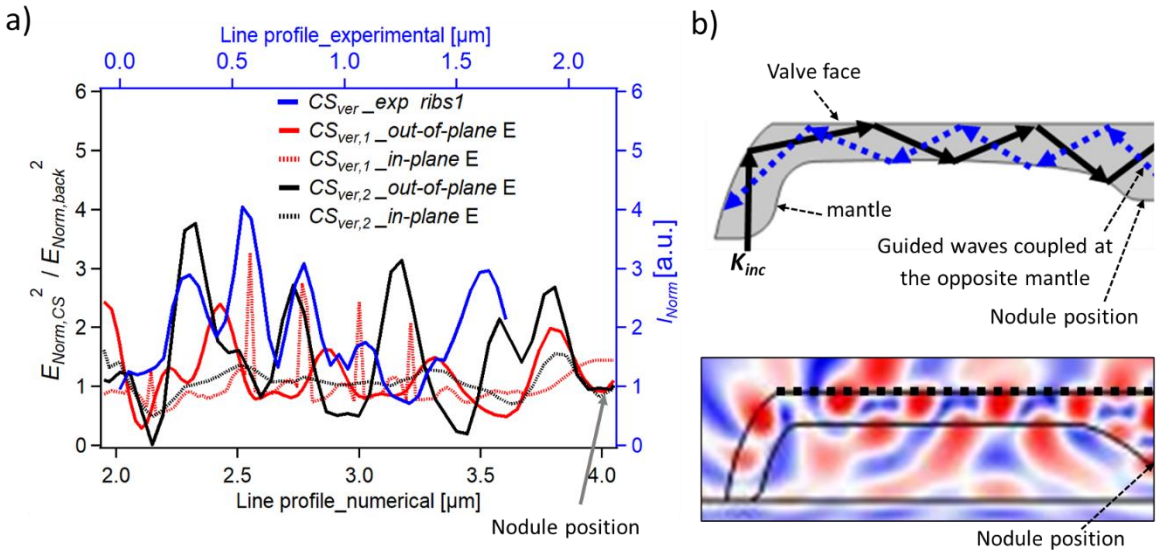

Fig. A.30. (**a**) Comparing the guided waves observed at the *GP* outer face at green laser (blue trace on blue axes, obtained from **Fig. 6.2a**) with the simulation results at a comparable position. (**b**) A sketch showing an imaginary path of the mantle-coupled guided waves inside $CS_{ver,2}$ that represents a rib (at top). A zoom-in the simulation results of $CS_{ver,2}$ at λ_{vacc} = 532 nm and *out-of-plane* **E** (at bottom), the dashed line shows the place of extracting numerical data shown in (**a**).

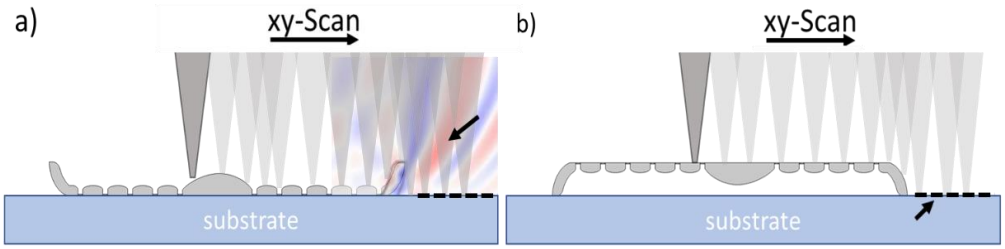

Fig. A.31. Sketches showing how the SNOM probe scans the inner (**a**) and the outer (**b**) *GP* valve face. After passing the valve mantle, the SNOM tip returns to the gelatine layer (the black dashed line). Therefore, the edge diffraction fringes outside the valve (indicated by the

black arrow in (**a**)) cannot be revealed in the collection mode. It should be noted that this is also the case for illumination mode.

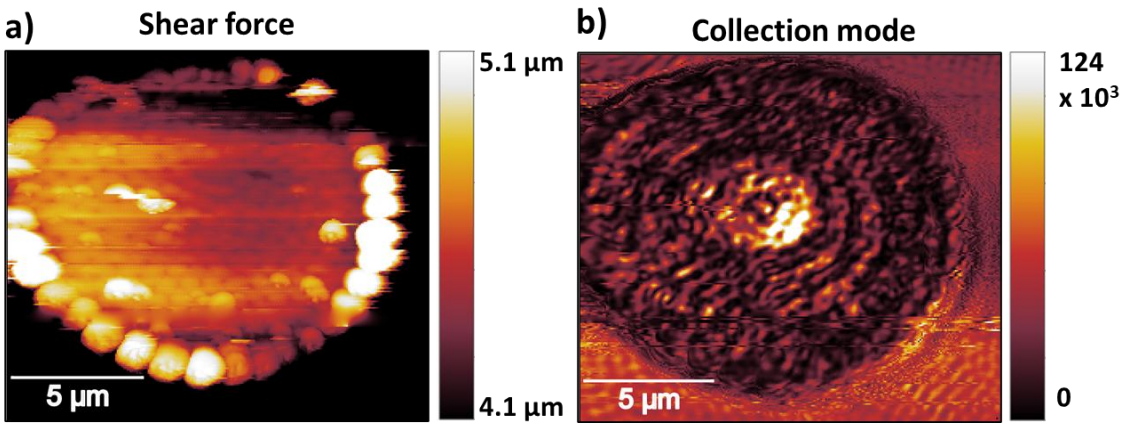

Fig. A.32. (**a**) SNOM shear-force image of another *Aula* valve showing its **outer face** upward. (**b**) SNOM optical image showing the optical response of this valve at green laser in collection mode at higher resolution than **Fig. 6.8c**. The intensity scales are given by integrated counts. The length scale bars have an estimated error up to ± 10%. The raw SNOM images were acquired by Professor Paul Fumagalli.

Appendix B: Developing a method for studying two-dimensional periodicities and symmetries of diatoms' pore arrays

The content shown in this appendix has already been published in:

Ghobara, M.; Tiffany, M.A.; Gordon, R.; Reissig, L. Diatom Pore Arrays' Periodicities and Symmetries in the Euclidean Plane: Nature Between Perfection and Imperfection. In: Diatom Morphogenesis; Wiley-Scrivener, Beverly, MA, USA, 2021; pp. 117–158, https://doi.org/10.1002/9781119488170.ch6. Used here with the permission of Wiley-Scrivener.

As mentioned in **subsection 1.2.2** (**Chapter 1**), in many cases, diatoms' pore arrays have strong resemblance to PC slabs. In order to determine whether these structures can function as PC and to predict their potential PC characteristics, for instance, through numerical analysis, there is a need first to investigate and assess the periodicities and symmetries of their pore arrays employing a systematic, straightforward method. Previous work has been reviewed in Ghobara *et al.* [123] that indicated such a method has not yet been reached.

From that perspective, this appendix aims to propose a method to reveal and define 2D periodicities and symmetries of pore arrays within single silica layers of the projected 2D surface of diatom frustules. Besides that, it shows the possible presence of distinct 2D Bravais lattices in diatoms and discusses how perfect diatoms could be in building their periodic pore arrays compared to perfect 2D Bravais lattices. It should be noted that the results presented here are examples and may not represent the general morphometric criteria of these species.

B.1. Methods

B.1.1. Disclosing diatoms' pore arrays

As mentioned before, the size of diatom pores ranges from a few nm to a few µm, depending on the species. Thus, optical microscopy often cannot provide a sufficient resolution for disclosing diatoms' pore arrays. Alternatively, electron microscopy can provide the required resolution to reveal and analyze such arrays. Therefore, this study is based on scanning electron micrographs (SEMs).

To examine a wide range of diatom geometries, showing pore arrays of distinct periodicities and symmetries, the SEMs library—kindly offered by **Dr. Mary Ann Tiffany** (USA)—was utilized. This library includes thousands of diatom SEMs showing distinct species and ultrastructural diversity. After surfing the library, a

number of SEMs were selected for further analysis, belonging to nine diatom species, including *Asterolampra marylandica*, *Asteromphalus hookeri*, *Arachinodiscus* sp., *Cocconeis* sp., *Haslea feriarum*, *Haslea* sp., *Pleurosigma* sp., *Roperia tesselata*, *Triceratium favus*. The species identification was also provided by **Dr. Mary Ann Tiffany**. Besides that, an additional five SEMs were selected from the literature, representing another five species, including *Gyrosigma balticum*, *Gyrosigma fasciola*, *Lindavia* sp., *Pleurosigma angulatum*, and *Thalassiosira pseudonana*.

B.1.2. The proposed method

The developed methodology can be summarized in three steps, illustrated below in detail and summarized in **Fig. B.1**.

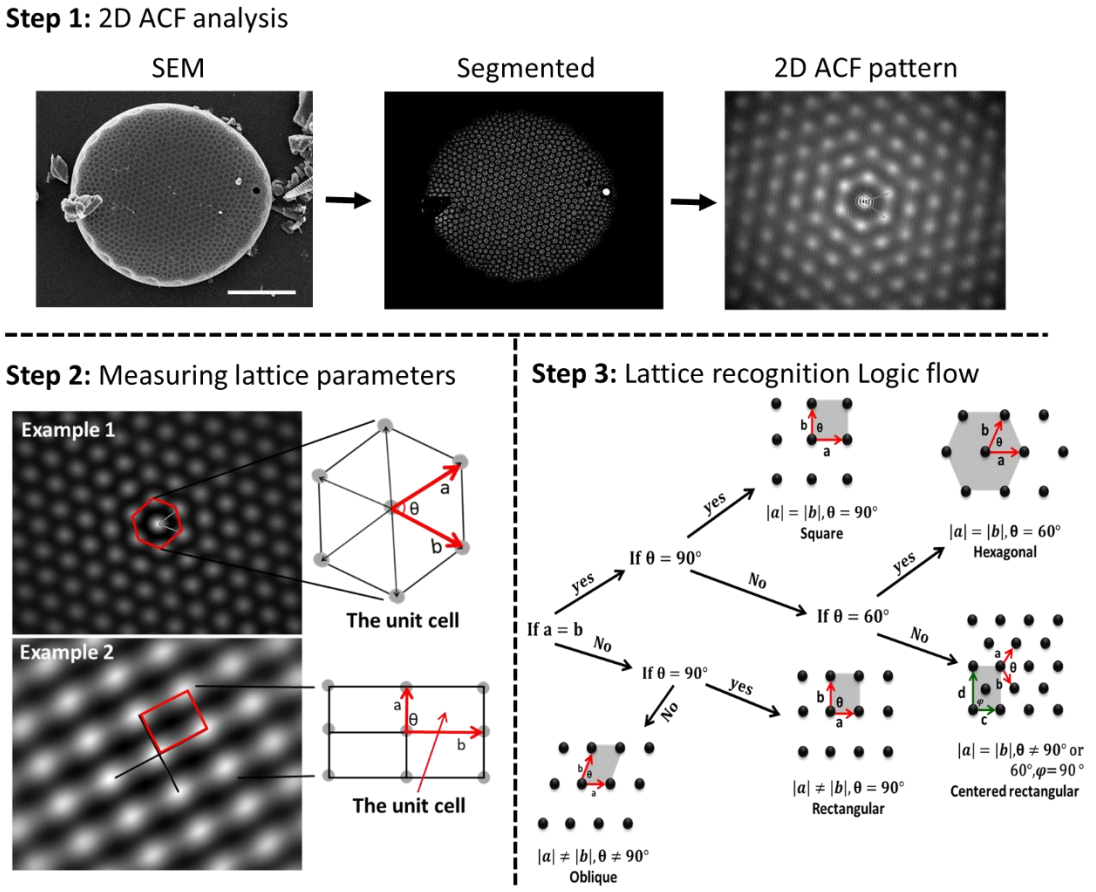

Fig. B.1. The proposed method for studying diatoms' pore arrays periodicities and symmetries. Examples 1 and 2 in **Step 2** represent 2D hexagonal and rectangular lattices, appearing in the corresponding 2D ACF patterns of thresholded micrographs of the inner face of a *Roperia tesselata* valve and of a *Haslea* sp. valve, respectively, both with 4x magnification. The red shapes can be seen as a representative of the unit cell of the 2D lattice. To assign the most similar 2D Bravais lattice, vector lengths **a** and **b**, as well as the angle **θ**, were extracted and compared with the flowchart in **step 3**. The imaginary unit cells of different 2D lattices **in step 3** are highlighted in grey, while **a**, **b**, and **θ** are considered the lattice parameters or constants, while **c**, **d**, and **ϕ** are given as additional related lattice parameters for the centered rectangular lattice. The red arrows represent the measured lattice vector lengths. This figure consists of merged figures from Ghobara *et al.* [123].

Step 1: Two-dimensional autocorrelation function analysis

The two-dimensional autocorrelation function (2D ACF) analysis is a mathematical technique widely used in image processing and signal analysis to disclose the correlation of a signal (or a feature) to its shifted (delayed) copy within two-dimensional data [332]. In the literature, 2D ACF analysis has been used in pattern recognition studies (see, for example, [333,334]). Similarly, here, it is used as a tool for studying periodicities and symmetries within the SEMs of diatom frustules and, thus, to extract the relevant parameters of a given pore array.

Utilizing raw SEMs in the 2D ACF analysis often gives inaccurate results. Therefore, the raw SEMs were segmented using **ImageJ** software [335] as follows. First, histogram equalization is used to enhance the contrast by adjusting the intensity distribution of image histogram, without losing the targeted details. Background subtraction was carried out when necessary to lower the noise. The micrographs were then converted into binary to maximize contrast. Thereafter, segmentation was carried out for the binary images through thresholding. The threshold value was variable and chosen to optimize the output image. Finally, the targeted porosity pattern was selected with the "clear surrounding" option. This method produced white pores on a black valve and black background, which we found gave optimal results, similar to the case of black pores on white valves and white background. It should also be noted that, in some cases, any still present noise or undesired details (such as impurities or structures of the layers below the targeted pores) were manually covered with black color.

The segmented micrographs were individually imported into **Gwyddion** software (version 2.51), and the correct image dimensions were specified in pixels or micrometers. Afterwards, the 2D ACF was automatically calculated for each micrograph to obtain the corresponding 2D ACF pattern, containing information about possible periodicity and symmetry within a given diatom pore array.

The 2D ACF analysis results are generally visualized as a 2D map of ACF (or coherence) values. Any observable periodicity in this image reveals information about occurring periodicities in the original micrograph, with the spatial distribution corresponding to the noise-free (averaged) lattice parameters in the original micrograph.

Step 2: Measuring lattice parameters based on the obtained 2D ACF pattern

Using the "measure lattice" function in Gwyddion software, the unit cell's parameters can be measured utilizing 2D ACF pattern. In case of a lattice structure observed in a given 2D ACF pattern, the structure around the central point of the 2D ACF pattern can usually be considered a representative of the unit cell of this lattice (**Fig. B.1**, **step 2**). It should be noted that the program, through its measure lattice

window, enables only the measurements starting from the central point of the unit cell at the center of the pattern. Three parameters were measured to define the lattice type: the vector lengths **a** and **b** and the angle **θ** between these two vectors. The measured values can be considered averaged values between all the lattice points in the respective direction.

Step 3: Lattice recognition logic flow

Following lattice parameters extraction, the results of these measurements were compared to the flowchart in **Fig. B.1** (**step 3**), and the type of 2D lattice was assigned based on the best-fit to a standard lattice for different degrees of lattice imperfection. In all cases, the values of vector length **a** did not have the same numerical values as the vector length **b**, and the angles were neither 60° nor 90°, leading to an assignment of the oblique pattern if no deviation from the standard values was accepted. However, it was noted that often the numerical values could, within a given precision window (5 or 10%), be related to the standard lattice parameters of one or several 2D Bravais lattices of corresponding dimensions.

To judge the values within an accepted deviation level, the numerical difference between vector lengths **a** and **b** was calculated and normalized to vector length **a** to obtain the percentage of the vector length deviation (**eq. B.1**). In analogy, the difference between the measured angle **θ** and the closest angle (either 60° or 90°) was calculated and normalized to its standard value to obtain the percentage angle deviation (**eq. B.2**). The results obtained were compared to the flow chart in **Fig. B.1**, with accepted deviation levels lower than 5% or 10%, respectively.

$$Deviation\ of\ vector\ length\ (\boldsymbol{b})\ from\ vector\ length\ (\boldsymbol{a})\ in\ percentage\ (\%) = \frac{|\boldsymbol{b}-\boldsymbol{a}|}{\boldsymbol{a}} \times 100 \quad \textbf{(B.1)}$$

$$Deviation\ of\ angle\ (\boldsymbol{\theta})\ from\ the\ closest\ angle\ (60°\ or\ 90°)\ in\ percentage\ (\%) = \frac{|\boldsymbol{\theta}-60°(or\ 90°)|}{60°\ (or\ 90°)} \times 100 \quad \textbf{(B.2)}$$

B.1.3. Assessing reproducibility and accuracy of 2D ACF-based analysis

In order to estimate how reproducible the 2D ACF results are, steps 1 and 2 (of the proposed method) were repeated three times for selected examples. The obtained values for each lattice parameter were averaged and the corresponding standard deviation was calculated. The magnitude of the obtained standard deviation is associated with the possible error in image processing and 2D ACF-based measurements.

To assess the accuracy of 2D ACF-based measurements, a comparison between the bare-hand measurements (*i.e.*, measuring pore spacing and in between

angles by hands, performed via imageJ software) and 2D ACF-based measurements (the averaged lattice parameters obtained by the proposed method, performed via Gwyddion software) was carried out by calculating the probability of the measured 2D ACF value to fall within the range of the measured value obtained by bare-hand measurements (*i.e.*, applying the so-called **standard score test**). To do this, first, the deviation between the values was calculated for each parameter separately: $|x_{hands} - x_{ACF}|$. Then the width of the probability window t_σ of the normal distribution with standard deviation σ was calculated using **eq. B.3**. It should be noted that the standard deviation σ, extracted from the bare-hand measurements, was calculated via the STDEV function in a spreadsheet and is mainly associated with the variation of lattice constants across the chosen area of the valve.

$$t_\sigma = \frac{|x_{hands} - x_{ACF}|}{\sigma} \quad \textbf{(B.3)}$$

Then the probability of the 2D ACF value to lie outside the normal distribution of the bare-hand measurements was extracted from Table A (Appendix A in [336]), and the probability of a statistical match between the 2D ACF value and the bare-hand measured value was calculated applying the following equation:

$$Prob(inside\ t_\sigma) = 100\% - Prob\ (outside\ t_\sigma) \quad \textbf{(B.4)}$$

If the probability is large, the accuracy of the 2D ACF method as compared to the bare-hand measurements was seen satisfactory. It should be noted that this probability decreased (for the same deviation) if the bare-hand measurements were more precise, corresponding to a smaller variation in lattice parameters across the sample.

B.2. Results and discussion

B.2.1. Recognition of periodicities and symmetries of 2D pore arrays in diatom micrographs based on 2D Autocorrelation Function

The 2D lattice parameters, *i.e.*, lattice spacing and angles, can be retrieved from reciprocal space (*k*-space) that can be obtained by applying two-dimensional Fast Fourier Transform (2D FFT) analysis on the original micrograph. However, it often has a comparably low resolution, especially for large periods when the reciprocal lattice peaks become very close, which could hamper its use for lattice recognition and measurements [337]. Additionally, the vectors in *k*-space correspond to the reciprocal lattice, which complicates the assignment. In contrast, 2D ACF analysis offers better resolution, and its lattice vectors correspond to those in direct space (*i.e.*, original micrograph). Some important remarks, which were observed while applying 2D ACF analysis on diatom SEMs, will be discussed in the following paragraphs to demonstrate the limitations and best procedures of this analysis,

which have been considered while developing the proposed method. It should be noted that similar remarks were also observed in the case of 2D FFT analysis, as illustrated in more detail in Ghobara *et al.* [123].

Using raw SEMs in 2D ACF analysis without prior segmentation or processing could give representative results. However, in many cases, that gives unclear results (*e.g.*, **Fig. B.2a**) related to the presence of several sources of noise in the raw SEMs, including; the resolution of the scanning electron microscope, its magnification, the stability of the applied voltage to the device, the image background, and the presence of debris covering valves/girdle bands. That is why segmentation through, for example, thresholding (*e.g.*, **Fig. B.2b**) is recommended before performing 2D ACF and using its output images in lattice recognition studies.

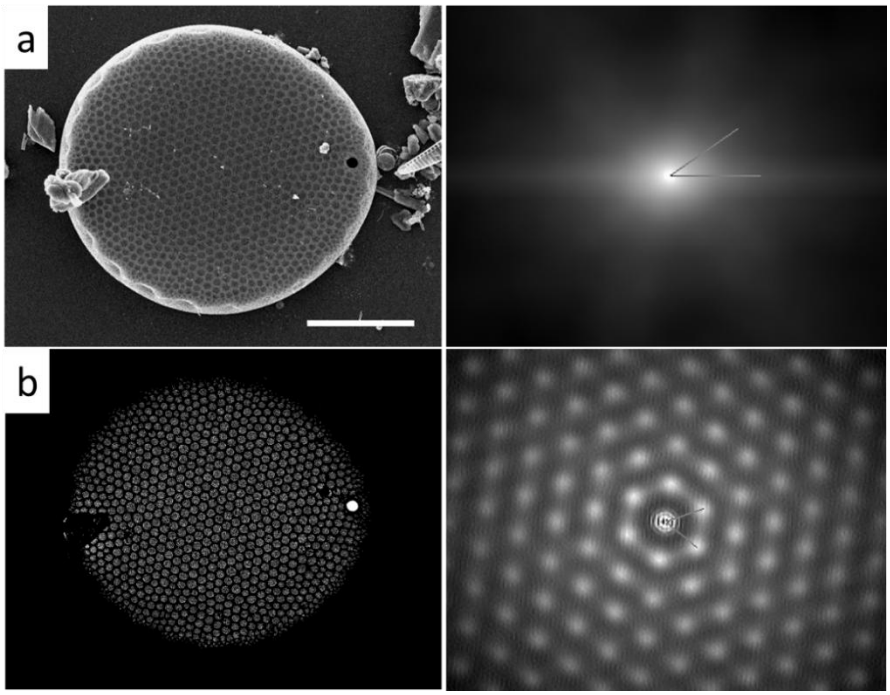

Fig. B.2. SEM of the outer face of a *Roperia tesselata* valve (**a**), and its threshold (**b**), along with their corresponding 2D ACF patterns at right (4x magnified). The scale bar in (**a**) is 20 µm. This figure is modified from Ghobara *et al.* [123].

Moreover, a difference in the 2D ACF pattern was noticed when comparing processed micrographs with different brightness/darkness levels of the features in the background or the porosity (**Fig. B.3**). In general, the clearest 2D ACF patterns were obtained after maximizing the contrast between the pores and a homogeneous background, from which all remaining information (such as the presence of a valve edge) was removed. This can be either achieved via white pores on a black valve and black background (**Fig. B.3a**), or via black pores on a white valve and white background (**Fig. B.3d**), as it removes all the interference from the background and the valve with the periodic signals from pores. It should, however, be noticed that for Gwyddion, an image of white pores on black background corresponds to

"particles on a substrate" with height given when importing the image, and black pores on white background corresponds to "pores/holes on a substrate" with given depth. Nevertheless, there was no difference in the obtained 2D ACF pattern in both cases.

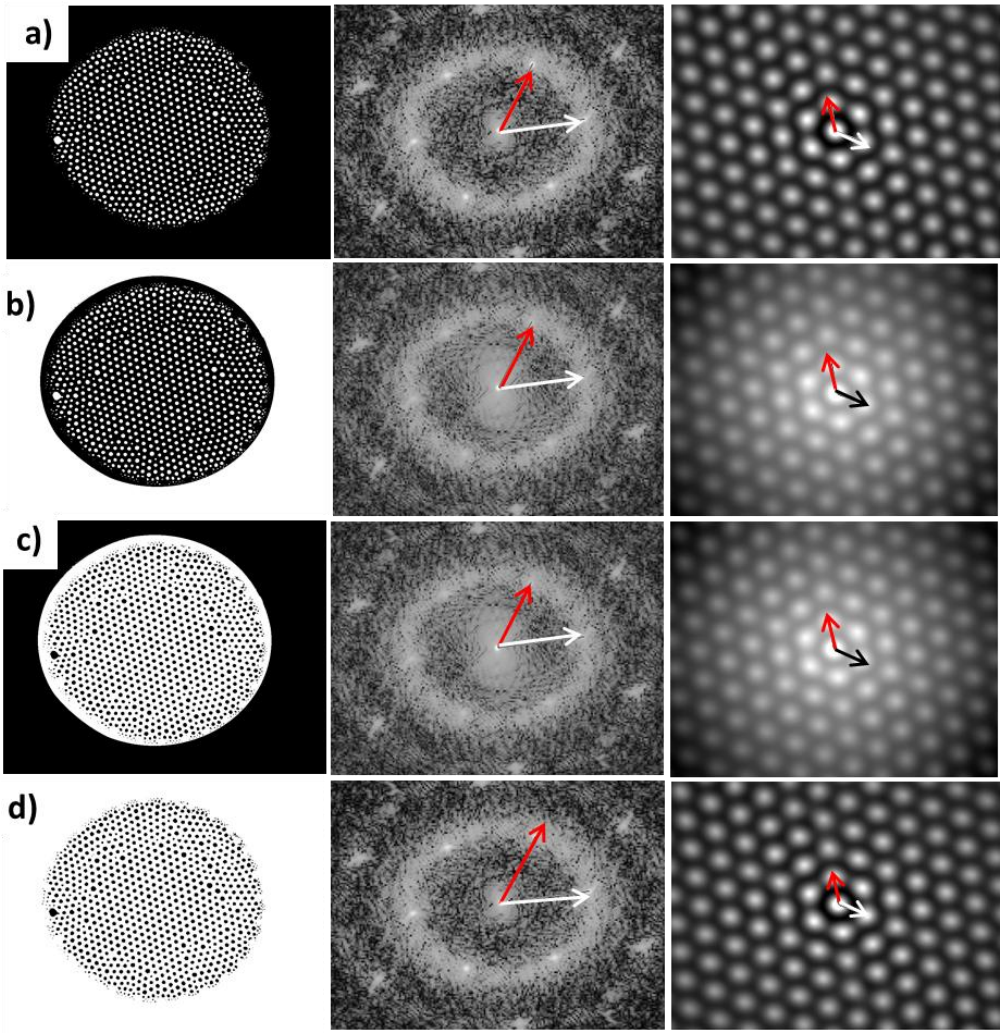

Fig. B.3. A threshold of the same micrograph shows the inner face of a *Roperia tesselata* valve with different brightness/darkness of background/porosity. (**a**) A black background and valve, with white pores. (**b**) A white background and pores, with black valve. (**c**) A white valve, with black background and pores. (**d**) A white background and valve, with black pores. Each micrograph has its corresponding 2D PSDF and 2D ACF shown to its right. The drawn arrows refer to comparable lattice vectors in the direct and reciprocal space. Both 2D PSDF and 2D ACF have 4x magnification. This figure is adapted from Ghobara *et al.* [123].

Additionally, a tilt of the valve in a micrograph could lead to a distortion of its 2D ACF pattern (as seen in **Fig B.4**) and, thus, incorrect lattice assignment. Therefore, using tilted valves is not recommended for the study of 2D pore arrays; otherwise, a correction for the tilt should be carried out [122]. Apart from the tilt during acquisition, the natural curvature of the surface of interest can also hamper the analysis when using the 2D projection obtained in the micrographs. In such a case, it

would be necessary to reduce the area only to contain the pores of an almost flat region unaffected by the curvature too much.

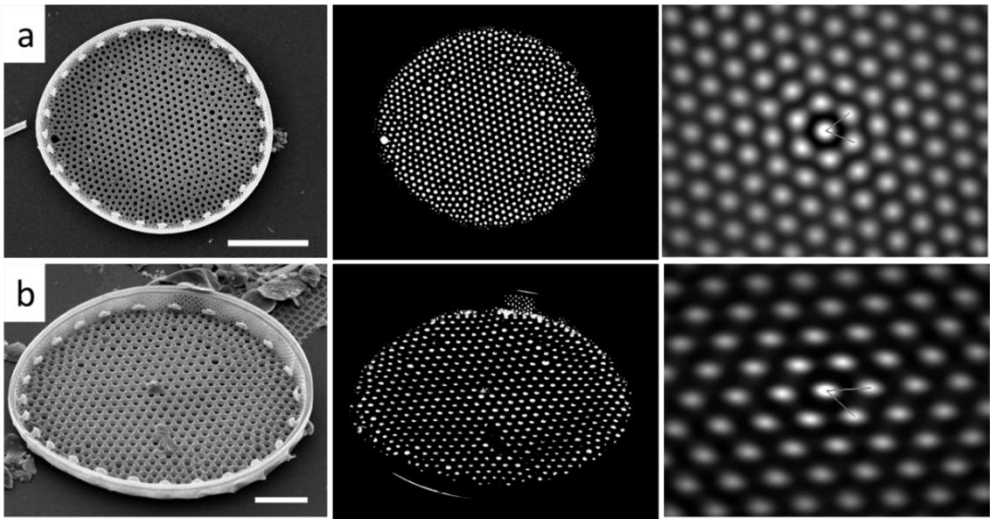

Fig. B.4. SEM of the inner face of a *Roperia tesselata* valve in an upright position (**a**), and in a tilted position (**b**), along with their corresponding segmented micrographs (in the middle) as well as 2D ACF patterns (at right). The scale bar is 20 µm in (**a**) and 10 µm in (**b**). This figure is modified from Ghobara *et al.* [123].

Furthermore, using the complete valve in 2D ACF is sometimes unsuitable due to possible interference between distinct groups of 2D pore arrays (having differently-oriented lattice vectors) within the valve that could lead to incorrect 2D ACF pattern, as shown in **Fig. B.5**. In this case, the target group of pore arrays should be selected for the study after segmentation, *e.g.*, by cutting the micrograph or using the "clear surrounding" option in ImageJ and performing a separate 2D ACF analysis for each group to determine the periodicity and symmetry within this group.

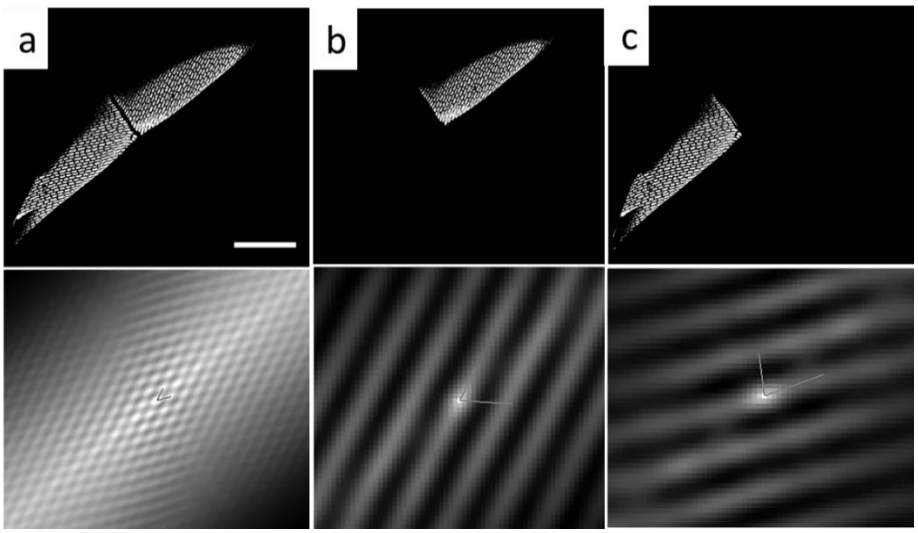

Fig. B.5. (**a**) A segmented micrograph of the SEM of the inner face of a *Haslea feriarum* valve with apparent bilateral symmetry (Scale bar = 10 µm), (**b**) the separated upper part, and (**c**) the separated lower part, along with their corresponding 2D ACF pattern at the bottom,

showing 1D linear periodicity of the successive striae. The false pattern in (**a**) does not represent the true periodicity in the valve but rather an interference emerging from the overlap of the two patterns appearing in (**b** and **c**), resulting in a seemingly 2D lattice. This figure is adapted from Ghobara *et al.* [123].

Finally, it should also be noted that the 2D ACF analysis will not demonstrate any lattice defects as the Gwyddion software ignores the missing values in the lattice. Thus, this method will not be suitable for studying defects, *i.e.*, missing points (pores) within the lattice, in the periodic pore arrays.

B.2.2. The reproducibility and accuracy of lattice parameters' measurements using the proposed method

The precision of the proposed methodology, from the segmentation to parameter measurements, was in the range of four digits in both the case of lengths and the case of angles (see, *e.g.*, **Table B.2**). This means that if the whole process repeated for a given pattern, it will repeat the results with these levels of uncertainty. Thus, the results are highly reproducible for the same micrograph and the same pattern.

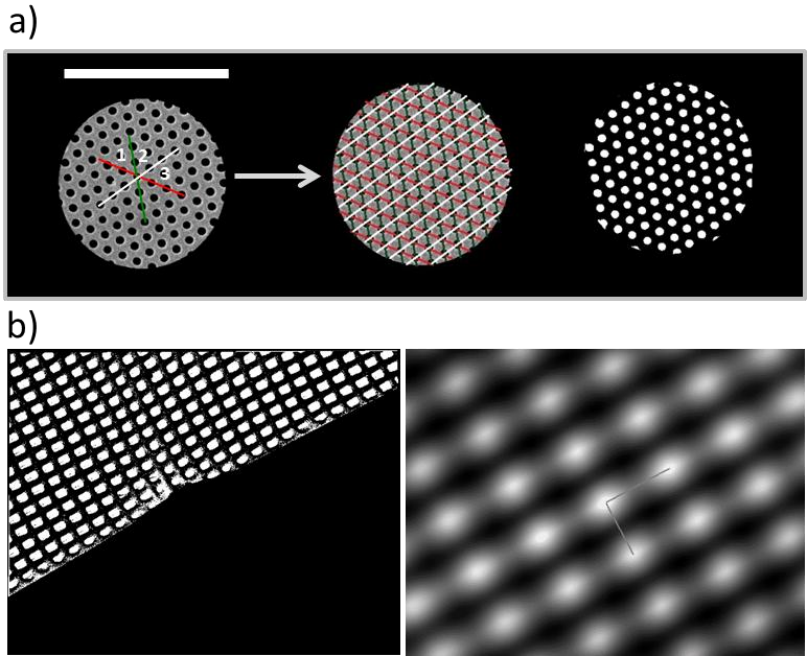

Figure B.6. (**a**) A selected circle at an SEM of the inner face of a *Roperia tesselata* valve showing the 2D pore arrays at the center, and the corresponding segmented micrograph. The red, green, and white lines represents the directions of different lattice vectors $\mathbf{a_1}$, $\mathbf{a_2}$, and $\mathbf{a_3}$, respectively (Scale bar = 20 µm). The angles between the different lines were marked as 1, 2, and 3 respectively. (**b**) A cut from a segmented SEM micrograph of the inner face of a *Haslea* sp. valve (micrograph size = 1024 x 800 pixels) and its corresponding 2D ACF pattern (4x magnified). This figure consists of merged figures modified from Ghobara *et al.* [123].

As mentioned in **subsection B.1.3**, in order to explore the accuracy of the 2D ACF analysis for measuring lattice parameters using Gwyddion software, compared

to the bare-hand measurements of the 2D lattice parameters using ImageJ, the probability of a match between the accurate 2D ACF value and the normal distribution of the bare-hand measurements was calculated for three distinct examples; (i) the linear spacing between the successive striae that appeared in the inner face of a *Haslea feriarum* valve (**Fig B.5b**), (ii) 2D pore arrays at a selected circle from the inner face of a *Roperia tesselata* valve (**Fig B.6a**), and (iii) the 2D pore arrays that appeared in the inner face of a *Haslea* sp. valve (**Fig B.6b**). The results were summarized in **Table B.1**, **Table B.2**, and **Table B.3**, respectively.

Table B.1. The comparison of bare-hand measurements of the linear spacing between successive striae in the SEM of the inner face of a *Haslea feriarum* valve (illustrated in **Fig. B.5b**), and the 2D ACF analysis of the corresponding segmented micrograph. This table is reproduced from Ghobara *et al.* [123].

Method of measurement	**linear spacing (µm)**
Measurements via bare-hand for the original micrograph (ImageJ software) (center to center)	0.46 ± 0.04
Measurements via 2D ACF analysis for the thresholded micrograph with black background (Gwyddion software)	0.454 ± 0.004
Prob(inside t_σ)	88.08 %

Table B.2. The comparison of the bare-hand measurements of 2D lattice parameters and the 2D ACF analysis of the segmented micrograph of a selected circle in the SEM of the inner face of a *Roperia tesselata* valve (illustrated in **Fig. B.6a**). This table is reproduced from Ghobara *et al.* [123].

Method of measurement	**Lattice spacing a_1 (Red line) (µm)**	**Lattice spacing a_2 (Green line) (µm)**	**Lattice spacing a_3 (White line) (µm)**	**Angle 1 (degree)**	**Angle 2 (degree)**	**Angle 3 (degree)**
Measurements via bare-hand for the original micrograph (ImageJ software) (center to center)	1.95 ± 0.05	1.83 ± 0.07	1.85 ± 0.06	60 ± 3	63 ± 3	58 ± 2
Measurements via 2D ACF analysis for the thresholded micrograph	1.914 ± 0.002	1.816 ± 0.001	1.845 ± 0.001	59.17	63.09 ± 0.04	57.77 ± 0.03

(Gwyddion software)						
Prob(inside t_σ)	51.85 %	84.15 %	93.62 %	77.95%	97.61%	90.45 %

Table B.3. The comparison of the bare-hand measurements of 2D lattice parameters and the 2D ACF analysis of segmented micrographs of the SEM of the inner face of a *Haslea* sp. valve (illustrated in **Fig. B.6b**). This table is reproduced from Ghobara *et al.* [123].

Method of measurement	**Lattice spacing a (px)**	**Lattice spacing b (px)**	**Angle 1 (degree)**	**Angle 2 (degree)**
Measurements via bare-hand for the original micrograph (ImageJ software) (center to center)	38 ± 1	46 ± 2	92 ± 3	90 ± 3
Measurements via 2D ACF analysis for the thresholded micrograph (Gwyddion software)	37.305 ± 0.006	46.076 ± 0.008	90.37 ± 0.01	89.63 ± 0.01
Prob(inside t_σ)	48.39 %	96.81 %	58.92 %	90.45 %

Although the probability was variable, it was deemed acceptable for all studied parameters. This implies that the match between the bare-hand measurements and the 2D ACF extracted values is perfectly reasonable, and the agreement between the two methods is satisfactory. Thus, we can depend on the 2D ACF method in lattice recognition and measurements with high accuracy. However, it should be noted that the information obtained easily with the bare-hand measurements of the lattice variation within the valve is less accessible in the 2D ACF measurements, as the coherence is also influenced by the sampling size.

B.2.3. Exploring the periodicities and the possible presence of different 2D Bravais lattices in the studied micrographs employing the proposed method

Non-periodic pores

When cultivated in optimal conditions, most diatoms synthesize well-engineered valve and girdle bands with periodic to quasi-periodic porosity, usually arranged in the striae. However, as became apparent throughout this study, a few species exhibit irregular pore arrangements, such as the pores appearing at the outer face of *Thalassiosira pseudonana* valve (**Fig. B.7**). As can be seen, no periodic relations are observed between its pores in the 2D ACF pattern.

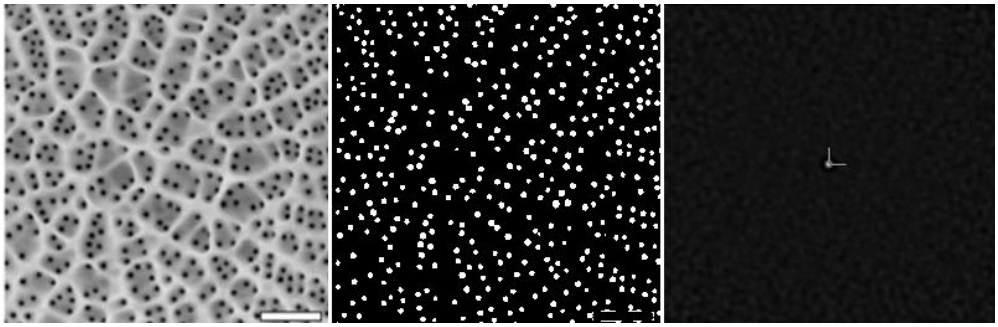

Fig. B.7. A close-up SEM of the outer face of a *Thalassiosira pseudonana* valve (at left, scale bar = 0.2 µm) with its corresponding segmented micrograph (in the middle) and 2D ACF pattern showing no periodicity (at right). This SEM is reproduced from Kröger *et al.* [70]. The whole figure is modified from Ghobara *et al.* [123].

Linear periodicity of pores in striae (1D periodicity)

As already explained, most diatom species, centrics and pennates, show regular to quasi-regular linear striae, extending from the annulus (in case of centrics) or from the sternum (in case of pennates) reaching the outline of the valve. These striae can be considered the first level of pore periodicity (1D periodicity) present in diatom silica layers. **Fig. B.8** shows linear periodicity within a single stria in a pennate valve.

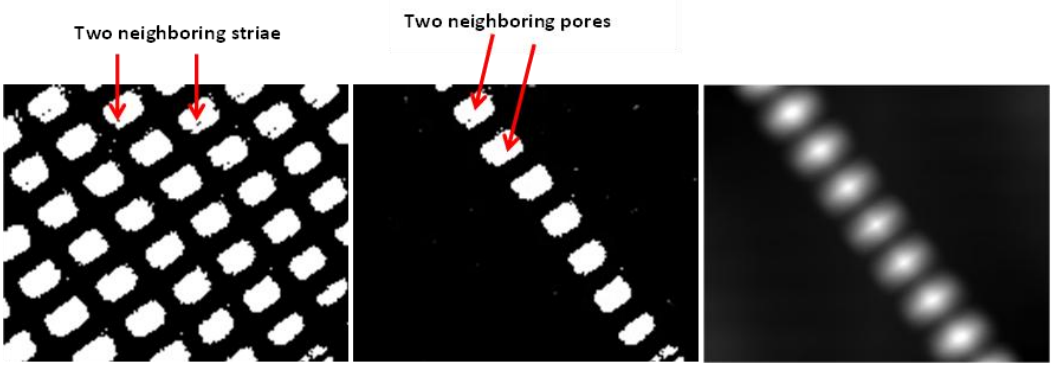

Fig. B.8. A segmented SEM of a zoom-in the inner face of a *Haslea* sp. valve (at left). An isolated single stria shows a linear periodicity between its neighboring pores (in the middle), which appears clearly in the corresponding 2D ACF pattern (at right). This figure is modified from Ghobara *et al.* [123].

According to the distance and angle relations between the pores of neighboring striae, the presence or absence of extra periodicities can be determined. Throughout the study, an additional circular periodicity (branching striae), additional linear periodicity (*e.g.*, **Figs. B.5b-c**), or further 2D lattice structures with periodicities and symmetries in 2D (see below) were observed.

Different 2D Bravais lattices in diatom pore arrays

Using the proposed method, the possible presence of a 2D lattice in a given 2D periodic pore array can be detected, and the lattice parameters can be measured

and compared to the five 2D Bravais lattices through the lattice recognition logic flow. Examples of all 2D Bravais lattices, with different levels of imperfection, were observed while studying the pore arrays of distinct diatom valves (**Table B.4**). This can be considered an addition to the literature, where—to the best of my knowledge—only 2D hexagonal and 2D square lattices were reported [123].

Table B.4. The lattice parameters and lattice types found in some of the studied examples using the proposed method. Length is in pixels, while angle is in degrees. This table is adapted from Ghobara *et al.* [123].

Species	Fig.	vector length a (px)	vector length b (px)	Angle between the two vectors (degree)	Deviation of vector length b compared to vector length a (%)	Deviation of angle θ compared to closest perfect angle (%)	Lattice type with deviation up to 5%	Lattice type with deviation up to 10%
Roperia tesselata (outer face)	**B.9a**	23.18	23.65	57.9°	2	3.5	Hexagonal	Hexagonal
Roperia tesselata (inner face)	**B.9b**	23.18	24.01	57.6°	3.6	4	Hexagonal	Hexagonal
Triceratium favus	**B.9c**	25.06	25.74	61.1°	2.7	1.8	Hexagonal	Hexagonal
Asterolampra marylandica (outer face)	**B.10a**	52.72	55.72	57.7°	5.7	3.8	Oblique	Hexagonal
Asteromphalus hookeri (inner face)	**B.10b**	12.09	13.26	56.1°	9.7	6.5	Oblique	Hexagonal
Cocconeis sp.	**B.12b**	32.78	38.03	54.5°	16	9.2	Oblique	Oblique
Haslea sp.	**B.6b**	37.30	46.08	90.4°	23.5	0.4	Rectangular	Rectangular
Pleurosigma sp.	**B.12a**	39.55	41.99	69.3°	6.2	15.5	Oblique	Centered rectangular
Gyrosigma balticum	**B.11b**	34.88	29.58	96.5°	15.2	7.2	Oblique	Rectangular
Gyrosigma fasciola	**B.11a**	39.52	42.45	87.3°	7.4	3	Rectangular	Square

Pleurosigma angulatum	**B.11c**	25.67	24.89	63.6°	3	6	Centered rectangular	Hexagonal

All the numerical values of lattice parameters were to some degree imperfect compared to the mentioned 2D Bravais lattices, which means that all mentioned examples would be assigned to the 2D oblique lattice if no imperfection levels were tolerated. However, in most cases, allowing a small degree of imperfection, the lattice parameters were very close to other types of 2D lattices.

Interestingly, among the examples studied here, two centric diatoms showed 2D pore arrays featuring a 2D hexagonal lattice with a deviation of only up to 5% from the perfect lattice. This includes the pore arrays that appear at the outer and inner valve faces of *Roperia tesselata* (**Fig. B.9a** and **b**, respectively) and the inner face of a *Triceratium favus* valve (**Fig. B.9c**). These results—combined with previous reports in the literature—suggest that the 2D hexagonal lattice could be a common feature in the valves of centric diatoms, with different degrees of imperfection.

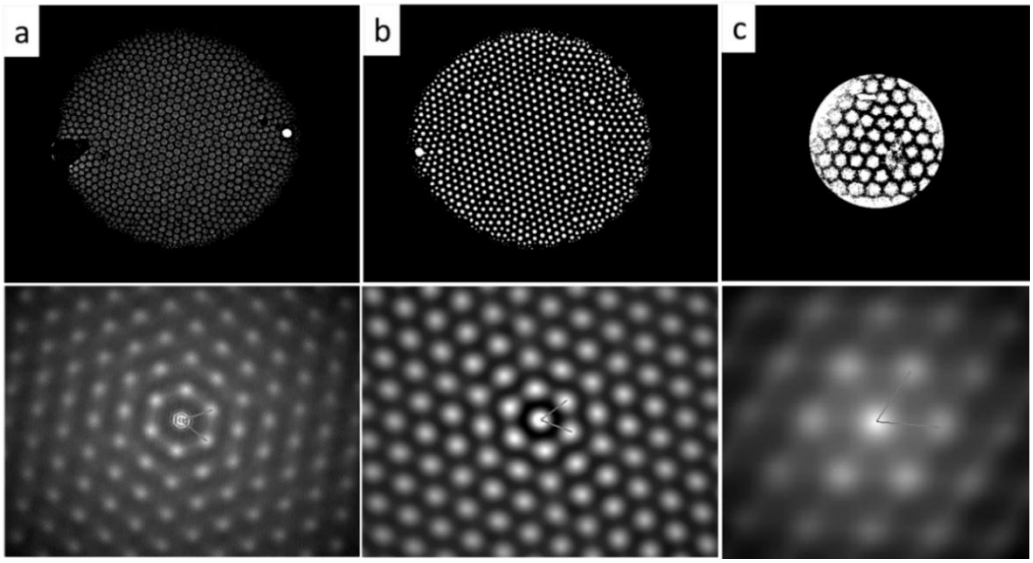

Fig. B.9. Examples of pore arrays with almost perfect 2D hexagonal lattice, deviations up to 5%. (**a** and **b**) A segmented SEM micrograph of the outer and inner faces of *Roperia tesselata* valve (micrograph size = 1024 x 800 pixels), respectively, and their corresponding 2D ACF patterns at the bottom (4x magnified). It should also be noted that the two valves belonged to two different frustules, however, showed very similar pattern with an almost perfect 2D hexagonal lattice. (**c**) a segmented SEM micrograph of the inner face of a *Triceratium favus* valve (micrograph size = 512 x 459 pixels), with its sharp edges removed, and its corresponding 2D ACF pattern at the bottom (4x magnified). This figure consists of merged figures modified from Ghobara *et al.* [123].

Moreover, a clear example of the 2D rectangular lattice was observed during the study of the 2D pore arrays appearing at the inner face of a *Haslea* sp. valve (**Fig. B.6b**). This lattice may be very common in pennates, where the neighboring striae tend to be parallel to each other and perpendicular to the sternum, thus, leaving an

angle of almost 90° between the lattice vectors, while the spacing between the two neighboring striae is often larger than the spacing between the neighboring pores in the same stria. This means, in this type, the lattice vector length between the two parallel striae is larger than that between two neighboring pores in the same stria, which is a characteristic of a 2D rectangular lattice.

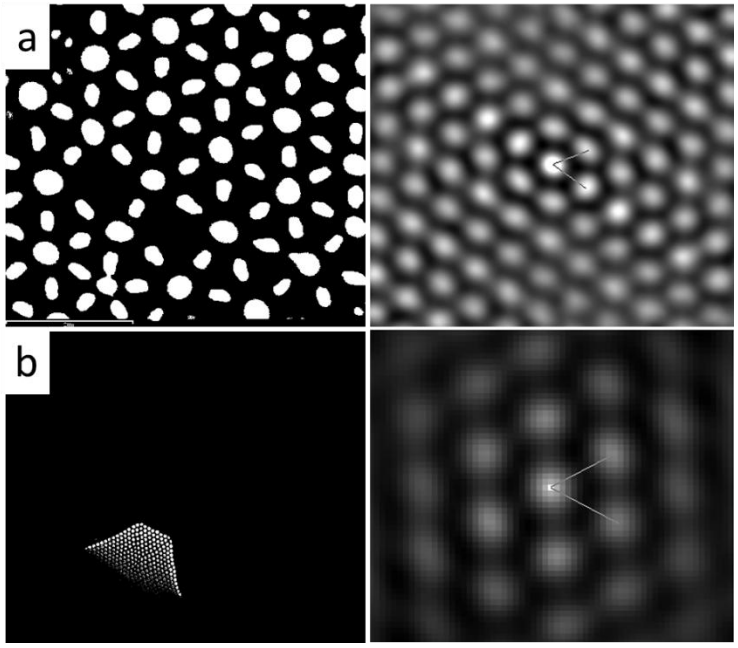

Fig. B.10. (**a**) A segmented SEM micrograph of a zoom-in the outer face of a *Asterolampra marylandica* valve (micrograph size = 512 x 459 pixels) and its corresponding 2D ACF pattern at right. (**b**) A segmented separated part of an SEM of the inner face of a *Asteromphalus hookeri* valve (micrograph size = 1021 x 785 pixels) and its corresponding 2D ACF pattern at right (16x magnified). This figure is reproduced from Ghobara *et al.* [123].

Furthermore, the pennate diatom *Gyrosigma fasciola* reported here as an example of the presence of pore arrays with 2D square lattice in pennates if we accept the deviation in lattice parameters up to 10% compared to the perfect 2D square lattice (**Table B.4**, **Fig. B.11a**). In the literature, the 2D square lattice was reported for a few centrics and pennates. In centrics, this lattice seems to only occur within the pore arrays of girdle bands. For instance, Fuhrmann *et al.* [42] reported the 2D square lattice for the pore arrays of girdle bands of the centric diatom *Coscinodiscus granii*, while the valves showed a 2D hexagonal lattice. This was further confirmed by Goessling *et al.* [125], as they reported the presence of 2D square lattices in the girdle bands of *Thalassiosira pseudonana, Coscinodiscus granii, Coscinodiscus radiates*, and *Coscinodiscus wailesii*. Thus, 2D square lattice might be frequent in the girdle bands of centrics.

Interestingly, one of the studied examples, *Pleurosigma angulatum*, has a 2D centered rectangular lattice if we accept a deviation of up to 5% (**Table B.4**, **Fig.**

B.11c). Additionally, *Pleurosigma* sp. (**Fig. B.12a**) showed also a 2D centered rectangular lattice if we accept a deviation up to 10%.

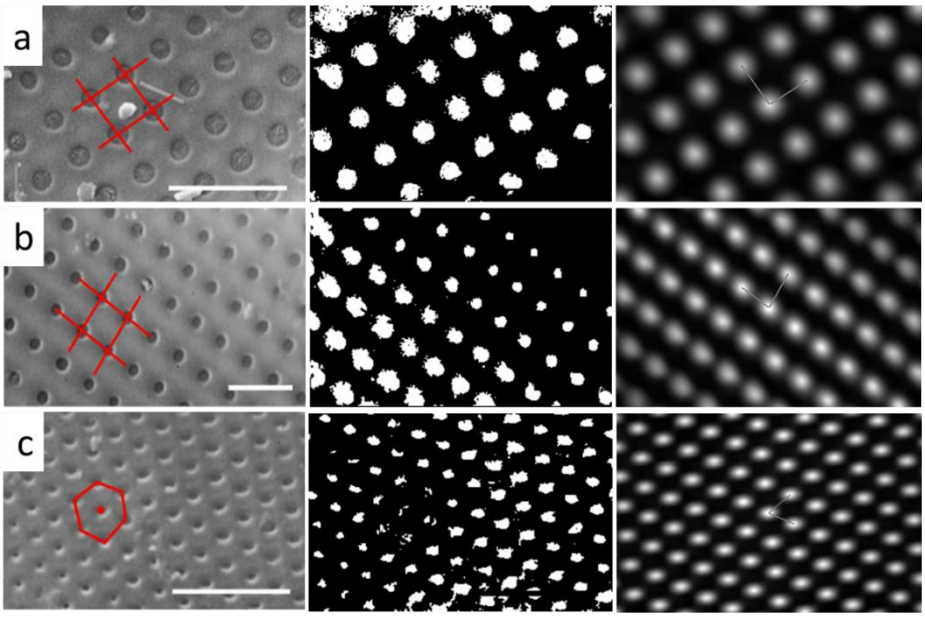

Fig. B.11. SEMs showing a zoom-in the 2D pore arrays of the valves of *Gyrosigma fasciola* (**a**), *Gyrosigma balticum* (**b**), and *Pleurosigma angulatum* (**c**) at left, the corresponding segmented images in the middle, and 2D ACF patterns at right. The micrograph size of (**a**) = 276 x 179 pixels, (**b**) = 276 x 182 pixels, and (**c**) = 276 x 180 pixels. The SEMs (with the red drawings) are reproduced from Goessling *et al.* [338]. The whole figure consists of merged figures modified from Ghobara *et al.* [123].

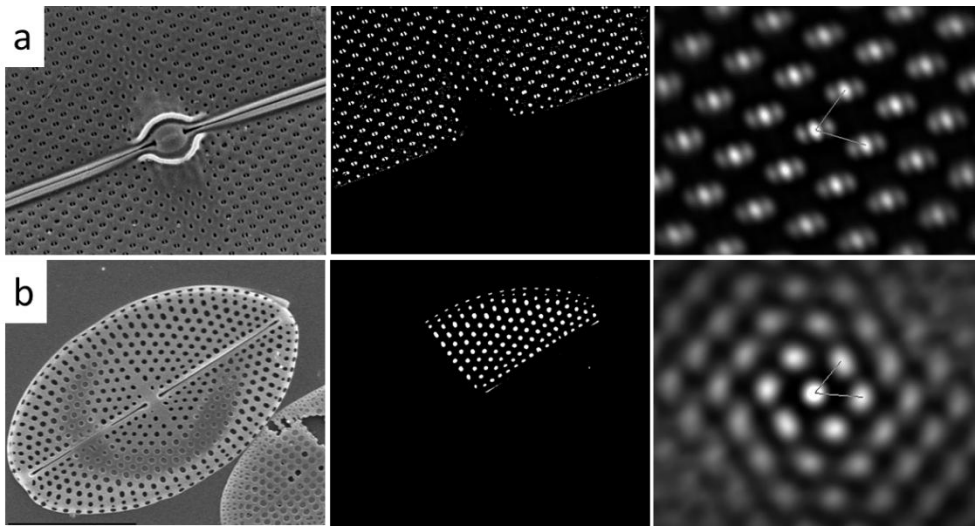

Fig. B.12. (**a**) SEM of the inner face of a *Pleurosigma* sp. valve (micrograph size = 1,024 × 800 pixels) at left, a selected segmented part of the valve in the middle, and its corresponding 2D ACF pattern at right (4x magnified). (**b**) SEM of the outer face of a *Cocconeis* sp. valve (micrograph size = 1,021 × 847 pixels) at left, a selected segmented part of the valve in the middle, and its corresponding 2D ACF pattern at right (4x magnified). This figure consists of merged figures modified from Ghobara *et al.* [123].

B.2.4. The perfection in diatom pore arrays: limitations and conclusions

Although the suggested method could provide a valuable tool for studying diatom pore arrays' periodicities and symmetries that anyone can use, a modification of this method should be considered in future—as discussed in Ghobara *et al.* [123]—to include the **standard deviation of the lattice** (*i.e.*, the change of the lattice perfection over a given diatom surface, for example, from a valve center to its edges), and thus, enabling the judgement on the perfection of a given lattice in a more precise way. This should be achieved, in future work, by extracting the standard deviation directly from the 2D ACF analysis, which was not possible using the current approach.

As shown in **Table B.4**, if we only considered the obtained averaged lattice parameters (which were in a good match with the lattice parameters extracted via bare-hand measurements, see **subsection B.2.2**), some examples approach perfection in lattice parameters (others than oblique) with a deviation level below 5% compared to the perfect 2D Bravais lattices, such as *Roperia tesselata* and *Haslea* sp. It should be noted that the standard deviation in the lattice parameters extracted by bare-hand measurements for *Roperia tesselata* was also only up to 5% (see **Table B.2**). That likely means *Roperia tesselata* could build 2D pore arrays of an almost perfect 2D hexagonal lattice. This is also the case for *Haslea* sp. (see **Table B.3**), which could build an almost perfect 2D rectangular lattice.

Furthermore, the valves of some diatom species show a connected pore array, such as the case of *Roperia tesselata* valves (**Figs. B.9a** and **b**), while other diatom species show distinct groups of pore arrays in their valves with additional rotational and/or reflectional symmetries, as the examples shown in **Figs. B.12** and **B.13**. Some examples show a high reproducibility of the lattice perfection level among their distinct groups of pore arrays, while others do not (see further Ghobara *et al.* [123]).

All in all, studying the perfection level of 2D pore arrays is crucial for the numerical analysis of the light modulation capabilities of a given valve, *e.g.*, to investigate their ability to exhibit optical resonances or a photonic bandgap. When we have a connected pore array over a valve surface with a 2D lattice approach perfection (of deviations below 5%), the numerical analysis using a 3D single unit cell with periodic boundary conditions could be representative. While by increasing the imperfections or variations between distinct valve parts, the unit cell model will not be valid, and the analysis of larger structures with many unit cells—or, if possible, the complete valve structure—is required. The same conclusion is obtained for the case of a single valve with distinct groups of pore arrays of additional reflectional and/or rotational symmetries, such as the examples shown in **Figs. B.12** and **B.13**.

Such valves cannot be considered as a single finite-size 2D PC, as the lattice vector directions are changing between distinct parts, but rather as a combination of smaller and distinct 2D PCs. That will probably lead to interesting optical and photonic features that are awaiting to be explored.

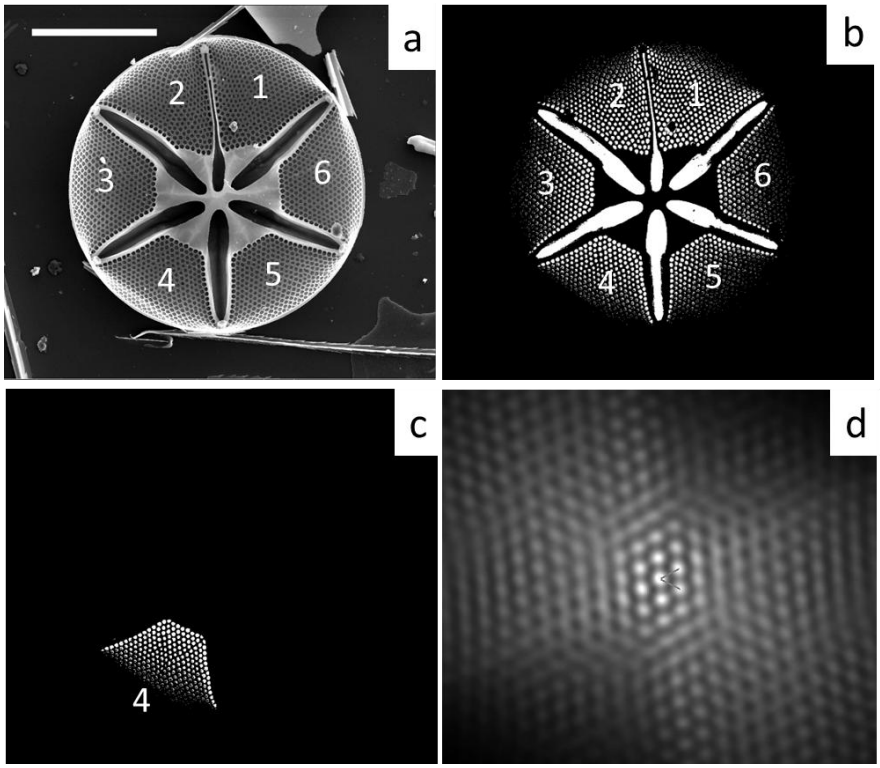

Fig. B.13. (**a**) SEM of the inner face of an *Asteromphalus hookeri* valve (image size = 1,021 × 885 pixels) and (**b**) its segmentation, showing distinct pore groups (numbered from 1 to 6) with rotational symmetry. (**c**) An example illustrating the idea of isolating distinct pore array groups, showing group number 4 and (**d**) its corresponding 2D ACF pattern (4x magnified). Scale bar of the SEM = 30 µm. This figure is modified from Ghobara *et al.* [123].

Appendix C: A Preliminary study on incorporating diatom valves as optical building blocks into MISM organic photodetectors

In the conventional Schottky-barrier optoelectronic devices, named after Walter H. Schottky, a photovoltaic semiconductor (abbr. **S**) is brought in direct contact with a metal electrode (abbr. **M**). In such devices, the **excitons** (*i.e.*, electron-hole pairs) generated within the semiconductor—by absorbing photons of higher energy than the semiconductor bandgap—can be separated and generate a photocurrent (**DC current**) based on the **Schottky barrier** (caused by the difference in the working functions of the two materials and band bending at the interface) [339]. Although the conventional MS devices exhibited low efficiency, they have been improved by different strategies, for instance, by introducing an ultra-thin insulating layer [340,341] or an oxide layer [342] between the metal and semiconductor, which enabled their utilization in various fields, including the fabrication of photodetectors and solar cells.

In recent years, **organic semiconductors** have been increasingly employed in optoelectronic devices (including photodetectors) as an alternative to inorganic semiconductors due to their flexibility, relatively low cost, the ability to tune their bandgap, and being more friendly to the environment [343–345]. In organic semiconductors, the band gap is determined based on the difference between the so-called **HOMO** (*i.e.*, highest occupied molecular orbital) and **LUMO** (*i.e.*, lowest unoccupied molecular orbital) levels, analogous to the valence and conduction bands in the inorganic semiconductors, respectively. Despite the merits, organic semiconductors also have some drawbacks, if compared to inorganic semiconductors, such as their poor stability, poor charge mobility, and intrinsic short diffusion length (*i.e.*, the average distance that the charge carriers can travel within the material without recombining). In recent years, different approaches have been developed to overcome such drawbacks and, thus, enable commercial applications [346,347].

In 2010, Hu *et al.* [348] observed that employing a thick organic semiconductor layer in an **MSM** device dramatically changes the device behavior. When illuminating that device, a transient signal was obtained instead of the steady-state current obtained in the conventional MSM (**Fig. C.1a**). By switching the light off, another transient signal of an opposite polarity was obtained (**Fig. C.1a**). Such anomalous behavior was attributed to the poor conductivity of the thick organic semiconductor (due to the short diffusion length of charge carriers), where a large

part of the film acts as an insulating layer (see Figure 3 in [349]). To validate this assumption, an **MISM** device was fabricated (by inserting a thick insulating layer between a thin S layer and one of the metal electrodes) and tested, where the anomalous transient signal was also obtained [350].

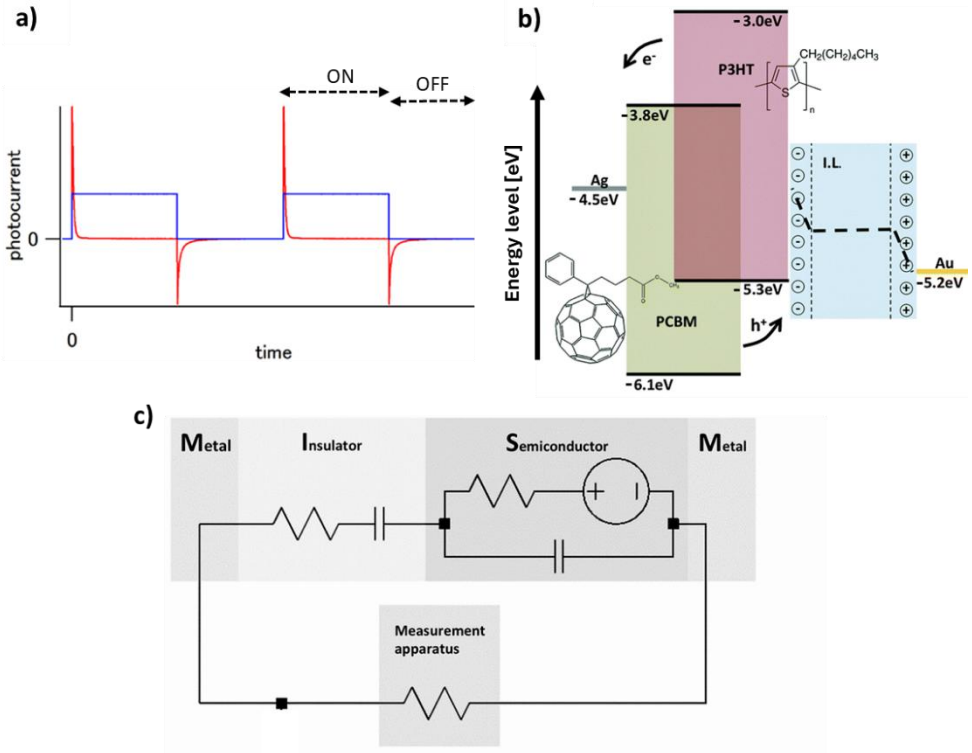

Fig. C.1. (**a**) a simple plot showing an example of the response of MSM device (the DC current in blue) compared to MISM device (transient signal in red) when illuminated with a flickering signal (light ON/OFF). (**b**) Energy-level diagram of an example of organic MISM device, showing the EDL formed in the IL layer. (**c**) Simplified sketch of the proposed equivalent circuit to the device. **Fig.** (**a**) is reproduced from Mori [351], while **Figs.** (**b**) and (**c**) are adapted and modified from Reissig *et al.* [345].

To simplify the MISM device, it can be seen as a **photodiode in a series with a capacitor** [352]. In that context, when the light is on, the rise and decay of the transient signal peak could be attributed to the photogenerated charges within the S layer and the charging of the capacitor element, respectively. By switching the light off, the rise and decay of the generated peak can be attributed to discharging that capacitor [352]. It has been proposed that the **potential difference** across the I layer becomes crucial in determining the charge selectivity at the electrodes and, thus, the signal polarity (see section 4.2 in [351]). Moreover, an equivalent circuit simulating and explaining the behavior of MISM devices has also been proposed (**Fig. C.1c**), showing that the electronic properties (*i.e.*, capacitance and resistance) of S and I layers play crucial roles in shaping the transient signal (*e.g.*, determining the associated rise and decay times) [344].

Interestingly, utilizing organic ionic liquids (**IL**) as an insulating layer led to a pronounced improvement in the obtained transient signal of MISM devices attributed to their large dielectric constants [353]. When operating IL-based MISM device, **electric double layers** (**EDLs**) are formed at the interfaces of IL with the adjacent M and S layers (see, *e.g.*, **Fig. C.1b**). Many studies have been conducted on organic photodetectors with IL-based MISM or MISIM (by adding an additional insulating layer) architectures [344,345,351,354–356].

This Appendix aims to demonstrate the preliminary attempt to incorporate diatom valves as optical elements into IL-based MISM organic photodetectors, seeking to enhance their performance (*e.g.*, signal magnitude).

C.1. Methods

C.1.1. Photoactive electrodes fabrication

In general, $\mathbf{M_1ISM_2}$ photodetector devices consist of two metal electrodes ($\mathbf{M_1}$, $\mathbf{M_2}$) with a photoactive semiconductor layer (**S**) and an insulating (**I**) layer in between. As the On-Tip On-Dip method [355] will be employed here for evaluating the devices' performance (as described in **subsection C.1.2**), the fabrication of only the photoactive electrodes (consisting of **S** layer on top of a metal electrode $\mathbf{M_2}$) was required. Here, a gold film was utilized as $\mathbf{M_2}$ (abbr. $\mathbf{M_{Au}}$). While the heterojunction blend of the semiconductor polymer poly(3-hexylthiophene-2,5-diyl) (**P3HT**, Rieke metals, USA) and the fullerene derivative [6,6]-Phenyl C_{61} butyric acid methyl ester (**PCBM**, Solenne BV, Netherlands) was utilized as the active **S** layer (abbr. $\mathbf{S_{PP}}$). In this system, the P3HT and PCBM are considered p-type and n-type semiconductors, respectively. All fabricated electrodes were stored in dark under vacuum till analyzed.

Reference photoactive electrode (abbr. $\mathbf{S_{PP}M_{Au}}$)**:**

First, metal electrode $\mathbf{M_{Au}}$ was fabricated by thermally evaporating a gold film onto a glass substrate (of dimensions 13 x 26 mm) using the same **PVD** chamber used in **subsection 3.5.1** (**Chapter 3**) and at the same vacuum conditions (10^{-6} Torr). Before depositing the gold film, a thin film of chromium (**Cr**) was evaporated on the glass substrate with an evaporation rate of 0.1 Å/s, reaching a final thickness of 100 Å (=10 nm) to enhance the adhesion of the gold film to the glass substrate. Following that, the gold film was deposited with an evaporation rate of 1 Å/s, reaching a final thickness of 1000 Å (=100 nm).

Thereafter, **Dr. Martina Gilic** deposited a thin layer of $\mathbf{S_{PP}}$ (P3HT:PCBM of a ratio 1:1, dissolved in chlorobenzene with a total concentration of 20 mg.ml^{-1}) on top of the gold electrode via spin coating (3000 rpm for 1 min). Following that, she

annealed the $\mathbf{S_{PP}}$ layer for 10 min in an inert gas atmosphere (to avoid contamination with oxygen and water vapor that can influence its performance) and in dark (to avoid its photodegradation). It should be noted that the spin coating and annealing parameters were optimized by **Dr. Martina Gilic** in the light of previous work [351], and by monitoring the characteristic UV-Vis spectrum of the obtained active layer (measured for $\mathbf{S_{PP}}$ films deposited over quartz glass and annealed under the same conditions).

Diatom-based photoactive electrode:

Two different approaches were followed to investigate the influence of adding *Ethmo* valves—as optical building blocks—to the photoactive electrode, as demonstrated below.

Approach I:

In this approach, the fabricated electrode (abbr. $\mathbf{S_{PP+Ethmo}M_{Au}}$) was the same as the reference electrode but with the presence of *Ethmo* valves mixed with the $\mathbf{S_{PP}}$ layer. About 15 mg of the dry powder of *Ethmo* valves was mixed with the P3HT:PCBM solution while preparing it, before spin coating.

Approach II:

In this approach, the fabricated electrode (abbr. $\mathbf{S_{PP}M_{Au+Ethmo}}$) was different from the reference electrode, as it was prepared by employing the method used to fabricate the SERS hybrid substrates to obtain a 10 nm gold film over a homogenous layer of *Ethmo* valves, which was prepared as described in **subsection 3.1.2** (**Chapter 3**). Afterwards, **Dr. Martina Gilic** spin-coated and annealed the $\mathbf{S_{PP}}$ layer, employing the same method used for the reference electrode.

C.1.2. Photocurrent measurements using On-Tip On-Dip method

The photocurrent measurements shown here were carried out **together with Professor Louisa Reissig**. The methods for testing and analyzing the performance of MISM photodetectors—which are based on P3HT:PCBM as an active layer and ionic liquid (**IL**) as an insulating layer—have already been established in previous studies (*e.g.*, [345,351]). Among the developed methods, the On-Tip On-Dip method has been utilized as a facile method to test the performance of these devices [355]. Here, this method will be employed to obtain preliminary information on the influence of *Ethmo* valves on the performance of the fabricated photoactive electrodes when integrated into the MISM device architecture.

Fig. C.2 illustrates the home-built experimental setup used for the photocurrent measurements utilizing the On-Tip On-Dip method, which is located at AG Reissig, Physics department, FU Berlin. A green LED (λ_{max} ≈ 530 nm), fixed in a

home-built LED light box, was utilized as a source of light signal. The LED light was coupled to an optical fiber (1 mm core, M71L01, Thorlabs, USA) through a condenser lens to guide the light signal to the device. The emitting end of the optical fiber was fixed on an aluminum holder (**Al**). The LED light box was connected to a function generator (TEXIO FG-274) to trigger a square-wave modulated light signal (the light is flickering between ON and OFF). The flickering frequency was controlled via the function generator, while the signal intensity was controlled via the LED light box.

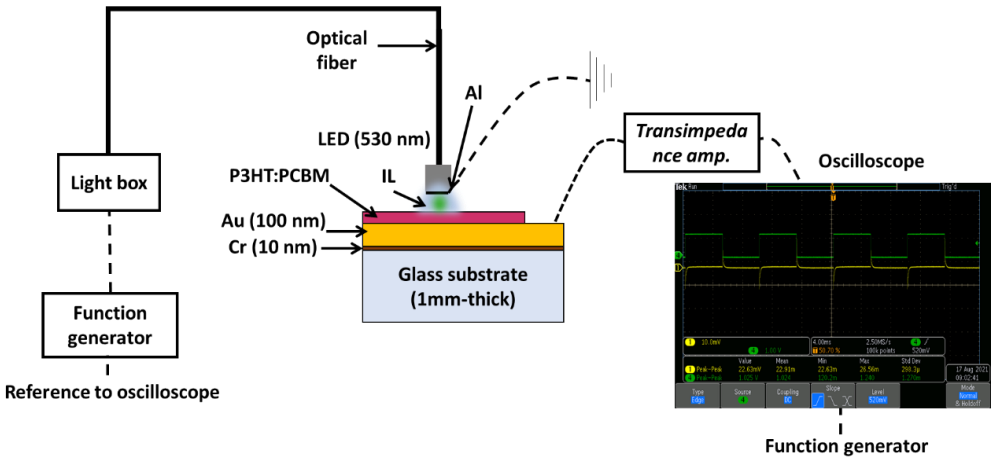

Fig. C.2. A schematic diagram illustrates the experimental setup used in the photocurrent measurements, employing the On-Tip On-Dip method.

In this setup, the photoactive electrode was fixed in a home-built device holder. The $\mathbf{M_{Au}}$ (as being the **working electrode**) was connected to a low-noise transimpedance amplifier (Femto DLPCA-200, FEMTO Messtechnik GmbH, Germany), which was connected to a digital oscilloscope (Tektronix MDO3024, up to 200 MHz, Tektronix UK Ltd., UK). By this, the obtained photocurrent during measurements can be amplified, monitored, and recorded. The function generator was connected to the oscilloscope (as a reference signal).

Directly before the measurements, the fabricated photoactive electrodes were exposed to air. Due to the expected influence of air on the performance of the active layer, a fixed time (≈ 8 min) was spent to prepare the electrode for measurements, which enables comparing the performance of distinct electrodes. The measurements were started by **completing the architecture of the MISM device.** For this, a drop of IL (1-Ethyl-3-methylimidazolium tetrafluoroborate, TCI, >97.0%, abbr. **EMIM BF_4**) was dropped on top of the $\mathbf{S_{PP}}$ layer. Following that, the optical fiber tip was dipped into the **IL** drop, as illustrated in **Fig. C.2**. Then, the aluminum holder (as being the **counter electrode** $\mathbf{M_{Al}}$) was grounded. When illuminating the device with the flickering light (ON/OFF) signal—of a given frequency—the characteristic **transient signal** was obtained, amplified by factor of 10^4, monitored on the oscilloscope, averaged (64 times), and recorded. It should be noted that the photocurrent direction can be determined during the measurements.

Each device was analyzed separately under the same conditions, which includes the light intensity (monitored by a silicon photodiode built-in the device holder), the size and position of IL drop, and the distance between $\mathbf{S_{PP}}$ and $\mathbf{M_{Al}}$.

Each device was studied for at least 80 min to investigate the **short-time stability** of the obtained transient signal at a frequency where a full decay (unless otherwise stated) for the light ON and light OFF peaks occurs, as the example shown in **Fig. C.3**. When the obtained signal became relatively stable over time, a **frequency-dependency study** was carried out by changing the flickering frequency from the function generator (between **10 Hz** and **100 KHz**) and recording the transient signal.

C.1.3. Data analysis

The recorded data was imported to **Igor pro** software for further analysis. The recorded signals were in volt (**V**), as the transimpedance amplifier converted the photocurrent into voltage. Therefore, each signal was converted back to current (in ampere **A**) through dividing it by the amplification factor 10^4. The intensity of the signal was estimated by measuring peak-to-peak value (abbr. $\boldsymbol{I_{pkpk}}$, which equals $\boldsymbol{I_{pk,ON}} + \boldsymbol{I_{pk,OFF}}$), as demonstrated in **Fig. C.3**. Rise and decay times for the light ON and OFF peaks could also be extracted from the signal (see further [351]).

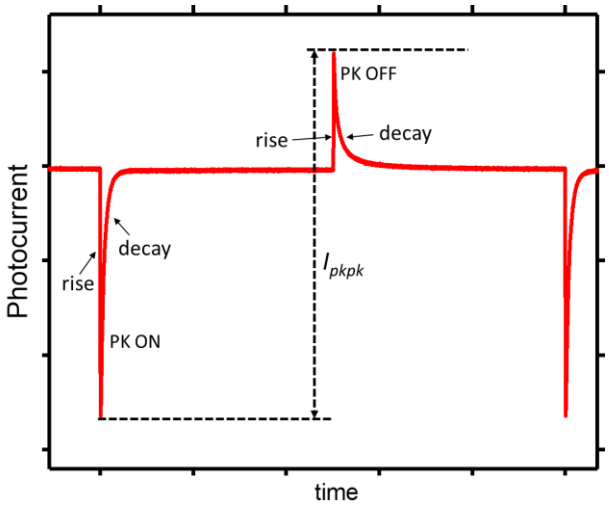

Fig. C.3. An example of the obtained transient signal, showing a full decay for the light on and off peaks.

C.2. Results and discussion

C.2.1. The description and ultrastructure of the utilized diatom sample

The diatom sample used in this study (which was available in sufficient amounts for the study in the lab at that time) was mainly composed of microscopic fragments belonging to the giant diatom *Ethmodiscus rex* (***Ethmo***), as can be seen in **Fig. C.4**.

Such fragments are observed in a typical *Ethmodiscus* ooze (see plate 2, 3 in [357]). The irregular diatom fragments have a flake-shaped morphology and a simple, porous structure (**Fig. C.4**). The average pore diameter is about 1 µm, while the average lattice spacing (center-to-center) is about 1.5 µm. The approximate thickness of the valve fragments is about 1 µm.

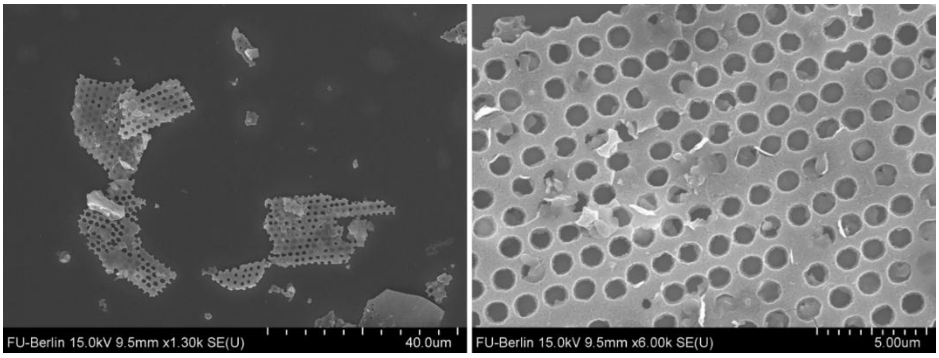

Fig. C.4. SEMs show the overall morphology (at the left) and the ultrastructure (at the right) of *Ethmo* valve fragments utilized in fabricating diatom-based photoactive electrodes. The raw SEMs were acquired by Dr. Martina Gilic.

C.2.2. The obtained active layer

The used spin coating conditions should produce a thin **S_{PP}** layer of a thickness at around **50 nm**, as can be understood from [351]. **Fig. C.5** shows the UV-Vis spectra of the obtained **S_{PP}** layer over quartz at different situations. Peaks at the UV spectral range are correlated to PCBM, while the peaks at the Vis spectral range are correlated to P3HT [351]. After annealing **$S_{PP+Ethmo}$** film, the magnitude of the PCBM peaks was much reduced in the obtained UV-Vis spectra if compared to the annealed **S_{PP}** film. The optical micrographs of the **$S_{PP+Ethmo}$** film also suggest that there were changes introduced to the active layer microstructure by introducing *Ethmo* fragments (**Fig. C.6**).

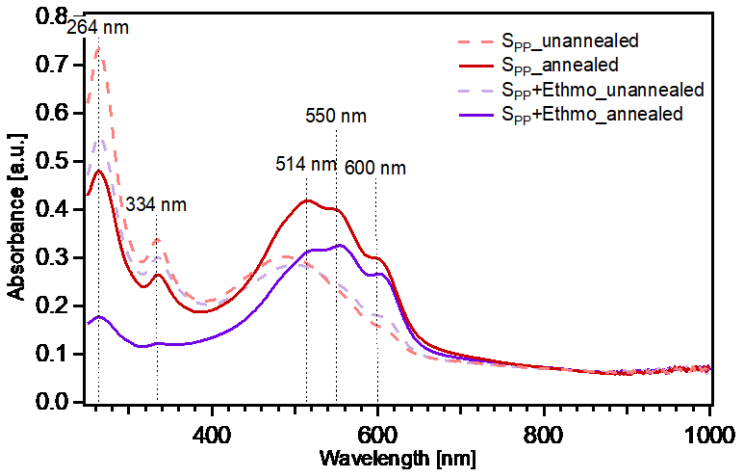

Fig. C.5. The UV-Vis spectra of the **S_{pp}** layer (spin coated on quartz glass) before and after annealing, with and without *Ethmo* fragments. The UV-Vis measurements were carried out by Dr. Martina Gilic.

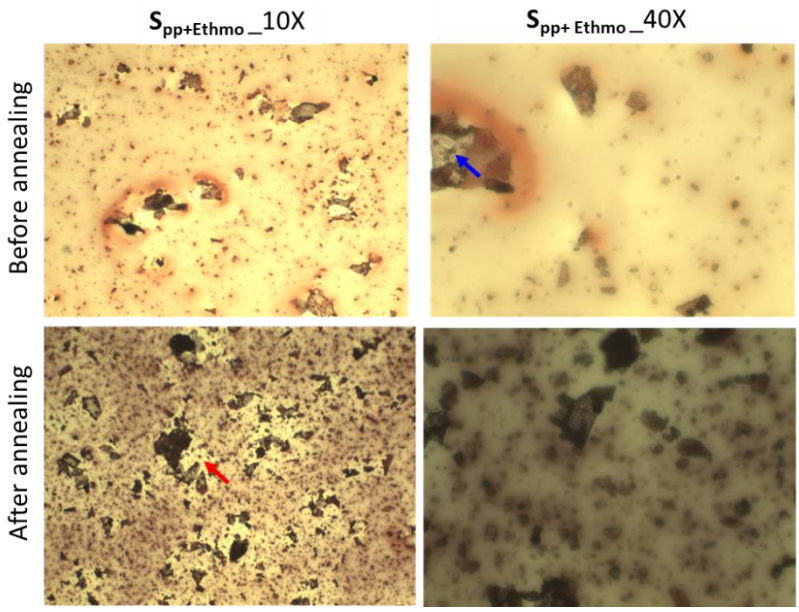

Fig. C.6. Optical micrographs of $S_{pp+Ethmo}$ layer (spin coated on quartz glass) before and after annealing under 10x and 40x objectives. The blue arrow indicates a part of an *Ethmo* fragment exposed to air (can be seen as a defect in the film), while the red arrow indicates a colorless zone within the $S_{pp+Ethmo}$ annealed film (expecting less P3HT).

C.2.3. Comparing the response of distinct MISM photodetectors

Reference photodetector ($M_{Al}I_{IL}S_{PP}M_{Au}$)

The reference photodetector generated the characteristic transient photocurrent signal when exposed to the flickering (ON/OFF) light (**Fig. C.7a**). In the used setup, the negative polarity of the light ON peak (abbr. **Pk ON**) indicates that the working electrode M_{Au} (of higher working function) was extracting electrons at the M_{Au}/S_{PP} interface when the Light is ON (**Fig. C.7a**). This result agrees with previous work on comparable device architectures [345], where the equal ratio of P3HT and PCBM led to electron extraction at the working electrode, influenced by the potential difference between the S layer and counter electrode.

The PK ON showed a faster rise and decay time than the PK OFF, which may be attributed to the lower resistance within the S_{pp} layer and the faster charging of the capacitor under illumination, as suggested by Mori [351]. By operating the device, the signal intensity I_{PKPK} was decreasing over time, simultaneously with increasing the decay times (**Figs. C.7a** and **b**). Such behavior was also observed in [345,351] and has been linked to the reduction in extracted charges from the S_{PP} layer, probably associated with the influence of the ionic liquid by filling the traps or photoinduced ions expulsion/inclusion within the S_{PP} layer over operation time. The reduction in I_{PKPK} became slower by the time (**Fig. C.7b**), probably approaching an equilibrium situation. It should be noted that by storing the photoactive electrode in the dark and retesting it, a partial restoration of the signal intensity was observed, which was dependent on the resting time and storage conditions.

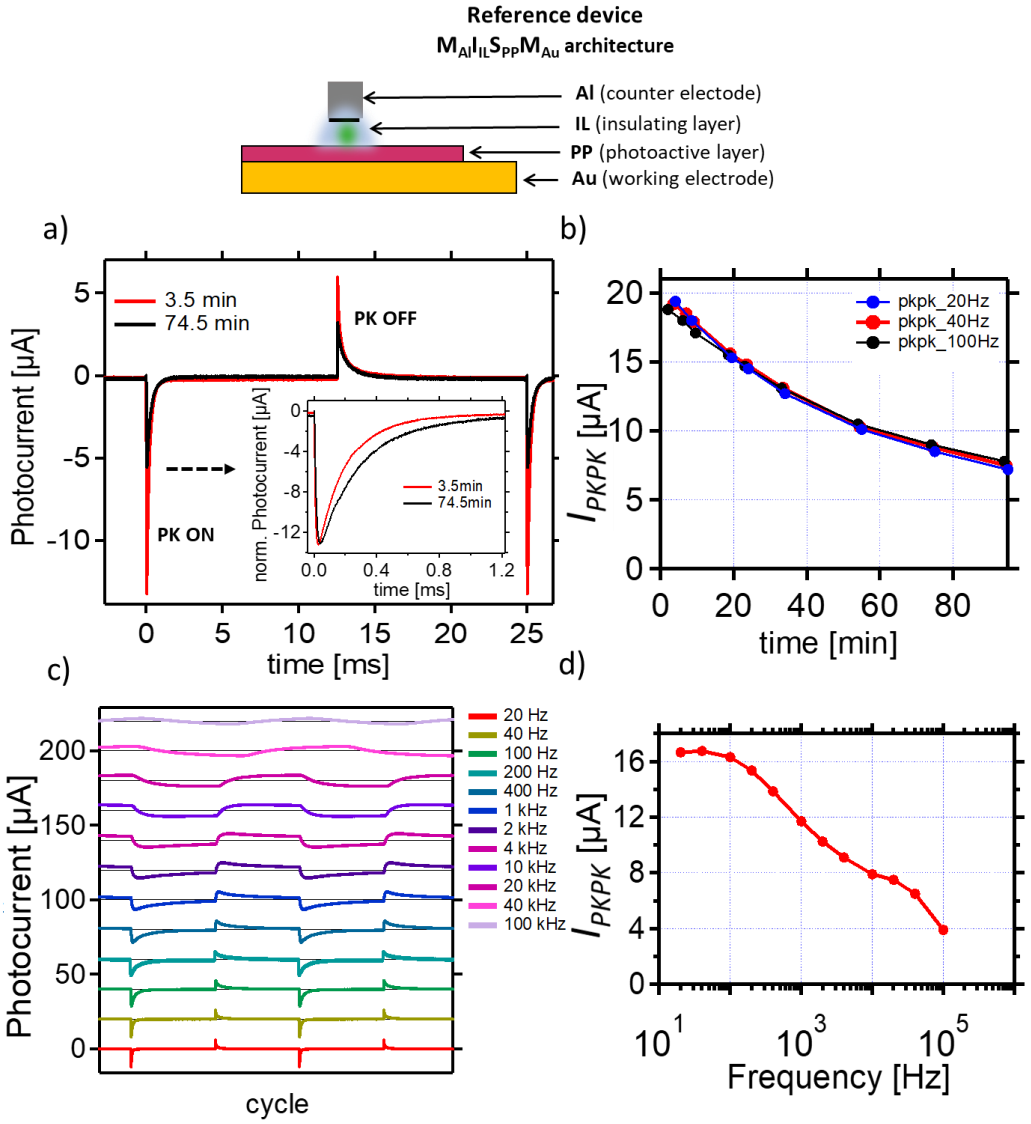

Fig. C.7. A sketch of the reference device architecture (at the top). (**a**) The generated transient signal (recorded at 40 Hz) at different times from the first exposure to the flickering light signal. The inset shows the normalized Light ON peaks, illustrating that the decay time became slower over operation time. (**b**) The time-dependence of I_{PKPK} value at three frequencies that showed an almost full decay for the transient peaks. (**c**) The changes in the transient signal shape and magnitude at different frequencies. (**d**) The frequency-dependence of I_{PKPK} value. The standard deviation (extracted from the oscilloscope) of the average I_{PKPK} values shown in (**b**) and (**d**) was up to ± 0.8 μA.

Figs. C.7c and **d** show the dependency of the transient signal shape and magnitude on the flickering light frequency. The device reached almost a full decay for the PK ON and OFF at frequencies 20, 40, and 100 Hz. By increasing the frequency, the **charging/discharging** of the capacitor at the interfaces of the IL layer cannot be fully accomplished (the decay of the transient peaks is cut off). This observation was increased by increasing frequency till the device behavior was changed and the I_{pkpk} value dramatically dropped.

Diatom-based Photodetectors

Figs. C.8 and **C.9** illustrate the photocurrent results of diatom-based MISM photodetectors. In general, the transient signal intensity (I_{pkpk} value) of diatom-based devices was significantly lower than that of the reference device. When diatom-based devices were exposed to the flickering light, the transient signal appeared as a negative PK ON (positive PK OFF), indicating that the electrons were extracted at the $\mathbf{M_{Au}/S_{PP}}$ interface, similar to the reference device. Additionally, a double peak behavior was observed in both cases, which indicated the presence of competing currents, as suggested in [345,351]. That means there were also holes extracted at $\mathbf{M_{Au}/S_{PP}}$ interface. After a few minutes, the polarity was inverted to have a positive PK ON (negative PK OFF), which indicated that the extraction of holes at the $\mathbf{M_{Au}/S_{PP}}$ interface became more favourable.

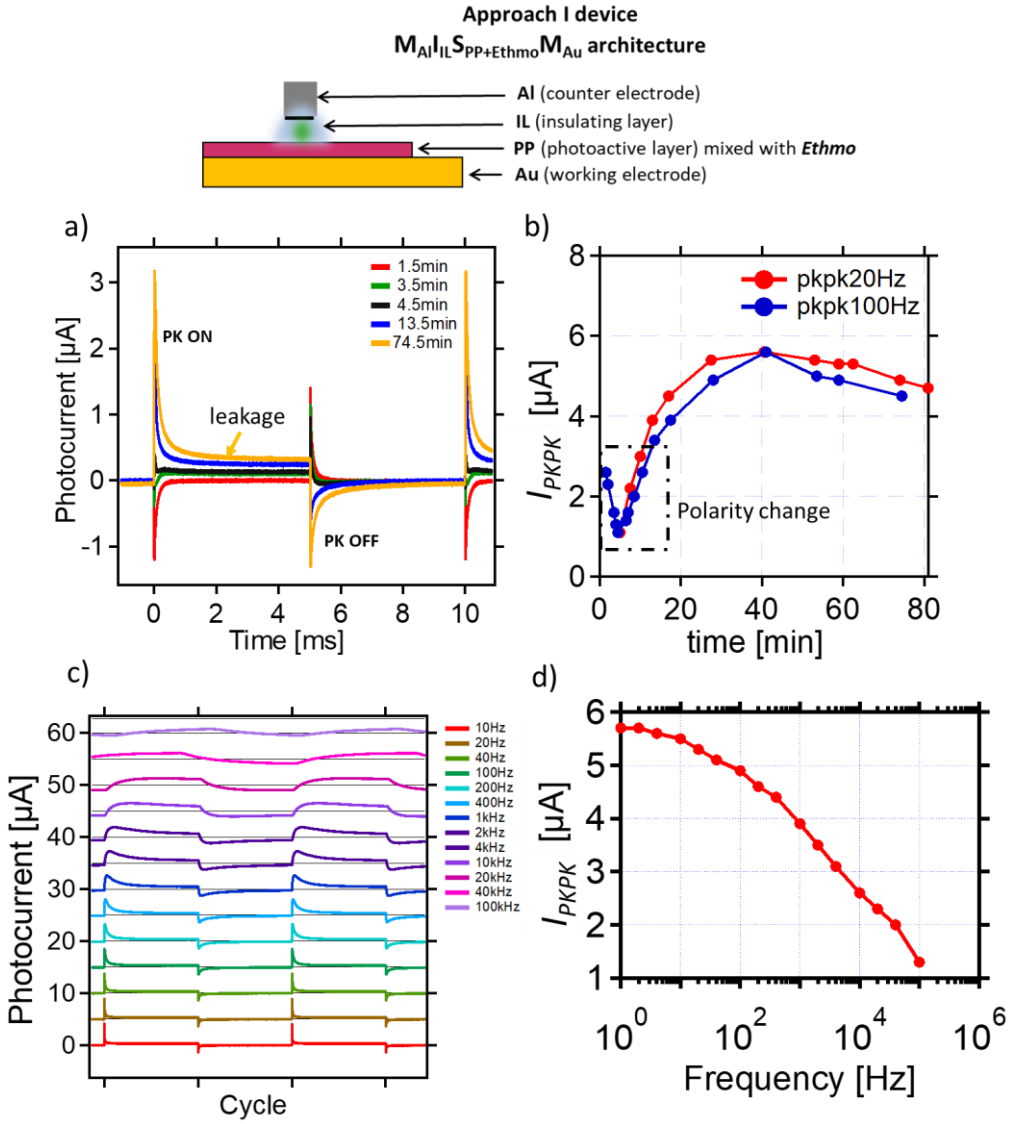

Fig. C.8. A sketch of the diatom-based device (Approach I) architecture (at the top). (**a**) The generated transient signal (recorded at 100 Hz) at different times from the first exposure to the ON/OFF light signal. (**b**) The time-dependence of I_{PKPK} value at two different frequencies.

(**c**) The changes in the transient signal shape and magnitude at different frequencies. (**d**) The frequency-dependence of I_{PKPK} value. The standard deviation of the average I_{PKPK} values shown in (**b**) and (**d**) was up to ± 1.2 µA.

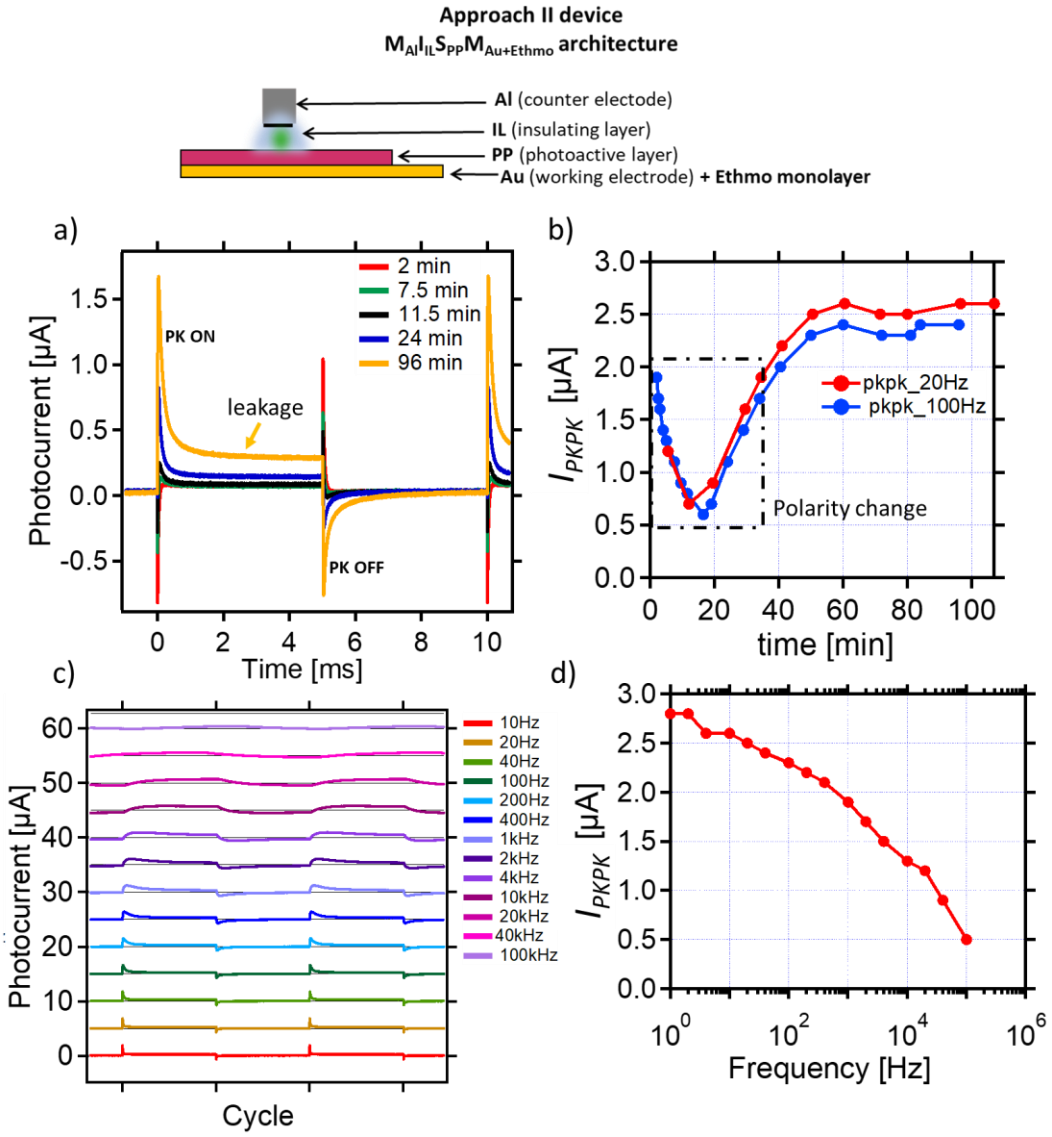

Fig. C.9. A sketch of the diatom-based device (Approach II) architecture (at the top). (**a**) The generated transient signal (recorded at 100 Hz) at different times from the first exposure to the ON/OFF light signal. (**b**) The time-dependence of I_{PKPK} value at two different frequencies. (**c**) The changes in the transient signal shape and magnitude at different frequencies. (**d**) The frequency-dependence of I_{PKPK} value (**d**). The standard deviation of the average I_{PKPK} values shown in (**b**) and (**d**) was up to ± 0.5 µA.

In the case of $\mathbf{M_{Al}I_{IL}S_{PP+Ethmo}M_{Au}}$ device, the polarity inversion was likely associated with the changes introduced to the $\mathbf{S_{PP}}$ layer by inserting *Ethmo* fragments, which is evident in the UV-Vis spectrum and optical micrographs of the $\mathbf{S_{PP+Ethmo}}$ layer (See **subsection C.2.2**). Introducing *Ethmo* fragments seemed to change the microstructure of the P3HT:PCBM blend, as some places of the annealed film had colorless zones, which might indicate the presence of only PCBM (**Fig. C.6**).

The UV-Vis spectrum suggested that the amount of PCBM was much reduced after annealing (**Fig.C.5**), which might be correlated to specific unknown interactions of PCBM molecules and *Ethmo* fragments that need further investigations. Such changes may lead to decreasing the fermi level of the blend, thus influencing the potential difference across the IL layer and consequently, the signal polarity, a situation similar to using a higher ratio of P3HT relative to PCBM, reported in [345,351]. The *Ethmo* fragments also seemed to introduce defects to the $\mathbf{S_{PP}}$ layer (see **Fig. C.6**, blue arrow), which could influence the electronic properties of the layer.

A similar scenario can be suggested for the $\mathbf{M_{Al}I_{IL}S_{PP}M_{Au+Ethmo}}$ device where the presence of *Ethmo* fragments monolayer underneath the 10 nm gold layer could influence the spin coating and annealing of the P3HT:PCBM film, but also adding to that the increased resistance of the ultrathin Au working electrode if compared to the 100 nm Au working electrode of $\mathbf{M_{Al}I_{IL}S_{PP+Ethmo}M_{Au}}$ and reference devices, which likely also contributed to the observed reduction in the signal intensity (**Fig. C.9a** *vs.* **C.8a**). Despite that, it was remarkable to obtain the charges still extracted from such ultrathin film with a magnitude still comparable to the $\mathbf{M_{Al}I_{IL}S_{PP+Ethmo}M_{Au}}$ device of 100 nm working electrode. Possible localized SPR effects associated with the ultrathin film could be an interesting feature to investigate in future work; however, the thickness needs to be optimized first to increase the signal magnitude.

After the polarity inversion, by operating $\mathbf{M_{Al}I_{IL}S_{PP+Ethmo}M_{Au}}$ device, the I_{pkpk} value increased until reaching a maximum before slowly decreasing (**Fig. C.8b**). A steady-state positive current (leakage) of about 0.3 µA (after an operating time ≈ of 74 min) was observed only in the PK ON, which was increasing with time (**Fig. C.8a**). This might be attributed to the presence of trapped charges inside $\mathbf{S_{PP+Ethmo}}$ layer accumulating over time. In the case of $\mathbf{M_{Al}I_{IL}S_{PP}M_{Au+Ethmo}}$ device, the polarity inversion needed a longer time (**Fig. C.9b**), while the steady-state positive current was also about 0.3 µA (after an operating time ≈ of 96 min) (**Fig. C.9a**).

C.3. Conclusion and future work

It can be concluded from the literature, as well as the light modulation capabilities illustrated in this thesis, that incorporating diatom valves within (or in proximity) the photoactive layer of any optoelectronic device would increase the local electric field $\mathbf{E_{loc}}$ within that layer, thus enhancing its absorption. Nevertheless, integrating *Ethmo* fragments into the photoactive electrode of MISM devices using the previous approaches seems to deteriorate their performance, probably by influencing the electronic properties of the $\mathbf{S_{PP}}$ layer. In this case, even if diatoms enhanced the absorption of the $\mathbf{S_{PP}}$ layer, the ability to extract the photogenerated charges

decreased. The presence of defects in the $\mathbf{S_{PP}}$ layer, double peak behavior, and the observed leakage are all problems that need to be solved.

Future work should consider testing other approaches for integrating diatom valves into the device architecture to solve the observed problems. One approach, as already mentioned, could achieved by optimizing the $\mathbf{M_{Al}I_{IL}S_{PP}M_{Au+Ethmo}}$ device, which can be carried out by optimizing the thickness of the gold layer and/or by inserting an additional insulating layer between $\mathbf{M_{Au+Ethmo}}$ and $\mathbf{S_{PP}}$ layers (to facilitate spin coating of a smooth $\mathbf{S_{PP}}$ layer on top), obtaining an MISIM architecture. Alternatively, the diatom valves can also be mixed with the **IL** layer, which can be settled on top of the $\mathbf{S_{PP}}$ layer. In this case, the light will reach diatom valves first before being scattered. In this approach, the type of ionic liquid (its electric permittivity) is expected to change the light modulation abilities of these valves. Another approach is to employ different methods to form the $\mathbf{S_{PP}}$ layer rather than spin coating. Finally, we should, in all cases, select the suitable valves (and if possible, their orientation on the substrate) that could strongly enhance $\mathbf{E_{loc}}$ (*e.g.*, by initiating GMR or Talbot effect) within the spectral window of the device (*i.e.*, at the range of wavelengths that can be detected by the device).

List of publications

Peer-reviewed articles

Ghobara, M., Oschatz, C., Fratzl, P., & Reissig, L. (**2023**) Numerical Analysis of the Light Modulation by the Frustule of *Gomphonema Parvulum*: The Role of Integrated Optical Components. *Nanomaterials*, *13*, 113. Doi: 10.3390/nano13010113.

Gilic, M., **Ghobara, M.**, & Reissig, L. (**2023**) Tuning SERS Signal via Substrate Structuring: Valves of Different Diatom Species with Ultrathin Gold Coating. *Nanomaterials*, *13*, 1594. Doi: 10.3390/nano13101594.

Articles in preparation

Ghobara, M., Gilic, M., Fumagalli, P., & Reissig, L. Light Focusing by Side-Illumination of Diatom Valves. *In preparation*.

Peer-reviewed book chapters

Ghobara, M., Mazumder, N., Vinayak, V., Reissig, L., Gebeshuber, I.C., Tiffany, M.A., & Gordon, R. (**2019**). On light and diatoms: A photonics and photobiology review, In: *Diatoms: Fundamentals & Applications [DIFA, Volume 1 in the series: Diatoms: Biology & Applications, series editors: Richard Gordon & Joseph Seckbach]*. J. Seckbach and R. Gordon (eds.), Wiley-Scrivener, Beverly, MA, USA, pp. 129-190. DOI: 10.1002/9781119370741.ch7.

Ghobara, M.M., Tiffany, M.A., Gordon, R. & Reissig, L. (**2021**). Diatom pore arrays' periodicities and symmetries in the Euclidean plane: nature between perfection and imperfection. In: Diatom Morphogenesis *[DIMO, Volume in the series: Diatoms: Biology & Applications, series editors: Richard Gordon & Joseph Seckbach]*. V. Annenkov, J. Seckbach, and R. Gordon (eds.), Wiley-Scrivener, Beverly, MA, USA: 117-158. DOI: 10.1002/9781119488170.ch6.

Peer-reviewed Conference papers

Ghobara, M., Oschatz, C., Fratzl, P., & Reissig, L. (**2021**). Light Modulation by a Small Pennate Diatom Valve: The Case of *Gomphonema parvulum.* In: IEEE Photonics Conference (IPC) 2021, Vancouver, Canada (Online), 18-21 October. DOI:10.1109/IPC48725.2021.9592922.

Gilic, M., **Ghobara, M.**, & Reissig, L. (**2022**). Boosting Surface-Enhanced Raman Scattering by Ultrathin Golden Film on Bio-Photonic Crystals. In: Proceedings of the Optica Advanced Photonics Congress 2022, Maastricht, Limburg, Netherlands (Online), 24-28 July. DOI: 10.1364/BGPPM.2022.JW3A.52.

Conference abstracts

Ghobara, M., Gordon, R., & Reissig, L. (**2019**) Diatom frustules: A biomaterial with promising photonic properties. In: Photonica2019, Belgrade, Serbia, 26-30 August.

Ghobara, M., Gordon, R., & Reissig, L. (**2020**) Diatom frustules: A biomaterial with promising photonic properties. In: the 13th Annual Meeting Photonic Devices, Zuse institute, Berlin, Germany, 12-14 February.

Ghobara, M., Oschatz, C., Fratzl, P., & Reissig, L. (**2021**) An Analytical Approach for Understanding Light Modulation by Diatom Frustules. In: the 6th Molecular life of Diatoms meeting (online), 12 – 14 July.

Gilic, M., **Ghobara, M.**, & Reissig, L. (**2021**) Boosting surface plasmon resonances of thin golden film by bio photonic crystals. In: Photonica2021, Belgrade, Serbia, 23-27 August.

Reissig, L., **Ghobara, M.**, Tiffany, M.A., & Gordon, R. (**2021**) Shedding light on the perfections and imperfections in the symmetries and periodicities of diatom pore arrays. Online International Diatom Symposium 2021.

Gilic, M., **Ghobara, M.**, & Reissig, L. (**2022**) Photonic crystal behavior of biosilica influence of frustule's morphology on SERS sensitivity. In: the 15th Photonics workshop, Belgrade, Serbia, 13-16 March.

Ghobara, M., & Reissig, L. (**2022**) Photonic jets generated by pennate diatom valves. In: the 14th Annual Meeting Photonic Devices, Zuse institute, Berlin, Germany, 28-29 April.

Ghobara, M., Oschatz, C., Gilic, M., Fumagalli, P., & Reissig, L. (**2023**) Light Focusing in Pennate Diatoms: Can Living Diatoms See? In: the 8th European Phycological Congress (EPC8), Brest, France, 20-26 August.

Other irrelevant peer-reviewed publications during the doctoral period

Mohamed, A., **Ghobara, M.**, Abdelmaksoud, M., & Mohamed, G.G. (**2019**) A novel and highly efficient photocatalytic degradation of malachite green dye via surface modified polyacrylonitrile nanofibers/biogenic silica composite nanofibers. *Separation and Purification Technology*, 210, 935-942. DOI: 10.1016/j.seppur.2018.09.014

Ghobara, M. & Mousa, A.M. (**2019**) Diatomite in use: Nature, modification, commercial applications, and prospective trends. In: *Diatoms: Fundamentals & Applications [DIFA, Volume 1 in the series: Diatoms: Biology & Applications, series editors: Richard Gordon & Joseph Seckbach]*. J. Seckbach and R. Gordon (eds.), Wiley-Scrivener, Beverly, MA, USA: 471-510. DOI: 10.1002/9781119370741.ch19.

Abdel Wahab, H., Malek, A., & **Ghobara, M.** (**2020**). Effects of some plant extracts, bioagents, and organic compounds on botrytis and sclerotinia molds. *Acta Agrobotanica*, 73(2). DOI: 10.5586/aa.7321.

K. Manoylov and **Ghobara, M.** (**2021**). Introduction for a Tutorial on Diatom Morphology. In: *Diatom Morphogenesis [DIMO, Volume in the series: Diatoms: Biology & Applications, series editors: Richard Gordon & Joseph Seckbach]*. V. Annenkov, J. Seckbach, and R. Gordon (eds.), Wiley-Scrivener, Beverly, MA, USA: 1-18. DOI: 10.1002/9781119488170.ch1.

Ghobara, M., Gordon, R., & Reissig, L. (**2021**). The mesopores of raphid pennate diatoms: Toward natural controllable anisotropic mesoporous silica microparticles. In: *Diatom Morphogenesis [DIMO, Volume in the series: Diatoms: Biology & Applications, series editors: Richard Gordon & Joseph Seckbach].* V. Annenkov, J. Seckbach and R. Gordon (eds.), Wiley-Scrivener, Beverly, MA, USA: 383-409. DOI:10.1002/9781119488170.ch16.

Ghobara, M., El-Sheekh, M., Hamed, A.F., Abdelhamid, M.A.A., & Pack, S.P. (**2023**). Diatom Nanostructured Biosilica. In: *Value-added Products from Algae*. A. Abomohra and S. Ende (eds.), Springer, Cham. DOI: 10.1007/978-3-031-42026-9_14.

Liesegang, M., **Ghobara, M.**, Matting, S., & Wirth, R. (**2024**) The colourful optical appearance of centric diatom fossil frustules with diagenetic nanocrystalline calcite fill. *Facies*, 70, 1 (2024). DOI: 10.1007/s10347-023-00675-6.

Reissig, L., **Ghobara, M.**, Maibohm, C., & Goessling, J.W. (**2024**). A Journey to Mars with Diatoms on Board. In: *Diatom Photosynthesis [a Volume in the series: Diatoms: Biology & Applications, series editors: Richard Gordon & Joseph Seckbach].* J.W. Goessling, J. Serôdio, and J. Lavaud (eds.), Wiley-Scrivener, Beverly, MA, USA: 551-581. DOI: 10.1002/9781119842156.ch18.

Acknowledgments

First, I would like to thank **Prof. Dr. Louisa Reissig**, who supervised, encouraged, and helped me a lot during the first three years of my PhD. She also helped me a lot while transitioning from biology to physics and gave me the proper training on experimental and numerical techniques, enabling me to conduct the research work successfully. I would also like to thank her for the countless fruitful discussions, comments, and positive criticism that encouraged me to make more effort. Thanks also for her helpful comments and suggestions on earlier versions of my thesis.

I would like to express my sincere gratitude to my supervisor **Prof. Dr. Paul Fumagalli** for accepting me as a PhD student in his group upon the recommendation of Prof. Dr. Louisa Reissig. I am really grateful for his kindness, wisdom, knowledge, and unlimited support, and for guiding me through difficult times to reach the final steps in my thesis. Without his help, this thesis will not be there. He also helped me develop more toward physics. On a personal level, I learnt from his wisdom and leadership many lessons. I would also like to thank him very much for his helpful comments and suggestions on different versions of my thesis.

I would like to appreciate and thank **Prof. Dr. Stephanie Reich**, my second supervisor, for her help, understanding of the challenges I faced during my PhD journey, and the fruitful discussions and suggestions at different stages of my thesis.

I am deeply grateful to **Dr. Martina Gilic** and would like to thank her very much for all the work that we did together during her PostDoc in the department and all fruitful discussions. She has also helped me to learn more about Raman spectroscopy and SERS substrates. She also helped me with many SEMs images she captured during our research work. She was really a good friend who advised me during the hard times I faced in my PhD journey. I am really grateful for her help.

I am really grateful to **Dr. Yasser Shokr** for all the mental support, discussions, and advice he offered during my PhD. He was more than a brother and helped me settle in Berlin.

I would like to thank all my colleagues from **AG Fumagalli** and **AG Reissig**, whom I enjoyed discussions with. I would also like to thank people from other research groups in the department who gave me access to their labs and equipment during my PhD time, including **AG Heberle**, **AG Bolotin**, and **AG Reich**. My sincere thanks also go to the administrative members of the department, **Mrs Badow**, **Mrs Endrias**, and **Mrs Cech** for their unlimited help and support.

My sincere thanks also go to **Dr. Cathleen Oschatz** (Max Planck Institute of Colloids and Interfaces, Potsdam, Germany) for collaboration through providing

many samples, 3D FIB-SEM and SEM data, and fruitful discussions. Her insightful work helped me to reach a greater understanding of the topic.

I am deeply thankful to **Prof. Dr. Richard Gordon** (Retired from the University of Manitoba, Canada) for his unlimited help and support since my graduation. His work on diatoms has motivated me since then. He really helped me a lot to develop my understanding and writing and mentored me to achieve more success.

Great thanks to **Dr. Marry Ann** (USA) for providing many SEMs, her insightful work and fruitful cooperation.

I deeply appreciate and thank **Prof. Dr. Abdelfattah Zalat** (Department of Geology, Tanta University, Egypt) for all the training and experience given to me during my master's thesis preparation (2013 – 2016). This training helped me a lot in my PhD.

On a personal level, I cannot find words enough to express my thanks to my lovely wife **Mai**, who supported my dream since the beginning, helped me in all steps, and did her best in raising our kid **Lian** during my busy times while preparing the thesis. I would also like to thank my sisters Marwa and Safa, my in-laws, and my close friends, especially **Eng. Ahmed Mohsen**, for their support and help during my journey. I deeply thank my parents (who passed away) for believing in me and supporting me to become better. I owe them a lot and cannot find words to express that.

Finally, I would like to thank the **Deutsche Forschungsgemeinschaft** (DFG) for their funding for more than three years. I also appreciate the **Physics Department** (FU Berlin) for providing a six-month Corona fund to help me and my family recover Corona time. Deep thanks to **Prof. Paul Fumagalli** for providing the funds needed to complete my thesis.

Declaration of authorship

I declare to the Freie Universität Berlin that I have completed the submitted dissertation independently and without the use of sources and aids other than those indicated. The present thesis is free of plagiarism. I have marked as such all statements/contents that are taken literally or in content from other writings or colleagues. This dissertation has not been submitted in the same or similar form in any previous doctoral procedure.

I agree to have my thesis examined by a plagiarism examination software.

Berlin, 2024
Mohamed Ghobara